博士論文（要約）

Study on emergent multiple quadrupolar phases in two-dimensional spin-1 quantum magnets

（2 次元スピン 1 量子磁性体における四極子秩序の創出）

田中 克大

Abstract

In this thesis, we study the quadrupolar phases in quantum spin systems. The spin quadrupolar phases in the absence of the dipolar order are also known as spin nematic phases, in analogy with the nematic phase in the liquid crystals. The spin nematic phase has been intensively studied since 2000's. A typical platform realizing the spin nematic order is the spin-1 bilinear-biquadratic model, where the biquadratic interaction, $(\boldsymbol{S}_i \cdot \boldsymbol{S}_j)^2$, written in terms of spin-1 operator, $\boldsymbol{S}_i$, is a main source for generating the quadrupole moments on the spin-1 sites. However, the system with large biquadratic interaction is elusive in reality, since the biquadratic interaction is generated from the higher-order exchange processes of electrons than the Heisenberg interactions, so that the former is often much smaller than the latter and gives way to magnetic orderings. In spin-1/2 systems, more realistic situations realizing the spin nematic phases have been proposed. In the vicinity of the ferromagnetic phase, the bound two-magnons condense, generate the quadrupole moments on bonds, and form the spin nematic phase. There, the kinetic motion of the single-magnons, which destabilizes the nematic order and contributes to the magnetic order, is suppressed by the competing antiferromagnetic and/or ring-exchange interactions. Actually, some experiments have reported the possible realization of spin nematic phases in spin-1/2 frustrated ferromagnets.

Unlike the usual magnetic orders, the quadrupolar moment does not directly couple to the magnetic field, which makes the spin nematic order a sort of "hidden order". Many theoretical proposals for probing the spin nematic phase have been given, while so far they are not fully successfully applied to experimental measurements. Moreover, the actual search of spin nematics in materials has been done in a high magnetic field with the aim to detect the two-magnon bound state. This restricts the search for the spin nematics to the limited numbers of materials with small enough magnetic interactions to access the fully-saturated state. The present study aims to add some clue for experimentally detecting the spin nematic phase in a handy way, and to offer another platform which allows us to find the quadrupolar phase with ease.

Firstly, we investigate the magnetic field effect on the thermodynamic properties of spin-1 nematic phase in two-dimension. We find the characteristic field-dependence of the peak in the specific heat that indicates the paramagnetic-to-ferroquadrupolar phase transition temperature; the transition temperature once slightly increases in an applied magnetic field, and decreases in a larger field. This reentrant behavior is the entropic effect which can be understood in analogy with the Pomeranchuk effect in ^{3}He, and may serve as a smoking gun for experiments.

Secondly, we discuss the ground states of the spin-1 dimer-based triangular lattice forming a bilayer to understand the nature of the ruthenium dimer materials $Ba_3MRu_2O_9$,

where M is the divalent cation. In $Ba_3MRu_2O_9$, a pair of Ru^{5+}-ions placed face to face form a dimer, and the dimers form a two-dimensional triangular lattice structure. In this family of materials, the spin-liquid-like nonmagnetic phase was recently found next to the gapped singlet phase. There appeared a theoretical proposal that the antiferroquadrupolar spin nematic phase is realized next to the singlet phase in the spin-1/2 dimer-based triangular lattice. However, the size of the spin the ruthenium ions host is large, possibly $S = 1$, and the spin-1/2 dimer system may not give a proper description. Motivated by these studies, we examined the spin-1 dimers, and find that several types of spin quadrupolar phases formed by triplet dimers widely appear thanks to the larger degrees of freedom than spin-1/2. We classify these quadrupolar phases by the internal degrees of freedom of dimers, the staggered spin moment and vector-chirality, and argue that one of them next to the singlet phase might correspond to the intriguing nonmagnetic phase in $Ba_3MRu_2O_9$.

In addition, we give a theoretical support on the reason why the dimer structure has an advantage for designing the materials with spin nematic phases. As mentioned earlier, the major driving force of the spin nematics is the large biquadratic interaction between triplets. By the perturbation calculation starting from the Mott insulating electronic state, we reexamine this interaction, finding that the dimer structure actually has a route to have a large biquadratic interaction comparable to the Heisenberg one, when some particular geometry of the electronic hopping between dimers is considered.

Our study on spin dimers also provides some clue to unify the theoretical description of spin-1 and spin-1/2 based nematics; we find that the low-energy physics of both the spin-1 dimer and spin-1/2 dimer based systems are described on an equal footing, since both are mapped to the same spin-1 hard-core bosonic model. From this finding, we set our future perspective to describe a variety of quadrupolar/spin-nematic phases — spin nematics of spin-1 quantum spin system, spin-1/2 system on a low-dimensional lattices near the ferromagnetic phase or at high fields, and the dimer system — using the common local operators, which is the set of four internal degrees of freedom of spin-1/2 dimer. In this thesis, we investigate the spin-1/2 two-leg ladder system in a high field as a first step, and show how the two-magnon bound state can be redescribed using the dimer-based formulation which we adopted previously for both the spin-1 and spin-1/2 based dimer systems without the magnetic field.

Contents

List of publications

The main contents of this thesis were published in the following two articles;

- Katsuhiro Tanaka and Chisa Hotta,

  "Finite-temperature thermodynamic properties of spin-1 nematics in an applied magnetic field",

  Physical Review B **102**, 140401(R) (2020) [1].

  The contents in Chapter 2 was published in this paper.

- Katsuhiro Tanaka and Chisa Hotta,

  "Multiple quadrupolar or nematic phases driven by the Heisenberg interactions in a spin-1 dimer system forming a bilayer",

  Physical Review B **101**, 094422 (2020) [2].

  The contents in Chapter 3 was published in this paper.

We also discuss in Chapter 4 the contents given in the following article, which are closely related to the topics in Chapter 3 and Chapter 5.

- Katsuhiro Tanaka, Yuto Yokoyama, and Chisa Hotta,

  "Origin of Biquadratic Exchange Interactions in a Mott Insulator as a Driving Force of Spin Nematic Order",
  Journal of the Physical Society of Japan **87**, 023702 (2018) [3].

Chapter 1

Introduction

In this Chapter, we overview the previous studies on the multipolar orders, particularly the spin quadrupolar order known as spin nematic orders, and outline the motivation and purpose of this thesis.

1.1 Quadrupolar order in quantum spin systems

Electrons have a variety of degrees of freedom, such as the charges, orbitals, and spins, and there are multipole moments corresponding to those degrees of freedom, which widely appear in the symmetry-broken phases in the condensed matters. For the charges, the ferroelectricity appears when the electric dipoles are ordered and break the spatial inversion symmetry [4]. When the orbital degrees of freedom is regarded as the pseudospin, the orbital ordering, where electrons occupy the same kinds of orbitals of all ions with orbital degeneracy, is the dipolar order of pseudospins [5, 6]. Higher-rank multipoles, e.g., the electric quadrupoles and the magnetic octupoles, appear in the heavy-fermion systems [7]. Moreover, the quantum mechanical framework of the multipole operators for the multiple atoms or orbitals has been developed [8–12], which is actually applied to the characterization of emergent phenomena in materials [13].

In quantum spin systems, the quadrupolar ordering of the spins without magnetic order has been discussed for years, which is called spin nematic order. The possibility of the quadrupolar ordering of spins was first discussed by Blume and Hsieh using the spin-1 model with the Heisenberg interactions $\boldsymbol{S}_i \cdot \boldsymbol{S}_j$ and the biquadratic interactions $(\boldsymbol{S}_i \cdot \boldsymbol{S}_j)^2$ (the bilinear-biquadratic model which we see in detail below), where $\boldsymbol{S}_i = {}^t\left(S_i^x \quad S_i^y \quad S_i^z\right)$ is the spin-1 operator [14]. From the mean-field approach, they proposed that the quadrupolar orderings are realized if the biquadratic interactions are sufficiently large. Chen and Levy analyzed the bilinear-biquadratic model with the molecular field approximation [15]. Andreev and Grishchuk termed this quadrupolar order spin nematics, and they extended the concept of the quadrupolar order to the spin-1/2 systems where the quadrupolar moments are defined by two spin-1/2's [16].

Spin nematics owes its name to the nematic order of the liquid crystals. When the liquid crystal molecules, which have elliptical shapes, align without the positional order where the positions of the liquid crystals are fixed, the nematic order is realized. For the quantum spins, the spin quadrupolar moments do not have a specific direction, and when

the quadrupolar moments align, the spin nematic order, the spin version of the nematic order, is realized [1].

1.2 Spin nematic phases in the spin-1 systems

To write a part of this section and the next section (Sec. 1.3), we partly referred to Ref. [17].

1.2.1 Order parameter

The order parameter of the spin nematic phases or the spin quadrupolar phases is the spin quadrupolar moment which is the rank-2 symmetric traceless tensor and is defined as

$$Q_i^{\alpha\beta} = S_i^\alpha S_i^\beta + S_i^\beta S_i^\alpha - \frac{2}{3} S\left(S+1\right)\delta_{\alpha\beta}, \tag{1.1}$$

where $\alpha, \beta = x, y, z$, and $\delta_{\alpha\beta}$ is the Kronecker's delta [2]. When $\boldsymbol{S}_i$ is the spin-1/2 operator, the quadrupolar operator $Q_i^{\alpha\beta}$ is always zero, which can be derived by the anticommutation relation of the spin-1/2 operators given as $S_i^\alpha S_i^\beta + S_i^\beta S_i^\alpha = \frac{1}{2} I \delta_{\alpha\beta}$, where I is the identity operator. Therefore, the quadrupolar moment defined on-site (Eq. (1.1)) is meaningful only for $S \geq 1$, and the quadrupolar order is typically discussed in spin-1 systems.

Since $Q_i^{\alpha\beta}$ is the rank-2 symmetric traceless tensor, the number of linearly independent components in $Q^{\alpha\beta}$ is five. Conventionally, the five components are chosen as [3]

$$\boldsymbol{Q}_i = \begin{pmatrix} Q_i^{x^2-y^2} \\ Q_i^{3z^2-r^2} \\ Q_i^{xy} \\ Q_i^{yz} \\ Q_i^{zx} \end{pmatrix} = \begin{pmatrix} (S_i^x)^2 - (S_i^y)^2 \\ \frac{1}{\sqrt{3}}\left[3\left(S_i^z\right)^2 - S\left(S+1\right)\right] \\ S_i^x S_i^y + S_i^y S_i^x \\ S_i^y S_i^z + S_i^z S_i^y \\ S_i^z S_i^x + S_i^x S_i^z \end{pmatrix}, \tag{1.3}$$

which is a similar form to the electronic wave-function of the d-orbital.

In the light of the symmetry breaking, the spin nematic order partially breaks the SU(2) symmetry [4]. For the spin nematic order, the rotational symmetry of spins is broken, but the time-reversal symmetry is kept since the magnetic (dipolar) order is lost. We can confirm it in a one-site system; let us consider the spin-1 state given as

$$|\psi_i\rangle = \sum_{\alpha=x,y,z} d_{i,\alpha} |\alpha\rangle . \tag{1.4}$$

[1] Unlike the nematic order in the liquid crystals, where the positional order is not present, the positions of the spin quadrupolar moments are fixed on sites if we consider the lattice systems.

[2] $\delta_{\alpha\beta} = \begin{cases} 1 & (\alpha = \beta) \\ 0 & (\alpha \neq \beta) \end{cases}$.

[3] Using $Q_i^{\alpha\beta}$, $Q_i^{x^2-y^2}$ and $Q_i^{3z^2-r^2}$ are expressed as

$$Q_i^{x^2-y^2} = \frac{1}{2}\left(Q_i^{xx} - Q_i^{yy}\right), \; Q_i^{3z^2-r^2} = \frac{1}{2\sqrt{3}}\left(2Q_i^{zz} - Q_i^{xx} - Q_i^{yy}\right). \tag{1.2}$$

[4] Or O(2) symmetry for the spin nematics in the spin-1/2 systems in a magnetic field.

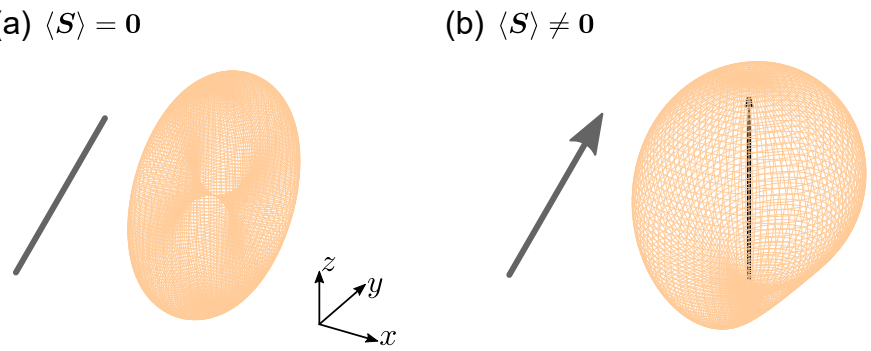

Figure 1.1: (a) Schematic picture of the quadrupolar state $\langle \boldsymbol{S} \rangle = \boldsymbol{0}$ (left) and the spin-component distribution (right) when $\boldsymbol{d} = {}^t\begin{pmatrix}1 & 0 & 0\end{pmatrix}$. (b) Same as (a) for the magnetic state $\langle \boldsymbol{S} \rangle \neq \boldsymbol{0}$. The arrow in the spin-component distribution denotes the magnetization along the z-axis.

Here, $d_{i,\alpha}$ is the complex coefficient and $|\alpha\rangle$ is the time-reversal invariant basis states given as [17–19]

$$|x\rangle = \frac{\mathrm{i}}{\sqrt{2}}\left(|+1\rangle - |-1\rangle\right), \ |y\rangle = \frac{1}{\sqrt{2}}\left(|+1\rangle + |-1\rangle\right), \ |z\rangle = -\mathrm{i}\,|0\rangle\,, \tag{1.5}$$

where $|n\rangle$ $(n = 0, \pm 1)$ denotes the spin-1 state with $S^z = n$. The vector representation of $d_{i,\alpha}$, $\boldsymbol{d}_i = {}^t\begin{pmatrix}d_{i,x} & d_{i,y} & d_{i,z}\end{pmatrix}$, is called $\boldsymbol{d}$-vector. Using the $\boldsymbol{d}$-vector, the expectation value of the spin and quadrupolar moments are given as

$$\langle \boldsymbol{S}_i \rangle = \langle \psi_i | \boldsymbol{S}_i | \psi_i \rangle = -\mathrm{i} \begin{pmatrix} d_y^* d_z - d_z^* d_y \\ d_z^* d_x - d_x^* d_z \\ d_x^* d_y - d_y^* d_x \end{pmatrix}, \tag{1.6}$$

$$\langle \boldsymbol{Q}_i \rangle = \langle \psi_i | \boldsymbol{Q}_i | \psi_i \rangle = - \begin{pmatrix} |d_{i,x}|^2 - |d_{i,y}|^2 \\ \frac{1}{\sqrt{3}}\left(2\,|d_{i,z}|^2 - |d_{i,x}|^2 - |d_{i,y}|^2\right) \\ \left(d_{i,x}^* d_{i,y} + d_{i,y}^* d_{i,x}\right) \\ \left(d_{i,y}^* d_{i,z} + d_{i,z}^* d_{i,y}\right) \\ \left(d_{i,z}^* d_{i,x} + d_{i,x}^* d_{i,z}\right) \end{pmatrix}. \tag{1.7}$$

When $\boldsymbol{d}$ has only the real components, $|\psi_i\rangle$ is time-reversal invariant, and $\langle \boldsymbol{S}_i \rangle$ becomes zero, while $\langle \boldsymbol{Q}_i \rangle$ have nonzero components, which expresses the spin nematic state as shown in Fig. 1.1(a). Once $\boldsymbol{d}$ has an imaginary component, $|\psi_i\rangle$ breaks the time-reversal symmetry, and $\langle \boldsymbol{S}_i \rangle$ takes nonzero values at the same time, which is the magnetic state (see Fig. 1.1(b)).

1.2.2 A canonical model: bilinear-biquadratic model

As was already discussed in the first stage of the studies on the spin nematics [14, 15], one of the main origins of the spin nematic phases are the biquadratic exchange interactions $(\boldsymbol{S}_i \cdot \boldsymbol{S}_j)^2$. This can be understood by the fact that for $i \neq j$ the biquadratic interactions

$(\boldsymbol{S}_i \cdot \boldsymbol{S}_j)^2$ can be rewritten using the quadrupolar operator as [17, 19] [5]

$$(\boldsymbol{S}_i \cdot \boldsymbol{S}_j)^2 = \frac{1}{2}\boldsymbol{Q}_i \cdot \boldsymbol{Q}_j - \frac{1}{2}\boldsymbol{S}_i \cdot \boldsymbol{S}_j + \frac{1}{3}S^2 (S+1)^2 . \tag{1.9}$$

To discuss the spin nematic phases in spin-1 systems, the spin-1 bilinear-biquadratic (BLBQ) model [14, 15];

$$\mathcal{H}_{\mathrm{BLBQ}} = \sum_{\langle i,j \rangle} \left[J\boldsymbol{S}_i \cdot \boldsymbol{S}_j + K (\boldsymbol{S}_i \cdot \boldsymbol{S}_j)^2 \right] \tag{1.10}$$

is very often used [6]. In this model, the Heisenberg (bilinear) interactions, $\boldsymbol{S}_i \cdot \boldsymbol{S}_j$, which usually lead to the magnetic orderings, and the biquadratic interactions, $(\boldsymbol{S}_i \cdot \boldsymbol{S}_j)^2$, which break the magnetic orderings and induce the quadrupolar (nematic) orderings, compete with each other. We can see the competition between the magnetic and quadrupolar orderings more explicitly by rewriting the Hamiltonian (Eq. (1.10)) using Eq. (1.9) as

$$\mathcal{H}_{\mathrm{BLBQ}} = \sum_{\langle i,j \rangle} \left[\left(J - \frac{K}{2} \right) \boldsymbol{S}_i \cdot \boldsymbol{S}_j + \frac{K}{2}\boldsymbol{Q}_i \cdot \boldsymbol{Q}_j + \frac{K}{3}S^2 (S+1)^2 \right] . \tag{1.11}$$

One can naively expect that the quadrupolar phase is realized when $\left| J - \frac{K}{2} \right| < \left| \frac{K}{2} \right|$, or $|J| < |K|$, and many analytical and numerical studies on the BLBQ models have shown that the quadrupolar phases do appear when $|J| \lesssim |K|$. In order to discuss how the magnetic properties are modified by the parameters J and K, frequently the parameters are rewritten as $J = \cos\theta$ and $K = \sin\theta$ with $-\pi < \theta \leq \pi$ [7], and the BLBQ Hamiltonian is rewritten as

$$\mathcal{H}_{\mathrm{BLBQ}} = \sum_{\langle i,j \rangle} \left[\cos\theta \boldsymbol{S}_i \cdot \boldsymbol{S}_j + \sin\theta (\boldsymbol{S}_i \cdot \boldsymbol{S}_j)^2 \right] \tag{1.12}$$

(see e.g., the phase diagrams in Figs. 1.2, 1.5(a)).

One-dimensional systems

Chubukov draw the ground state phase diagram of the BLBQ model on the one-dimensional chain by the bosonization technique [21], where he found a gapped dimerized phase with quadrupolar correlations in addition to the Haldane phase with a spin gap, a gapless trimerized phase, and a ferromagnetic phase. It then became controversial whether the non-dimerized spin nematic ordered phase exists between the dimerized phase induced by the Berry phase and the ferromagnetic phase. The spin nematic ordered phase is the condensate of director $\boldsymbol{d}$, and its coupling with the $\mathbb{Z}_2$ gauge field defined along the closed

[5] When $i = j$, Eq. (1.9) does not hold, and instead

$$\boldsymbol{Q}_i \cdot \boldsymbol{Q}_i = \frac{4}{3}S^2 (S+1)^2 - S(S+1) \tag{1.8}$$

holds.

[6] Here, $\sum_{\langle i,j \rangle}$ is the summation over a certain pair of spins i and j. In most cases, the nearest-neighbor pairs are adopted.

[7] Or equivalently $0 \leq \theta < 2\pi$ depending on the articles.

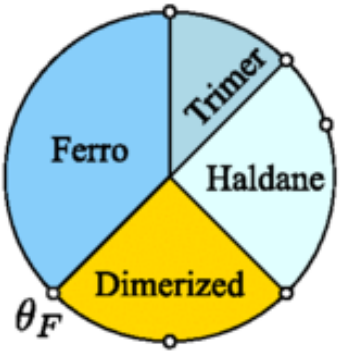

Figure 1.2: Phase diagram of the spin-1 bilinear-biquadratic model on the one-dimensional chain. Figure is taken from Ref. [20] (©2014 American Physical Society).

time loop gives an appropriate effective model for the quantum dynamics of $\boldsymbol{d}$ describing the disorders of the spin nematics. It was proposed that the dimerization occurs because the Berry phase associated with the gauge field leads to dimerization when the nematic order is disordered by condensing the $\mathbb{Z}_2$ disclinations [22, 23]. This phenomenon is in analogy with antiferromagnetic Heisenberg chain with the half-integer ($S = 1/2$) and integer spins ($S = 1$), where the presence of the Berry phase makes the excitations those in the former gapless and in the latter gapped. Hu and coworkers examined this effect in more detail [20]; from the low-energy effective theory, they found that the spin nematic order in the mean-field picture melts by the large quantum fluctuation and transforms to the gapped state and that the dimerization occurs by the Berry phase effect. They confirmed the dimerization by the density-matrix renormalization group calculations and concluded that the non-dimerized spin nematic phase does not exist. The dimerized phase with dominant quadrupolar correlations continues up to the boundary with the ferromagnetic phase. This dimerized phase with nematic correlations is one of the symmetry-protected topological phases consisting of the quadrupoles [24].

Although the non-dimerized spin nematic phase is not realized in the BLBQ models on the single chain, Läuchli, Schmidt, and Trebst showed that the spin nematic phase appears on the weakly-coupling two-leg ladder, where both of the interactions on the rungs and legs are described by the BLBQ interactions [25].

Two- and Three-dimensional systems

Papanicolaou studied the ground states of the BLBQ models by the semiclassical $1/N$-expansion approach which may give a reasonably accurate description of the three-dimensional model and pointed out the possibility of the quadrupolar ordering [27]. K. Tanaka, A. Tanaka, and Idogaki gave a rigorous proof that the BLBQ model on the cubic lattice has the ferro-quadrupolar long-range ordered ground state when $2.664J < K \leq 2J < 0$ [8] [28]. Harada and Kawashima performed the quantum Monte Carlo simulations and obtained the ground state properties of the model on the cubic lattice by the extrapolation of the order parameters of the finite-temperature to zero temperature [26]. They further performed the quantum Monte Carlo simulations on the square and cubic

[8] The notation is changed from the original article [28] to match the above BLBQ Hamiltonian (Eq. (1.10)).

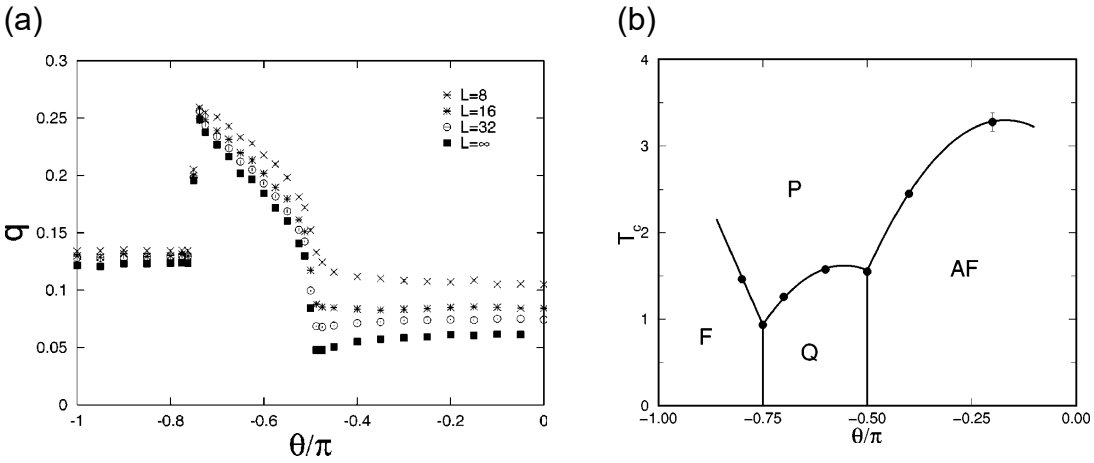

Figure 1.3: Studies on the spin-1 bilinear-biquadratic model in Eq. (1.12) by the quantum Monte Carlo approach. (a) Order parameter q of the ground state for the square lattice. (b) Phase diagram of at finite-temperature in the cubic lattice. Figures are taken from Ref. [26] (©2002 American Physical Society).

lattices when the biquadratic interaction parameter K is negative [26]; they identified the nematic order parameter in the square lattice at zero temperature as shown in Fig.1.3(a), confirming the mean-field argument [14] and semiclassical theory [27]. However, in two dimensions, the observed broad peak at the temperature that roughly corresponds to the development of the quadrupole moment is concluded not as a sign of the typical phase transition. By contrast, the nematic phase of the cubic lattice is robust at finite temperature (see Fig. 1.3(b)), which is identified by the size scaling analysis.

The ferroquadrupolar phase on the bipartite lattices is thus well established, while the antiferroquadrupolar phase needed to be examined in more detail. This is because the ground states are massively degenerate "semi-ordered" states when the variational or semiclassical methods are applied [27]. Tóth and coworkers examined by the numerical diagonalizations the region where the semi-ordered (SO) state is realized in the semiclassical approach [27] (See Fig. 1.4(a)), and obtained the results which suggest the semi-ordered phase is the three-sublattice antiferroquadrupolar phase in the fully-quantum picture [30]. Then, the studies by the series expansion [31] and the infinite projected entangled pair states methods [29] also indicated the presence of the three-sublattice antiferroquadrupolar phase on the square lattice. Figure 1.4(b) shows the details, where the SO region is divided into several phases when the quantum treatment is given.

The three-sublattice antiferroquadrupolar phase can be more naturally realized on a triangular lattice. Such studies were rather developed motivated by the triangular lattice compound $NiGa_2S_4$ [32]. Tsunetsugu and Arikawa studied the antiferroquadrupolar phase of the BLBQ model on the triangular lattice by the mean-field approximation and the bosonization method [33, 34]. They investigated the bosonic excitation from the antiferroquadrupolar ground states, and obtained the static and dynamical spin correlations, finding a gapless excitation which has a linear dispersion around the Γ-point. This excitation leads to the non-zero spin susceptibility even at $T = 0$ and the specific heat proportional to T^2 at low temperature. Parallelly, Läuchli, Mila, and Penc also examined the ground state and the excitation of the BLBQ model on the triangular lattice by

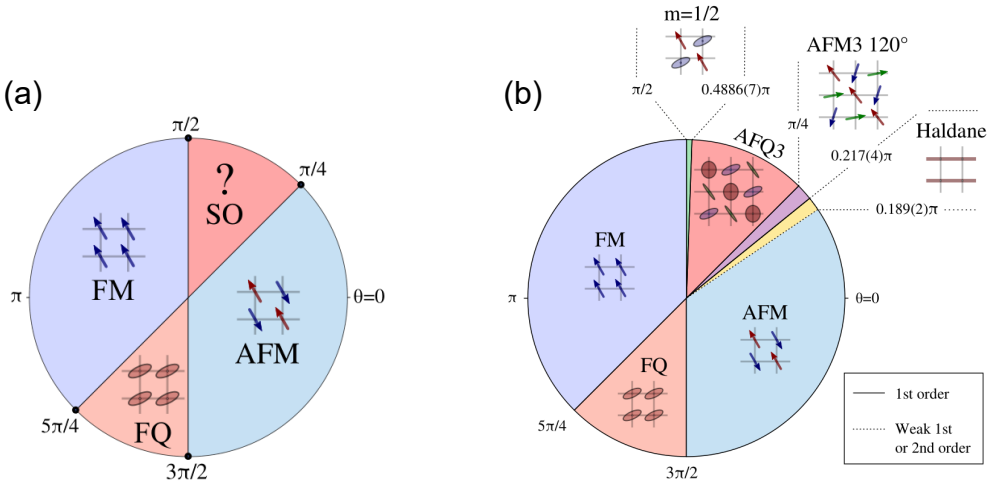

Figure 1.4: Phase diagram of the spin-1 bilinear-biquadratic model on the square lattice by (a) the semiclassical approach by Papanicolaou [27] and (b) the infinite projected entangled pair states approach by Niesen and Corboz [29]. Figures are taken from Ref. [29] (©2017 I. Niesen and P. Corboz, under the Creative Commons Attribution 4.0 International (CC BY 4.0) License).

the variational method and the numerical diagonalization (Fig. 1.5(a)) [19]. They found that the ferroquadrupolar phase appears when $-3\pi/4 < \theta \lesssim -0.11\pi$, and the antiferroquadrupolar phase is realized when $\pi/4 < \theta < \pi/2$. They observed the finite spin susceptibility at $T = 0$ and the T^2 scaling of the specific heat found in Ref. [33] also in the ferroquadrupolar phase. In their ground-state phase diagram in a magnetic field based on the analytical and variational approaches, the 2/3-plateau region appears in the magnetization process in the antiferroquadrupolar phase (Fig. 1.5(b)). Bhattacharjee, Shenoy and Senthil argued by the more simple mean-field approach that instead of the noncollinear antiferroquadrupolar phase proposed by Tsunetsugu and Arikawa, the ferroquadrupolar phase appears for $NiGa_2S_4$ when the biquadratic interaction is large [35]. While this result seems to be rather unrealistic compared to the previous ones, if one considers the effect of the uniaxial anisotropy along the z-axis, the large easy-plane anisotropy favors the ferroquadrupolar order, as indicated by the cluster mean-field approach by Moreno-Cardoner *et al.* [36].

We briefly mention other lattices in two and three dimensions. For the kagome lattice, the ferroquadrupolar and antiferroquadrupolar ground states appear similarly to the case on the square and triangular lattices [37, 38]. However, the parameter range where the antiferroquadrupolar phase is realized is narrower. On the honeycomb lattice, the BLBQ model has the ground state with ferroquadrupolar order similar to the case on other types of lattices. The semiclassical analysis predicted the existence of the antiferroquadrupolar phase on the honeycomb lattice, but the tensor renormalization group calculation showed that the antiferroquadrupolar phase is not realized, and instead the plaquette valence-bond solid phase appears [39]. On the pyrochlore lattice, it was proposed that the biquadratic interactions can become large due to large electron-phonon couplings in some chromium spinel materials ACr_2O_4 ($A = \mathrm{Zn}, \mathrm{Cd}, \mathrm{Hg}$) with Cr^{3+} carrying $S = 3/2$ [40–44], which indicates that the magnetic properties of ACr_2O_4 can be well described by the BLBQ

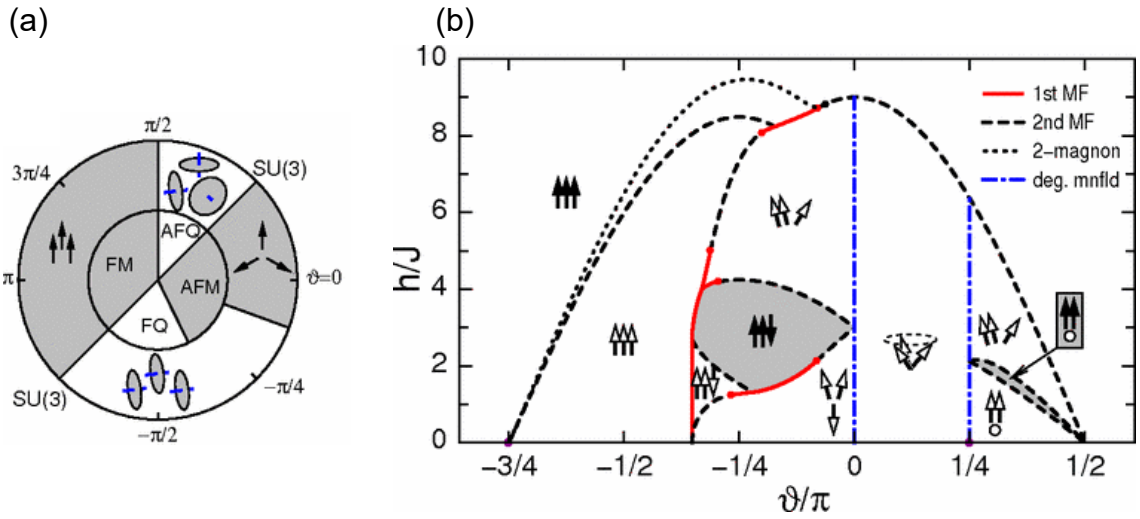

Figure 1.5: (a) Ground state phase diagram of the spin-1 bilinear-biquadratic model on the triangular lattice without magnetic field, where $J = \cos\theta$ and $K = \sin\theta$. The inner circle represents the results of the variational calculations, and the outer circle describes the results of the numerical diagonalizations. FM, AFM, FQ, and AFQ denote the ferromagnetic, antiferromagnetic, ferroquadrupolar spin nematic, and antiferroquadrupolar spin nematic phases, respectively. (b) Ground state phase diagram in a magnetic field. Figures are taken from Ref. [19] (©2006 American Physical Society).

model [45]. The classical analog of the quantum spin nematic phase, the collinear spin state characterized not by the magnetic moments but by the quadrupolar moments, was discussed using the bilinear-biquadratic model with classical spins [46]. Takata, Momoi, and Oshikawa examined the ground state of the spin-3/2 BLBQ model on the pyrochlore lattice and showed that the spin nematic phase exists in a high field region [47].

Thermodynamic properties

As mentioned previously (see Fig. 1.3), Harada and Kawashima studied the finite-temperature properties of the BLBQ model on the square and cubic lattices without magnetic field by the quantum Monte Carlo simulations [26]. They suggested that there are no finite-temperature phase transitions including the Kosterlitz–Thouless type ones in the ferroquadrupolar region on the square lattice. They also demonstrated that the finite-temperature phase transition to the ferroquadrupolar phase occurs on the cubic lattice.

On the triangular lattice, Stoudenmire, Trebst, and Balents studied the finite-temperature properties of the ferroquadrupolar phase without magnetic field by the semi-classical approximation with classical Monte Carlo simulations [49]. Their phase diagram and the specific heat are shown in Figs. 1.6(a) and 1.6(b). The possible finite temperature phase transitions between the paramagnetic–ferroquadrupolar and ferroquadrupolar–antiferromagnetic phases or a crossover is marked by the peaks in the specific heat. In the present thesis, we adopt this method to the same BLBQ model and discuss the effect of the finite magnetic field. There, we discuss shortly in Sec. 2.2.4.2 that since the system is in two dimensions, the ferroquadrupolar phase is realized not by a simple symmetry

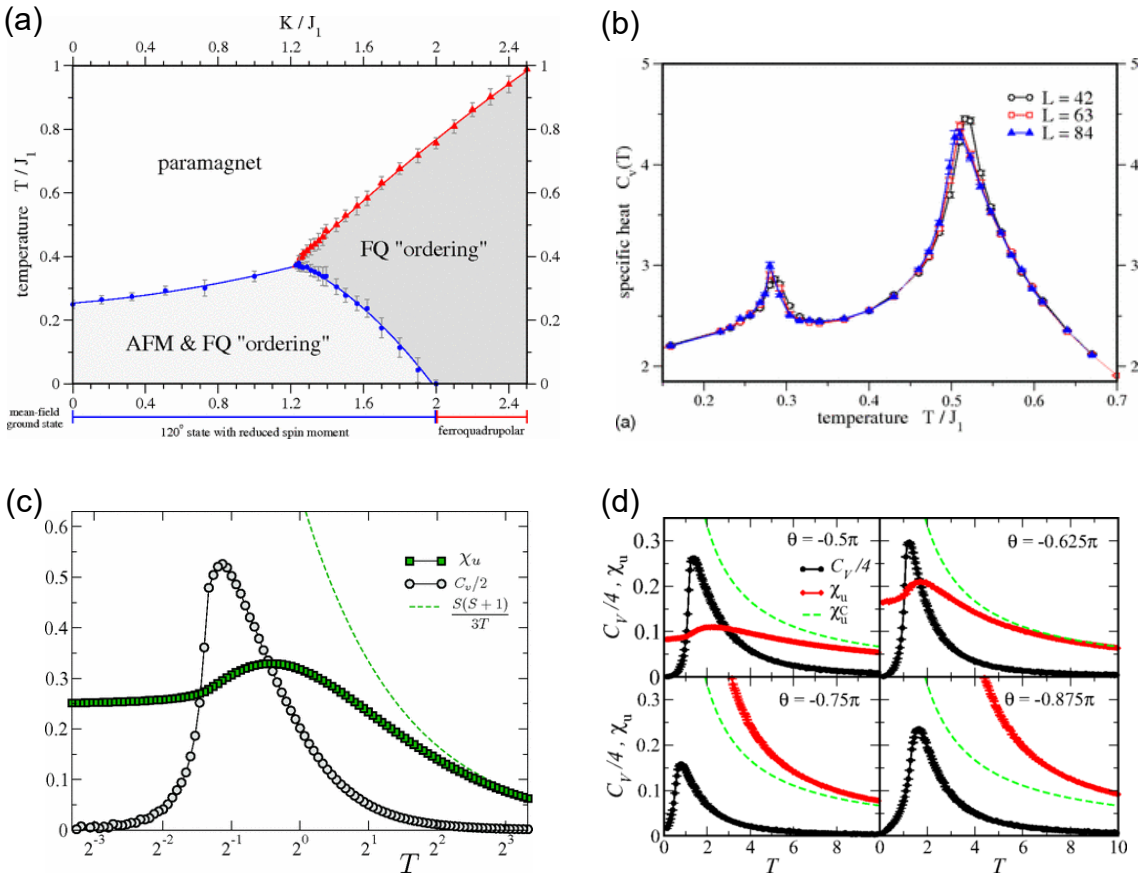

Figure 1.6: Thermodynamic properties of the spin-1 BLBQ model on the triangular lattice. (a) The phase diagram and (b) the temperature dependence of the specific heat at $K/J = 1.5$ by the semiclassical approximation by Stoudenmire *et al.* (c), (d) Specific heat C_v and uniform susceptibility χ_u calculated by the quantum Monte Carlo simulation. (c) Results for $J = 0$ by Kaul. (d) Results by Völl and Wessel. The peak position of (c) differs by a factor of 3 from (d), possibly because the factor of K and J is mistaken in the former (see Ref. [48]). Figures (a), (b) are taken from Ref. [49] (©2009 American Physical Society). Figures (c) and (d) are taken from Refs. [50] (©2012 American Physical Society) and [48] (©2015 American Physical Society), respectively.

breaking transition. Kaul pointed out that the ferro-biquadratic model [9], whose ground state is the ferroquadrupolar order, can avoid the negative sign problem, and studied the finite-temperature properties by the quantum Monte Carlo simulations [50]. His results on the specific heat and susceptibility are shown in Fig. 1.6(c). Völl and Wessel further performed the quantum Monte Carlo simulations in the region where the ground states are the ferroquadrupolar and ferromagnetic order and obtained the thermodynamic properties and the dynamical structure factors of spin and quadrupoles [48] as in Fig. 1.6(d). They explicitly showed that the specific heat in the ferroquadrupolar phase at low-temperature is proportional to T^2, which is in agreement with the previous study by the linear flavor-wave theory [19], while the specific heat is linear in T in the ferromagnetic phase. Also, the dispersion relations estimated from the dynamical structure factors were consistent with the results of the flavor-wave calculations.

Field-theoretical approach

Ivanov and Kolezhuk developed the low-energy effective field theory of the spin-1 BLBQ model on the one- and two-dimensional systems [18]. They showed that the low-energy dynamics of the BLBQ model with $5\pi/4 \lesssim \theta$ can be described by the RP^2 non-linear sigma model.

1.3 Spin nematic phases in the spin-1/2 systems

1.3.1 Quadrupolar and higher-rank multipolar orders

Spin nematic phases appear also in the spin-1/2 systems. As we mentioned above, quadrupolar operators defined on-site is always zero in the spin-1/2 systems. However, the quadrupolar moments can be defined on-bond which connects the two spin-1/2's as

$$Q^{\alpha\beta}_{i_1 i_2} = s^{\alpha}_{i_1} s^{\beta}_{i_2} + s^{\beta}_{i_1} s^{\alpha}_{i_2} - \frac{2}{3} \left(\boldsymbol{s}_{i_1} \cdot \boldsymbol{s}_{i_2} \right) \delta_{\alpha\beta}, \tag{1.13}$$

and the spin nematic order appears as the order of these on-bond spin quadrupolar moments. The possibility of this bond-nematic phase was pointed out by Andreev and Grishchuk [16].

A representative example realizing the spin nematic phase in spin-1/2 systems is the ferromagnetic J_1–J_2 Heiseberg model on the square lattice [51–55]. Motivated by the experiments on the square lattice compounds with ferromagnetic nearest-neighbor interactions and antiferromagnetic next-nearest-neighbor interactions in $Pb_2VO(PO_4)_2$ [56] and $(CuCl)LaNb_2O_7$ [57], Shannon, Momoi, and Sindzingre studied the spin-1/2 J_1–J_2–K square lattice, where the nearest-neighbor ferromagnetic Heisenberg interactions J_1, and the next-nearest-neighbor antiferromagnetic interactions J_2 and/or the ring-exchange interactions K compete with each other in an applied magnetic field h (Fig. 1.7) [51]. They showed that the spin nematic phase with the d-wave type quadrupolar order appears in the vicinity of the fully-polarized ferromagnetic phase. When the interactions between J_1 and J_2 and/or K are frustrated, the kinetic motion of the single magnons with $\Delta S^z = -1$, which contribute to the dipolar magnetic orders when condensed, is suppressed, and the

[9] $J = 0$ and $K = -1$, or $\theta = -\pi/2$ in the BLBQ model (Eq. (1.10)).

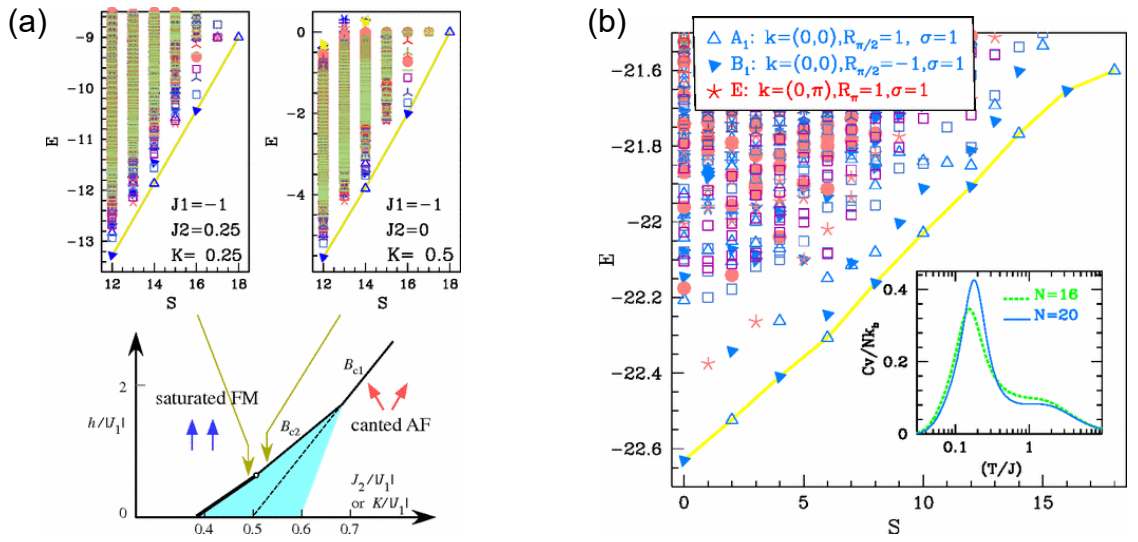

Figure 1.7: (a) Schematic phase diagram of the square lattice on the plane of $J_2/|J_1|$ or $K/|J_1|$ and $h/|J_1|$. The insets show the energy spectra of the high-spin states expressing the phase transitions into the spin nematic phase. (b) Energy spectrum of the frustrated square lattice of 36 spins with $J_1 = -1$, $J_2 = 0.4$ and $K = 0$, where the spin nematic phase is realized. The inset shows that the temperature dependence of the specific heat for the square lattice of 16 and 20 spins with the same parameters as those of the main panel. Figures are taken from Ref. [51] (©2006 American Physical Society).

two-magnon bound state with $\Delta S^z = -2$ has lower energy than that of the single magnons. Then, when the Bose–Einstein condensation of the magnon pair occurs, the spin nematic phase is realized. As a result, the lowest excitation is $\Delta S = 2$, and the low-lying states in the energy spectrum which constitute the ground state have a period-2 structure, namely, only the states with even-$S_{\rm tot}$ appear as the tower of states (Fig. 1.5). Ueda and Totsuka studied the same J_1–J_2 model without K on the square lattice by modifying the interactions to the strongly coupled plaquette unit with J_1 and J_2 and the weaker interactions, λJ_1 and λJ_2, between these plaquettes [52]. By extending the bond-operator mean-field theory to the plaquette unit, and by dealing with λ perturbatively, they compared the excitation energies of triplet and quintet to see which will close the gap first. When $J_1/J_2 \sim -2$ the quintet and the singlet condense where one may expect the condensation of bound magnons interpreted as spin nematic order. Shindou and Momoi developed a mean-field theory using slave-bosons, and proposed that the spin nematic phase is expressed as the resonating valence-bond states of triplets [53].

The study on the spin nematic order is also motivated by the ^{3}He on graphite, where the gapless spin-liquid-like behavior was observed [59, 60]. Momoi and Shannon performed the instability analysis of the ferromagnetic phase and the classical Monte Carlo simulations on the spin-1/2 model with multiple spin exchange interactions on the triangular lattice [61]. They found that when the four-spin interactions are introduced, the spin nematic state with the condensation of bound two-magnon is realized at the instability of the ferromagnetic phase. Their classical Monte Carlo simulation also indicated the rapid decrease of the spin correlations and the enhancement of the nematic correlations at low temperatures. Momoi, Sindzingre and Shannon studied the ground state of the

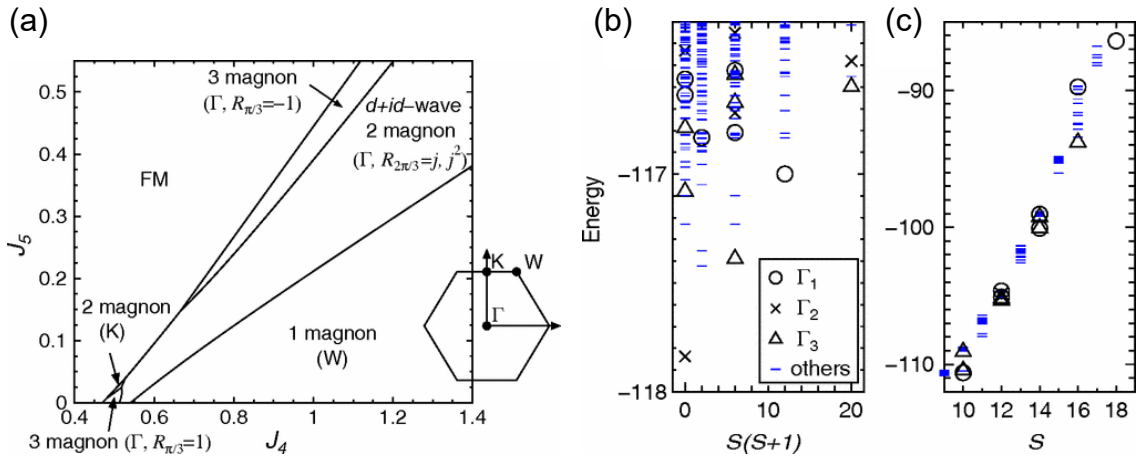

Figure 1.8: (a) Phase diagram obtained by the magnon instability analysis from the fully polarized ferromagnetic phase in the saturation field on the plane of J_5 and J_4. The model parameters are $J = -2$ and $J_6 = 2J_5$. The wave vectors and the spatial symmetries of the n-magnon states are denoted. The inset is the first Brillouin zone, where Γ-, K-, and W-points are defined. (b) Low-energy spectrum of the multiple spin exchange model with 36 spins. The parameters are set as $J = -2$, $J_4 = 0.5$, and $J_5 = J_6 = 0$. (c) Energy spectrum of the multiple spin exchange model with 36 spins near the fully-polarized state of $S = 18$. The parameters are set as $J = -2$, $J_4 = 1$, and $J_5 = \frac{1}{2}J_6 = 0.3$. Γ_1, Γ_2, and Γ_3 are given as $\Gamma_1 \equiv (R_{2\pi/3} = 1,\ R_\pi = 1,\ \sigma = 1)$, $\Gamma_2 \equiv (R_{2\pi/3} = 1,\ R_\pi = 1,\ \sigma = -1)$, and $\Gamma_3 \equiv (R_{2\pi/3} = j, j^2,\ R_\pi = 1)$, respectively. Figures are taken from Ref. [58] (©2012 American Physical Society).

spin-1/2 model on the triangular lattice with two-spin interactions and four-spin exchange interactions in a magnetic field aiming to describe the ^{3}He on graphite. They show that the spin triatic order, the octupolar order of spins, is realized between the fully polarized ferromagnetic phase and the canted antiferromagnetic phase. In the spin triatic phase, the condensation of bound three-magnon occurs similarly to the condensation of the bound two-magnon in the spin quadrupolar phase [62]. Momoi, Sindzingre, and Kubo showed that the solid ^{3}He thin film forming the triangular lattice, where each ^{3}He nucleus carries spin-1/2, exhibits the spin nematic phase [58], by the multiple-spin exchange interactions.

The spin nematic phases have been realized near the saturation field also in one-dimensional systems as the quadrupolar quasi-long-range order since the long-range orderings are suppressed by the quantum fluctuations [63–69]. Kecke, Momoi and Furusaki studied the J_1–J_2 chain, where the nearest-neighbor interaction J_1 and the next-nearest-neighbor interaction J_2 compete [64]. They constructed the n-magnon excited state by applying s^- to the fully-polarized ferromagnetic state, and calculated their energy dispersions, finding that the lowest-lying excitations are almost always the multi-magnon ones with momentum π. Hikihara, Kecke, Momoi, and Furusaki examined the ground states of the J_1–J_2 chain with $J_1 < 0$ and $J_2 > 0$ in a magnetic field using the numerical methods and the field-theoretical approach [66]. Similar calculations were performed by Sudan, Lüscher, and Läuchli [67]. Zhitomirsky and Tsunetsugu constructed the two-magnon states from the full saturation, and gave an analytical treatment to describe the spin nematic order in a high field [68]. They predicted that the spin nematic order is

realized in a high-field region of $LiCuVO_4$, which was later confirmed (see Fig. 1.13). The investigation aiming at a high-field region of $LiCuVO_4$ was performed also by Ueda and Totsuka [70], and Sato, Hikihara and Momoi [71].

Another example where the spin nematic phase is realized in the one-dimensional system is the two-leg ladder. Hikihara and Yamamoto studied the Heisenberg model with ring-exchanges in a magnetic field on the two-leg ladder, and showed that the quasi-long-range order of the magnon-pairing is realized next to the fully-polarized ferromagnetic phase [72].

The studies on spin nematics are also performed on the Shastry–Sutherland lattice [73], the orthogonal dimer system which probably describes $SrCu_2(BO_3)_2$ [74]. Momoi and Totsuka [75] started from the limit of the decoupled dimers, and performed the perturbation calculation of the inter-dimer interactions, deriving the effective hard-core boson model where the singlet is the vacuum and the triplet with $S^z = +1$ is the bosonic particle [76]. They showed that the strong geometrical frustration of the Shastry–Sutherland lattice strongly suppresses the hopping of a single triplet, and instead the bound state of triplet itinerates by the correlated hopping processes. The two-triplet bound states were confirmed by several studies [77–79]. Wang and Batista examined the low-energy excitation and the dynamics by the variational method, and found two kinds of spin nematic phases [80]. One is the antiferroquadrupolar spin nematic phase which was already found in Ref. [75], and the other is the plaquette spin nematic phase which they newly found.

1.3.2 Vector-chiral orders: p-type nematics

So far, the spin nematic phases as the order of quadrupolar moments of spins, the rank-2 symmetric tensor, have been discussed. The rank-2 tensor operators can be constructed by spin operators also in an antisymmetric form, namely, the vector-chiral operator,

$$\boldsymbol{p}_i = \boldsymbol{s}_{i_1} \times \boldsymbol{s}_{i_2} = \begin{pmatrix} s^y_{i_1} s^z_{i_2} - s^z_{i_1} s^y_{i_2} \\ s^z_{i_1} s^x_{i_2} - s^x_{i_1} s^z_{i_2} \\ s^x_{i_1} s^y_{i_2} - s^y_{i_1} s^x_{i_2} \end{pmatrix}, \tag{1.14}$$

can be considered as another rank-2 tensor. When the magnetic order is suppressed and the vector-chiral correlation, $\langle \boldsymbol{p}_i \cdot \boldsymbol{p}_j \rangle$, develops, the vector-chiral order is realized. This vector-chiral order is sometimes called the spin nematic order. To distinguish the order of the quadrupolar moments and that of the vector-chiral operator, the former is called n-type nematic order and the latter is called p-type nematic order [16] [10]. The vector-chiral order is elusive in much the same way as the n-type nematic order. In Refs. [66, 67], in addition to the quasi-long-range orderings of the quadrupolar and higher-rank multipolar moments, the long-range orderings of vector-chirality, $\boldsymbol{s}_{i_1} \times \boldsymbol{s}_{i_2}$, are observed.

The vector-chiral ordering is actually found in two-dimensional model. Läuchli and coworkers showed that this p-type vector chiral order is realized on the square lattice where the antiferromagnetic Heisenberg interactions and the ring-exchange interactions compete with each other [81]. Their phase diagram and the results of the Anderson tower analysis are shown in Fig. 1.9. The distinct difference of the p-type nematic order from

[10] Usually, the order of $\boldsymbol{s}_{i_1} \times \boldsymbol{s}_{i_2}$ is simply called the vector-chiral order, and the word "spin-nematic" is reserved for the quadrupolar order.

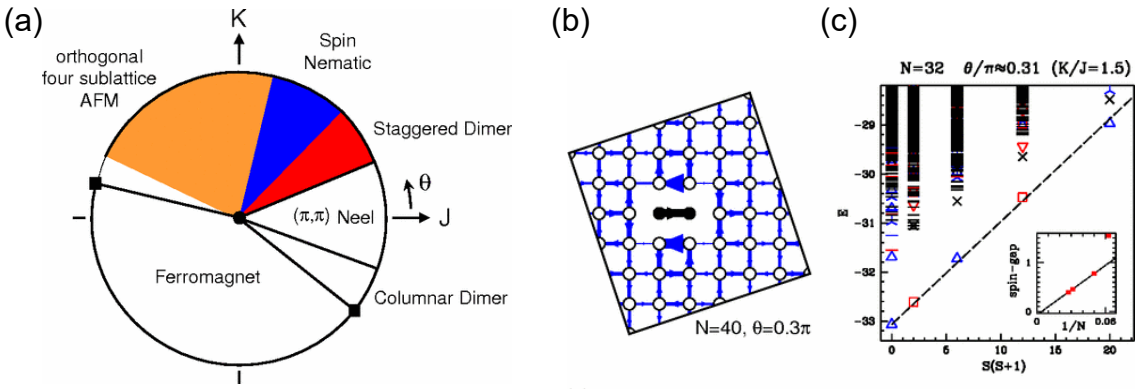

Figure 1.9: (a) Schematic phase diagram of the Hamiltonian with the Heisenberg interactions $J = \cos\theta$ and the ring-exchange interactions $K = \sin\theta$ on the square lattice. (b), (c) Results of the numerical diagonalization on the square lattice with 40 spins. (b) Spatial vector-chirality correlations. The bold black bond is the reference bond, and the width of the lines on each bond is proportional to the absolute value of the correlation. (c) Energy spectrum of the Hamiltonian of 32 spins with $K/J = 1.5$, in the p-type spin nematic phase. The inset is the result of the finite-size scaling of the spin gap, which suggests that the spin gap becomes zero in the $N \to +\infty$ thermodynamic limit. Figures are taken from Ref. [81] (©2005 American Physical Society).

the n-type one is that it is not located next to the fully polarized or ferromagnetic phases, and that the low-energy excitation is not characterized by the multi-magnon bound state. In fact, the tower of states in Fig. 1.9(c) consists of $\Delta S = 1$ series of states, since there is a vector-chiral long-range order of magnetic moments that can contribute to the single magnon excitations.

Another proposal realizing the p-type nematics in the two-dimensional system was given by Chandra and Coleman [82], utilizing the spiral spin structure. Also, Gor'kov and Sokol parallelly reached the similar result as Chandra and Coleman [83].

1.4 Spin nematic phases in dimer systems

So far most of the spin nematic phases are found next to the ferromagnetic phase or in the strong magnetic field near the saturation [11]. However, recently, there have been some studies showing that the spin nematic phases appear even without a magnetic field by utilizing the dimer structure [12].

Totsuka, Lecheminant and Capponi examined the spin-1/2 Hamiltonian with Heisenberg interactions J and ring-exchange interactions K_4 on the two-leg ladder shown in Fig. 1.10 [84]. Regarding the pair of two spins on each rung as the dimer, they map the two-leg ladder onto the spin-1 hard-core boson chain where the dimer singlet state is the vacuum of boson and the dimer triplet state is the boson carrying the spin-1 [85]. They analyzed the hard-core boson model and draw a mean-field ground-state phase diagram

[11] The spin-1 systems can be regarded as a sort of the ferromagnetic system, where two electron spins ferromagnetically align by the Hund's coupling inside each magnetic ion.

[12] The Shastry–Sutherland lattice can be regarded as the dimer system, but the spin nematic phases on the lattice are realized in a magnetic field.

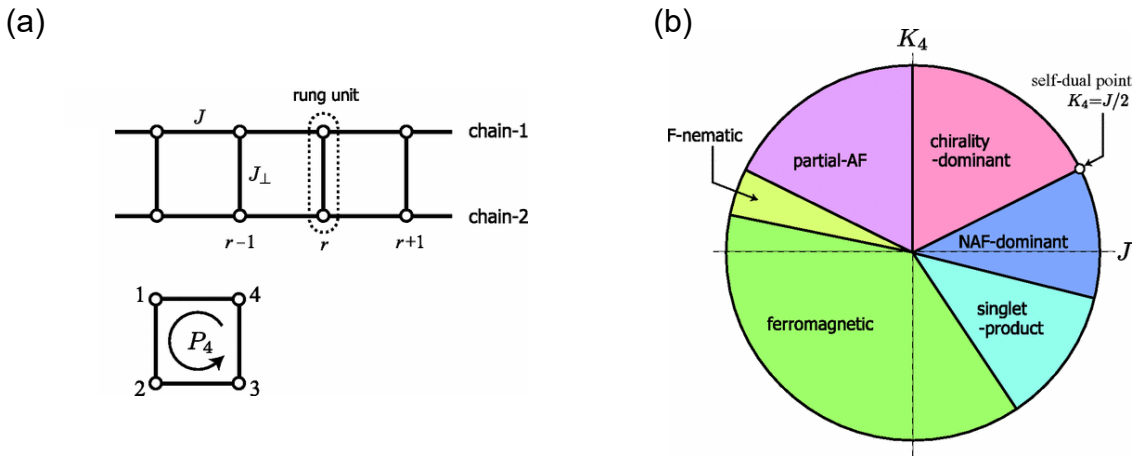

Figure 1.10: (a) Two-leg ladder. The square below denotes the ring-exchange interactions P_4, which moves the spins counterclockwise. (b) Mean-field phase diagram of the hard-core boson model varying the parameters $J = \cos\theta$ and $K_4 = \sin\theta$. Figures are taken from Ref. [84] (©2012 American Physical Society).

in Fig. 1.10(b), and further examined how the quantum fluctuation effect melts the mean-field phases. Notice that although the mean-field approximation generates a fictitious long-range order with distinct order parameters in the antiferromagnetic and chiral types of phases, denoted as NAF-dominant and chirality-dominant ones in this phase diagram, they give the power-low decaying correlations in reality, particular of one-dimension by the strong quantum fluctuation. In the analysis, they noticed that the phases can be systematically classified from two aspects; the magnetic properties of the spin-1 bosons, and the internal degrees of freedom of the dimer bosons. The former is whether the spin-1 makes the magnetic states or the nonmagnetic, quadrupolar states. In the latter aspect, the internal degrees of freedom given as

$$\boldsymbol{q}_i = \frac{1}{2}\left(\boldsymbol{s}_{i_1} - \boldsymbol{s}_{i_2}\right), \ \boldsymbol{p}_i = \boldsymbol{s}_{i_1} \times \boldsymbol{s}_{i_2}, \tag{1.15}$$

are the order parameters. We adopt this classification in the present thesis.

Yokoyama and Hotta studied the ground states of two-dimensional bilayer triangular lattice that consists of dimers antiferromagnetically coupled spin-1/2's [86]. They mapped the spin dimer model onto the spin-1 hard-core boson model in a way similar to Ref. [84], and examined the hard-core boson model through the instability analysis and the numerical diagonalization. They showed that two spin nematic ordered phases, the three-sublattice antiferroquadrupolar order where the triplet bosons fully occupy the dimers, and the quadrupolar order with kagome structure, are realized by introducing the two-types of ring-exchange interactions between two neighboring dimers (Fig. 1.11). In contrast to the previous cases realizing the ferroquadrupolar spin nematic phase next to the ferromagnetic phase, the antiferroquadrupolar spin nemtatic phase appears next to the singlet phase and not related to the ferromagnetic or magnetically polarized phases here. These phases appear because the ring exchange interaction that cyclically permutates the inter-dimer spins in the cross geometry, denoted as K_{T} in Fig. 1.11(a), is transformed to the strong biquadratic interaction between the two spin-1's occupying the neighboring

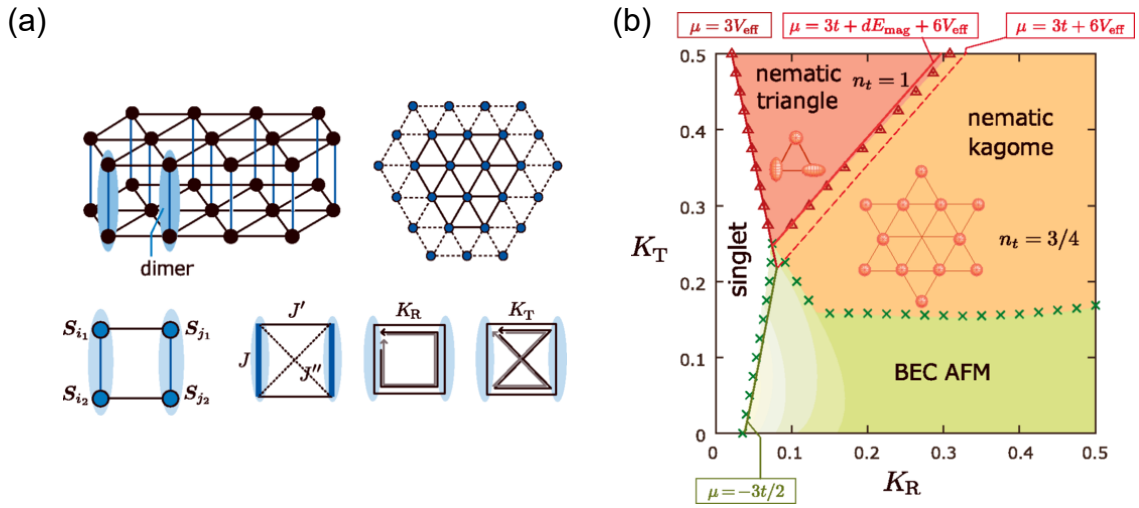

Figure 1.11: (a) Spin-1/2 dimer triangular lattice forming a bilayer. (b) Phase diagram on the plane of K_{R} and K_{T} fixing the parameters to be $J = 1$, $J' = 2K_{\mathrm{R}}$ and $J'' = 0$. Figures are taken from Ref. [86] (©2018 American Physical Society).

dimers carried by the triplet bosons. The mechanism of generating a large biquadratic interaction by the ring exchange interactions is studied in Chap. 4.

The dimer system with ferromagnetically coupled spin-1/2's shown schematically in Fig. 1.12(a) was studied by Hikihara, Misawa and Momoi, using the mean-field, analytical, and many-variables Monte Carlo approaches [87]. In their case, the strong ferromagnetic interactions work inside the dimers, and as in the previous cases, spin nematic phase appears next to the ferromagnetic phase. In this phase, they showed that the inter-dimer Heisenberg interactions, $J_{\parallel}$ and $J_{\times}$, are converted to the biquadratic interaction at the second order perturbation from the strongly coupled limit of isolated ferromagnetic dimers (fully triplet product state) even without the ring-exchange interactions.

In the context of where and how the quadrupolar moments emerge, it can be said that these spin-dimer systems interpolate the picture of the spin-1 systems and the spin-1/2 systems. In these spin-dimer systems, the quadrupolar moments are defined on the strongly coupled dimer bond consisting of two spins-1/2's, which resembles the non-dimer spin-1/2 systems such as the ferromagnetic J_1–J_2 Heisenberg model on the square lattice, where the quadrupolar moments are defined on-bond. On the other hand, if we regard the dimer as a unit of the lattice, namely "site", the quadrupolar moments are well-defined as an on-"site"-operator, similarly to the spin-1 systems where the quadrupolar moments are defined on each site. This quadrupolar picture is distinctively different from the non-dimer spin-1/2 systems, where the spin-1/2 on each site can contribute to the several quadrupolar moments on different bonds to which it is connected, namely, the quadrupolar moments are not spatially distinguished or well-separated.

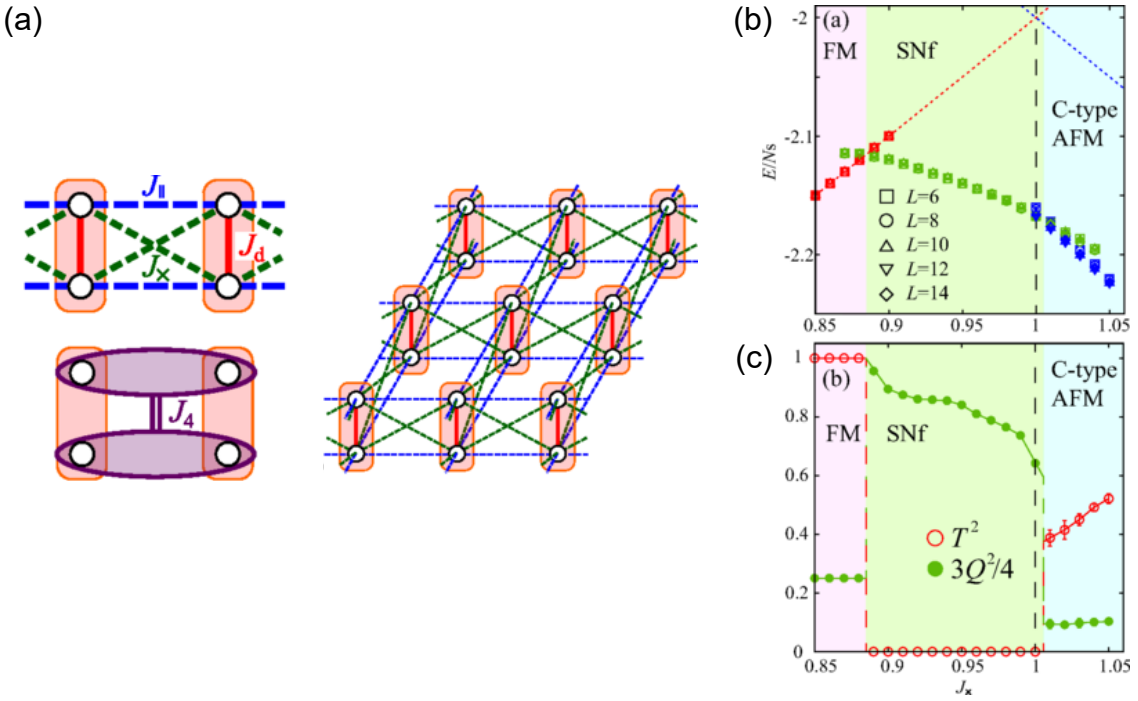

Figure 1.12: (a) Two-dimensional spin-1/2 ferromagnetic ($J_d < 0$) dimer lattice forming a bilayer. (b), (c) Results of many-variables Monte Carlo calculations on the square lattice for $J_d = -8$, $J_\parallel = -1$ and $J_4 = 0$. (b) $J_\times$ dependence of the energy densities of the ferromagnetic (FM), ferroquadrupolar spin nematic (SNf), and C-type antiferromagnetic (AFM) phases. (c) $J_\times$ dependence of the squared values of the local total-spin moment, T^2, and those of the normalized quadrupolar moment, $3Q^2/4$. Figures are taken from Ref. [87] (©2019 American Physical Society).

1.5 Developments of the experimental probes toward detection of the spin nematic phases

The spin nematics are one of the "hidden" orders since they are often invisible to local magnetic probes like neutron scattering or magnetic resonances. In fact, the nematic order parameter does not couple directly to the magnetic field so that it only shows featureless paramagnetic-like responses to the static magnetic field. For these reasons, most of the studies so far have focused on the dynamical properties, such as nuclear magnetic resonance, inelastic neutron scattering, or the electron spin resonances. Here, we introduce some of the theoretical proposals and the experimental reports related to spin nematics.

Nuclear magnetic resonances

Sato, Momoi, and Furusaki proposed that the relaxation rate in nuclear magnetic resonances (NMR), $1/T_1$, can capture the quasi-long-range multipolar correlation of the Tomonaga–Luttinger liquid (TLL) phase [88]. From the effective field theory, they found that the temperature dependences of $1/T_1$ in a magnetic field differs between the standard antiferromagnetic TLL phase and the multipolar TLL phase. For the former they find $1/T_1 \sim T^{2K-1} + T^{1/(2K)-1}$, where K is the TLL parameter, and regardless of the value of K, $1/T_1$ diverges when $T \to 0$. By contrast, in the latter phase, the spin-1/2 ferromagnetic J_1–J_2 chain shows $1/T_1 \sim T^{2K-1}$, and in a high-field region with $1/2 < K$ it decays as the temperature is lowered. They also calculated the dynamical spin structure factors in the p-th multipolar phase, i.e. p-magnon bound state [13], at zero-temperature. They found that the gapless modes which mainly contribute to the longitudinal component, $S^{zz}(k,\omega)$, appear at $k = \pm\pi\,(1-2M)\,/p$, where M is the magnetization, and the transverse component, $S^{+-}(k,\omega)$, is gapped. This is in sharp contrast to the antiferromagnetic TLL phase, where $S^{+-}(k,\omega)$ is gapless.

Sato, Hikihara, and Momoi investigated the magnetic field and temperature dependences of $1/T_1$ in the quadrupolar TLL phase on the ferromagnetic J_1–J_2 chain [89]. They derived the analytical formula of $1/T_1$ at finite-temperature by the field-theoretical approach, which includes some temperature-independent parameters. They evaluated the values of those parameters from the numerical calculations at zero temperature, and obtained the temperature dependence of $1/T_1$ in an explicit form, showing that in the quadrupolar TLL phase $1/T_1$ nonmonotonically varies with field at low-temperature; it first decreases since the TLL parameter increases and then increases near the saturation field as the TLL velocity approaches zero. They performed a similar calculation in the octupolar TLL phase in the same model [90].

Smerald and Shannon developed the continuum theory of the $1/T_1$ focusing on the quadrupolar fluctuations [91]. They showed that the sharp but non-divergent cusp appears in the temperature dependence of the $1/T_1$ at the partially-polarized paramagnetic–antiferroquadrupolar phase transition, which is different from the divergent behavior of $1/T_1$ at the antiferromagnetic phase transition.

[13] For example, $p = 2$ for the quadrupolar phase, where two magnons are bound.

Inelastic neutron scattering

To understand the spin nematics from the excitation spectrum, Smerald and coworkers focused on the inelastic neutron scattering [92, 93]. They developed the continuum field theory, and calculated the anticipated inelastic neutron scattering spectra in the spin nematic phases.

Electron spin resonances

Furuya proposed that the electron spin resonance (ESR) can be a useful tool for detecting the quadrupolar TLL phase in the one-dimensional frustrated ferromagnetic chain [94]. He disclosed how the linewidth of the ESR spectra depends on the magnetic-field-angle θ; in the usual TLL phase with quasi-long range antiferromagnetic order, the linewidth varies with the period of π, while in the quadrupolar TLL phase the period of $\pi/2$ is observed.

Furuya and Momoi extended the approach in Ref. [94] to the two-dimensional models, and showed that the ferroquadrupolar long-range order can be detected by the frequency shift of the electron paramagnetic resonance (EPR) peak in the ESR spectrum [95]. For the antiferroquadrupolar long-range ordered case, the frequency shift is no longer useful, but it can be captured instead by the additional peaks to the EPR peak, which originate from the excitations of the bounded two-magnon and the single magnon with the finite wave-vector.

Magnetocaloric effects

Schmidt, Thalmeier, and Shannon studied the magnetocaloric effect on the ferromagnetic J_1–J_2 Heisenberg model on the square lattice [96]. They showed that between the canted antiferromagnetic phase and the ferromagnetic phase, there is another phase which is characterized by the two-magnon instability, which is consistent with the previous proposal on the spin nematic order on the model [51]. They found that the magnetocaloric effect is enhanced near the saturation field due to the large degeneracy in low-energy excitations, which is a characteristic of the frustrated system, and predicted that the sign of the magnetocaloric effect changes from positive to negative at the subcritical field when the system is magnetically ordered.

Other recent proposals

Michaud, Vernay, and Mila developed the theoretical framework of inelastic light scattering in spin-1 magnets using the two-orbital Hubbard model [97], and proposed that the Raman scattering can be utilized for tracing a quadrupolar order.

Sato and Morisaku proposed that the laser or electromagnetic waves have the potential to detect the spin nematic order [98]. They showed that the two-magnon bound state is excited through the two-photon absorption process by the strong THz laser. The magnon pair carries the angular momentum $2\hbar$, and in the excitation spectrum, they can be distinguished from the single-magnon, whose excitations occur through the one-photon absorption process with angular momentum $\hbar$.

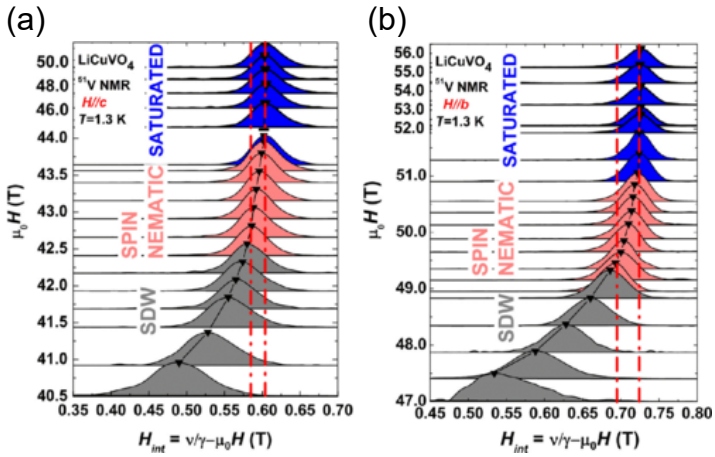

Figure 1.13: Results of the ^{51}V NMR measurements of $LiCuVO_4$ at $T = 1.3$ K in various magnetic fields of (a) $H \parallel c$ and (b) $H \parallel b$, where the peak intensity is normalized. The black triangles denote the peak positions of the NMR spectra, which indicates that the peak moves towards the fully-polarized state. The NMR spectra are differently colored on the basis of the magnetic properties; gray, light red, and blue regions correspond to the spin-density wave, spin nematic, and fully-polarized states, respectively. The region where the internal local magnetic field, $H_{\rm int}$, is changed by a magnetic field but its distribution is unchanged is sandwiched by the dash-dotted red lines. Figures are taken from Ref. [101] (©2017 American Physical Society).

1.6 Experimental proposals

Candidate materials which realize the spin-nematic phase have been proposed, most of which have J_1–J_2 chain or J_1–J_2 square lattice structures with $J_1 < 0$ and $J_2 > 0$. Examples of the former are $LiCuVO_4$ [99–101], $NaCuMoO_4(OH)$ [102], $A_2Cu_2Mo_3O_{12}$ ($A = \mathrm{Rb}, \mathrm{Cs}$) [103, 104], and $PbCuSO_4(OH)_2$ [105, 106], and those of the latter is $(CuCl)LaNb_2O_7$ [57], $Cu_3V_2O_7(OH)_2 \cdot 2H_2O$ [107, 108], $AA'VO(PO_4)_2$ ($AA' = \mathrm{Pb}_2, \mathrm{BaCd}, \mathrm{BaZn}, \mathrm{SrZn}$) [56, 109, 110]. Below, we pick up three representative examples whose possibility of the spin nematic phases has been intensively investigated.

$LiCuVO_4$

One of the first candidate materials with spin nematic phase is $LiCuVO_4$. In $LiCuVO_4$, Cu^{2+}-ions carry the spin-1/2, and form the quasi-one-dimensional J_1–J_2 chain structure with ferromagnetic $J_1 = -1.6$ meV, antiferromagnetic $J_2 = 3.8$ meV, and ferromagnetic interchain $J = -0.4$ meV interactions [99]. Svistov *et al.* measured the magnetization at low-temperature in a high field and observed another phase between the phase with the collinear structure of modulated spins at intermediate field region and the fully-polarized phase in a saturation field [100]. Combining the preceding theoretical proposal of the realization of the spin nematic phase in $LiCuVO_4$ [68], they suggested the phase found is the spin nematic phase. Orlova *et al.* investigated the magnetic properties in a high-field using the ^{51}V NMR and the magnetization measurements [101]. As shown in Fig.1.13, they found the high-field region next to the saturated phase, where the width of the NMR spectrum does not change, similarly to the fully-polarized ferromagnetic phase.

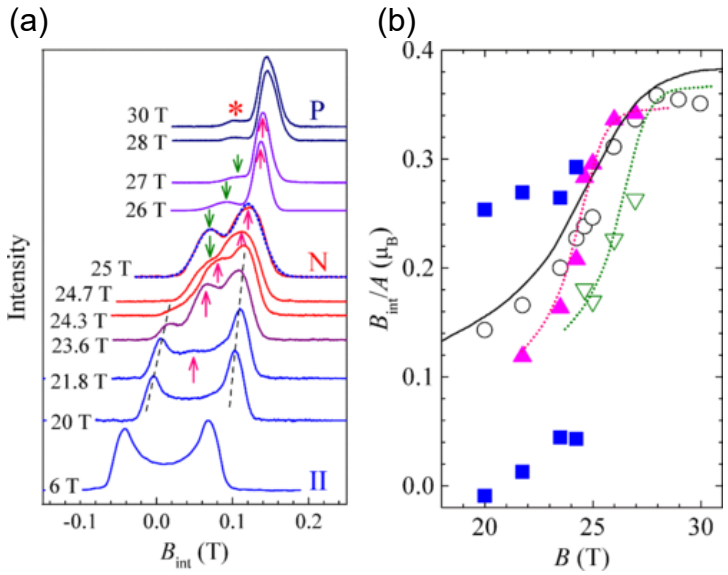

Figure 1.14: Results of the NMR measurements of $Cu_3V_2O_7(OH)_2 \cdot 2H_2O$. (a) NMR spectra in various magnitudes of the magnetic field measured at 0.3–0.4 K. The magnetic field is applied perpendicular to *ab*-plane. (b) Local spin polarization in various magnetic fields. Figures are taken from Ref. [113] (©2017 American Physical Society),

They identified the region as the spin nematic phase because the spin nematic phase has a homogeneous magnetization and no transverse magnetic order and thus the width of the NMR lines is unchanged. A recent study on the magnetocaloric effect and the magnetoacoustic measurement also indicated that the existence of the spin nematic phase in a high field [111]. Hirobe *et al.* measured the spin Seebeck effect in a low-field region of $LiCuVO_4$, and found that the effect is suppressed as the magnetic field is increased, which they ascribed to the development of magnon-pair correlation [112].

$Cu_3V_2O_7(OH)_2 \cdot 2H_2O$

A candidate of spin nematic material in two dimensions is volborthite $Cu_3V_2O_7(OH)_2 \cdot 2H_2O$, which has spin-1/2 carried by Cu^{2+}. The material takes the deformed kagome lattice structure, and there are two types of Cu^{2+}-ions whose local environments are different [107, 108]. It was proposed later that this system should be understood as the coupled frustrated chains, where ferromagnetic J_1–J_2 Heisenberg chains are connected by the antiferromagnetic Heisenberg interactions, rather than the kagome lattice with spatial anisotropy [115]. This is because the density functional theory calculation shows that Cu^{2+}-ions in different environments host different orbitals, $3d_{3z^2-r^2}$ and $3d_{x^2-y^2}$, respectively. However, this type of orbital orderings is unlikely to occur; the succeeding experiment showed that all Cu ions are in the $d_{x^2-y^2}$ orbital at low-temperature [116]. In addition, there is an experimental ambiguity in that a wide 1/3-plateau observed at 28 T $\lesssim B \lesssim$ 74 T at 1.4 K for the single crystal [117] was not observed for the polycrystalline samples [118, 119], and thus further investigation on the description of this material was needed. The coupled frustrated chain model may not properly explain all these issues. A more recent study examined the material

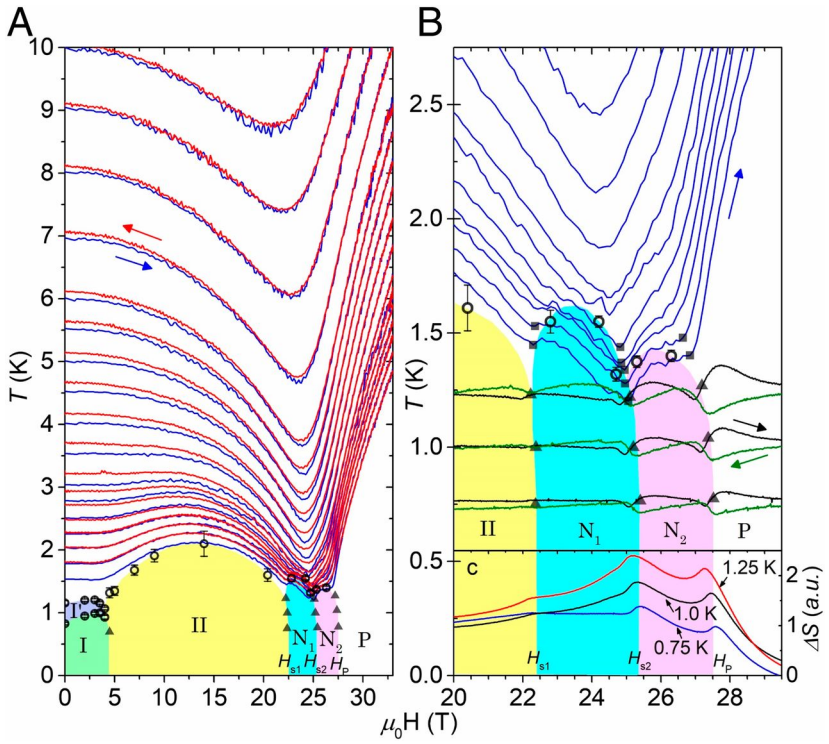

Figure 1.15: Results of the magnetocaloric effect measurements of $Cu_3V_2O_7(OH)_2 \cdot 2H_2O$. Figure is taken from Ref. [114] (©2019 Y. Kohama, H. Ishikawa, A. Matsuo, K. Kindo, N. Shannon, and Z. Hiroi, under Creative Commons Attribution-NonCommercial-NoDerivatives License 4.0 (CC BY-NC-ND 4.0)).

by the density functional theory based on the structural data of the single crystal and proposed that $Cu_3V_2O_7(OH)_2 \cdot 2H_2O$ in a low field should be regarded as the coupled trimers rather than as the coupled frustrated chains [120]. There, each trimer takes total-$S = 1/2$ state, and the trimers form the (effective) spin-1/2 square lattice which has the nearest-neighbor ferromagnetic Heisenberg interactions and two kinds of next-nearest-neighbor antiferromagnetic Heisenberg interactions as the dominant couplings. Based on the analysis of the coupled trimer model, the absence of the 1/3-plateau in the powder samples was explained, and the existence of the spin nematic phase just below the 1/3-plateau was suggested, which was naively expected in Ref. [117]. Yoshida *et al.* performed the ^{51}V NMR measurement [113] (see Fig. 1.14). They observed in the vicinity of the 1/3-plateau region the NMR spectrum similar to the one inside the plateau, which implies the spin nematic phase, as was seen in $LiCuVO_4$ [101]. They also found that the g-factor estimated in the plateau region takes about two or three times larger values than that in the paramagnetic region [121], which indicates the bound multimagnon excitations. Kohama and coworkers measured the magnetocaloric effect and the specific heat in a magnetic field and gave a clue that there is a thermodynamic phase just before reaching the 1/3-plateau phase [114] (see Fig. 1.15). Combining those thermodynamic results with the previous NMR measurements [113, 117], they indicated that the phase next to the 1/3-plateau phase is the spin nematic phase.

$BaCdVO(PO_4)_2$

Another candidate realizing the spin nematic phase on the spin-1/2 J_1–J_2 square lattice is $BaCdVO(PO_4)_2$. The series of vanadium phosphates, $AA'VO(PO_4)_2$, where V^{4+} ion carries spin-1/2, are the examples of the spin-1/2 J_1–J_2 square lattice compound with ferromagnetic J_1 and antiferromagnetic J_2 interactions [109, 110]. Among them, $BaCdVO(PO_4)_2$ has a rather small J_2 interaction. The crystal structure of this material was studied by Meyer and the collaborators [124]. The magnetic susceptibility and the specific heat were investigated by Nath *et al.* using the polycrystalline sample [109], and the interaction parameters are estimated as $J_1 \simeq -3.6$ K and $J_2 \simeq 3.2$ K. The magnetic and thermodynamic investigations using the single-crystal sample was performed by Povarov and coworkers [122]. Although $BaCdVO(PO_4)_2$ undergoes the antiferromagnetic phase transition at $T_N \simeq 1$ K without magnetic field [109], they pointed out that below 0.15 K an additional quantum phase to the antiferromagnetic phase appear near the saturation field from the measurement of the specific heat and magnetocaloric effect, implying the existence of the high-field spin nematic phase (see Fig. 1.16(a)). Skoulatos *et al.* performed the neutron scattering and the ac magnetic susceptibility measurements [123]. Both measurements suggested that the spin moments are mostly fluctuating in a zero field, and the unpolarized components of the spin moments fluctuate from 3.8 T to 4.5 T which is the saturation field, which suggests the realization of the spin nematic phase (see Fig. 1.16(b)).

$Ba_3MRu_2O_9$

Although it has not been discussed in the context of spin nematics, we introduce $Ba_3MRu_2O_9$ with divalent cation M, since it motivates us to study the spin-1 dimer

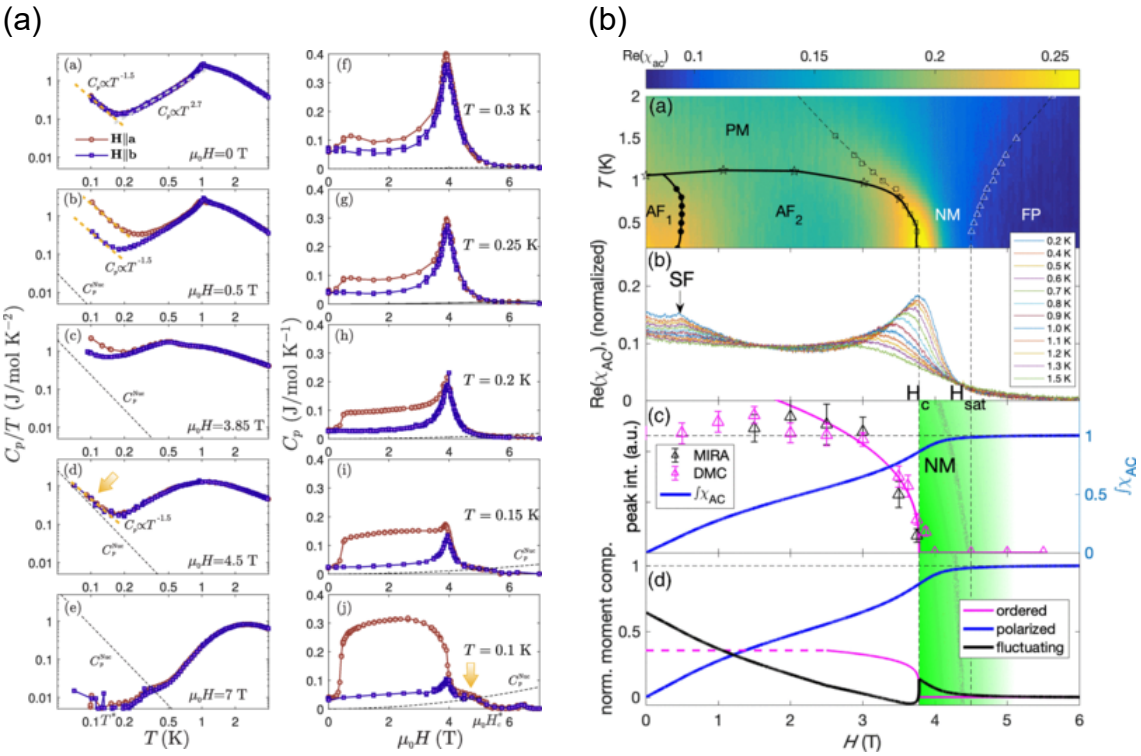

Figure 1.16: Experimental results of $BaCdVO(PO_4)_2$. (a) (left) Temperature dependence of the specific heat in various magnetic fields. (right) Magnetic field dependence of the specific heat at a variety of temperatures. The arrows in $\mu_0 H = 4.5$ T data in the left column and in $T = 0.1$ K data in the right column express the additional contribution to the specific heat, which indicates the existence of the quantum phase in a high-field at low-temperature. (b) Temperature-magnetic field phase diagram. Figures (a) and (b) are taken from Refs. [122] (©2019 American Physical Society) and [123] (©2019 American Physical Society), respectively.

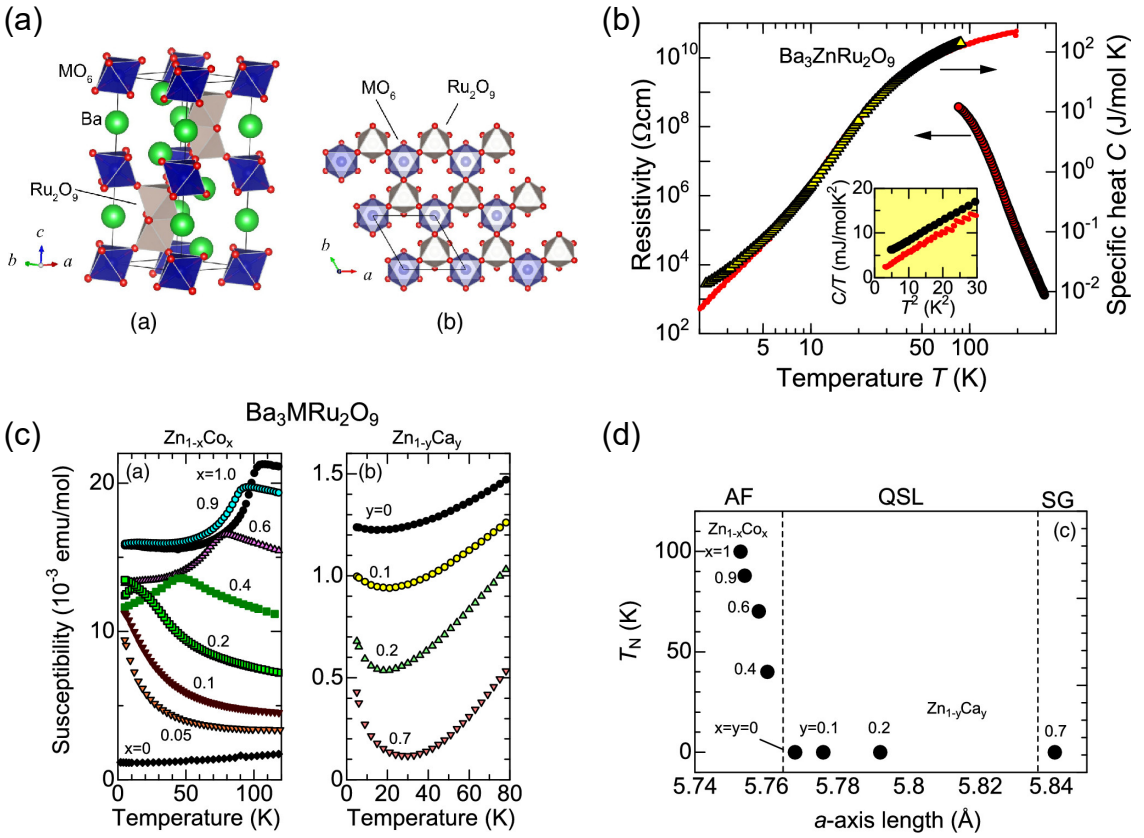

Figure 1.17: Experimental data of $Ba_3MRu_2O_9$. (a) Crystal structure. (b) Temperature dependence of the specific heat and resistivity of M = Zn. (c) Magnetic susceptibilities of $M = Zn_{1-x}Co_x$ (left) and $M = Zn_{1-y}Ca_y$ (right). (d) Néel transition temperature with respect to the length of a-axis, or the inter-dimer distance. AF, QSL, SG represent the Néel-antiferromagnetic, (possible) quantum spin-liquid, and spin gapped phases, respectively. Figures are reproduced with permission from Ref. [125] (©2017 The Physical Society of Japan).

system in Chapter 3. In a series of $Ba_3MRu_2O_9$ compounds [125–132], where M = Ca, Co, Ni, Cu, Zn, Sr, two RuO_6 octahedra form a dimer by face-sharing, and the dimers construct a two-dimensional triangular lattice as shown in Fig. 1.17(a). Along the inter-layer (c-axis) direction, the Ru^{5+} ions and M ions align as Ru–Ru–M–Ru–Ru–$\cdots$ with the dimerized Ru ions on top of each other and M ions out of face, whereas the inter-layer interactions between the Ru-dimer layer and the M layer do not largely affect the magnetic properties. Actually, when M is the magnetic ion such as Co, Ni, and Cu, the conductivity measurements suggested that the electrons can move in two-dimensional plane formed by Ru dimers [129] and the M ions are isolated.

In this series of materials, intriguing magnetic ground states have been reported experimentally. When M = Zn, the specific heat has no anomaly down to 2 K, and the magnetic susceptibility takes featureless structure down to 37 mK, which is much lower temperature than the energy of the intra-dimer interactions $J \sim$ 150–200 K [125, 126] (see Figs. 1.17(b), 1.17(c)). For the M = Co, Ni, and Cu compounds, the inter-dimer distances, the a-axis lengths, are shorter than that of M = Zn, and the antiferromagnetic phase transitions at $T_{\rm N} \sim$ 100 K are observed [128, 130], which are determined mainly by the inter-dimer interactions and do not largely change depending on the magnetic ions [130]. In the M = Ca or Sr compounds, the inter-dimer distances are longer than that of M = Zn, and the typical nonmagnetic singlet state is identified [127]. The magnetic ground states in various kinds of M are summarized in Fig. 1.17(d). The difference of the magnetic properties seems to be only in the difference of inter-dimer distances; the nontrivial nonmagnetic phase in M = Zn with intermediate inter-dimer distance appears between the antiferromagnetic phase and the gapped singlet phase.

1.7 Motivations and purpose

Although the physics of the spin nematics itself has been well established, there are remaining issues. First, despite many theoretical proposals and experimental efforts, the observation of the spin nematic order has been challenging, because the quadrupole moment does not directly couple to the magnetic field unlike the magnetic orders. Second, the spin nematic order is also quite elusive in theoretical models in reality. In spin-1 systems, a large biquadratic interaction is needed to suppress the magnetic order and to enhance the quadrupolar order. However, the biquadratic interaction is often much smaller than the Heisenberg interaction; for example, in the Mott insulators where the quantum magnets are realized, the typical biquadratic interaction is generated from the higher order perturbation processes from the strong coupling limit, while the Heisenberg interaction is from the lower order processes. Therefore, the realization of the materials with large biquadratic interactions is not easy in this case. In spin-1/2 systems, more realistic situations than those in the spin-1 systems have been proposed such as the frustrated J_1–J_2 models with ferromagnetic J_1 and antiferromagnetic J_2 interactions. However, it is not so frequent that ferromagnetic interactions are dominant in the materials. Although some candidate materials have been proposed as we introduced in this Chapter, most of them focus on the case at high fields where the magnetization almost saturates. This kind of experiment is possible only for materials with small magnetic interactions because the saturation field scales with J. From the theoretical point of view, the spin-1 nematics and the spin-1/2-based nematics have been separately discussed in most of the cases since they do not share the common description of the quadrupolar order parameters when defined in terms of the original spin-1 or spin-1/2; the canonical description of the on-site quadrupolar order in spin-1 systems and the conventional two-magnon bound state description in spin-1/2 systems are seemingly disconnected.

In the present thesis, we examine these issues from several different aspects. We start from the canonical spin-1 bilinear-biquadratic Hamiltonian and disclose the characteristic thermodynamic properties of the ferroquadrupolar spin nematic phase, which was overlooked in the previous studies on spin-1 nematics. We then construct the spin-dimer model where each dimer consists of a pair of spin-1's interacting antiferromagnetically to understand the properties of $Ba_3MRu_2O_9$. Another reason why we choose such a dimer model is that they can become a real platform for spin nematics or quadrupolar orderings; we find that the standard antiferromagnetic interactions might be useful to generate a variety of phases without the aid of the ferromagnetic interactions, explicit biquadratic interactions, or the high magnetic field. The large internal degrees of freedom of dimers shall play a crucial role. The dimer description helps us to clarify how the effective interactions that can play a similar role as the spin-1 biquadratic interaction can develop. Based on this consideration, we finally study the conventional high field two-magnon bound state based on the dimer description, with the perspective that the two-magnon bound state description of spin nematics in the spin-1/2 system and the canonical spin-1 nematics can be unified based on the language of dimers.

Organization of this thesis

This thesis is organized as follows. In Chapter 2, we study the magnetic field effect on the thermodynamic properties of the spin-1 nematics using the spin-1 BLBQ model. Performing the numerical simulation combining the semiclassical approximation and the classical Monte Carlo method, we find the small field-reentrant behavior of the ferroquadrupolar phase transition; the transition temperature from the paramagnetic phase to the ferroquadrupolar phase once increases in an applied magnetic field, and decreases in a larger magnetic field. We attribute this reentrant behavior to the entropic effect, which originates from the different robustness against the magnetic field between the paramagnetic and ferroquadrupolar phases.

We study the ground states of the spin-1 dimer triangular lattice forming a bilayer in Chapter 3. We show that the low-energy manifold of the system can be described by the spin-1 hard-core boson model, where the triplet and singlet dimers are regarded as the boson with spin-1 and the vacuum, respectively. Performing the numerical diagonalization, we find the multiple quadrupolar phases consisting of triplet dimers, which we classify by the internal degrees of freedom of dimers. We discuss the possible correspondence of the spin-1 dimer system to $Ba_3MRu_2O_9$, where the nontrivial nonmagnetic ground states are found next to the singlet phase.

In Chapter 4, we evaluate the spin-1 Heisenberg and biquadratic interactions from a microscopic view. Performing the perturbation calculations in the strong coupling region, we show that the biquadratic interaction can take a large value in the spin dimer structure.

We describe the spin nematic phase in spin-1/2 systems in a high magnetic field using the dimer-basis in Chapter 5. We investigate the two-leg ladder system as a one-dimensional realization of the dimer, and discuss how the two-magnon bound state is explained in terms of the dimers.

Chapter 6 is devoted to the summary of this thesis.

Chapter 2

Magnetic field effect on the finite-temperature properties of spin-1 nematic phases

In this Chapter, we discuss the magnetic field effects on the finite-temperature properties of the spin nematic phases. Using the spin-1 bilinear-biquadratic model, a canonical model for discussing the spin nematics, we numerically examine how the finite-temperature properties of the spin nematic phase change by a magnetic field. We find a slight field-reentrant behavior in the ferroquadrupolar phase transition, namely, the transition temperature from the high-temperature paramagnetic phase to the ferro-nematic phase first increases by a small magnetic field, and then decreases by a larger magnetic field, which can be identified by the shift of the peak position of the specific heat. The mechanism of this field-reentrant behavior is the entropy effect. When a small magnetic field is applied, the entropy of the paramagnetic phase at high temperature region decreases, whereas that of the ferroquadrupolar phase is kept by changing the form of the quadrupolar moment. This reentrant behavior will give a fingerprint of the ferroquadrupolar phases, whereas it is not seen in the antiferroquadrupolar phase transition.

2.1 Model and Method

2.1.1 Model

We consider the spin-1 bilinear-biquadratic (BLBQ) model on the triangular and square lattices in a magnetic field,

$$\mathcal{H} = \sum_{\langle i,j \rangle} \left[J \hat{\boldsymbol{S}}_i \cdot \hat{\boldsymbol{S}}_j + K \left(\hat{\boldsymbol{S}}_i \cdot \hat{\boldsymbol{S}}_j \right)^2 \right] - h \sum_{i=1}^{N} \hat{S}_i^z. \tag{2.1}$$

Here, $\hat{\boldsymbol{S}}_i$ is the spin-1 operator of site-i [1]. The spin-1 bilinear (Heisenberg) and biquadratic interactions, and the magnetic field along the z-axis are denoted as J, K, and h, respec-

[1] In this Chapter, we explicitly use $\hat{\bullet}$ to express the quantum mechanical operators unlike Chapter 3, because we perform the one-body approximation, and quantum mechanical operators and the expectation values calculated by the 1-body approximated wave-functions should be distinguished.

tively [2], with J and K normalized as $J^2 + K^2 = 1$. The summation is taken over the nearest-neighbor pairs of sites, $\langle i, j \rangle$, and the number of sites is denoted as N.

Hereafter, we treat this system in a one-body semiclassical picture, and thus we briefly review the semiclassical ground states of the spin-1 BLBQ model (see also Chap. 1). For the triangular lattice, the ground state of the spin-1 BLBQ model has the ferroquadrupolar order when $K/J < \tan^{-1}(-2)$ with $0 < J$, or $K < J \leq 0$ [17, 19]. For the square lattice, the ferroquadrupolar phase is realized for $K < J < 0$ [30]. These variational results are qualitatively in good agreement with the results by the fully quantum approaches. When the external magnetic field is applied parallel to the z-axis, the ferroquadrupolar phase starts to have a magnetic moment in the z-direction, whereas the quadrupolar moment in the xy-plane remains robust. The ferroquadrupolar phase is replaced by the ferromagnetic phase with saturated magnetic moment at $h = z(J - K)$, where z is the coordination number [3].

2.1.2 Semiclassical SU(3) approximation with Monte Carlo simulation

We here adopt the semiclassical SU(3) approximation with classical Monte Carlo simulation (sSU(3)-MC), proposed by Stoudenmire, Trebst, and Balents [49]. This method is the extension of the product-state variational approach given successfully for the description of the spin nematic ground state to finite-temperature.

Below we explain the procedure of the sSU(3)-MC method following Ref. [49]. First, we approximate the many-body wave function, $|\Psi\rangle$, by the product-state of the one-body state in each site, $\{|\psi_i\rangle\}_{i=1,\cdots,N}$, as

$$|\Psi\rangle = \bigotimes_{i=1}^{N} |\psi_i\rangle\,, \ |\psi_i\rangle = \sum_{\alpha=x,y,z} d_{i,\alpha}\,|\alpha\rangle\,. \tag{2.2}$$

Here $|\alpha\rangle$ ($\alpha = x, y, z$) is the time-reversal invariant basis states of spin-1 given by Eq. (1.5), and $d_{i,\alpha}$ is the complex coefficients normalized as $\sum_{\alpha=x,y,z} |d_{i,\alpha}|^2 = 1$. Using this approximate many-body wave function (Eq. (2.2)), the expectation values of the energy is calculated as

$$\begin{aligned} E_{\mathrm{sSU(3)}} &= \langle\Psi|\mathcal{H}|\Psi\rangle \\ &= \sum_{\langle i,j\rangle} \Big[J\,|\boldsymbol{d}_i^* \cdot \boldsymbol{d}_j|^2 + (K-J)\,|\boldsymbol{d}_i \cdot \boldsymbol{d}_j|^2 + 1 \Big] + \mathrm{i}h \sum_{i=1}^{N} (\boldsymbol{d}_i^* \times \boldsymbol{d}_i)^z\,, \end{aligned} \tag{2.3}$$

where $\boldsymbol{d}_i = {}^t\begin{pmatrix} d_{i,x} & d_{i,y} & d_{i,z} \end{pmatrix}$. Then, the set of the coefficients $\{d_{i,\alpha}\}_{i=1,\cdots,N}$ is updated by the typical classical Monte Carlo samplings following the canonical ensemble of $\exp(-\beta E_{\mathrm{sSU(3)}})$. Here β is the inverse temperature; $\beta = 1/(k_{\mathrm{B}}T)$, where k_{B} is the Boltzmann constant [4]. Details of the classical Monte Carlo simulations are written in Sec. 2.1.3.

[2] In this Chapter, we denote the biquadratic interaction not as B but as K, because B might be confused with the magnetic field.

[3] For the square and triangular lattices, $z = 4$ and 6, respectively.

[4] Hereafter we set $k_{\mathrm{B}} = 1$.

The expectation value of the spin moment, $\boldsymbol{S}_i$, can be expressed using $\boldsymbol{d}_i$ as

$$\boldsymbol{S}_i = \left\langle \psi_i \middle| \hat{\boldsymbol{S}}_i \middle| \psi_i \right\rangle = -\mathrm{i} \begin{pmatrix} d_{i,y}^* d_{i,z} - d_{i,z}^* d_{i,y} \\ d_{i,z}^* d_{i,x} - d_{i,x}^* d_{i,z} \\ d_{i,x}^* d_{i,y} - d_{i,y}^* d_{i,x} \end{pmatrix}. \tag{2.4}$$

As given in Chap. 1, the quadrupolar operator is defined as

$$\hat{Q}_i^{\alpha\beta} = \hat{S}_i^{\alpha} \hat{S}_i^{\beta} + \hat{S}_i^{\beta} \hat{S}_i^{\alpha} - \frac{2}{3} S\left(S+1\right) \delta_{\alpha\beta}, \tag{2.5}$$

and its vector representation is given as

$$\hat{\boldsymbol{Q}}_i = \begin{pmatrix} \hat{Q}_i^{x^2-y^2} \\ \hat{Q}_i^{3z^2-r^2} \\ \hat{Q}_i^{xy} \\ \hat{Q}_i^{yz} \\ \hat{Q}_i^{zx} \end{pmatrix} = \begin{pmatrix} \left(\hat{S}_i^x\right)^2 - \left(\hat{S}_i^y\right)^2 \\ \frac{1}{\sqrt{3}} \left[3\left(\hat{S}_i^z\right)^2 - S(S+1) \right] \\ \hat{S}_i^x \hat{S}_i^y + \hat{S}_i^y \hat{S}_i^x \\ \hat{S}_i^y \hat{S}_i^z + \hat{S}_i^z \hat{S}_i^y \\ \hat{S}_i^z \hat{S}_i^x + \hat{S}_i^x \hat{S}_i^z \end{pmatrix}. \tag{2.6}$$

Then, the expectation value of the quadrupolar moment is calculated as

$$\boldsymbol{Q}_i = \left\langle \psi_i \middle| \hat{\boldsymbol{Q}}_i \middle| \psi_i \right\rangle = - \begin{pmatrix} |d_{i,x}|^2 - |d_{i,y}|^2 \\ \frac{1}{\sqrt{3}} \left(2\left|d_{i,z}\right|^2 - \left|d_{i,x}\right|^2 - \left|d_{i,y}\right|^2 \right) \\ \left(d_{i,x}^* d_{i,y} + d_{i,y}^* d_{i,x} \right) \\ \left(d_{i,y}^* d_{i,z} + d_{i,z}^* d_{i,y} \right) \\ \left(d_{i,z}^* d_{i,x} + d_{i,x}^* d_{i,z} \right) \end{pmatrix}. \tag{2.7}$$

We remark two points on this sSU(3)-MC method. Firstly, this method is equivalent to the approximation leaving the leading terms of the cumulant expansion of the partition function [49];

$$\begin{aligned} \mathcal{Z} &= \mathrm{Tr} \mathrm{e}^{-\beta \mathcal{H}} \\ &= \int \prod_{i=1}^{N} \mathrm{d}\Omega_{d_i} \, \langle \Psi | \mathrm{e}^{-\beta \mathcal{H}} | \Psi \rangle \\ &\approx \int \prod_{i=1}^{N} \mathrm{d}\Omega_{d_i} \mathrm{e}^{-\beta \langle \Psi | \mathcal{H} | \Psi \rangle} \\ &= \int \prod_{i=1}^{N} \mathrm{d}\Omega_{d_i} \mathrm{e}^{-\beta E_{\mathrm{sSU(3)}}}, \end{aligned} \tag{2.8}$$

where

$$\mathrm{d}\Omega_{d_i} = (2\pi)^2 \prod_{\alpha=x,y,z} \mathrm{d}\left(\mathrm{Re}\ d_{i,\alpha}\right) \mathrm{d}\left(\mathrm{Im}\ d_{i,\alpha}\right) \delta\left(\sum_{\alpha=x,y,z} |d_{i,\alpha}|^2 - 1 \right), \tag{2.9}$$

where $\delta(x)$ is the Dirac's delta. This may imply that the sSU(3)-MC is merely the mean-field treatment. However, this method has an advantage over both of the usual mean-field calculations at finite temperature and the classical approximation on spin moments. The usual mean-field calculations naturally assume the spatially uniform orientation of the expectation values of spin moments, while the sSU(3)-MC allows the difference of the wave function $|\psi_i\rangle$ or $\boldsymbol{d}_i$ among all sites within the ensemble averages, which can incorporate the spatial fluctuation effect. Also, the sSU(3)-MC can take in some amount of the quantum fluctuation effect other than the quantum condensation effect. In the MC sampling process, the stochastic MC average can take the inter-site quantum entanglement into account. In particular, when the long-range order of the ground state is well described by the product state of the unit which is locally entangled, which also applies to the present case [17, 19, 30], it is impossible to distinguish the thermal and quantum fluctuations, and this sSU(3)-MC treatment will give a good approximation. Similarly, the sSU(3)-MC has an advantage over the simple classical approximation, where the spins are treated as a unit vector [133]. The sSU(3)-MC correctly describes the quantum mechanical effect of the biquadratic interaction $\left(\hat{\boldsymbol{S}}_i \cdot \hat{\boldsymbol{S}}_j\right)^2$ which suppresses the spin moments and favors the quadrupolar moments, while the biquadratic term classically treated favors the collinear ordering of spins [49], which is different from the quantum quadrupolar order.

Secondly, through the sSU(3)-MC approximation, we formally simulate the classical system with complex unit vectors (Eq. (2.3)), and we do not include the quantum condensation effect at low-temperature. In fact, as we see in Sec. 2.2.2, the present description fails to reproduce the lowest temperature properties of the original model; the true quantum low-energy excitation is dominated by the three kinds of the energy branches represented by the three species of Schwinger bosons, which leads to the T^2-contribution to the specific heat [17, 19, 33, 35]. However, the excitations described by our approach give the constant specific heat originating from the law of equipartition of energy from the four classical degrees of freedom. Despite these inconsistencies, we believe that our theory captures the behavior of the model at around the phase transition point since it is already far away from $T = 0$; there, the thermal fluctuation will mask these quantum condensation effect and instead the collective behavior of the spins and quadrupoles becomes essential. Actually, the previous quantum Monte Carlo simulation indicates that the temperature dependence of the specific heat is off the T^2-behavior around $T \sim T_c/2$ [48].

2.1.3 Basics of the Markov chain Monte Carlo simulations

Here we briefly review the basic concept of the Markov chain Monte Carlo simulations for the calculation of the physical quantities of the (classical) many-body systems at finite temperature. To write this section (particularly Sec. 2.1.3.1), we partly referred to Refs. [134–136].

2.1.3.1 Markov-chain Monte Carlo sampling

The finite-temperature expectation values of the physical operator, O, is given as [5]

$$\langle O \rangle = \sum_{n=1}^{\dim \mathscr{H}} p_n \langle \Psi_n | O | \Psi_n \rangle, \qquad p_n = \frac{\mathrm{e}^{-\beta E_n}}{Z}, \qquad Z = \sum_n \mathrm{e}^{-\beta E_n}, \tag{2.10}$$

where $\dim \mathscr{H}$ is the dimension of the Hilbert space, Z is the partition function, and E_n and $|\Psi_n\rangle$ are the eigenenergy and eigenstate of n-th state, respectively [6]. However, in the many-body systems which we want to deal with, $\dim \mathscr{H}$ exponentially increases to the number of sites, and practically it is too difficult to perform the above calculation of the expectation values for large systems. Therefore, we take the Monte Carlo sampling following the canonical ensemble $\mathrm{e}^{-\beta E_n}$ as

$$\langle O \rangle \simeq \frac{1}{N_{\mathrm{MC}}} \sum_{n_{\mathrm{MC}}=1}^{N_{\mathrm{MC}}} O_{n_{\mathrm{MC}}}, \tag{2.11}$$

where $O_{n_{\mathrm{MC}}}$ the physical quantity of n_{MC}-th state generated following the canonical ensemble, and N_{MC} is the number of the generated states.

To properly generate the states in the Monte Carlo sampling following the canonical ensemble, the Markov process, where the transition probability to the new state is determined only by the present state, is utilized, which is called the Markov-chain Monte Carlo (MCMC) method [137]. In the MCMC process, regardless of the initial state, the distribution converges to the stationary (canonical) distribution if the samplings satisfy the following conditions [7];

- Ergodicity

  In the Markov process, each state can be changed into all the other states by the finite number of times of transition processes.

- Balance condition

  The following equation, i.e., balance condition, should hold;

  $$\sum_{n' \neq n} (p_n w_{n \to n'} - p_{n'} w_{n' \to n}) = 0, \tag{2.12}$$

  where $w_{n \to n'}$ is the transition probability from the n-th state to the n'-th state. This is derived from the Master equation for the stationary distributions.

Practically, the detailed balance condition,

$$p_n w_{n \to n'} = p_{n'} w_{n' \to n}, \qquad \forall n, n' \tag{2.13}$$

[5] For simplicity, here we consider the system with the discrete variables. When one consider the system with the continuous variables x, one should replace the summation $\sum_n$ by the integral $\int \mathrm{d}x$ appropriately.

[6] As we only consider the classical systems here, all operators can be treated as c-number.

[7] To be more precise, the aperiodicity should also be satisfied, but this condition can be included into the ergodicity conditions.

is used instead of the balance condition (Eq. (2.12)). Since it assumes that all of the summands in the balance condition are zero, the detailed balance condition is a sufficient condition of the balance condition [8]. To achieve the detailed balance condition, the Metropolis method [9] [137],

$$w_{n\to n'} = \min\left\{1, \mathrm{e}^{-\beta\Delta E}\right\}, \tag{2.14}$$

or the heat bath method,

$$w_{n\to n'} = \frac{\mathrm{e}^{-\beta\Delta E}}{1+\mathrm{e}^{-\beta\Delta E}}, \tag{2.15}$$

where $\Delta E = E_{n'} - E_n$, are typically used [10].

The susceptibilities are calculated as follows; the specific heat, $C(T)$, is given as [11]

$$C(T) = \frac{\partial}{\partial T}\langle E\rangle = -\frac{\partial\beta}{\partial T}\frac{\partial}{\partial\beta}\left(\frac{\partial}{\partial\beta}\ln Z\right) = \frac{\langle E^2\rangle - \langle E\rangle^2}{k_{\mathrm{B}}T^2}, \tag{2.16}$$

and the magnetic susceptibility is calculated as

$$\chi(T) = \frac{\partial}{\partial h}\langle S^z\rangle = \beta\frac{\partial^2}{\partial(\beta h)^2}\ln Z = \frac{\left\langle (S^z)^2\right\rangle - \langle S^z\rangle^2}{k_{\mathrm{B}}T}. \tag{2.17}$$

We also calculate the susceptibility of α-component of spin separately as

$$\chi^\alpha(T) = \frac{\left\langle (S^\alpha)^2\right\rangle - \langle S^\alpha\rangle^2}{k_{\mathrm{B}}T}. \tag{2.18}$$

where S^α is the averaged value of the α-component of the spin,

$$S^\alpha = \frac{1}{N}\sum_{i=1}^{N} S_i^\alpha. \tag{2.19}$$

2.1.3.2 Exchange Monte Carlo method

To accelerate the convergence to the equilibrium in the MCMC process, we utilize the exchange Monte Carlo method [139]. Exchange MC is one of the extended ensemble methods and originally introduced to resolve the problem in the spin glass systems where

[8] Thus, the detailed balance condition sometimes makes the MC sampling slower. In fact, acceleration of the Monte Carlo samplings by breaking the detailed balance conditions have also been proposed [138].

[9] In the Metropolis method, a new configuration with lower energy than the present configuration is always accepted, and one with higher energy is accepted with probability $\mathrm{e}^{-\beta\Delta E}$.

[10] In our explanation here, one may consider that we assume that the new states are always randomly selected, and the Metropolis method and the heat bath method only differ in the transition probability. However, to be more precise, the difference between the Metropolis method and the heat bath method is not simply in the choice of the transition probability. The Monte Carlo update consists of two processes, the proposal and the acceptance of the new states. In the Metropolis method, the new states are (uniform) randomly proposed, and whether one accepts or rejects those states are executed following the probability of the distribution. By contrast, in the heat bath method, the new states are proposed following the probability of the distribution, and the proposed states are always accepted.

[11] This is a kind of the fluctuation–response relation.

the states generated in the MC simulations are frequently trapped in the metastable states and do not reach the equilibrium states. In the exchange MC method, the exchanges of the configurations among multiple replicas are incorporated into the MCMC process of the usual update of the configurations.

Below we describe the procedure of the exchange MC method following Ref. [139]. We prepare M noninteracting replicas which share the common Hamiltonian. Then, the partition function of the whole system consisting of M-replicas is given as

$$Z_{\rm tot} = \prod_{m=1}^{M} Z_m, \qquad Z_m = \sum_{n_m} {\rm e}^{-\beta_m E_{m,n_m}}, \tag{2.20}$$

where β_m and Z_m (m = 1–M) are the inverse temperature and partition function of the m-th replica, respectively, and E_{m,n_m} is the energy of the n_m-th state of the m-th replica [12]. When the information of the baths $\{\beta_1, \cdots, \beta_M\}$ is given, the probability of finding the set of states $\{E_{m,n_m}, \beta_m\}$ is given as

$$P(\{E_{m,n_m}, \beta_m\}) = \prod_{m=1}^{M} p(E_{m,n_m}, \beta_m), \qquad p(E_{m,n_m}, \beta_m) = \frac{1}{Z_m} {\rm e}^{-\beta_m E_{m,n_m}}. \tag{2.21}$$

Exchanges of two states of the replicas m and m' are performed following the detailed balance conditions [13],

$$\begin{aligned} &P(\underbrace{E_{1,n_1}, \beta_1}_{(1)}; \cdots ; \underbrace{E_{m,n_m}, \beta_m}_{(m)}; \cdots ; \underbrace{E_{m',n_{m'}}, \beta_{m'}}_{(m')}; \cdots ; \underbrace{E_{M,n_M}, \beta_M}_{(M)}) W(E_{m,n_m}, \beta_m | E_{m',n_{m'}}, \beta_{m'}) \\ &= P(\underbrace{E_1, \beta_1}_{(1)}; \cdots ; \underbrace{E_{m',n_{m'}}, \beta_m}_{(m)}; \cdots ; \underbrace{E_{m,n_m}, \beta_{m'}}_{(m')}; \cdots ; \underbrace{E_{M,n_M}, \beta_M}_{(M)}) W(E_{m',n_{m'}}, \beta_m | E_{m,n_m}, \beta_{m'}), \end{aligned} \tag{2.22}$$

where $W(E_{m,n_m}, \beta_m | E_{m',n_{m'}}, \beta_{m'})$ is the probability of exchanging the n_m-th state in m-th replica and $n_{m'}$-th state in m'-th replica, so the ratio of $W(E_{m,n_m}, \beta_m | E_{m',n_{m'}}, \beta_{m'})$ and $W(E_{m',n_{m'}}, \beta_m | E_{m,n_m}, \beta_{m'})$ satisfies

$$\begin{aligned} &\frac{W(E_{m,n_m}, \beta_m | E_{m'}, \beta_{m'})}{W(E_{m',n_{m'}}, \beta_m | E_{m',n_{m'}}, \beta_m)} \\ &= \frac{P(E_{1,n_1}, \beta_1; \cdots ; E_{m',n_{m'}}, \beta_m; \cdots ; E_{m,n_m}, \beta_{m'}; \cdots ; E_{M,n_M}, \beta_M)}{P(E_{1,n_1}, \beta_1; \cdots ; E_{m,n_m}, \beta_m; \cdots ; E_{m',n_{m'}}, \beta_{m'}; \cdots ; E_{M,n_M}, \beta_M)} \\ &= \frac{{\rm e}^{-\beta_m E_{m',n_{m'}} - \beta_{m'} E_{m,nm}}}{{\rm e}^{-\beta_m E_{m,n_m} - \beta_{m'} E_{m',n_{m'}}}} \\ &= {\rm e}^{-\Delta}, \end{aligned} \tag{2.23}$$

[12] Although we distinguish the energies by the index m, E_{m,n_m} only depends on n_m and is independent of m, since all M noninteracting replicas share the common Hamiltonian.

[13] This construction does not satisfy the detailed balance conditions in each step in the exact meaning. Nevertheless, this method is faster than the method exactly satisfying the detailed balance conditions Also, when one regards two MCSs as one set of MCS, the detailed balance condition is again satisfied.

where

$$\Delta = (\beta_{m'} - \beta_m)\left(E_{m,n_m} - E_{m',n_{m'}}\right). \tag{2.24}$$

Therefore, to satisfy the detailed balance condition in the exchange of the replicas, we should set the transition probability as

$$W(E_{m,n_m}, \beta_m | E_{m',n_{m'}}, \beta_{m'}) = \min\left\{1, \mathrm{e}^{-\Delta}\right\} = \begin{cases} 1 & (\Delta < 0) \\ \mathrm{e}^{-\Delta} & (0 \leq \Delta) \end{cases}, \tag{2.25}$$

if we apply the Metropolis update. The procedure of MCMC simulation with replica exchange is summarized as follows;

1. Set initial configurations of each replica.
2. Local update in each replica independently and parallelly.
3. Exchange trials of configurations of two replicas following the detailed balance conditions [14].
4. Go to 2.

2.2 Magnetic field effect on the finite-temperature properties of the ferroquadrupolar phase

We perform the sSU(3)-MC calculation, where each Monte Carlo step (MCS) consists of the N-times single spin update by the Metropolis method and the succeeding replica exchange trials between neighboring two replicas by the Metropolis method. Starting with independent initial configurations, we perform multiple runs (typically $O(10^1)$, depending on the system size) and calculate the averages by the jackknife resampling. Each run includes 10^6–10^7 MCS for the equilibration and the measurements of the physical quantities, respectively. The intervals of the temperatures between replicas are set to be equal, and the number of replicas is 30–50, which depends on the system size. The details on the single spin update and the jackknife resampling are given in Appendix A.

2.2.1 Phase diagram and susceptibilities

We discuss the physical properties of the ferroquadrupolar phase at finite-temperature. In Fig. 2.2(a), we show the phase diagram on the plane of T and h for the triangular lattice with $(J, K) = (0, -1)$, where the ground state is the ferroquadrupolar order [17, 19]. The system size is $L \times L$ with $L = 12$–36 (see Fig. 2.1), and we take the periodic boundary condition. The transition temperature, T_c, is determined by the peak position of the specific heat. We show the temperature dependence of the specific heat $C(T)/N$ for various values of the magnetic field in Fig. 2.2(b). When a small magnetic field, $h \lesssim 1$, is

[14] In the exchange trials, any pairs of replicas can be exchanged, but typically the neighboring replicas are exchanged to increase the exchange probability. Actually, exchanges between the neighboring pairs are performed in the original paper [139].

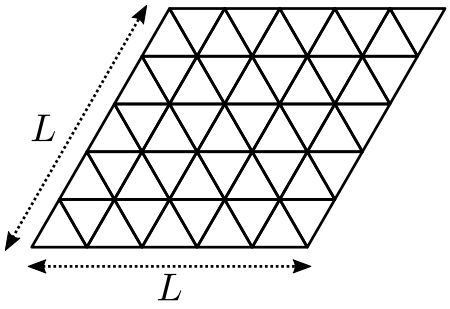

Figure 2.1: Triangular lattice with $L \times L$ sites.

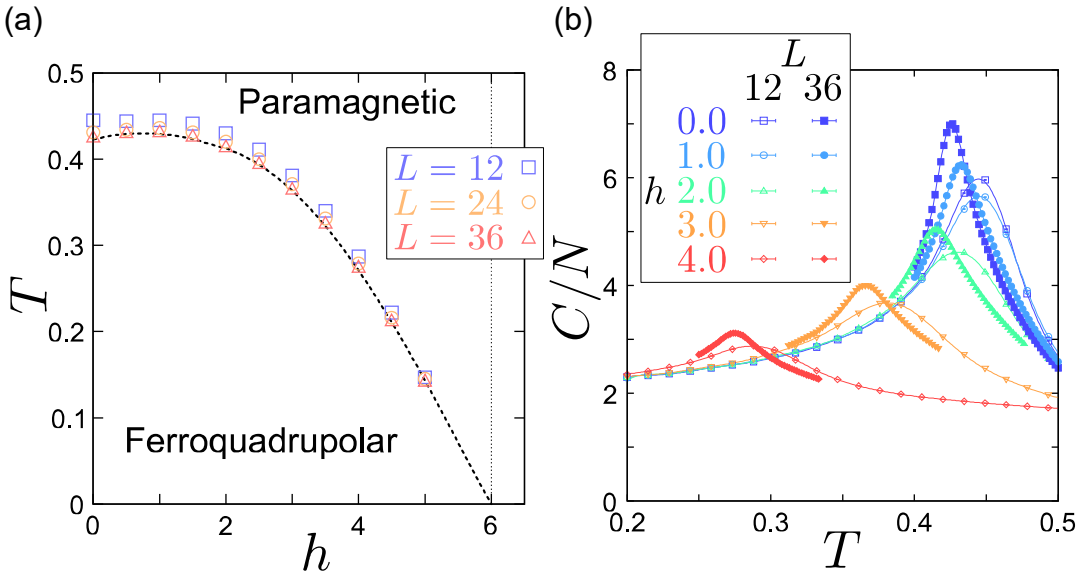

Figure 2.2: Results of the sSU(3)-MC calculations in the spin-1 BLBQ model on the triangular lattice with $(J, K) = (0, -1)$. (a) Phase diagram on the plane of h and T. Squares, circles, and triangles denote the temperatures where the specific heat have a peak, which are estimated by the Gaussian kernel approximation in the $L = 12$, 24, and 36 samples, respectively. (b) Temperature dependence of the specific heat C/N for various magnitudes of the magnetic field h. Open and filled symbols represent the results in the $L = 12$ and 36 samples, respectively. Figures are taken from Ref. [1] (Copyright ©2020, American Physical Society).

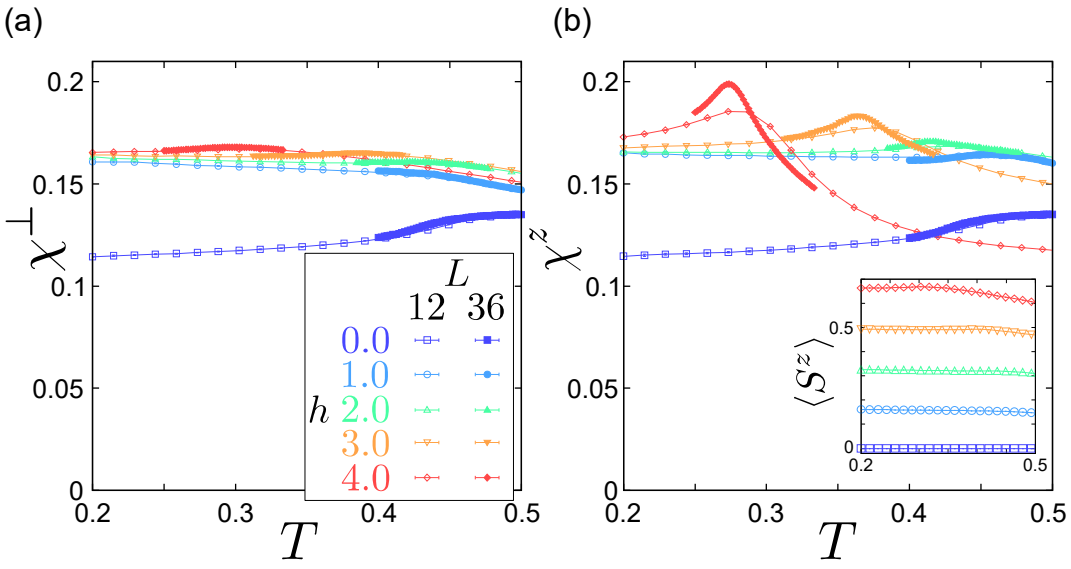

Figure 2.3: Temperature dependence of the magnetic susceptibilities of (a) the perpendicular and (b) parallel components in the spin-1 BLBQ model on the triangular lattice with $(J, K) = (0, -1)$ and various magnitudes of the magnetic field h. Open and filled symbols denote the results in the $L = 12$ and 36 samples, respectively. The inset in (b) shows the temperature dependence of the magnetization density in $L = 12$ samples. Figures are taken from Ref. [1] (Copyright ©2020, American Physical Society).

applied, the peak of the specific heat moves to higher temperature, and then shifts toward the lower temperature in a larger magnetic field. In Fig. 2.2(b), the results for $L = 12$ and 36 are shown together, showing that T_c becomes slightly lower and the peak intensity becomes stronger as the system becomes larger. However, the system size dependence is small.

In Figs. 2.3(a) and 2.3(b), we show the temperature dependence of the spin susceptibilities of the perpendicular and parallel components to the magnetic field, $\chi^{\perp} = (\chi^x(T) + \chi^y(T))/2$, and χ^z, respectively. We confirm that the susceptibility of the parallel component, χ^z, starts to show a peak structure around T_c in an applied magnetic field, which suggests that the magnetic moment parallel to the z-axis develops by a magnetic field. By contrast, the susceptibility of the perpendicular component, $\chi^{\perp}$, is almost flat and does not show a clear peak, while a tiny structure can be seen around T_c in a high field region. We show the temperature dependence of the magnetization density, $\langle S^z \rangle$, in the inset of Fig. 2.3(b). The magnetization density does not change much around the transition temperature, and that in the ferroquadrupolar phase is consistent with the known result for the ground state, $m = h/[z(J - K)] = h/6$ [17–19].

2.2.2 Entropic effect

2.2.2.1 Low-temperature properties

The semiclassical SU(3) Hamiltonian is formally a classical one which describes the interactions between the complex unit vectors $\boldsymbol{d}_i$ which represents the one-body wave function on site-i. Similarly to the case of the classical XY models [140, 141], the low-temperature

thermodynamic quantities of the semiclassical SU(3) Hamiltonian can be evaluated by starting from the ground states and considering the low-energy harmonic branches which appears by taking the thermal fluctuation into consideration.

The complex $\boldsymbol{d}$-vector on each site, $\boldsymbol{d}_i$, can be separated into the real and imaginary parts as $\boldsymbol{d}_i = \boldsymbol{u}_i + \mathrm{i}\boldsymbol{v}_i$, where $\boldsymbol{u}_i, \boldsymbol{v}_i \in \mathbb{R}^3$. $\boldsymbol{u}_i$ and $\boldsymbol{v}_i$ satisfy the normalization condition of the $\boldsymbol{d}$-vector, $|\boldsymbol{u}_i|^2 + |\boldsymbol{v}_i|^2 = 1$, and the overall phase can be fixed such that $\boldsymbol{u}_i$ and $\boldsymbol{v}_i$ are always orthogonal, $\boldsymbol{u}_i \cdot \boldsymbol{v}_i = 0$ [16–18]. For the ground states, regardless of the presence or absence of the magnetic field, and the lattice geometry, $\boldsymbol{u}_i$ and $\boldsymbol{v}_i$ can be chosen to be site-independent as $\boldsymbol{u}_i = \boldsymbol{u}_0$ and $\boldsymbol{v}_i = \boldsymbol{v}_0$ [15], and are determined analytically. The lowest energy excitation by the thermal fluctuation can be expressed by varying these vectors of the ground states as

$$\boldsymbol{u}_i = \boldsymbol{u}_0 + \delta\boldsymbol{u}_i,\ \boldsymbol{v}_i = \boldsymbol{v}_0 + \delta\boldsymbol{v}_i. \tag{2.26}$$

Below we particularly discuss only the case where $(J, K) = (0, -1)$ on the triangular lattice without a magnetic field for simplicity, while we argue later that the results do not change qualitatively even when the magnetic field and/or the bilinear (Heisenberg) terms. When $(J, K) = (0, -1)$, The ground state has the ferroquadrupolar order, and $\boldsymbol{u}_0$ and $\boldsymbol{v}_0$ can be chosen as

$$\boldsymbol{u}_0 = \begin{pmatrix} 1 \\ 0 \\ 0 \end{pmatrix},\ \boldsymbol{v}_0 = \boldsymbol{0}. \tag{2.27}$$

Then, the above local constraints on site-i are rewritten as

$$\begin{cases} 2\delta u_i^x + (\delta\boldsymbol{u}_i)^2 + (\delta\boldsymbol{v}_i)^2 &= 0 \qquad \text{(normalization)} \\ \delta v_i^x + \delta\boldsymbol{u}_i \cdot \delta\boldsymbol{v}_i &= 0 \qquad \text{(overall phase fixing)} \end{cases}. \tag{2.28}$$

Then, the energy evaluated by the product state of the one-body wave functions can be rewritten up to $O(\delta^2)$ as

$$\begin{aligned} &E_{\mathrm{sSU(3)}} \\ =& -\sum_{\langle i,j\rangle} \left[(\boldsymbol{u}_i \cdot \boldsymbol{u}_j - \boldsymbol{v}_i \cdot \boldsymbol{v}_j)^2 + (\boldsymbol{u}_i \cdot \boldsymbol{v}_j + \boldsymbol{v}_i \cdot \boldsymbol{u}_j)^2 + 1 \right] \\ =& -zN + \sum_{\langle i,j\rangle} \sum_{\alpha=y,z} \left[\left((\delta u_i^\alpha)^2 + (\delta v_i^\alpha)^2 \right) + \left(\left(\delta u_j^\alpha\right)^2 + \left(\delta v_j^\alpha\right)^2 \right) - 2\left(\delta u_i^\alpha \delta u_j^\alpha - \delta v_i^\alpha \delta v_j^\alpha\right) \right]. \end{aligned} \tag{2.29}$$

Here, the terms including δu_i^x and δv_i^x are dropped using the constraints. Performing the Fourier transform given as

$$\delta\boldsymbol{u}_{\boldsymbol{k}} = \frac{1}{\sqrt{N}} \sum_{i=1}^{N} \mathrm{e}^{-\mathrm{i}\boldsymbol{k}\cdot\boldsymbol{r}_i} \delta\boldsymbol{u}_i,\ \delta\boldsymbol{v}_{\boldsymbol{k}} = \frac{1}{\sqrt{N}} \sum_{i=1}^{N} \mathrm{e}^{-\mathrm{i}\boldsymbol{k}\cdot\boldsymbol{r}_i} \delta\boldsymbol{v}_i, \tag{2.30}$$

[15] This also holds for the case with antiferroic orderings with multiple sublattices, where there are as many numbers of $\boldsymbol{u}_0$ and $\boldsymbol{v}_0$ as the numbers of sublattices.

the energy $E_{\mathrm{sSU(3)}}$ can be diagonalized as

$$E_{\mathrm{sSU(3)}} = E_0 + \sum_{\boldsymbol{k}} E_{\boldsymbol{k}}, \tag{2.31}$$

where

$$E_0 = -zN, \tag{2.32}$$

$$E_{\boldsymbol{k}} = \sum_{\alpha=y,z} \left[(-\gamma_{\boldsymbol{k}} + z)\, \delta u^{\alpha}_{\boldsymbol{k}} \delta u^{\alpha}_{-\boldsymbol{k}} + (\gamma_{\boldsymbol{k}} + z)\, \delta v^{\alpha}_{\boldsymbol{k}} \delta v^{\alpha}_{-\boldsymbol{k}} \right], \tag{2.33}$$

$$\gamma_{\boldsymbol{k}} = 2 \left[\cos k_x + \cos\left(\frac{k_x + \sqrt{3} k_y}{2} \right) + \cos\left(\frac{k_x - \sqrt{3} k_y}{2} \right) \right]. \tag{2.34}$$

Performing the Gaussian integral, the partition function is given as [16]

$$Z \simeq \int \mathrm{e}^{-\beta E_{\mathrm{sSU(3)}}} \prod_{\boldsymbol{k}} \mathrm{d}(\delta u^{y}_{\boldsymbol{k}}) \mathrm{d}(\delta u^{z}_{\boldsymbol{k}}) \mathrm{d}(\delta v^{y}_{\boldsymbol{k}}) \mathrm{d}(\delta v^{z}_{\boldsymbol{k}}) \simeq \mathrm{e}^{-\beta E_0} \prod_{\boldsymbol{k}} \left[\frac{\pi^2}{\beta^2} \left(\det \mathcal{E}_{\boldsymbol{k}} \right)^{-\frac{1}{2}} \right], \tag{2.35}$$

where

$$\det \mathcal{E}_{\boldsymbol{k}} = \begin{pmatrix} -\gamma_{\boldsymbol{k}} + z & & & \\ & -\gamma_{\boldsymbol{k}} + z & & \\ & & \gamma_{\boldsymbol{k}} + z & \\ & & & \gamma_{\boldsymbol{k}} + z \end{pmatrix}. \tag{2.36}$$

Then, the statistical mechanical average of the energy density, $e(T, h = 0)$, is

$$e(T, h = 0) = \frac{1}{N} \left(-\frac{\partial}{\partial \beta} \ln Z \right) = \frac{E_0}{N} + 2 k_{\mathrm{B}} T, \tag{2.37}$$

and the specific heat in the low-temperature region, $c(T, h = 0)$, is

$$c(T, h = 0) = \frac{\partial}{\partial T} e(T, h = 0) = 2 k_{\mathrm{B}}. \tag{2.38}$$

We have assumed so far the case $h = 0$ and $J = 0$ with a ferroquadrupolar ground state on the triangular lattice. However, this result is nothing but a law of equipartition of energy, so that only the number of low-energy modes is responsible for the results, and the same conclusion on $e(T, h)$ and $c(T, h)$ holds even when the magnetic field h or the Heisenberg interaction J are introduced as far as the ground states remain ordered, and only the detailed forms of E_0 and $E_{\boldsymbol{k}}$ are modified. The results do not depend on the lattice geometry as far as it is in two-dimension, e.g., when we consider the same model on the square lattice.

2.2.2.2 Calculation of the entropy

The sSU(3)-MC calculation we performed is given for $0.2 \lesssim T$. To evaluate the thermodynamic entropy from the results of the calculation, we need to extrapolate these numerical

[16] Here, $\simeq$ means that the difference of the constant multiplications is allowed.

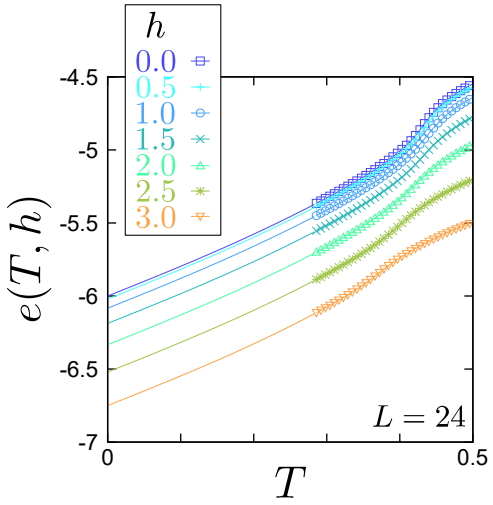

Figure 2.4: Temperature dependence of the energy density of the spin-1 BLBQ model on the triangular lattice with $(J, K) = (0, -1)$ in various values of the magnetic field in the $L = 24$ samples. Symbols represent the results of the sSU(3)-simulations, and the lines at lower temperature denote the energy densities evaluated by fitting the sSU(3)-MC results. Figures are taken from Ref. [1] (Copyright ©2020, American Physical Society).

results down to zero temperature. Based on the estimation above, the energy in the low-temperature region can be expressed as

$$e(T, h) = e(0, h) + 2k_{\mathrm{B}}T + \alpha(h)T^{\gamma(h)}, \tag{2.39}$$

where $e(0, h)$ is the ground state energy of $E_{\mathrm{sSU(3)}}$ given in Refs. [17, 19, 30], and $\alpha(h)T^{\gamma(h)}$ with $\gamma(h) > 1$ is the correction term for expressing the higher-temperature region. The actual values of $\alpha(h)$ and $\gamma(h)$ are evaluated by fitting the calculated energy data. The results of the fitting are shown in Fig. 2.4. Then, the specific heat density is given as

$$c(T, h) = \frac{\partial}{\partial T} e(T, h) = 2k_{\mathrm{B}} + \alpha(h)\gamma(h)T^{\gamma(h)-1}, \tag{2.40}$$

and the entropy density is calculated as

$$s(T, h) = \int_0^T \frac{c(T', h)}{T'} \mathrm{d}T = \int_0^T \frac{2k_{\mathrm{B}}}{T'} \mathrm{d}T' + \frac{\alpha(h)\gamma(h)}{\gamma(h) - 1} T^{\gamma(h)-1}. \tag{2.41}$$

The first term, $\displaystyle\int_0^T \frac{2k_{\mathrm{B}}}{T'} \mathrm{d}T'$, diverges, which is the artifact of the classical treatment of the low-energy modes. In fact, the original spin-1 BLBQ Hamiltonian is known to exhibit T^2 scaling of the specific heat at sufficiently low temperatures, which originates from the excitation of three-colored Schwinger bosons [19, 33, 48, 50]. This kind of quantum condensation effect is not taken into consideration in $E_{\mathrm{sSU(3)}}$, and instead the classical divergent term appears as an artifact. However, because it contributes to all of the cases as common constant shift where the above discussion holds regardless of the values of h and J, this term no longer plays an important role in discussing the higher temperature region where we are focusing. Thus we drop this diverging term, and deal with the following

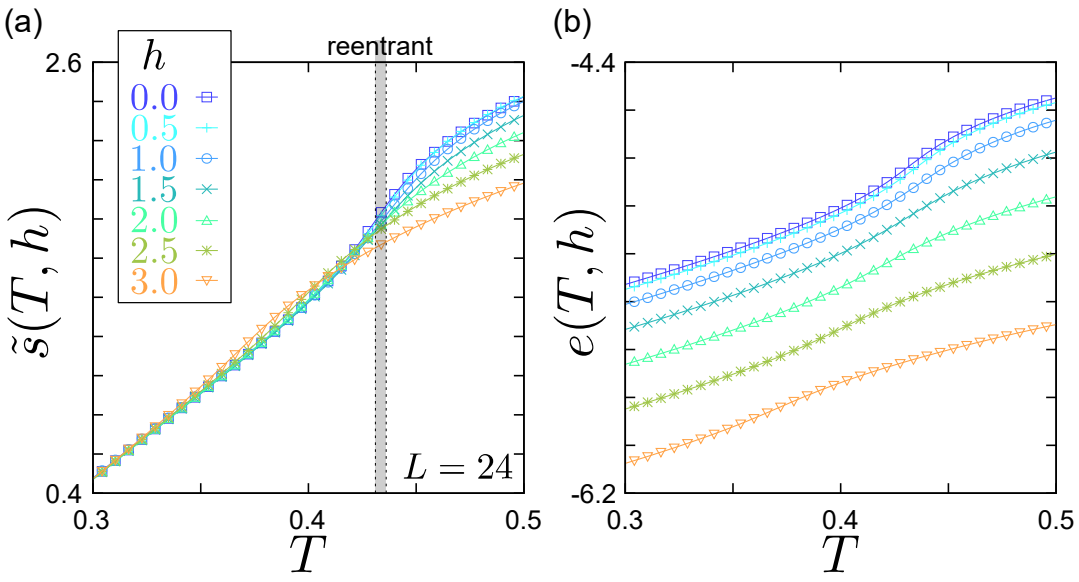

Figure 2.5: Temperature dependence of (a) the entropy density $\tilde{s}(T,h)$ and (b) the energy density $e(T,h)$ in the spin-1 BLBQ model on the $L=24$ triangular lattice with $(J,K)=(0,-1)$ and various magnitudes of the magnetic field h. The shaded area in (a) shows the region where the reentrant occurs in the $L=24$ samples. Figures are taken from Ref. [1] (Copyright ©2020, American Physical Society).

values [17];

$$\tilde{s}(T,h) = s(T,h) - \int_0^T \frac{2k_{\mathrm{B}}}{T'}\mathrm{d}T'. \tag{2.42}$$

In Fig. 2.5(a), we show the temperature dependence of $\tilde{s}(T,h)$ in a small magnetic field in the $L=24$ sample, and together the temperature dependence of the energy density, $e(T,h)$ of the $L=24$ sample in Fig. 2.5(b). In the ferroquadrupolar phase at lower temperature, the entropy density $\tilde{s}(T,h)$ remains almost unchanged or shows a slight increase in a magnetic field, whereas $\tilde{s}(T,h)$ in the paramagnetic phase at higher temperature decreases when the magnetic field is applied. By contrast, the energy density decreases by a nearly constant values with h common to both the paramagnetic and ferroquadrupolar phases, which is confirmed by the paramagnetic response to the magnetic field in both phases (see the inset of Fig. 2.3(b)). Thus, when we consider the Helmholtz free energy, $f(T,h)=e(T,h)-T\tilde{s}(T,h)$, the ferroquadrupolar phase becomes more stable in a small magnetic field region than the paramagnetic phase by the entropic effect, and the reentrant behavior occurs.

2.2.3 Magnetic field dependence of the quadrupolar moments

To see how the microscopic properties are affected by the magnetic field, we investigate the magnetic field dependence of the quadrupolar moments. At $T=0$, the $\boldsymbol{d}$-vector of the ferroquadrupolar ground state consists only of the real component and freely fluctuate

[17] We note that this expression is a formal one in the exact meaning since the second term in the right hand side diverges.

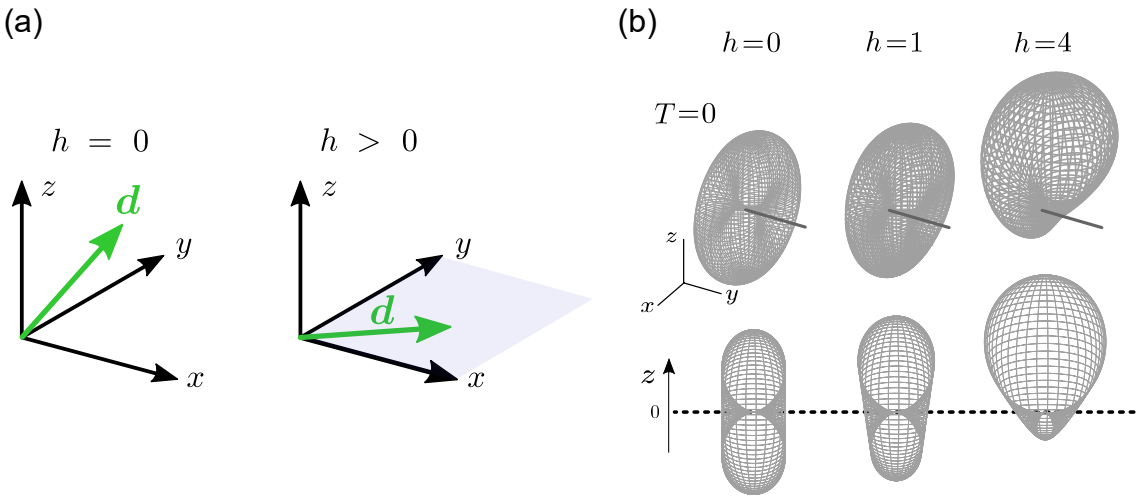

Figure 2.6: (a) Schematic picture of the $\boldsymbol{d}$-vectors in the ferroquadrupolar ground states at $h = 0$ (left) and $h \neq 0$ (right). At $h = 0$, the real $\boldsymbol{d}$-vector can point to an arbitrary direction. At $h \neq 0$, the $\boldsymbol{d}$-vector fluctuates inside xy-plane. (b) Distribution of the spin-component for the ferroquadrupolar ground states in various values of the magnetic field. Figure (b) is taken from Ref. [1] (Copyright ©2020, American Physical Society).

(see the left panel of Fig. 2.6(a)). When the magnetic field along the z-axis is applied to the ferroquadrupolar ground state, the $\boldsymbol{d}$-vector lies inside the xy-plane as shown in the right panel of Fig. 2.6(b) [18], namely, the (semiclassical) ground state has $d_{i,z} = 0$ and is expressed as

$$|\Psi\rangle = \bigotimes_{i=1}^{N} |\boldsymbol{d}_i\rangle\,, \qquad |\boldsymbol{d}_i\rangle = d_x\,|x\rangle + d_y\,|y\rangle\,. \tag{2.43}$$

This is because the Zeeman term is proportional to $\left(d^*_{i,x}d_{i,y} - d^*_{i,y}d_{i,x}\right)$, and couples to x- and y-components of the $\boldsymbol{d}$-vector, but not to the z-components [17, 19]. To gain the energy by the Zeeman term, the system tries to maximally develop $d_{i,x}$ and $d_{i,y}$, and resultantly suppresses $d_{i,z}$. The $d_{i,x}$ and $d_{i,y}$ components acquire the imaginary components, and the spin-component distribution in the $z < 0$ space shrinks and that in the $z > 0$ space expands (see Fig. 2.6(b)), which reflects the emergent finite magnetic moment along the z-axis ($z > 0$).

For the quadrupolar moments, we can see the different behavior of each component of $\boldsymbol{Q}_i$, whose formula is given in Eq. (2.7), against a magnetic field at $T = 0$, namely, Q_i^{xy} and $Q_i^{x^2-y^2}$ can have nonzero values, whereas Q_i^{yz} and Q_i^{zx} become zero due to $d_{i,z} = 0$. Therefore, we can prepare two types of the mean squared quadrupolar moments, $\bar{Q^2_{\rm in}}$ and $\bar{Q^2_{\rm out}}$, whose expressions are given as

$$\bar{Q^2_{\rm in}} = \frac{1}{2}\left[\left(Q^{x^2-y^2}\right)^2 + (Q^{xy})^2\right], \tag{2.44}$$

[18] Here, the 'plane' is $\mathbb{C}^2$, spanned by the two complex component vectors. When only the real components are used, this xy-plane is equivalent to $\mathbb{R}^4$, and the 'plane' means the 'hyperplane.'

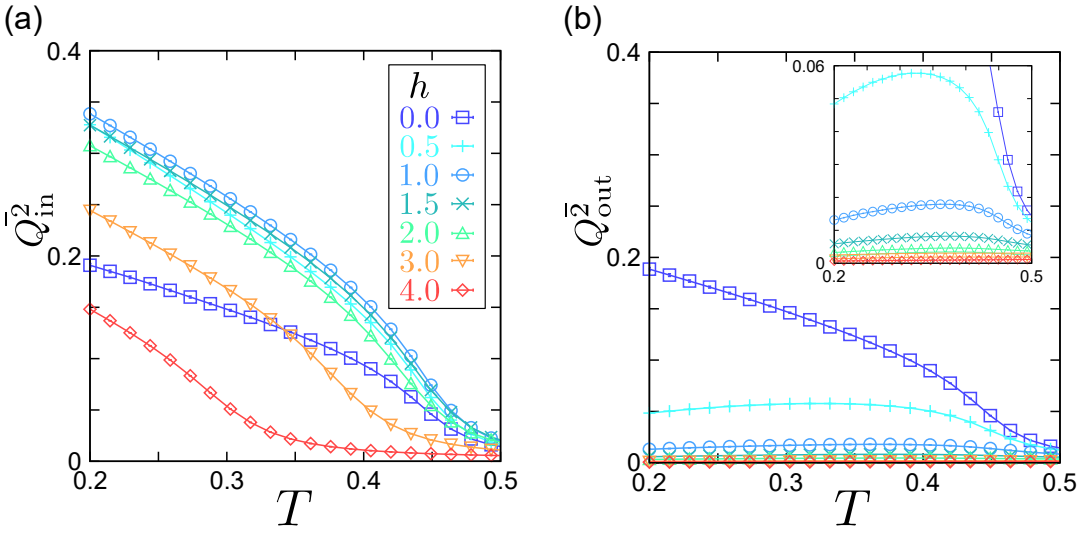

Figure 2.7: Temperature dependence of (a) $\bar{Q}^2_{\rm in}$ (Eq. (2.44)) and (b) $\bar{Q}^2_{\rm out}$ (Eq. (2.45)) for the triangular lattice with $L = 12$. The inset in (b) is the enlarged picture of small $\bar{Q}^2_{\rm out}$. Figures are taken from Ref. [1] (Copyright ©2020, American Physical Society).

$$\bar{Q}^2_{\rm out} = \frac{1}{2}\left[(Q^{yz})^2 + (Q^{zx})^2\right], \tag{2.45}$$

where $Q^{\alpha\beta}$ is the averaged value of the quadrupolar moment such as

$$Q^{xy} = \frac{1}{N}\sum_{i=1}^{N} Q_i^{xy}. \tag{2.46}$$

By definition, $\bar{Q}^2_{\rm in} \neq 0$ and $\bar{Q}^2_{\rm out} = 0$ hold in the ferroquadrupolar ground states in a magnetic field.

In Figs. 2.7(a) and 2.7(b), we show the temperature dependence of $\bar{Q}^2_{\rm in}$ and $\bar{Q}^2_{\rm out}$ in various magnitudes of the magnetic field. Without a magnetic field, all components in $\boldsymbol{Q}_i$, and thus $\bar{Q}^2_{\rm in}$ and $\bar{Q}^2_{\rm out}$ are equivalent, and their behaviors at finite-temperature are almost the same. When a magnetic field is applied, $\bar{Q}^2_{\rm in}$ once increases and then decreases in a larger field at $1 \lesssim h$. In contrast, $\bar{Q}^2_{\rm out}$ at finite-temperature, which has a small but finite value thanks to the thermal fluctuation which gives a finite $d_{i,z}$ monotonically decreases by applying a magnetic field. At $1 \lesssim h$, $\bar{Q}^2_{\rm out}$ almost becomes zero even at finite-temperature. These temperature dependencies of the quadrupolar moments suggest the crossover phenomenon from the low magnetic field region at $h \lesssim 1$ to the high magnetic field region at $1 \lesssim h$. In a low field, $\bar{Q}^2_{\rm in}$ can develop by selecting the xy-plane, while all quadrupolar fluctuations start to be suppressed by applying a larger magnetic field. In Fig. 2.8, we show the spin-component distribution at finite-temperature with and without magnetic field. At $T = 0.2$ with $h = 1$, the distribution taking a gourd-shape, which is to be contrasted to that at $T = 0.5$ with $h = 1$, suggests the development of the fluctuation in xy-plane with finite magnetic moment along the z-axis. In a larger field of $h = 4$, both of the distributions at high and low temperature regions have similar forms.

To identify that the reentrant behavior of the specific heat by the magnetic field is

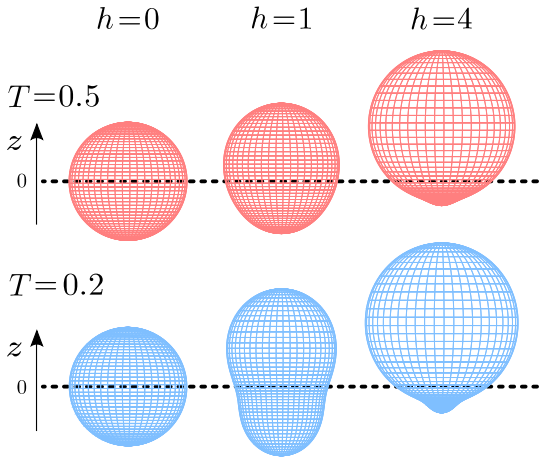

Figure 2.8: Distribution of the spin-component for the ferroquadrupolar phase at finite-temperature in various values of the magnetic field. Figure is taken from Ref. [1] (Copyright ©2020, American Physical Society).

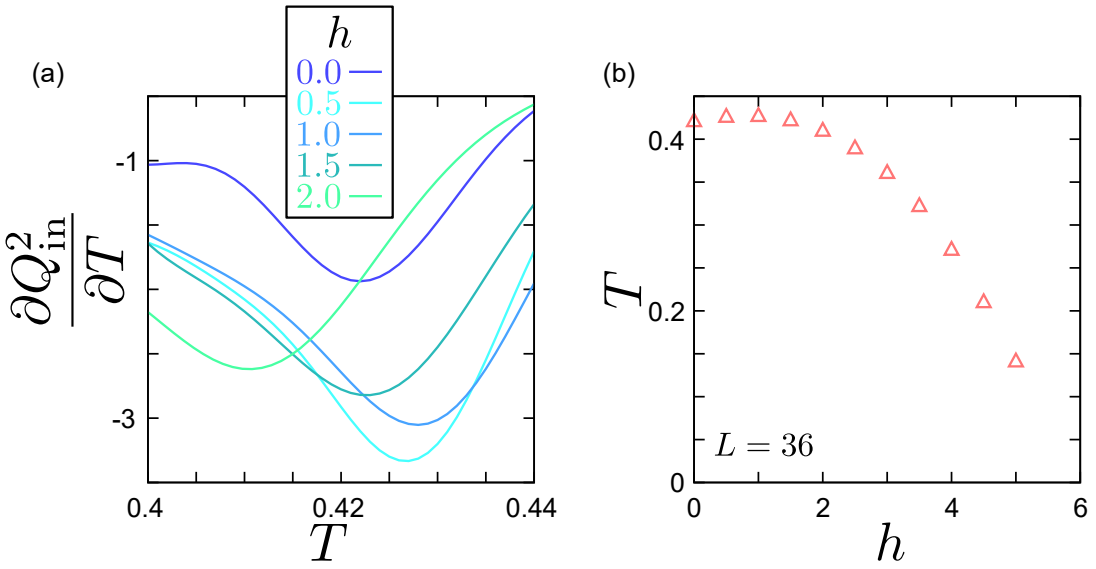

Figure 2.9: (a) Temperature dependence of $\frac{\partial \bar{Q}^2_{\rm in}}{\partial T}$ in various magnetic fields on the $L = 36$ triangular lattice estimated by the Gaussian kernel approximation. (b) The magnetic field dependence of the peak temperature of $\frac{\partial \bar{Q}^2_{\rm in}}{\partial T}$ on the $L = 36$ triangular lattice.

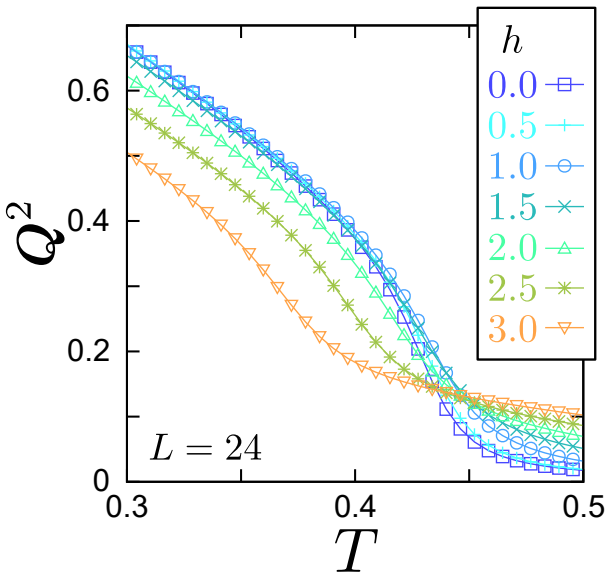

Figure 2.10: Temperature dependence of the squared quadrupolar moment, $\boldsymbol{Q}^2$, in various magnitudes of the magnetic field in the $L = 24$ triangular lattice (error bars are not shown).

due to the development of the quadrupolar moments, we estimate the temperature derivative of the in-plane components of the mean squared quadrupolar moments, $\frac{\partial \bar{Q}^2_{\rm in}}{\partial T}$ [19]. In Fig. 2.9(a), we show the temperature dependence of $\frac{\partial \bar{Q}^2_{\rm in}}{\partial T}$ on the triangular lattice with $L = 36$ in various magnitudes of the magnetic field, estimated by the Gaussian kernel approximation. When a small magnetic field is applied, the bottom positions of $\frac{\partial \bar{Q}^2_{\rm in}}{\partial T}$, where the quadrupolar moments most largely develop, moves toward the higher temperature. Then, the bottom positions go down to the low temperature at larger magnetic fields. Figure 2.9(b) shows the magnetic field dependence of the bottom positions of $\frac{\partial \bar{Q}^2_{\rm in}}{\partial T}$ in the $L = 36$ samples, which is similar to the T–h phase diagram in Fig. 2.2(a). This result is consistent with the reentrant behavior captured by the peak positions of the specific heat, which ensures that the reentrant behavior can be ascribed to the development of the quadrupolar moments.

In a low field, the entropy in the ferroquadrupolar phase is almost unchanged as shown in Fig. 2.5, while the in-plane and out-of-plane components of the quadrupolar moments changes by applying a magnetic field (see Fig. 2.7. To check the relation between the entropy and the quadrupolar moments, we evaluate the squared quadrupolar moment,

$$\boldsymbol{Q}^2 = \left(Q^{x^2-y^2}\right)^2 + \left(Q^{3z^2-r^2}\right)^2 + (Q^{xy})^2 + (Q^{yz})^2 + (Q^{zx})^2 \,. \tag{2.47}$$

In Fig. 2.10, we show the temperature dependence of $\boldsymbol{Q}^2$ when changing the magnetic field in the $L = 24$ samples. We find that $\boldsymbol{Q}^2$ is almost unchanged in a low field, $h \lesssim 1.5$, which

[19] Here, we first calculate the average of $Q^2_{\rm in}$, and then calculate the derivative of the average.

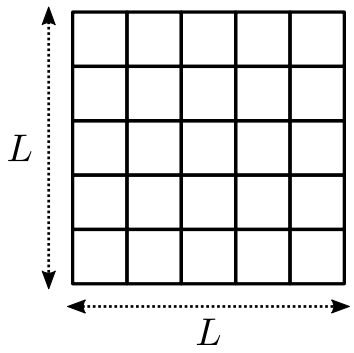

Figure 2.11: Square lattice with $L \times L$ sites.

will directly connect to the constant entropy against a low field [20]. Therefore, one can say that the whole value of the entropy is determined by the sum of each component rather than only the in-plane components, $\bar{Q^2_{\rm in}}$. Nevertheless, the contribution from $\bar{Q^2_{\rm in}}$ to the fluctuation, or the entropy, also becomes larger when $\bar{Q^2_{\rm in}}$ becomes larger by applying a small field.

2.2.4 Discussions and remarks

2.2.4.1 Independence of the lattice geometry

Here we show that the lattice geometry does not have a qualitative impact on the thermodynamic properties of the ferroquadrupolar phases, which indicates that this entropic effect is not due to the geometrical frustration effect. In addition to the calculation on the triangular lattice discussed above, we also performed the sSU(3)-MC simulation on the $L \times L$ square lattice with $L = 8$–32 (see Fig. 2.11). The parameters are set as $K/J = 2$ with $J, K < 0$, namely $(J, K) = (-1/\sqrt{5}, -2/\sqrt{5})$, where the semiclassical ground state has the ferroquadrupolar order [30]. In Fig. 2.12(a), we show the phase diagram on the plane of h and T, which indicates the small reentrant behavior by applying the magnetic field at $h \lesssim 0.25$. The temperature dependence of the specific heat $C(T)/N$ in the $L = 32$ sample in various magnitudes of the magnetic field is shown in Fig. 2.12(b), which shows that the peak position first shifts toward the higher temperature and then goes toward the lower temperature by a larger magnetic field.

In the same manner with the case of the triangular lattice, we estimate the energy density $e(T, h)$ at lower temperature by fitting the sSU(3)-MC data, and the entropy density $\tilde{s}(T, h)$. In Fig. 2.13(a), we show the energy density $e(T, h)$.

In Figs. 2.14(a) and 2.14(b), we show the temperature dependence of the spin susceptibility perpendicular and parallel to the magnetic field along the z-axis, $\chi^{\perp}$ and χ^{z}, respectively. The temperature dependence of the mean squared quadrupolar moments, $\bar{Q^2_{\rm in}}$ and $\bar{Q^2_{\rm out}}$, are shown in Figs. 2.14(c) and 2.14(d), respectively. One can confirm that these results are qualitatively the same as the ones in the triangular lattice (see Figs. 2.3,

[20] Note that other effects than the quadrupolar moments will become stronger in a larger magnetic field as $h \sim 3.0$, where $\boldsymbol{Q}^2$ deviates from the one in a lower field.

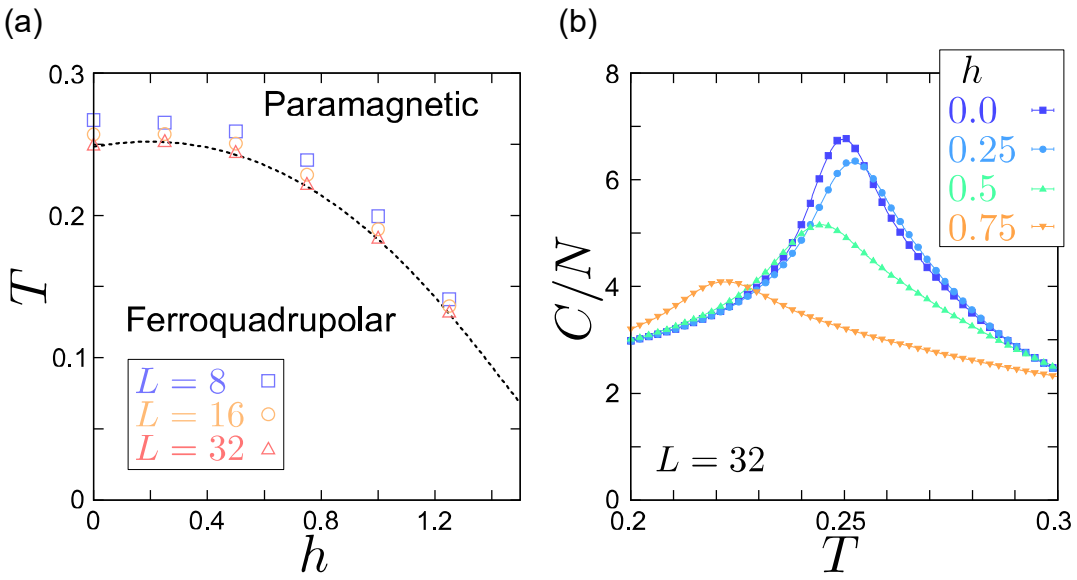

Figure 2.12: Results of the sSU(3)-MC simulation in the spin-1 BLBQ model on the square lattice with $K/J = 2$ and $J, K < 0$. (a) Phase diagram on the plane of h and T. Squares, circles, and triangles represent the peak positions of the specific heat estimated by the Gaussian kernel approximation in the $L = 8$, 16, and 32 samples, respectively. (b) Temperature dependence of the specific heat of the $L = 32$ samples in various values of the magnetic field. Figures are taken from Ref. [1] (Copyright ©2020, American Physical Society).

2.7).

We show the temperature dependence of the temperature derivative of $\bar{Q}^2_{\rm in}$, $\dfrac{\partial \bar{Q}^2_{\rm in}}{\partial T}$, with and without the magnetic field in Fig. 2.15(a), and the bottom position of $\dfrac{\partial \bar{Q}^2_{\rm in}}{\partial T}$ in Fig. 2.15(b). Similarly to the case of the triangular lattice, the bottom positions of $\dfrac{\partial \bar{Q}^2_{\rm in}}{\partial T}$ shows the small reentrant behavior.

In Fig. 2.16, we show the temperature dependence of $\boldsymbol{Q}^2$ when changing the magnetic field on the $L = 32$ square lattice. As in the triangular lattice, $\boldsymbol{Q}^2$ does not change much in a low field region, $h \lesssim 0.5$, which would lead to the (almost) constant entropy in the ferroquadrupolar phase at low temperature.

2.2.4.2 Properties of the ferroquadrupolar phase transition

Both of the original quantum Hamiltonian and the semiclassical Hamiltonian have the continuous symmetry, and the Mermin–Wagner theorem prohibits the finite-temperature phase transition that breaks the continuous symmetry [142]. However, the specific heat has a peak structure at T_c, which is also seen in the QMC calculations [48, 50]. This implies that the correlations actually develop, and topological phase transition like the Berezinskii–Kosterlitz–Thouless (BKT) transition [143–145] occurs. Actually, the excitation generating the topological defects with half-vortex and anti-(half)vortex was discussed in the low-dimensional spin-1 BLBQ models [18], and Pohle *et al.* numerically studied its dynamics and thermodynamics semiclassically and observed the generation of

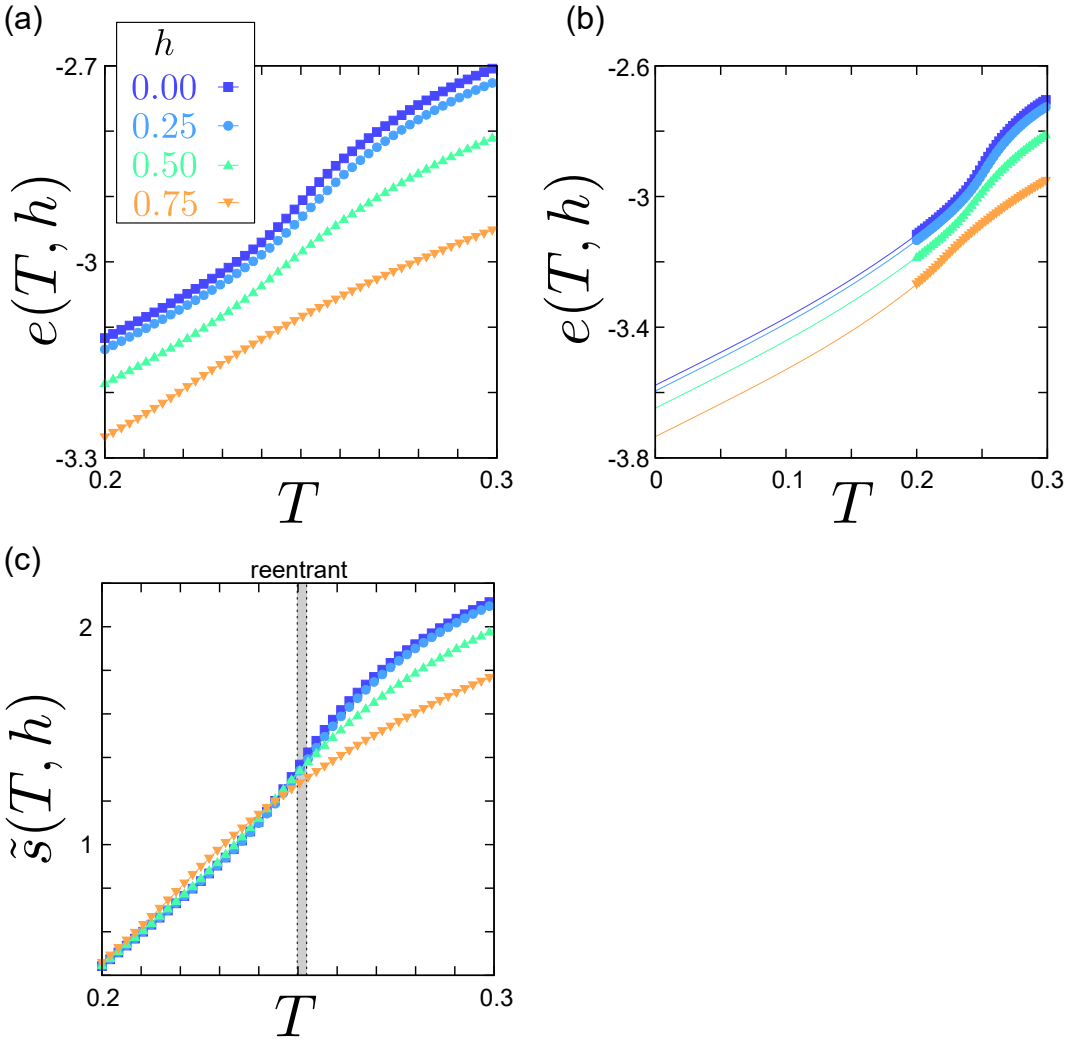

Figure 2.13: Results of the sSU(3)-MC calculation on the square lattice with $L = 32$. The parameters of the spin-1 BLBQ model are set as $K/J = 2$ and $J, K < 0$. (a) Energy density $e(T, h)$. (b) Energy density $e(T, h)$ from $T = 0$. Lines in the lower temperature is the energy estimated by fitting the sSU(3)-MC data shown with symbols. (c) Entropy density $\tilde{s}(T, h)$. Figures are taken from Ref. [1] (Copyright ©2020, American Physical Society).

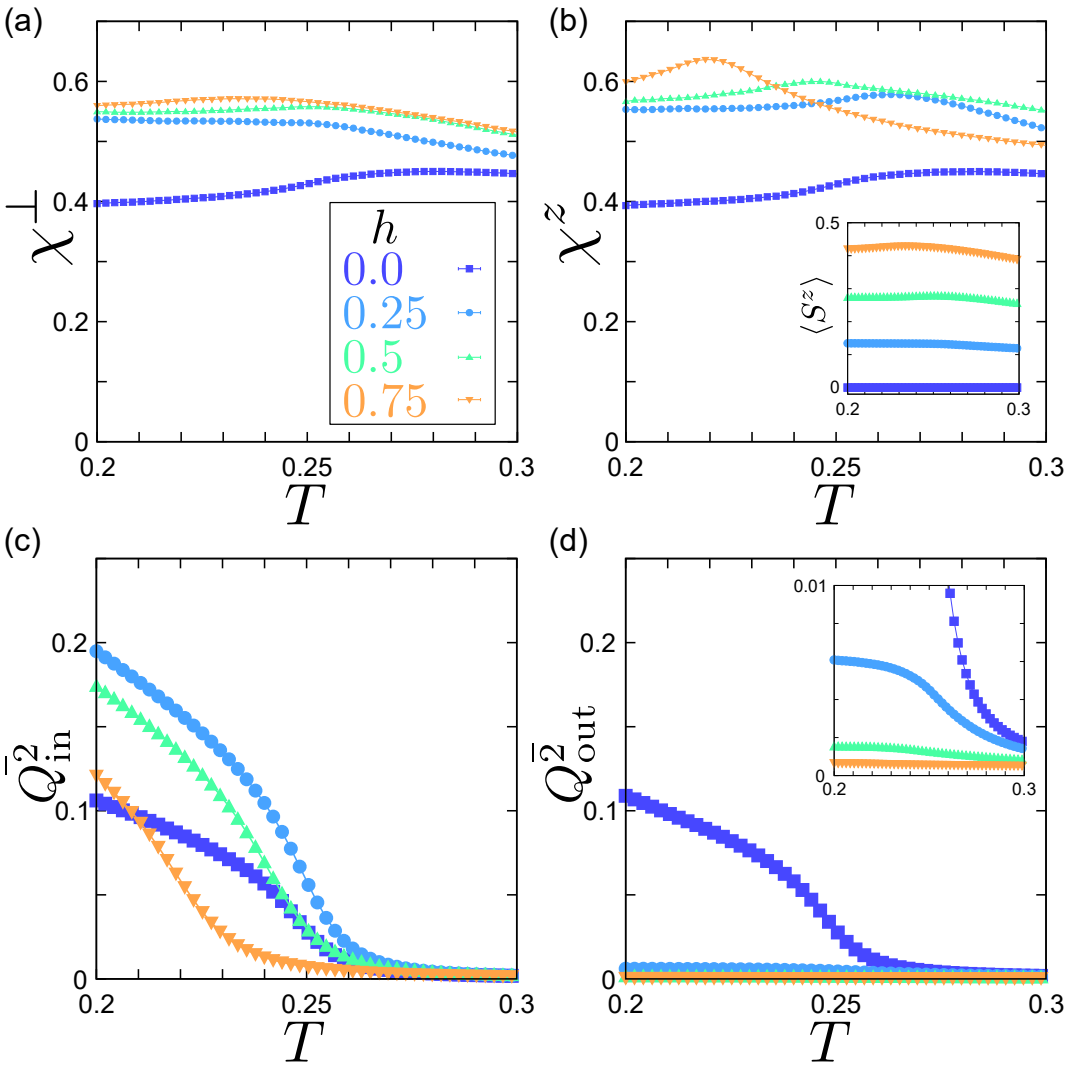

Figure 2.14: Results of the sSU(3)-MC calculation on the square lattice with $K/J = 2$ and $J, K < 0$, in the $L = 32$ sample. (a), (b) Temperature dependence of the spin susceptibility (a) perpendicular to the magnetic field, $\chi^{\perp}$ and (b) parallel to the magnetic field, χ^{z}. The inset in (b) is the temperature dependence of the magnetization density, $\langle S^z \rangle$. (c), (d) Temperature dependence of the mean squared quadrupolar moment. (c) $Q^2_{\rm in}$ and (d) $Q^2_{\rm out}$. The inset in (d) is the enlarged view of small $Q^2_{\rm out}$ region. Figures are taken from Ref. [1] (Copyright ©2020, American Physical Society).

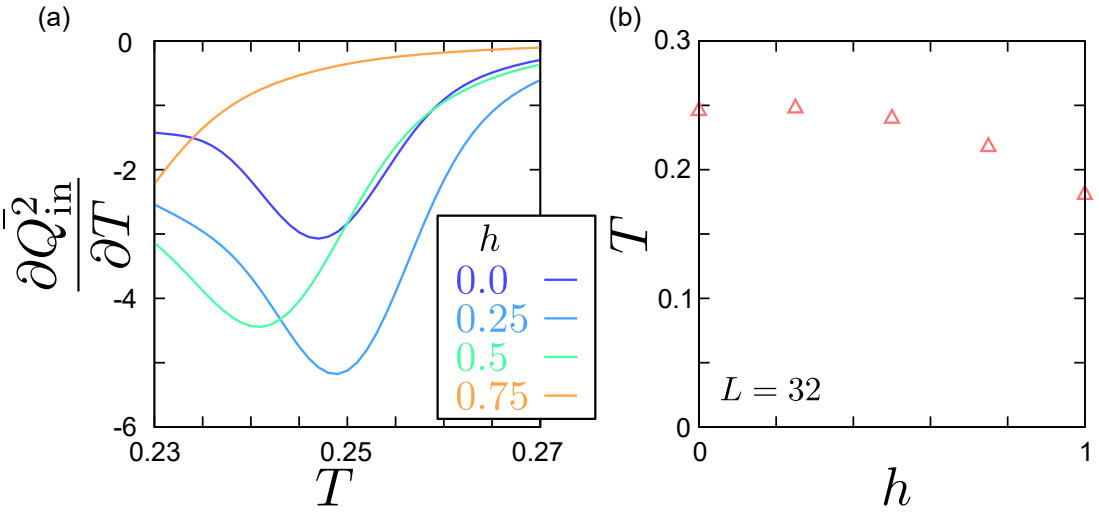

Figure 2.15: (a) Temperature dependence of $\frac{\partial \bar{Q}^2_{\rm in}}{\partial T}$ in various magnetic fields on the $L = 32$ square lattice estimated by the Gaussian kernel approximation. (b) The magnetic field dependence of the peak temperature of $\frac{\partial \bar{Q}^2_{\rm in}}{\partial T}$ on the $L = 32$ square lattice.

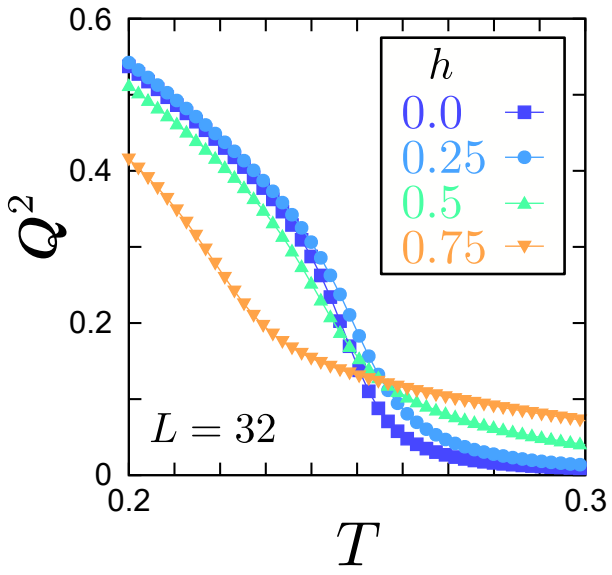

Figure 2.16: Temperature dependence of the squared quadrupolar moment, $\boldsymbol{Q}^2$, in various magnitudes of the magnetic field in the $L = 32$ square lattice (error bars are not shown).

the pair of half-vortex–anti-vortex in the ferroquadrupolar phase transition without magnetic field [146]. Similar half-vortex–antivortex structure is observed also on the antiferroic SU(3)-point in the spin-1 BLBQ model on the triangular lattice [147]. In that case, the transition temperature of the topological phase transition is generally slightly lower than that of the peak position of the specific heat. On the other hand, the absence of the BKT transition was suggested by the quantum Monte Carlo simulation for the ferroquadrupolar region of the spin-1 BLBQ model on the square lattice without a magnetic field, where they did not observe the algebraic decay of the correlation functions, which is characteristic of the topological phase below the BKT transition temperature. We consider that the system has the SU(2) symmetry without magnetic field, and to be exact the BKT phase transition does not occur. However, according to the homotopy group analysis [148], the generation of the topological defects consisting of the nematic directors itself is still allowed like the generation of the $\mathbb{Z}_2$ vortex in the classical Heisenberg model on the triangular lattice [149, 150], where the correlation functions decay exponentially. In the simulation in the spin-1 ferroquadrupolar region, this type of topological phase transition, which is slightly different from the exact BKT transition, may occur. In a magnetic field, the symmetry of the system is broken down to $O(2)$, and then the topological phase transition with the pair of half-vortex–anti-vortex, which now can be called the BKT transition, occurs.

In the actual materials, even when well described by the two-dimensional model, there are small but finite inter-layer interactions which connect the two-dimensional layers. Then, the finite-temperature phase transition to the ferroquadrupolar phase, and resultant field-reentrant behavior will be observed.

2.2.4.3 Correspondence to other entropic effects—Pomeranchuk effect in ^{3}He

The field-reentrant behavior found in the ferroquadrupolar phase transition in the spin-1 BLBQ model is due to entropic effect, and one can find the correspondence to other entropic phenomena. The most representative one will be the Pomeranchuk effect in ^{3}He [151, 152]. In ^{3}He, the liquid phase can be identified as the Fermi liquid with T-linear entropy, and the solid phase is regarded as the assembly of the spin-1/2 nuclei with weak interactions, and its entropy is constant unless the contribution of phonons becomes nonnegligible at higher temperature. Then, unlike the typical materials, where the solid phase has a smaller entropy than the liquid phase, the entropy of the solid phase, S_{solid}, becomes larger than that of the liquid phase, S_{liquid}, in the low-temperature region. From the Clausius–Clapeyron equation along the first-order transition lines between the solid and liquid phases given as

$$\left(\frac{\mathrm{d}P}{\mathrm{d}T}\right) = \frac{S_{\text{liquid}} - S_{\text{solid}}}{V_{\text{liquid}} - V_{\text{solid}}}, \tag{2.48}$$

where V_{liquid} and V_{solid} are the volumes of the liquid and solid phases of ^{3}He, respectively, the coexistence curve of the solid and liquid phases have a negative slope shown in Fig. 2.17(a) [21]. As a result, one can cool the system by applying a pressure, which is known as the Pomeranchuk effect.

[21] For the volume, $V_{\text{solid}} < V_{\text{liquid}}$ holds.

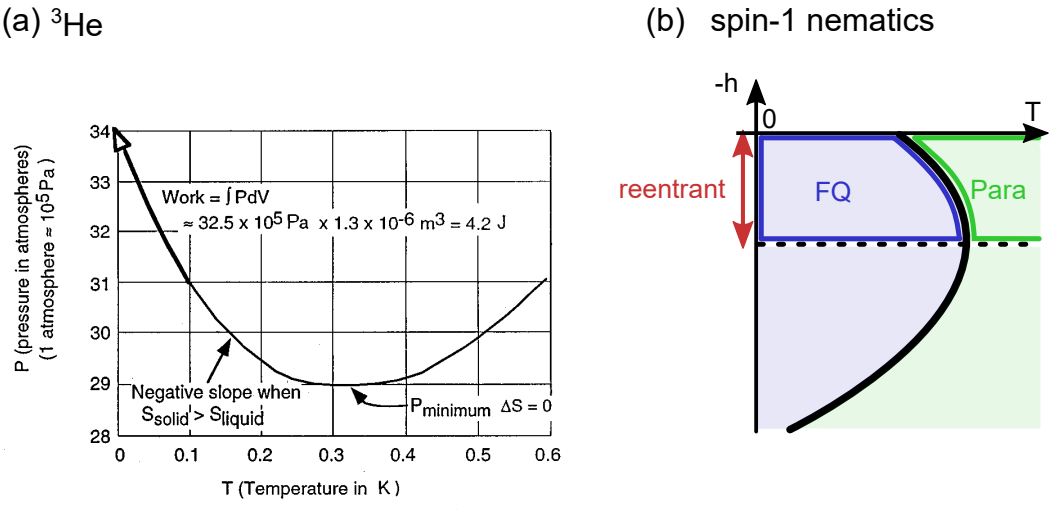

Figure 2.17: Correspondence between the Pomeranchuk effect in ^{3}He and the reentrant behavior in spin-1 ferro-nematics. (a) Pressure–temperature phase diagram of ^{3}He. Figure is taken from Ref. [151] (Copyright ©1997, American Physical Society). (b) Schematic $(-h)$–T phase diagram in spin-1 ferro-nematics. The negative slope at $T \lesssim 0.3$ K in (a) where the entropy of the solid phase is larger than that of the liquid phase corresponds to the negative slope in the $(-h)$–T phase diagram in (b) where the reentrant behavior is observed.

Table 2.1: Correspondence between ^{3}He and spin-1 nematics.

^{3}He	spin-1 nematics
solid	paramagnet
liquid	ferroquadrupole
$P \cdot V$	$-h \cdot \langle S^z \rangle$

If we make correspondence between the enthalpy term, $+PV$, in ^{3}He, and the Zeeman term, $-h\langle S^z\rangle$, in our spin-1 system, the Pomeranchuk effect can explain our reentrant behavior. The negative slope of the coexistece curve in ^{3}He corresponds to the negative slope in the reentrant region of the ferroquadrupolar–paramagnetic phase boundary in the $(-h)$–T phase diagram of the spin-1 BLBQ model, although the former is the first-order phase transition and the latter is possibly of second-order. Here, the decrease in entropy per unit, volume in ^{3}He and spin in spin-1 nematics, essentially works to raise the temperature. The correspondence between these two phenomena are summarized in Table 2.1.

The entropic phenomena similar to the Pomeranchuk effects can also be seen in other situations. The similar field-reentrant behavior in the phase transition between the UUD phase of the triangular lattice and the paramagnetic phase has been observed in the classical [153, 154] and quantum [155] magnets on the triangular lattice. In the quantum magnet Cs_2CuBr_4, for example, the quantum fluctuation effect in a frustrated geometry similarly works in a similar manner as the quantum fluctuation of the quadrupolar moments in the spin-1 ferro-nematics. Also, in $YbInCu_4$, a Kondo lattice compound, the Fermi liquid phase at low temperature with larger volume has a smaller entropy than the local moment phase at high temperature, and it was proposed that the first-order isostructural phase transition from the local moment phase to the Fermi liquid phase can cool the system similarly to the Pomeranchuk effect [156–158].

2.2.4.4 Antiferroquadrupolar phase on the triangular lattice

We briefly discuss the magnetic field effect on the finite-temperature properties of the antiferroquadrupolar phase on the triangular lattice. Semiclassically, the antiferroquadrupolar ground state is realized at $0 < J < K$ on the triangular lattice [17, 19, 33, 34]. In the antiferroquadrupolar phase without magnetic field, the three-sublattice structure given as

$$|\Psi\rangle = \bigotimes_{i=1}^{N/3} \left(|\boldsymbol{d}_{i,\mathrm{A}}\rangle \otimes |\boldsymbol{d}_{i,\mathrm{B}}\rangle \otimes |\boldsymbol{d}_{i,\mathrm{C}}\rangle\right) \tag{2.49}$$

is formed, where i_γ represents the lattice site with the index of the γ-sublattice ($\gamma = \mathrm{A}, \mathrm{B}, \mathrm{C}$), and $|\boldsymbol{d}_{i,\mathrm{A}}\rangle = |x\rangle$, $|\boldsymbol{d}_{i,\mathrm{B}}\rangle = |y\rangle$, and $|\boldsymbol{d}_{i,\mathrm{C}}\rangle = |z\rangle$, for example [22] [17, 19, 33, 34]. When the magnetic field is applied at $T = 0$, two of three sublattices, $|\boldsymbol{d}_{i_\mathrm{A}}\rangle = |x\rangle$ and $|\boldsymbol{d}_{i_\mathrm{B}}\rangle = |y\rangle$, acquire the magnetization along the z-axis with the complex coefficients in the $\boldsymbol{d}$-vector and fluctuate inside the xy-plane similarly to the case of the ferroquadrupolar phase in an applied field, whereas $|\boldsymbol{d}_{i_\mathrm{C}}\rangle = |z\rangle$ is unchanged.

We perform the sSU(3)-MC calculation on the triangular lattice with $K/J = 2$ and $J, K > 0$, or $(J, K) = (1/\sqrt{5}, 2/\sqrt{5})$, where the variational ground state is the antiferroquadrupolar order [17, 19, 33, 34]. The system size is $L \times L$ with $L = 12$ to 36 (see Fig. 2.1). We show the temperature–magnetic field phase diagram in a low-field region in Fig. 2.18(a). In contrast to the case of the ferroquadrupolar phase, T_c monotonically decreases as the magnetic field is applied. We can see the shift of T_c more clearly by the

[22] The word 'for example' means that other choices such as $(|\boldsymbol{d}_{i,\mathrm{A}}\rangle, |\boldsymbol{d}_{i,\mathrm{B}}\rangle, |\boldsymbol{d}_{i,\mathrm{C}}\rangle) = (|x\rangle, |z\rangle, |y\rangle)$ are allowed.

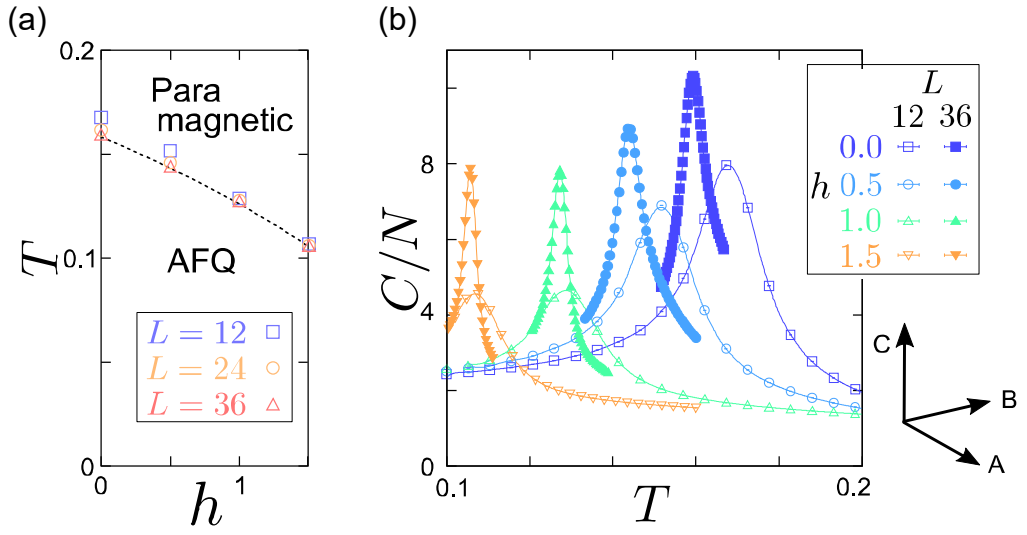

Figure 2.18: Results of the sSU(3)-MC simulation for the antiferroquadrupolar phase on the triangular lattice. The parameters are set as $K/J = 2$ with $J, K > 0$, namely $(J, K) = (1/\sqrt{5}, 2/\sqrt{5})$. (a) Phase diagram on the plane of h and T. (b) Temperature dependence of the specific heat $C(T)/N$ in several values of the magnetic field with $L = 12$ (open) and 36 (filled). Figures are taken from Ref. [1] (Copyright ©2020, American Physical Society).

temperature dependence of the specific heat shown in Fig. 2.18(b). In the ferroquadrupolar phase, $\boldsymbol{d}$-vectors freely fluctuate without magnetic field, and an applied magnetic field favors the fluctuation inside xy-plane. By contrast, in the antiferroquadrupolar phase, the $\boldsymbol{d}$-vectors in A- and B-sublattices are always fixed inside the xy-plane regardless of the absence or presence of the (low) magnetic field. Then, one could ascribe the absence of the reentrant behavior to the pinning of the relative positions of the $\boldsymbol{d}$-vectors among different sublattices. Therefore, we find that the reentrant behavior is characteristic of the ferroquadrupolar phase.

2.3 Summary of this Chapter

In this chapter, we found the characteristic field dependence of the ferroquadrupolar phase transition in the spin-1 bilinear-biquadratic model. Using the semiclassical SU(3) approximation combined with the classical Monte Carlo simulation, we numerically examined the magnetic field effect on the finite-temperature properties of the spin nematic phases in the spin-1 bilinear-biquadratic models. For the ferroquadrupolar phase, the peak position of the specific heat, which indicates the transition to the ferroquadrupolar phase, once moves toward the higher temperature, and then toward the lower temperature in a higher magnetic field. This small reentrant behavior by a magnetic field is ascribed to the entropic effect, which results from the different robustness between the paramagnetic and ferromagnetic phases against the magnetic field. In the paramagnetic phase at high temperature, the spins align when a magnetic field is applied, and the entropy rapidly decreases. By contrast, in the ferroquadrupolar phase at low temperature, the quadrupolar fluctuations remain when the spin moment is induced in a magnetic field, by making

use of the in-plane fluctuation perpendicular to the magnetic field, where the entropy is retained. We also confirmed that this reentrant behavior is not due to geometrical frustration effect, and does not occur in a low-field region in the antiferroquadrupolar phase transition. We consider that measuring the field dependence of the specific heat with the featureless magnetic susceptibility may give a thermodynamic clue to detect the spin-1 ferroquadrupolar phase in experiments.

Chapter 3

Multiple quadrupolar phases in the spin-1 dimer triangular lattice

In this Chapter, we show that several kinds of the quadrupolar phases appear in the bilayer triangular lattice consisting of antiferromagnetic spin-1 dimers. We derive the low-energy effective model of the spin-1 dimer triangular lattice in terms of the spin-1 hard-core bosons. In a dimer unit, the spin quintet state at high energy is excluded from the basis, and the remaining triplet and singlet states are represented by the hard-core boson with spin-1 and the vacuum, respectively, and the intra-dimer and inter-dimer magnetic interactions are transformed into several types of the interactions and kinetic terms of bosons. By numerically analyzing the effective model, we find three different classes of the quadrupolar phases of spin-1 bosons in addition to the trivial ferromagnetic/antiferromagnetic orderings. After clarifying the details of the phase diagrams, we finally discuss the possible relevance of our findings to $Ba_3MRu_2O_9$, where M is the divalent cation.

3.1 Overview

We deal with a lattice model whose unit is a dimer consisting of two spin-1's. The dimers align parallelly and form a bilayer triangular lattice as shown in Fig. 3.1. The following Hamiltonian is considered;

$$\mathcal{H} = \mathcal{H}_{\text{intra}} + \mathcal{H}_{\text{inter}}, \tag{3.1}$$

$$\mathcal{H}_{\text{intra}} = \sum_{i=1}^{N} \left[J \boldsymbol{S}_{i_1} \cdot \boldsymbol{S}_{i_2} + B \left(\boldsymbol{S}_{i_1} \cdot \boldsymbol{S}_{i_2} \right)^2 \right], \tag{3.2}$$

$$\mathcal{H}_{\text{inter}} = \sum_{\langle i,j \rangle} \sum_{\gamma=1,2} \left[J' \boldsymbol{S}_{i_\gamma} \cdot \boldsymbol{S}_{j_\gamma} + J'' \boldsymbol{S}_{i_\gamma} \cdot \boldsymbol{S}_{j_{\bar{\gamma}}} \right], \tag{3.3}$$

where $\boldsymbol{S}_{i_\gamma}$ denotes the spin-1 operator of the γ-th site on the i-th dimer, and N denotes the number of dimers. The summation $\langle i, j \rangle$ is taken over the nearest-neighbor dimer pairs, and for the site indices γ, we take $\bar{1} = 2$ and $\bar{2} = 1$. We consider the intra-dimer bilinear (Heisenberg) and biquadratic interactions, J and B, respectively, with $J, B > 0$, and the inter-dimer Heisenberg interactions, J' and J''.

Here, we describe the outline of the present Chapter. In Sec. 3.2, using the perturba-

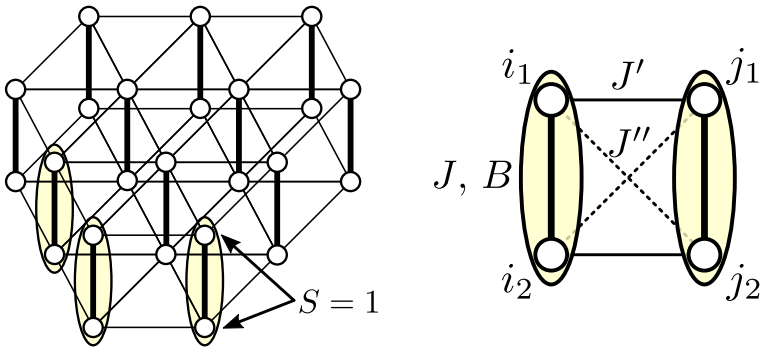

Figure 3.1: Bilayer triangular lattice consisting of spin-1 dimers. Figure is taken from Ref. [2] (Copyright ©2020, American Physical Society).

tion calculations, we transform the original spin Hamiltonian in Eq. (3.1) to the effective Hamiltonian of spin-1 hard-core bosons. Then the effective Hamiltonian is analyzed by the numerical diagonalization method on a finite-size cluster. The magnetic properties of the effective model are described in terms of the spin-1 operators, $\boldsymbol{\mathcal{S}}$.

After disclosing the overall features of the model, we analyze the low-lying states, namely, Anderson tower of states in Sec. 3.3. There, we find that a series of the order parameters based on the spin-1 bosons, $\boldsymbol{\mathcal{S}}$, is not enough to classify several different types of the quadrupolar orderings we found in the phase diagram. We then go back to the original spin model and additionally introduce the operators, $\boldsymbol{q}$ and $\boldsymbol{p}$, on a dimer bond other than $\boldsymbol{\mathcal{S}}$.

In Sec. 3.4, we discuss the difference among the aforementioned quadrupolar phases classified in Sec. 3.3. Possible relevance to the Ru-dimer materials $Ba_3MRu_2O_9$ is discussed in Sec. 3.5, and the summary of this Chapter is given in Sec. 3.6.

3.2 Effective spin-1 hard-core bosonic model

3.2.1 Derivation of the effective Hamiltonian of spin-1 bosons

3.2.1.1 Low-energy states of spin-1 dimers

First we consider an isolated spin-1 dimer whose local Hamiltonian is $\mathcal{H}_{\text{intra (1dimer)}} = J\boldsymbol{S}_{i_1}\cdot\boldsymbol{S}_{i_2} + B\left(\boldsymbol{S}_{i_1}\cdot\boldsymbol{S}_{i_2}\right)^2$. The energy eigenstates are classified into singlet ($|s\rangle$), triplet ($|t\rangle$), quintet ($|q\rangle$) [1]. The eigenenergies of these three multiplets $|\alpha\rangle$ ($\alpha = s,t,q$), $e(\alpha)$, are given as

$$\begin{aligned} e(s) &= -2J + 4B, \\ e(t) &= -J + B, \\ e(q) &= J + B. \end{aligned} \tag{3.4}$$

The B/J dependence of these energy eigenvalues are shown in Fig. 3.2(a). When B/J is small, the singlet is the ground state. When $1/3 < B/J$, the ground state is replaced

[1] Quintets are also called quintuplets.

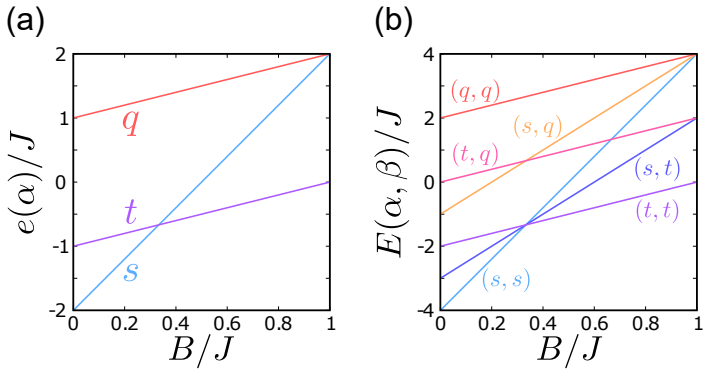

Figure 3.2: (a) B/J dependence of the energy eigenvalues of $\mathcal{H}_{\rm intra}$ of one spin-1 dimer. s, t, and q are the singlet, triplet, and quintet states, respectively. (b) B/J dependence of the energy eigenvalues of $\mathcal{H}_{\rm intra}$ of two disconnected spin-1 dimers, namely, $J' = J'' = 0$. (α, β) $(\alpha, \beta = s, t, q)$ denotes the eigenstates of the pair of two-dimers. Figures are taken from Ref. [2] (Copyright ©2020, American Physical Society).

by the triplet. The quintet states remain as high-energy excited states in the parameter region we consider.

In the perturbation calculation, we start from the limit of decoupled dimers, namely, $\mathcal{H}_{\rm inter} = 0$. There, the ground state is the product state of singlet on each dimer when $B/J < 1/3$, and the product state of triplet when $1/3 < B/J$. We introduce the inter-dimer interactions as a perturbation, $\mathcal{H}_{\rm inter} \neq 0$, up to second order with respect to J'/J and J''/J, and then the effective interactions between two neighboring dimers mainly appear. Therefore, we need to justify the exclusion of quintets for the pairs of isolated two dimers, whose states are labeled as α- and β-multiplets $(\alpha, \beta = s, t, q)$. Their energies $E(\alpha, \beta)$ are

$$\begin{aligned} E(s,s) &= -4J + 8B, \\ E(s,t) &= -3J + 5B, \\ E(s,q) &= -J + 5B, \\ E(t,t) &= -2J + 2B, \\ E(t,q) &= 2B, \\ E(q,q) &= 2J + 2B, \end{aligned} \tag{3.5}$$

and B/J dependence of $E(\alpha, \beta)$ is shown in Fig. 3.2(b). When $B/J < 2/3$, the two-dimer states including quintets have larger energies than the states without quintets. Based on the reasonable assumption that B/J is not so large, the effective Hamiltonian for the low-energy manifold of states including only singlets and triplets can be constructed.

In the second-order perturbation processes between two neighboring dimers, the intermediate high-energy states have at least one quintet, as we can see from the examples of the second-order perturbation processes shown in Fig. 3.3. Figure 3.3(a) shows the processes where the two-dimer state $|s, t_0\rangle$ goes back to the same state via the excited states including the quintets, $|t_0, q_0\rangle$, $|t_{+1}, q_{-1}\rangle$, and $|t_{-1}, q_{+1}\rangle$. Here, $|s\rangle$ is the singlet state, and $|t_\mu\rangle$ and $|q_\mu\rangle$ are the triplet and quintet states with $\mathcal{S}^z = \mu$, respectively. In Fig. 3.3(b), we

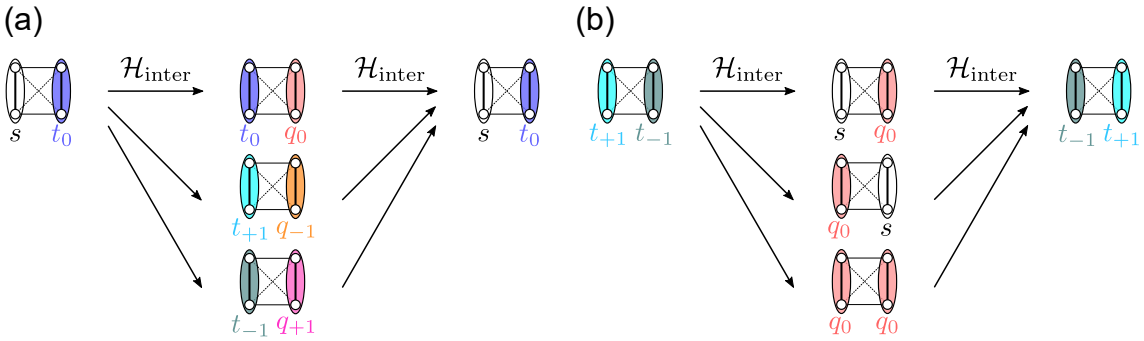

Figure 3.3: Examples of the second-order perturbation processes. (a) Processes where $|s, t_0\rangle$ goes back to the same state. (b) Processes where two triplets with $\mathcal{S}^z = +1$ and $\mathcal{S}^z = -1$ are exchanged, which contribute to the biquadratic interactions between two triplet dimers, $(\boldsymbol{\mathcal{S}}_i \cdot \boldsymbol{\mathcal{S}}_j)$. Figures are taken from Ref. [2] (Copyright ©2020, American Physical Society).

show the processes where two triplet dimer state with $\mathcal{S}^z = +1$ and $\mathcal{S}^z = -1$, $|t_{+1}, t_{-1}\rangle$, is transformed into $|t_{-1}, t_{+1}\rangle$ through the excited states, $|s, q_0\rangle$, $|q_0, s\rangle$, and $|q_0, q_0\rangle$. The details of the perturbation calculations are written in Appendix B. The low-energy basis consisting of singlet and triplet states can be described in terms of the spin-1 hard-core bosons. The singlet state corresponds to the vacuum, and the triplet states correspond to the hard-core bosons with spin-1 with the constraint of no double occupancy on a dimer. This type of treatment is equivalent to the bond-operator approach which was first developed for the spin-1/2 dimer systems [159, 160] and later extended to spin-1 dimer systems [161, 162] and also to general spin-S dimer systems [163]. For the bond-operator representation, we choose here the time-reversal invariant form of the basis states $\{|t_{i,\alpha}\rangle\}$ $(\alpha = x, y, z)$ given as

$$
\begin{aligned}
|t_{i,x}\rangle &= \frac{\mathrm{i}}{2}\left(|+1,0\rangle - |0,+1\rangle - |0,-1\rangle + |-1,0\rangle\right), \\
|t_{i,y}\rangle &= \frac{1}{2}\left(|+1,0\rangle - |0,+1\rangle + |0,-1\rangle - |-1,0\rangle\right), \\
|t_{i,z}\rangle &= -\frac{\mathrm{i}}{\sqrt{2}}\left(|+1,-1\rangle - |-1,+1\rangle\right).
\end{aligned} \tag{3.6}
$$

Here, the dimer states written on the right hand side, $|\mu_1, \mu_2\rangle$, denote the ones with $S^z_{i_1} = \mu_1$ and $S^z_{i_2} = \mu_2$. Detailed information on the bond-operator approach and the expression of the original spin operators $\boldsymbol{S}_{i_\gamma}$ with the bosonic operators are given in Appendix B.

3.2.1.2 Effective model

The triplet state with α-component, $|t_{i,\alpha}\rangle$, which is equivalent to the state where the spin-1 boson with α-component occupies the dimer, is described as $b^\dagger_{i,\alpha}|0\rangle$. Here $|0\rangle$ is the vacuum expressing the singlet state and $b^\dagger_{i,\alpha}$ is the creation operator of the spin-1 boson with α-component. The second order perturbation calculation in J'/J and J''/J gives the effective Hamiltonian described the above bosonic operator, $\mathcal{H}_{\rm eff}$, as,

$$
\mathcal{H}_{\rm eff} = E_0 + \mathcal{H}_\mu + \mathcal{H}_t + \mathcal{H}_P + \mathcal{H}_V + \mathcal{H}_\mathcal{J} + \mathcal{H}_\mathcal{B} + \mathcal{H}_{\rm 3body}, \tag{3.7}
$$

$$\mathcal{H}_\mu = -\mu \sum_{i=1}^{N} n_i, \tag{3.8}$$

$$\mathcal{H}_t = t \sum_{\langle i,j \rangle} \sum_{\alpha=x,y,z} \left(b_{i,\alpha}^\dagger b_{j,\alpha} + \text{h.c.} \right), \tag{3.9}$$

$$\mathcal{H}_P = P \sum_{\langle i,j \rangle} \sum_{\alpha=x,y,z} \left(b_{i,\alpha}^\dagger b_{j,\alpha}^\dagger + \text{h.c.} \right), \tag{3.10}$$

$$\mathcal{H}_V = V \sum_{\langle i,j \rangle} n_i n_j, \tag{3.11}$$

$$\mathcal{H}_J = \mathcal{J} \sum_{\langle i,j \rangle} \boldsymbol{\mathcal{S}}_i \cdot \boldsymbol{\mathcal{S}}_j n_i n_j, \tag{3.12}$$

$$\mathcal{H}_\mathcal{B} = \mathcal{B} \sum_{\langle i,j \rangle} \left(\boldsymbol{\mathcal{S}}_i \cdot \boldsymbol{\mathcal{S}}_j \right)^2 n_i n_j. \tag{3.13}$$

Here,

$$n_i = \sum_{\alpha=x,y,z} b_{i,\alpha}^\dagger b_{i,\alpha} \tag{3.14}$$

is the number operator, and the hard-core condition, $n_i = 0$ or 1 is imposed on the number operator. The operator $\boldsymbol{\mathcal{S}}_i$ is the spin-1 operator of i-th boson, where

$$\mathcal{S}_i^\alpha = -\mathrm{i} \sum_{\beta,\gamma} \varepsilon_{\alpha\beta\gamma} b_{i,\beta}^\dagger b_{i,\gamma}, \tag{3.15}$$

and $\varepsilon_{\alpha\beta\gamma}$ is the Levi–Civita symbol. We note that this spin-1 operator of i-th boson, $\boldsymbol{\mathcal{S}}_i$, is different from the spin-1 operator defined on the original bilayer spin model, $\boldsymbol{S}_{i_\gamma}$. This effective Hamiltonian has the SU(2) symmetry of the triplet bosons [84–86], which is kept as far as the magnetic field or some anisotropic interactions are not introduced [164] [2].

The parameters appearing in the effective Hamiltonian $\mathcal{H}_{\text{eff}}$ are obtained by the perturbation calculations, and are expressed using the parameters of the original Hamiltonian $\mathcal{H}$ as

$$E_0 = (-2J + 4B)\, N, \tag{3.16}$$

$$\mu = -J + 3B + \frac{20z}{27\,(J-B)} \left(J' - J'' \right)^2, \tag{3.17}$$

$$t = \frac{4}{3} \left(J' - J'' \right), \tag{3.18}$$

$$P = -\frac{4}{3} \left(J' - J'' \right), \tag{3.19}$$

$$V = \left[\frac{40}{27\,(J-B)} - \frac{8}{9\,(J+3B)} - \frac{2}{9J} \right] \left(J' - J'' \right)^2, \tag{3.20}$$

$$\mathcal{J} = \frac{1}{2} \left(J' + J'' \right) + \left[-\frac{4}{3\,(J+3B)} + \frac{1}{12J} \right] \left(J' - J'' \right)^2, \tag{3.21}$$

[2] In other words, it is different from the magnon-BEC in a magnetic field, where the SU(2) symmetry is broken.

$$\mathcal{B} = \left[-\frac{4}{9\,(J+3B)} - \frac{1}{144J} \right] \left(J' - J'' \right)^2 . \tag{3.22}$$

Here, z is the coordination number. The terms with μ, t, P and $\mathcal{J}$ contains the terms derived from the zeroth- and first-order perturbation processes, while the ones with V and $\mathcal{B}$ include only the terms originating from the second-order perturbation processes.

We note that the whole effective Hamiltonian of the second order perturbation also includes the 3-dimer interaction term, $\mathcal{H}_{\rm 3body}$. We compared the ground state energies of the original Hamiltonian, $\mathcal{H}$ (Eq. (3.1)), and of the effective Hamiltonian, $\mathcal{H}_{\rm eff}$ (Eq. (3.7)) with and without $\mathcal{H}_{\rm 3body}$, using a small cluster. Then we find that this $\mathcal{H}_{\rm 3body}$ term does not play an important role, and thus hereafter we discard $\mathcal{H}_{\rm 3body}$ for simplicity. Detailed information on the evaluation of this $\mathcal{H}_{\rm 3body}$ term is given in Appendix B. Furthermore, we see shortly that the other terms derived in the second order perturbation processes in Eq. (3.7) do not change the majority of the phases diagram, which allows us to discuss only the roles of t, P, and $\mathcal{J}$.

3.2.1.3 Numerical diagonalization of the Hamiltonian

We analyze this effective model using the numerical diagonalization method [3]. In the numerical diagonalization, the Hamiltonian of the quantum many-body system is expressed with certain many-body basis states $\{|\Phi_i\rangle\}_{i=1,\cdots,\dim \mathscr{H}}$ as

$$\begin{aligned}\mathcal{H} &= \sum_{i,j=1}^{\dim \mathscr{H}} |\Phi_i\rangle \langle\Phi_i|\mathcal{H}|\Phi_j\rangle \langle\Phi_j| \\ &= \begin{pmatrix} |\Phi_1\rangle & \cdots & |\Phi_{\dim \mathscr{H}}\rangle \end{pmatrix} \begin{pmatrix} \langle\Phi_1|\mathcal{H}|\Phi_1\rangle & \cdots & \langle\Phi_1|\mathcal{H}|\Phi_{\dim \mathscr{H}}\rangle \\ \vdots & \ddots & \vdots \\ \langle\Phi_{\dim \mathscr{H}}|\mathcal{H}|\Phi_1\rangle & \cdots & \langle\Phi_{\dim \mathscr{H}}|\mathcal{H}|\Phi_{\dim \mathscr{H}}\rangle \end{pmatrix} \begin{pmatrix} \langle\Phi_1| \\ \cdots \\ \langle\Phi_{\dim \mathscr{H}}| \end{pmatrix},\end{aligned} \tag{3.23}$$

and the Hamiltonian matrix,

$$H = \begin{pmatrix} \langle\Phi_1|\mathcal{H}|\Phi_1\rangle & \cdots & \langle\Phi_1|\mathcal{H}|\Phi_{\dim \mathscr{H}}\rangle \\ \vdots & \ddots & \vdots \\ \langle\Phi_{\dim \mathscr{H}}|\mathcal{H}|\Phi_1\rangle & \cdots & \langle\Phi_{\dim \mathscr{H}}|\mathcal{H}|\Phi_{\dim \mathscr{H}}\rangle \end{pmatrix}, \tag{3.24}$$

is numerically diagonalized. The j-th eigenvalue of H, E_j, is the j-th energy eigenvalue. Using the corresponding eigenvectors of E_j, $\begin{pmatrix} c_{j,1} \\ \vdots \\ c_{j,\dim \mathscr{H}} \end{pmatrix}$, the j-th eigenstate is expressed as $|\Psi_j\rangle = \sum_{i=1}^{\dim \mathscr{H}} c_{j,i} |\Phi_i\rangle$ [4]. The expectation value of physical quantities $\mathcal{O}$ for j-th

[3] The word 'exact' diagonalization is generally used, but the meaning of 'exact' here is 'numerically exact'.

[4] The number of indices i can often be reduced from $\dim \mathscr{H}$ by the block diagonalization using the conserved quantities such as $S^z_{\rm tot}$.

eigenstate $|\Psi_j\rangle$, $\langle O\rangle_j$, is calculated as [5]

$$\langle O\rangle_j = \langle\Psi_j|\mathcal{O}|\Psi_j\rangle\,. \tag{3.25}$$

To diagonalize the Hamiltonian matrix, we used the Lanczos method [165] to obtain the information of the ground states, and the thick-restart Lanczos method [166, 167] to obtain the low-energy excited states [6]. The details of these algorithms are explained in Appendix C.

3.2.1.4 Physical quantities

In analyzing the ground state properties of the effective model $\mathcal{H}_{\text{eff}}$, we calculate the following physical quantities using the numerical diagonalization method. The boson density per dimer denoted as

$$\langle n_t\rangle = \frac{1}{N}\sum_{i=1}^{N}\langle n_i\rangle\,, \tag{3.26}$$

and the structure factor of the boson density given as

$$N(\boldsymbol{k}) = \frac{1}{N}\sum_{i,j=1}^{N}\langle n_i n_j\rangle\,\mathrm{e}^{\mathrm{i}\boldsymbol{k}\cdot(\boldsymbol{r}_i-\boldsymbol{r}_j)}. \tag{3.27}$$

The magnetic properties of the effective model is analyzed by the spin and quadrupolar structure factors of spin-1 bosons,

$$\mathcal{S}(\boldsymbol{k}) = \frac{1}{N}\sum_{i,j=1}^{N}\langle\boldsymbol{\mathcal{S}}_i\cdot\boldsymbol{\mathcal{S}}_j n_i n_j\rangle\,\mathrm{e}^{\mathrm{i}\boldsymbol{k}\cdot(\boldsymbol{r}_i-\boldsymbol{r}_j)}, \tag{3.28}$$

$$\mathcal{Q}(\boldsymbol{k}) = \frac{1}{N}\sum_{i,j=1}^{N}\langle\boldsymbol{\mathcal{Q}}_i\cdot\boldsymbol{\mathcal{Q}}_j n_i n_j\rangle\,\mathrm{e}^{\mathrm{i}\boldsymbol{k}\cdot(\boldsymbol{r}_i-\boldsymbol{r}_j)}, \tag{3.29}$$

where $\boldsymbol{\mathcal{Q}}_i$ is the five-component vector representation of the quadrupolar operator of spin-1 bosons, whose explicit form is given in terms of $\boldsymbol{\mathcal{S}}_i$ as

$$\boldsymbol{\mathcal{Q}}_i = \begin{pmatrix}\mathcal{Q}_i^{x^2-y^2}\\ \mathcal{Q}_i^{3z^2-r^2}\\ \mathcal{Q}_i^{xy}\\ \mathcal{Q}_i^{yz}\\ \mathcal{Q}_i^{zx}\end{pmatrix} = \begin{pmatrix}(\mathcal{S}_i^x)^2-(\mathcal{S}_i^y)^2\\ \frac{1}{\sqrt{3}}\left[3(\mathcal{S}_i^z)^2-\mathcal{S}(\mathcal{S}+1)\right]\\ \mathcal{S}_i^x\mathcal{S}_i^y+\mathcal{S}_i^y\mathcal{S}_i^x\\ \mathcal{S}_i^y\mathcal{S}_i^z+\mathcal{S}_i^z\mathcal{S}_i^y\\ \mathcal{S}_i^z\mathcal{S}_i^x+\mathcal{S}_i^x\mathcal{S}_i^z\end{pmatrix}. \tag{3.30}$$

In a system where the spin-1 operator is defined on each site such as the spin-1 BLBQ model, the quadrupolar operator $\boldsymbol{Q}_i$ is the "on-site" operator. By contrast, in a system which has a spin-1/2 on each site, the quadrupolar operator is the "on-bond" operator, in need of constructing a spin-1 from two spin-1/2's [16, 51]. In our spin-1 dimer system, each

[5] We implicitly assume that the eigenvectors $|\Psi\rangle$ are normalized, $\||\Psi\rangle\| = 1$.

[6] We also performed the full-diagonalization when the size of the matrix is small.

dimer has two spin-1 operators, $\boldsymbol{S}_{i_1}$ and $\boldsymbol{S}_{i_2}$, and the spin-1 operator expressing the triplet states, $\boldsymbol{\mathcal{S}}_i$, is defined on a dimer bond, whose constituents are the two spin-1 operators, $\boldsymbol{S}_{i_1}$ and $\boldsymbol{S}_{i_2}$. Therefore, one can also set the "on-bond" type spin-1 quadrupolar operator on dimer bonds as

$$Q_{i_{12}}^{\alpha\beta} = S_{i_1}^{\alpha} S_{i_2}^{\beta} + S_{i_1}^{\beta} S_{i_2}^{\alpha} - \frac{2}{3} \left(\boldsymbol{S}_{i_1} \cdot \boldsymbol{S}_{i_2} \right) \delta_{\alpha\beta}, \tag{3.31}$$

just like the spin-1/2 cases. Then, one finds that $\boldsymbol{\mathcal{Q}}_i$ and $\boldsymbol{Q}_{i_{12}}$ are equivalent for the triplet states, namely,

$$\langle t_\alpha | Q_{i_{12}}^{\mu\nu} | t_\beta \rangle = \langle t_\alpha | \mathcal{Q}_i^{\mu\nu} | t_\beta \rangle \tag{3.32}$$

holds for $\alpha, \beta, \mu, \nu = x, y, z$. In the same way, when the "on-bond" type spin-1 operator is defined on dimer bonds as

$$S_{i_{12}}^{\alpha} = S_{i_1}^{\alpha} + S_{i_2}^{\alpha}, \tag{3.33}$$

$\boldsymbol{\mathcal{S}}_i$ and $\boldsymbol{S}_{i_{12}}$ equivalently work for the triplet states, namely,

$$\langle t_\alpha | S_{i_{12}}^{\mu} | t_\beta \rangle = \langle t_\alpha | \mathcal{S}_i^{\mu} | t_\beta \rangle \,, \tag{3.34}$$

holds for $\alpha, \beta, \mu = x, y, z$.

In our effective Hamiltonian, the number of spin-1 bosons per dimer can vary from 0 to 1, unlike the spin-1 BLBQ models where the spin-1 operator always exists on every site [19]. The spin-1 BLBQ model can be regarded as the limiting case with $\langle n_t \rangle = 1$ in our bosonic model, because these two models have the same definitions of the spin (Eq. (3.15)) and quadrupolar operators (Eq. (3.30)). Thus, we can utilize the analysis performed in the spin-1 BLBQ models for our bosonic model. There are the SU(3) points in the spin-1 BLBQ models. At these points, the three components of the spin-1 operator $\boldsymbol{\mathcal{S}}_i$ given in Eq. (3.15) and the five components of the quadrupolar operator $\boldsymbol{\mathcal{Q}}_i$ defined in Eq. (3.30) form the eight elements of the SU(3) Lie algebra. It is known that the quantum phase transitions between the magnetic and the spin quadrupolar (nematic) phases occur. In the numerical calculations, these transitions are characterized by the point where the spin and quadrupolar structure factors, $\mathcal{S}(\boldsymbol{k})$ and $\bar{\mathcal{Q}}(\boldsymbol{k}) = \frac{3}{5}\mathcal{Q}(\boldsymbol{k})$ (Eqs. (3.28), (3.29)) take the same values. Therefore we make use of this normalized quadrupolar structure factor $\bar{\mathcal{Q}}(\boldsymbol{k})$ so as to determine the quantum phase transitions between the magnetic and quadrupolar phases of spin-1 bosons.

3.2.2 Results of the $\mathcal{S} = 1$ bosonic model

3.2.2.1 Ground state phase diagram

We perform the numerical diagonalization of $\mathcal{H}_{\text{eff}}$ on the $N = 12$ triangular lattice [7], where we take the periodic boundary condition. The lattice geometry is shown in Fig. 3.4(a), and the first Brillouin zone of the triangular lattice is given in Fig. 3.4(b). The primitive

[7] The coordination number z is 6.

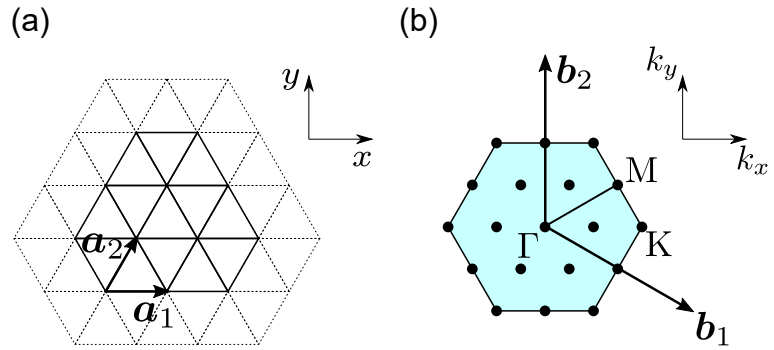

Figure 3.4: (a) The geometry of the $N = 12$ triangular lattice. Bold lines represent the 12-site cluster, and dotted lines connect the sites under the periodic boundary condition. The vectors $\boldsymbol{a}_1$ and $\boldsymbol{a}_2$ are the primitive vectors of the triangular lattice. (b) The first Brillouin zone of the triangular lattice in the reciprocal space. Dots denote the wave numbers we consider in the calculation for the $N = 12$ triangular lattice. The vectors $\boldsymbol{b}_1$ and $\boldsymbol{b}_2$ are the reciprocal lattice vectors corresponding to $\boldsymbol{a}_1$ and $\boldsymbol{a}_2$, respectively.

vectors, $\boldsymbol{a}_1$ and $\boldsymbol{a}_2$, are given as

$$\boldsymbol{a}_1 = \begin{pmatrix} 1 \\ 0 \end{pmatrix}, \ \boldsymbol{a}_2 = \begin{pmatrix} \frac{1}{2} \\ \frac{\sqrt{3}}{2} \end{pmatrix}, \tag{3.35}$$

and the corresponding reciprocal lattice vectors, $\boldsymbol{b}_1$ and $\boldsymbol{b}_2$, are given as [8]

$$\boldsymbol{b}_1 = \begin{pmatrix} 2\pi \\ -\frac{2\pi}{\sqrt{3}} \end{pmatrix}, \ \boldsymbol{b}_2 = \begin{pmatrix} 0 \\ \frac{4\pi}{\sqrt{3}} \end{pmatrix}. \tag{3.36}$$

The characteristic points in the reciprocal space, Γ-, K-, and M-points are given as

$$\Gamma = (0, 0), \ \mathrm{K} = \left(\frac{4\pi}{3}, 0\right), \ \mathrm{M} = \left(\pi, \frac{\pi}{\sqrt{3}}\right). \tag{3.37}$$

The phase diagrams varying J'/J and J''/J are shown in Fig. 3.5(a) for the fixed value of $B/J = 0.2$ and Fig. 3.5(b) for $B/J = 0.4$. When $J' \sim J'' > 0$, the antiferromagnetic (AFM) phases appear owing to the antiferromagnetic interactions $\mathcal{J} > 0$ between the spin-1 bosons. The AFM phases are divided into the solid and Bose–Einstein Condensate (BEC) phases by the boson density, $\langle n_t \rangle \approx 1$ (AFM-solid) and $\langle n_t \rangle \lesssim 0.9$ (AFM-BEC). When $J' \sim J'' < 0$, the ferromagnetic (FM) phases, FM-solid with $\langle n_t \rangle \sim 1$ and FM-BEC with $\langle n_t \rangle \lesssim 0.9$, are stabilized owing to the ferromagnetic interactions $\mathcal{J} < 0$ between the spin-1 bosons. When $J' - J'' < 0$ or $J' - J'' > 0$, two different kinds of the ferroquadrupolar (FQ) phases of spin-1 bosons, FQ-BEC and FQ-p-BEC phases, are realized over a wide parameter region. Throughout the phase diagrams both at $B/J = 0.2$ and $B/J = 0.4$, we do not find a spatial structure of the bosonic numbers, namely, the structure factors of the boson density $N(\boldsymbol{k})$ take the maximum values at Γ-point, which suggests that the bosons uniformly distribute over the system, and that the translational symmetry breaking

[8] The vectors $\boldsymbol{a}_i$ and $\boldsymbol{b}_j$ satisfy $\boldsymbol{a}_i \cdot \boldsymbol{b}_j = 2\pi\delta_{i,j}$.

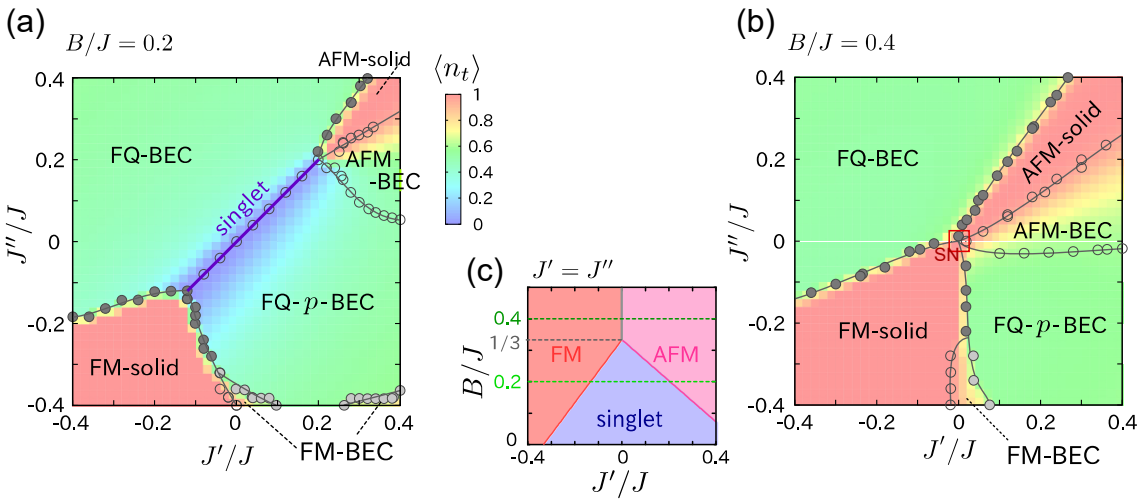

Figure 3.5: Ground-state phase diagrams of the spin-1 dimer triangular lattice at (a) $B/J = 0.2$ and (b) 0.4 on the plane of J'/J and J''/J, determined by the analysis of the results of the numerical diagonalization of the low-energy effective model of the spin-1 bosons with $N = 12$. Filled and open circles denote the first- and second-order phase transitions, respectively, and the phase transitions between FM-BEC and FQ-p-BEC phases is weakly first-order. FM, AFM, FQ denote the ferromagnetic, antiferromagnetic, and ferroquadrupolar phases, respectively. $\langle n_t \rangle \approx 1$ and $\langle n_t \rangle \lesssim 0.9$ correspond to the solid and BEC phases of bosons, respectively. The boson (triplet) density is expressed by the colors in the phase diagrams. The spin nematic (SN) phase is enclosed in the small J'/J, J''/J region marked with the red square in (b). (c) Phase diagram on the plane of J'/J and B/J at $J' = J''$. The horizontal lines with the value of B/J fixed correspond to the $J' = J''$ diagonal lines of the phase diagrams in (a) and (b). Figures are taken from Ref. [2] (Copyright ©2020, American Physical Society).

long-range orderings of bosonic degrees of freedom, or the particle orderings, do not occur.

We determine the phase boundaries on the basis of the particle-number and magnetic properties. As for the former, the phases are separated by whether the bosons (almost) fully occupy the dimers, $\langle n_t \rangle \approx 1$, and form a system equivalent to the quantum spin-1 system (solid), or the bosons are partially occupied, $\langle n_t \rangle \lesssim 0.9$, and form a BEC state. As for the magnetic properties, the phases are classified by what types of correlations develop, which is identified by $\mathcal{S}(\boldsymbol{k})$ and $\mathcal{Q}(\boldsymbol{k})$. The values of $\mathcal{S}(\boldsymbol{k})$ and $\mathcal{Q}(\boldsymbol{k})$ are dependent on the bosonic density, $\langle n_t \rangle$, but the spatial modulations of spin and quadrupolar correlations are the purely magnetic ones, because $\langle n_t \rangle$ is almost uniform in space as we mentioned above. The existence of the long-range orders is examined in Sec. 3.3.

3.2.2.2 $J' = J''$ line

We start from $J' = J'' = 0$, where the ground state is the product state of the isolated dimers. As we see from the parameters shown in Eqs. (3.9), (3.10), (3.11), (3.13), the parameters t, P, V, and $\mathcal{B}$ are the linear or quadratic functions of $(J' - J'')$. Therefore, these parameters exactly become zero along the $J' = J''$ line, namely, the inter-dimer interactions, $\mathcal{H}_{\rm inter}$, cancel out due to the frustration effect except for the Heisenberg interaction between spin-1 bosons, $\mathcal{J}$.

At $B/J = 0.2$, the singlet product state, or $\langle n_t \rangle = 0$, is the ground state when $J' = J''$. We evaluate the end point of these singlet ground states in the following procedure. Along the $J' = J''$ line, the effective Hamiltonian of spin-1 bosons (Eq. (3.7)) is reduced to the following one;

$$\mathcal{H}_{J'=J''} = -\mu \sum_{i=1}^{N} n_i + \mathcal{J} \sum_{\langle i,j \rangle} \boldsymbol{\mathcal{S}}_i \cdot \boldsymbol{\mathcal{S}}_j n_i n_j, \tag{3.38}$$

with $\mu = -J + 3B$ and $\mathcal{J} = J'$. The second term in the right hand side, $\mathcal{J} \sum_{\langle i,j \rangle} \boldsymbol{\mathcal{S}}_i \cdot \boldsymbol{\mathcal{S}}_j n_i n_j$, works as effective attractive interactions between spin-1 bosons because this term gains the magnetic interaction energy when two neighboring dimers are occupied by spin-1 bosons. Then, we can confirm a first-order phase transition between FM/AFM-solid phase with $\langle n_t \rangle = 1$ and singlet phase with $\langle n_t \rangle = 0$. We obtain the phase boundary by comparing the energies of two phases, $E_1(N)$ and $E_0(N)$, where the following relationship holds;

$$E_1(N) = E_0(N) - \mu N + 3N e_{\rm bond}. \tag{3.39}$$

Here, $e_{\rm bond}$ is the energy per bond evaluated from the ground state of the spin-1 Heisenberg model, $\mathcal{J} \sum_{\langle i,j \rangle} \boldsymbol{S}_i \cdot \boldsymbol{S}_j$, on the $N = 12$ triangular lattice (see Fig. 3.4(a)). We show the resultant phase diagram on the plane of $J'/J = J''/J$ and B/J in Fig. 3.5(c). The $\langle n_t \rangle = 0$ singlet phase shown as the straight line in Fig. 3.5(a) shrinks toward smaller $|J'|$ value as the biquadratic interaction B/J increases, and the line disappears at $B/J = 1/3$. When $1/3 < B/J$, the FM/AFM solid phase with $\langle n_t \rangle = 1$ appears on the whole $J' = J''$ line. The singlet state in the phase diagram at $B/J = 0.2$ (Fig. 3.5(a)) is realized not only on the $J' = J''$ line, but spans over a finite range of $|J' - J''|$. It is confirmed by the instability analysis discussed in Sec. 3.4.

3.2.2.3 Ferromagnetic and antiferromagnetic phases

At $B/J = 0.2$, the FM and AFM phases spread from the endpoints of the singlet phase appearing at $J' \simeq J''$ which we discussed right above. Figure 3.6 shows the total energy density $e_{\rm all}$, and the partial energy densities, e_t, e_P, $e_{\mathcal{J}}$, and $e_{\mathcal{B}}$, the triplet density $\langle n_t \rangle$, and the structure factors of spins and quadrupoles at Γ-, K-, and M-points in the reciprocal space. Here, e_X corresponds to the contribution from $\mathcal{H}_X$ in Eq. (3.7), e.g., e_t is the contribution from $\mathcal{H}_t$ (Eq. (3.9)). We change the value of J'/J with the fixed values of $J''/J = -0.2$ and $+0.1$. When $J''/J = -0.2$, a jump in the physical quantities is observed at the transition point around $J'/J = -0.1$ from the FM-solid phase to the FQ-p-BEC phase. The FM-solid phase gains a large amount of energy from $e_{\mathcal{J}}$ compared to other phases, which suggests that the Heisenberg interactions $\mathcal{J}$ play a dominant role to stabilize the FM-solid phase (see Fig. 3.6(a)). Actually, in this phase, the spin structure factor $\mathcal{S}(\boldsymbol{k})$ has a peak at the Γ-point, whereas $\mathcal{S}(\boldsymbol{k})$ in the other points and $\mathcal{Q}(\boldsymbol{k})$ remain small, which is shown in Fig. 3.6(c). In the FM-solid phase, the bosons are fully occupied, i.e., $\langle n_t \rangle = 1$.

When we change the parameter J'/J keeping $J''/J = +0.1$ constant, the boson density $\langle n_t \rangle \lesssim 0.55$ does not change much and the BEC state is realized. The phase transitions along this $J''/J = +0.1$ line are second-order. When $0.3 \lesssim J'/J$, the spin structure factor $\mathcal{S}(\boldsymbol{k})$ at the K-point begins to overwhelm the quadrupolar structure factor $\mathcal{Q}(\boldsymbol{k})$ at the Γ-point. Following the treatment given in Ref. [19] (see Sec. 3.2.1.4 for details), we identify this phase as the AFM-BEC phase. According to the analysis, the phase boundaries shown in Fig. 3.5 are separated into first- and second-order phase transitions, denoted by the filled and open circles, respectively [9].

3.2.2.4 Ferroquadrupolar phases

We confirmed two kinds of quadrupolar phases in the phase diagram, FQ-BEC in $J' < J''$ region and FQ-p-BEC in $J' > J''$. As shown in Figs. 3.6(e) and 3.6(f), both of the boson density $\langle n_t \rangle$ and the quadrupolar structure factor $\mathcal{Q}(\boldsymbol{k})$ decrease down to zero at the phase boundary where the singlet phase is realized, which indicates that the phase transition is of second-order. In the FQ-p-BEC phase, another order parameter starts to increase, which is $Q(\boldsymbol{k} = \mathrm{K})$.

In Figs. 3.7, we show the two-point correlations of quadrupolar moments between site-1 and site-j, $\langle \boldsymbol{\mathcal{Q}}_1 \cdot \boldsymbol{\mathcal{Q}}_j \rangle$ for both of FQ-BEC and FQ-p-BEC phases. In the FQ-BEC phase, the quadrupolar correlation almost uniformly develops in space, while in the FQ-p-BEC phase, the quadrupolar correlations between the nearest-neighbor sites are suppressed and those between the next-nearest-neighbor sites ferroically develops, namely, the quadrupolar correlation develops in the period of twice the lattice spacing. This three-sublattice-like configuration of the quadrupolar moments is reflected in the peak of the quadrupolar structure factor $\mathcal{Q}(\boldsymbol{k})$ at the K-point. We also show the two-point correlations of boson densities between site-1 and site-j, $\langle n_1 n_j \rangle$ in Fig. 3.7, which suggests that the bosons almost uniformly distribute in space. Thus it is indicated that the three-sublattice-like structure of $\boldsymbol{\mathcal{Q}}$ seen in FQ-p-BEC phase is not due to the spatially-modulated distribution of bosons, but is realized purely by the correlation effect of the

[9] There are also some boundaries regarded as the weak first-order phase transitions.

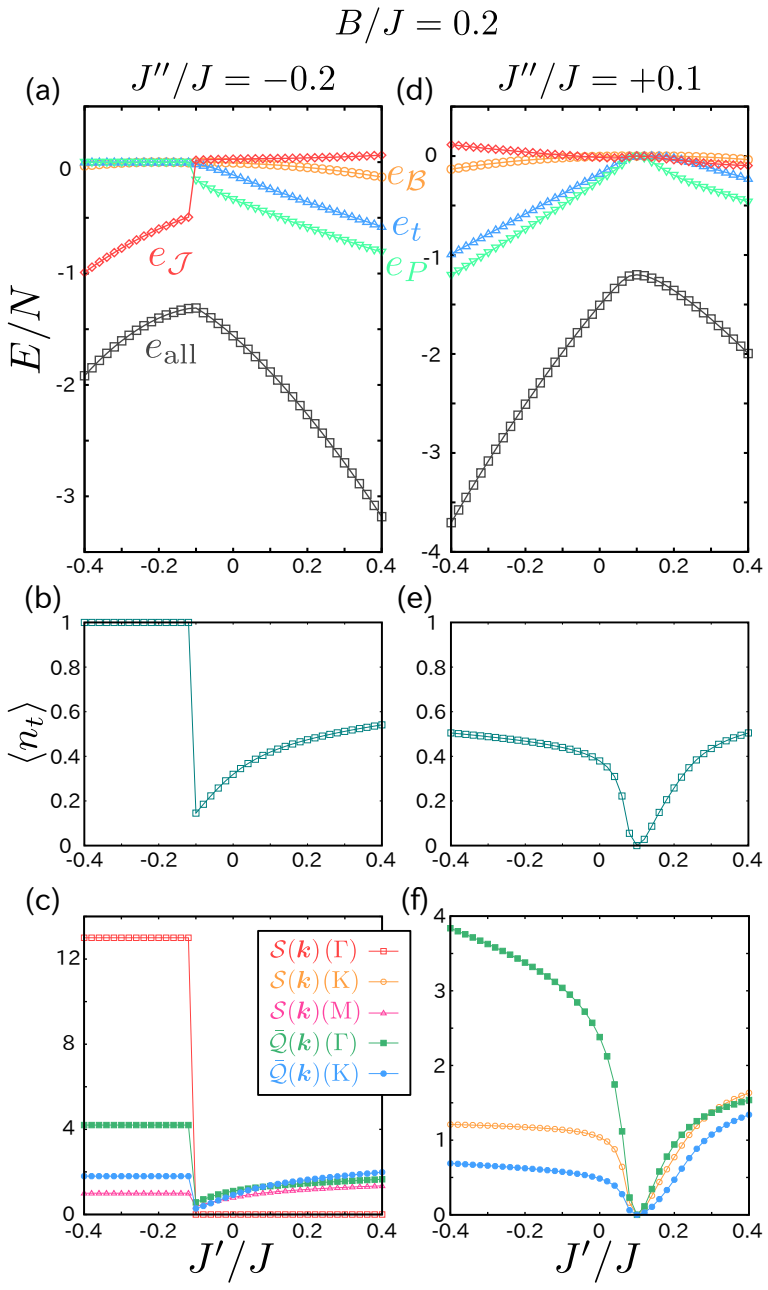

Figure 3.6: J'/J dependence of the physical quantities at $B/J = 0.2$. (a)-(c) Results at $J''/J = -0.2$. (d)–(f) Results at $J''/J = +0.1$. (a), (d) Total energy density $e_{\rm all}$, and the energy densities of some terms in the effective model, e_t, e_P, $e_{\mathcal{J}}$, and $e_{\mathcal{B}}$. (b), (e) Boson density $\langle n_t \rangle$. (c), (f) Spin (Eq. (3.28)) and quadrupolar (Eq. (3.29)) structure factors at Γ-, K-, and M-points in the reciprocal space. For the quadrupolar structure factors, the normalized value $\bar{\mathcal{Q}}(\boldsymbol{k}) = \frac{3}{5}\mathcal{Q}(\boldsymbol{k})$ is shown to compare the spin and quadrupolar structure factors. Figures are taken from Ref. [2] (Copyright ©2020, American Physical Society).

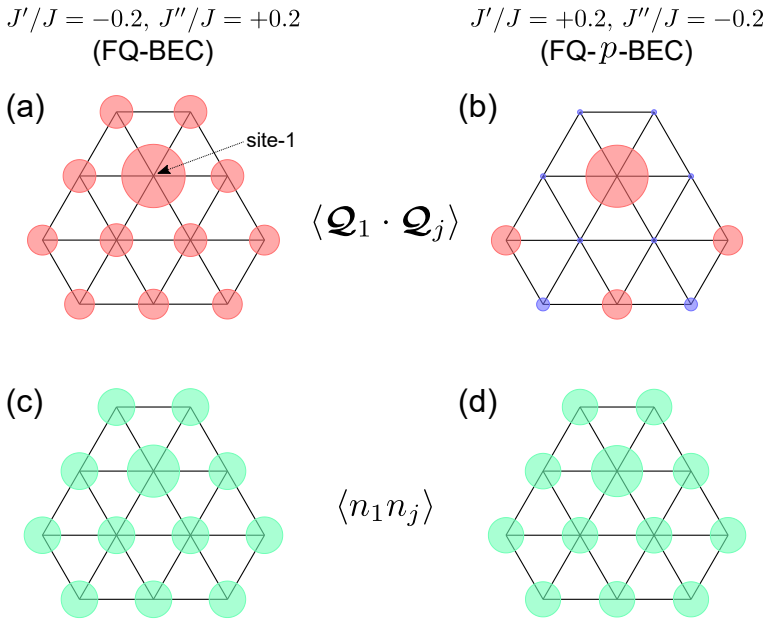

Figure 3.7: Two-point correlations between site-1 and site-j at $(J'/J, J''/J) = (-0.2, 0.2)$ in FQ-BEC phase and at $(J'/J, J''/J) = (0.2, -0.2)$ in FQ-p-BEC phase for $B/J = 0.2$. (a), (b) the quadrupolar correlations $\langle \boldsymbol{\mathcal{Q}}_1 \cdot \boldsymbol{\mathcal{Q}}_j \rangle$. (c), (d) the boson density correlations $\langle n_1 n_j \rangle$. The areas of the circles are proportional to the absolute values of the correlations, $|\langle \boldsymbol{\mathcal{Q}}_1 \cdot \boldsymbol{\mathcal{Q}}_j \rangle|$, or $|\langle n_1 n_j \rangle|$. Blue and red circles appeared in (a) and (b) denote the signs of the quadrupolar correlations $\langle \boldsymbol{\mathcal{Q}}_1 \cdot \boldsymbol{\mathcal{Q}}_j \rangle$, negative and positive, respectively. Figures are taken from Ref. [2] (Copyright).

spin degrees of freedom, $\boldsymbol{\mathcal{S}}_i$. There, the nearest-neighbor correlations of the quadrupolar moments are suppressed, whereas the next-nearest-neighbor ones are ferroic.

3.2.2.5 Case of $B/J = 0.4$

Next we discuss the case $B/J = 0.4$, where the chemical potential μ becomes positive. As we discussed above, the singlet phase appearing at $B/J = 0.2$ no longer exists, and when the inter-dimer Heisenberg interactions, J' and J'', are introduced, the product state of the triplet dimer at $J' = J'' = 0$ transforms into the phases we discussed above. In Fig. 3.8, we show the J'/J dependence of the energy densities, boson density, and the spin and quadrupolar structure factors, which is to be compared with Fig. 3.6 for $B/J = 0.2$ case. We observe the first-order phase transitions between the FM-solid and the FQ phases. In the FQ-BEC phase, the boson density is stable around $\langle n_t \rangle \approx 0.55$, indicating that the overall nature of the BEC phase does not qualitatively change by B/J. We note that the smaller J' and J'' region at $B/J = 0.4$ includes the spin nematic phase, which should be distinguished from both of the FQ-BEC phase and the FQ-p-BEC phases (see Sec. 3.3 in detail).

3.2.2.6 Order of perturbation

The interaction parameters in the effective bosonic model (Eqs. (3.16)–(3.22) contains the zeroth-, first- and second-order perturbation terms. When we discard the second-order perturbation terms, V and $\mathcal{B}$ disappear. In order to see how much the second-order terms qualitatively contribute to the ground state phase diagram, we additionally perform the numerical diagonalization limiting the interaction parameters up to the first order in J'/J and J''/J on the $N = 12$ triangular lattice. The resultant phase diagram on the plane of J'/J and J''/J at $B/J = 0.2$ and 0.4 are shown in Figs. 3.9(a) and 3.9(b), respectively. These phase diagrams are qualitatively identical to the ones in Fig. 3.5, which indicates that the second-order perturbation terms such as V and $\mathcal{B}$ do not play a significant role in the phase diagrams. It is also suggested that the second-order terms involving three-sites, $\mathcal{H}_{\rm 3body}$, neglected for simplicity, do not seem to change the phase diagram qualitatively.

3.3 Long-range orders and classifications of multiple quadrupolar phases

So far, using the spin-1 bosonic language, we have discussed the magnetic properties of the spin-1 dimer triangular lattice based on the results of the numerical diagonalization of the effective model on the $N = 12$ triangular lattice. As the numerical diagonalization is performed on the small finite size cluster, one should carefully examine the finite-size effect and the existence of the symmetry-breaking long-range orders. However, in the present case, the finite-size effect is expected to be negligible. This is because, in the previous study on the same effective model in Ref. [86] which is exactly equivalent to the spin-1/2 dimer model on the same lattice as ours, the finite-size effect turned out to be almost negligible; the phase boundaries obtained by the results of the numerical diagonalization with $N = 12$ and those obtained by the analytical results for arbitrary

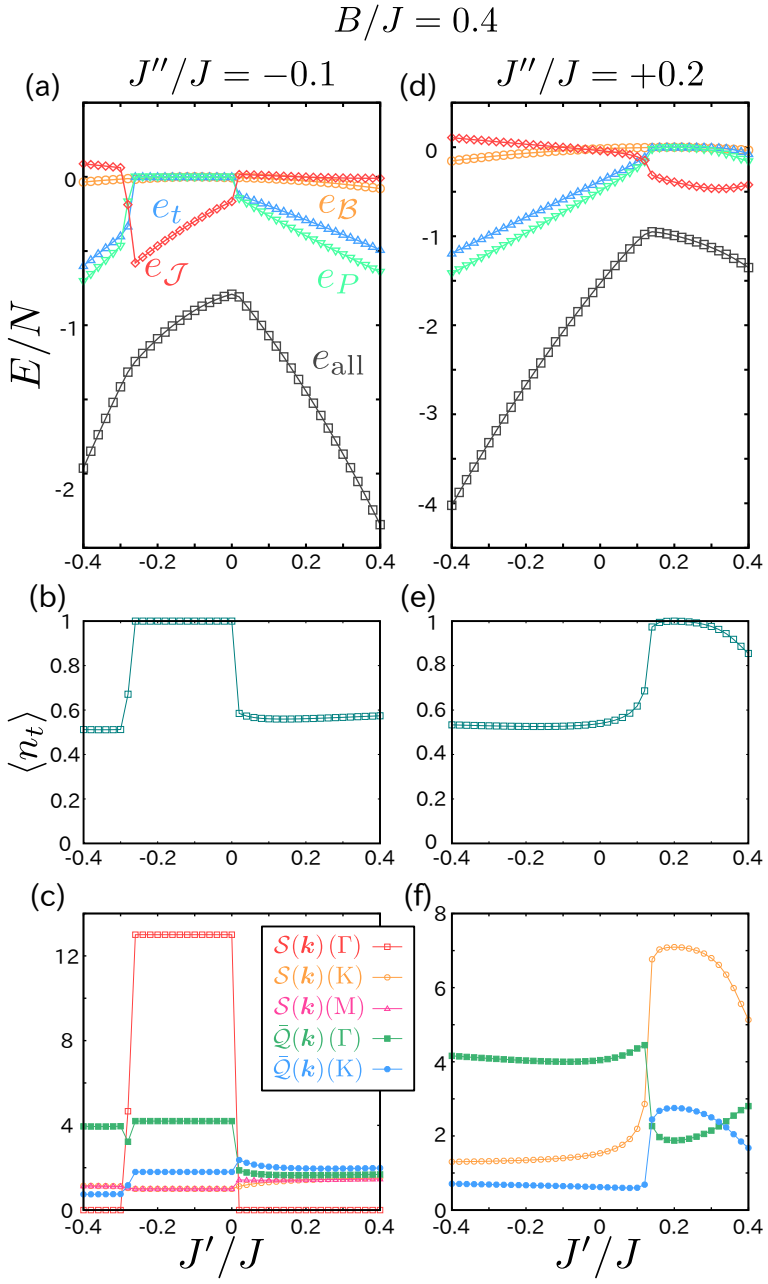

Figure 3.8: J'/J dependence of the physical quantities at $B/J = 0.4$. (a)-(c) Results at $J''/J = -0.1$. (d)–(f) Results at $J''/J = +0.2$. (a), (d) Total energy density $e_{\rm all}$, and the energy densities of some terms in the effective model, e_t, e_P, $e_{\mathcal{J}}$, and $e_{\mathcal{B}}$. (b), (e) Boson density $\langle n_t \rangle$. (c), (f) Spin (Eq. (3.28)) and quadrupolar (Eq. (3.29)) structure factors at Γ-, K-, and M-points in the reciprocal space. For the quadrupolar structure factors, the normalized value $\bar{\mathcal{Q}}(\boldsymbol{k}) = \frac{3}{5}\mathcal{Q}(\boldsymbol{k})$ is shown to compare the spin and quadrupolar structure factors. Figures are taken from Ref. [2] (Copyright ©2020, American Physical Society).

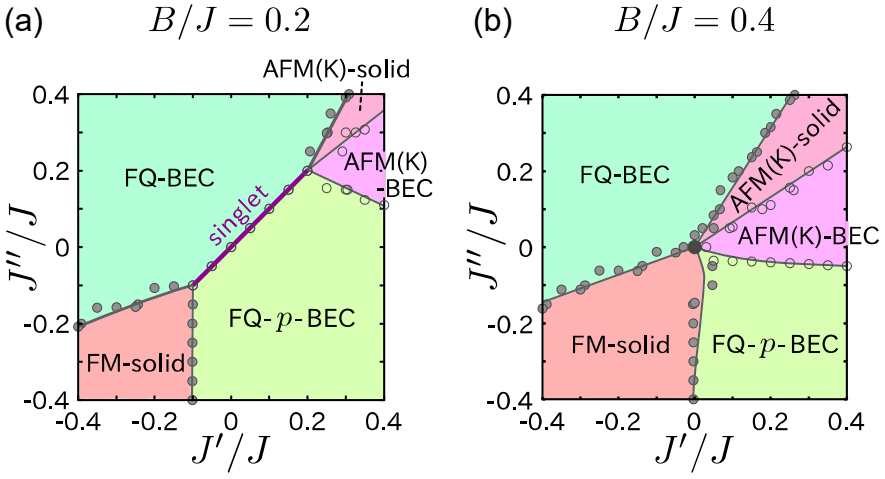

Figure 3.9: Phase diagrams of the effective model on the plane of J'/J and J''/J, whose interaction parameters are limited up to the first order in J'/J and J''/J at (a) $B/J = 0.2$ and (b) $B/J = 0.4$. The phase diagrams are obtained by analyzing the results of the numerical diagonalization on the $N = 12$ triangular lattice. Figures are taken from Ref. [2] (Copyright ©2020, American Physical Society).

N quantitatively agree well. Therefore, here we only need to discuss whether there is a true symmetry-breaking long-range order in each phase appearing in Sec. 3.2. For this purpose, we performed the Anderson tower analysis [168], calculating the low-energy excitation spectra by the thick-restart Lanczos method [166, 167].

3.3.1 Basics of the Anderson tower analysis

Before we discuss the long-range orders in our spin-1 dimer triangular lattice, we briefly review the Anderson tower analysis. The Anderson tower analysis [168] [10] is one of the unbiased tool for detecting the long-range orders in the ground states of the quantum many-body systems from the calculations of the finite-size clusters. In their energy spectra, the low-lying states or the quasi-degenerate joint states (QDJS) can appear as the lowest-energy levels which scale as a linear function of $S_{\rm tot}(S_{\rm tot}+1)$. The QDJS imply the existence of the long-range order breaking the continuous symmetry [11] [168, 170–174], where the slope collapses in proportional to $1/N$, where N is the system size.

In the numerical analysis, the Anderson tower analysis was introduced to show the long-range orderings in the ground state of the spin-1/2 antiferromagnetic Heisenberg model on the triangular lattice [170, 171], and later applied to demonstrate the absence of the long-range orderings of the ground state of the spin-1/2 antiferromagnetic Heisenberg model on the kagome lattice [175]. When the energy spectrum forms the low-lying states, the symmetries of the low-lying states are examined to determine the possible symmetry breaking in the ground-states. The QDJS consists of the energy eigenstates with specific

[10] This is also called as 'tower-of states analysis', etc.

[11] As we describe the QDJS as a function of $S_{\rm tot}(S_{\rm tot}+1)$, hereafter we implicitly assume the spin systems and the continuous symmetry broken is SU(2). However, the Anderson tower analysis can be applied also to SU(N) systems. Then, $S_{\rm tot}(S_{\rm tot}+1)$, the Casimir operator in SU(2) group, is replaced by the Casimir operator of SU(N) systems. For example, see Ref. [169] for the SU(4) symmetric case.

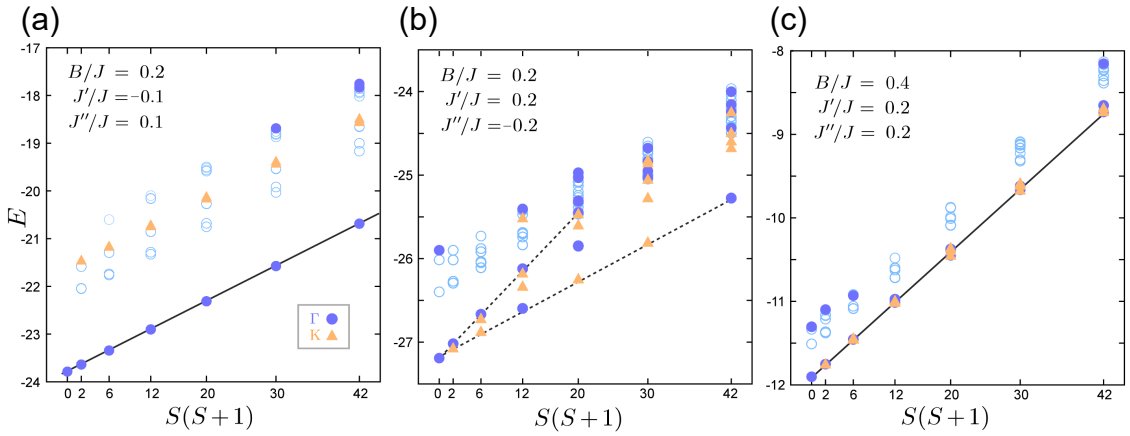

Figure 3.10: Low-energy spectra with respect to $S(S+1)$ in the (a) FQ-BEC, (b) FQ-p-BEC, and (c) AFM-solid phases for the $N = 12$ cluster. Filled circles and triangles denote the eigenstates whose momenta are characterized by the Γ- and K-points in the reciprocal space, and the momenta of the eigenstates with open circles are not determined in our calculations. The eigenstates on the solid lines in (a) and (c) will collapse and construct the degenerate ground states in the $N \to +\infty$ thermodynamic limit, which indicates the long-range orders. Figures are taken from Ref. [2] (Copyright ©2020, American Physical Society).

spatial symmetries such as the translational symmetry and the reflection symmetry reflecting the symmetry-breaking long-range orders. For example, when the 120° Néel order is realized on the triangular lattice, the sublattice spins form a biaxial rotator which is characterized by the spin component perpendicular to the rotating plane, and there appear $2S_{\rm tot}+1$ states in each $S_{\rm tot}$-sector [12].

3.3.2 Anderson tower analysis in the spin-1 dimer triangular lattice and classification of multiple phases

3.3.2.1 Internal degrees of freedom of the FQ phases

In Figs. 3.10(a)–(c), we show the low-energy spectra in the FQ-BEC, FQ-p-BEC, and AFM-solid phases, respectively. For the cases of the FQ-BEC (Fig. 3.10(a)) and the AFM-BEC (Fig. 3.10(c)) phases, we confirm the clear QDJS depicted by the solid lines. In Fig. 3.10(a), the QDJS consist of all $S_{\rm tot}$-sectors, $S_{\rm tot} = 0, 1, 2, 3, \cdots$, where each $S_{\rm tot}$ sector has only one state with Γ-point, which characterizes the U(1) uniaxial rotator type excitation. This low-lying state is clearly different from the one known for the spin-1 ferroquadrupolar (ferro-nematic) ordered phase, where the QDJS is constructed only by the even $S_{\rm tot}$-sectors with Γ-points [17] (cf. see Fig. 3.13(a)). This implies that the quadrupolar moment $\boldsymbol{\mathcal{Q}}_i$ is insufficient for the classification of the multiple quadrupolar phases of spin-1 bosons appearing in the dimer systems. In fact, the quadrupolar moment

[12] The trivial degeneracy for each $S_{\rm tot}$ is not considered.

Table 3.1: Classification of multiple phases using the order parameters $\boldsymbol{q}$, $\boldsymbol{p}$, $\boldsymbol{\mathcal{S}}$, and $\boldsymbol{\mathcal{Q}}$, and the types of boson distributions, solid (S) or liquid (L). FQ-BEC phase corresponds to the F-nematic phase in Ref. [84]. Table is reproduced from TABLE I in Ref. [2] (Copyright).

Phases	$\langle \boldsymbol{q} \rangle$	$\langle \boldsymbol{p} \rangle$	$\langle \boldsymbol{\mathcal{S}} \rangle$	$\langle \boldsymbol{\mathcal{Q}} \rangle$	Boson
SN (n-nematic)	$\boldsymbol{0}$	$\boldsymbol{0}$	$\boldsymbol{0}$	$\neq \boldsymbol{0}$	S
Chiral (p-nematic)	$\boldsymbol{0}$	$\neq \boldsymbol{0}$	$\boldsymbol{0}$	$\neq \boldsymbol{0}$	L
FM	$\boldsymbol{0}$ (S) or $\neq \boldsymbol{0}$ (L)	$\boldsymbol{0}$	$\neq \boldsymbol{0}$	$\neq \boldsymbol{0}$	S or L
AFM	$\boldsymbol{0}$ (S) or $\neq \boldsymbol{0}$ (L)	$\neq \boldsymbol{0}$	$\neq \boldsymbol{0}$	$\neq \boldsymbol{0}$	S or L
FQ-BEC	$\neq \boldsymbol{0}$	$\boldsymbol{0}$	$\boldsymbol{0}$	$\neq \boldsymbol{0}$	L

$\mathcal{Q}_i^{\alpha\beta}$ defined on a dimer bond can be decomposed as

$$\mathcal{Q}_i^{\alpha\beta} = -\left\{ \frac{3}{4}\left[\left(q_i^\alpha q_i^\beta + p_i^\alpha p_i^\beta \right) + \left(q_i^\beta q_i^\alpha + p_i^\beta p_i^\alpha \right) \right] - \frac{2}{3}\delta_{\alpha\beta} \right\} n_i, \tag{3.40}$$

where $\boldsymbol{q}_i$ and $\boldsymbol{p}_i$ are the internal degrees of freedom of a dimer [84], namely, the staggered spin operator of the two spins and the vector-chiral spin operator,

$$\boldsymbol{q}_i = \frac{1}{2}\left(\boldsymbol{S}_{i_1} - \boldsymbol{S}_{i_2} \right), \quad \boldsymbol{p}_i = \boldsymbol{S}_{i_1} \times \boldsymbol{S}_{i_2}. \tag{3.41}$$

These two operators are related to the annihilation and creation operators of spin-1 bosons in our model as $b_{i,\alpha} \propto q_i^\alpha - \mathrm{i}p_i^\alpha$, and $b_{i,\alpha}^\dagger \propto q_i^\alpha + \mathrm{i}p_i^\alpha$, respectively [13]. When at least $\langle \boldsymbol{q}_i \rangle \neq \boldsymbol{0}$ or $\langle \boldsymbol{p}_i \rangle \neq \boldsymbol{0}$ holds, we obtain $\langle \boldsymbol{\mathcal{Q}}_i \rangle \neq \boldsymbol{0}$, while the inverse is not always fulfilled. The structure factors of these operators are set as

$$\mathcal{N}(\boldsymbol{k}) = \frac{1}{N}\sum_{i,j=1}^{N} \langle \boldsymbol{q}_i \cdot \boldsymbol{q}_j \rangle \, \mathrm{e}^{\mathrm{i}\boldsymbol{k}\cdot(\boldsymbol{r}_i - \boldsymbol{r}_j)}, \tag{3.44}$$

$$\mathcal{C}(\boldsymbol{k}) = \frac{1}{N}\sum_{i,j=1}^{N} \langle \boldsymbol{p}_i \cdot \boldsymbol{p}_j \rangle \, \mathrm{e}^{\mathrm{i}\boldsymbol{k}\cdot(\boldsymbol{r}_i - \boldsymbol{r}_j)}, \tag{3.45}$$

respectively.

We give the classification of the quadrupolar phases of spin-1 bosons in terms of these internal degrees of freedom in Table 3.1. The conventional spin nematic (SN) phase seen in the spin-1 BLBQ models has $\langle \boldsymbol{\mathcal{Q}}_i \rangle \neq \boldsymbol{0}$ with other magnetic order parameters vanishing, and takes place only when the distribution of the (single) boson is a solid and the boson

[13] To be precise,

$$b_{i,\alpha} \simeq \mathrm{i}\frac{\sqrt{3}}{2\sqrt{2}}\left(q_i^\alpha - \mathrm{i}p_i^\alpha \right), \quad b_{i,\alpha}^\dagger \simeq -\mathrm{i}\frac{\sqrt{3}}{2\sqrt{2}}\left(q_i^\alpha + \mathrm{i}p_i^\alpha \right) \tag{3.42}$$

hold. Here, $\simeq$ means that this formula is derived under the approximation neglecting the quintet states. Equivalently,

$$q_i^\alpha \simeq \mathrm{i}\frac{\sqrt{2}}{\sqrt{3}}\left(b_{i,\alpha}^\dagger - b_{i,\alpha} \right), \quad p_i^\alpha \simeq \frac{\sqrt{2}}{\sqrt{3}}\left(b_{i,\alpha}^\dagger + b_{i,\alpha} \right) \tag{3.43}$$

hold.

cannot move around. Here, the quadrupolar order $\langle \boldsymbol{\mathcal{Q}}_i \rangle \neq \mathbf{0}$ is generated neither by $\langle \boldsymbol{q}_i \rangle \neq \mathbf{0}$ nor by $\langle \boldsymbol{p}_i \rangle \neq \mathbf{0}$, but is generated by $\langle q_i^\alpha q_i^\beta \rangle \neq 0$ or $\langle \mathcal{S}_i^\alpha \mathcal{S}_i^\beta \rangle \neq 0$ [14]. When $\langle \boldsymbol{p}_i \rangle \neq \mathbf{0}$ and $\langle \boldsymbol{q}_i \rangle = \langle \boldsymbol{\mathcal{S}}_i \rangle \neq \mathbf{0}$, the vector-chiral degrees of freedom condenses, and form a nematic order where all kinds of the magnetic orderings are suppressed. This vector-chiral ordered phase is often called p-nematic phase, which is distinguished from the SN phase (n-nematic phase). In the SN (n-nematic) phase, the Anderson tower of states are formed only by the multiple $S_{\rm tot}$-sectors in units of multi-bosons. In that case, only the bound multi-boson states are allowed as the quasiparticles [17, 51, 62]. By contrast, in the vector-chiral (p-nematic) phase, the standard single-magnon excitations are allowed, and the low-lying states consist of all of the $S_{\rm tot}$-sectors [81].

The typical magnetic phases, the FM and AFM phases, are supported by $\langle \boldsymbol{\mathcal{S}}_i \rangle \neq \mathbf{0}$ [15]. In the FQ-BEC phase, $\langle \boldsymbol{q}_i \rangle \neq \mathbf{0}$ and $\langle \boldsymbol{p}_i \rangle = \mathbf{0}$, where the spin moments induced on the two spins on dimers always take an antiparallel state, and keep the dimer unit nonmagnetic, namely, $\langle \boldsymbol{\mathcal{S}}_i \rangle = \mathbf{0}$. The spin moments form a ferromagnetic long-range order inside each two-dimensional layer.

Based on the above classification, the FQ-BEC phase can be regarded as the F-nematic phase found in the spin-1/2 two-leg ladder [84], where the ferroic ordering of the staggered spin moments $\langle \boldsymbol{q}_i \cdot \boldsymbol{q}_j \rangle > 0$ is realized, and the SU(2) symmetry is broken down to U(1). In Fig. 3.11, we show the triplet density $\langle n_t \rangle$ and the structure factors when J'/J is varied from the FQ-BEC ($J'/J \lesssim 0.15$), the FQ-p-BEC ($0.15 \lesssim J'/J \lesssim 0.25$), to the AFM-BEC ($0.25 \lesssim J'/J$) phases. The FQ-BEC phase is characterized by the enhancement of $\mathcal{N}(\boldsymbol{k})$ at the Γ-point. In the FQ-p-BEC phase, not only $\mathcal{N}(\boldsymbol{k})$ at the K-point but also $\mathcal{C}(\boldsymbol{k})$ at the Γ-point take large values. When the phase changes from the FQ-p-BEC phase into the AFM-BEC phase, $\mathcal{C}(\boldsymbol{k})$ decreases.

We show the tower of states in the FQ-p-BEC phase in Fig. 3.10(b), which exhibits an intriguing structure. If we take in all the states below the upper dotted line as the low-lying states, the structure of the low-lying states is consistent with the biaxial rotator, indicating the 120° Néel ordering. However, the low-lying excitetd states here are not well separated from the states with higher energies. By contrast, in the AFM-solid phase, we can confirm the clear tower of states structure with $(2S_{\rm tot}+1)$ degenerate states shown in Fig. 3.10(c), suggesting the 120° Néel order of $\mathcal{S}=1$ moments. It may be expected that a sort of 120° Néel ordering of $\boldsymbol{q}_i$-moment compatible with the geometry of the triangular lattice, which is similar to the FQ-BEC phase (see Table 3.1). There, the 120° long-range order of $\boldsymbol{S}_{i_\mu}$ inside each layer is realized, and each dimer is kept nonmagnetic. This state corresponds to the NAF phase in the spin-1/2 two-leg ladder sytstem in Ref. [84]. Alternatively, we can also focus only on the lowest energy eigenstates in each $S_{\rm tot}$-sector on the lower broken line. Then, the $S_{\rm tot} = 0, 3, 6, \cdots$ states at the Γ-point and the $S_{\rm tot} = 1, 2, 4, 5, \cdots$ states at the K-point imply the p-type nematic property, which is similar to the p-type nematic

[14] We implicitly assume $\alpha \neq \beta$ here.

[15] To be more precise, in the AFM phase, $\langle \boldsymbol{\mathcal{S}}_i \rangle = \mathbf{0}$, but the space-modulated spin moment

$$\boldsymbol{\mathcal{S}}_{\boldsymbol{q}} = \frac{1}{N} \sum_{i=1}^{N} \mathrm{e}^{\mathrm{i}\boldsymbol{q}\cdot\boldsymbol{r}_i} \boldsymbol{\mathcal{S}}_i \tag{3.46}$$

takes a nonzero value. The modulated spin moment is merely the linear combination of $\boldsymbol{\mathcal{S}}_i$, and we include it into $\langle \boldsymbol{\mathcal{S}}_i \rangle = \mathbf{0}$ in a broader sense.

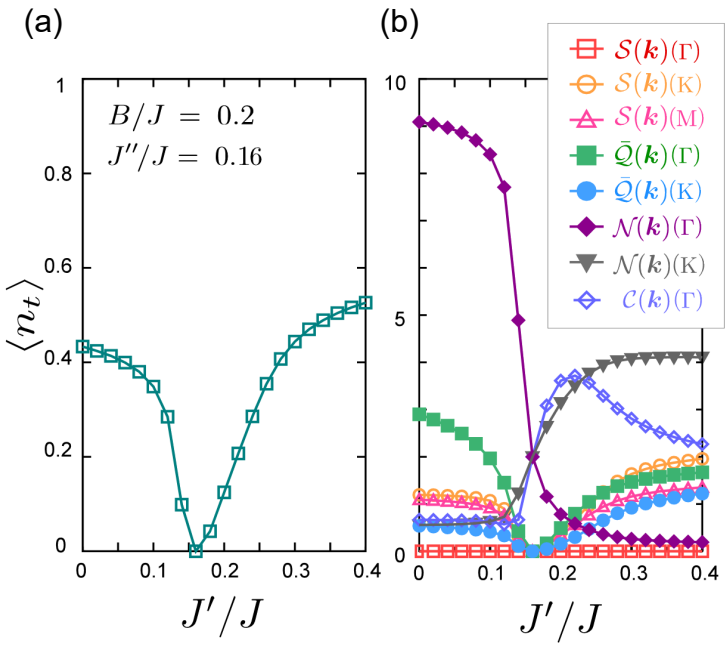

Figure 3.11: J'/J dependence of (a) the triplet density, and (b) the structure factors at the Γ-, K-, and M-points. $\mathcal{N}(\boldsymbol{k})$ (Eq. (3.44)) and $\mathcal{C}(\boldsymbol{k})$ (Eq. (3.45)) that provide the detailed information on teh magnetic properties of the spins $\boldsymbol{S}_{i_\gamma}$ inside the dimers are also shown. J'/J is changed from the FQ-BEC ($J'/J \lesssim 0.15$), the FQ-p-BEC ($0.15 \lesssim J'/J \lesssim 0.25$), to the AFM-BEC ($0.25 \lesssim J'/J$) phases. Figures are taken from Ref. [2] (Copyright ©2020, American Physical Society).

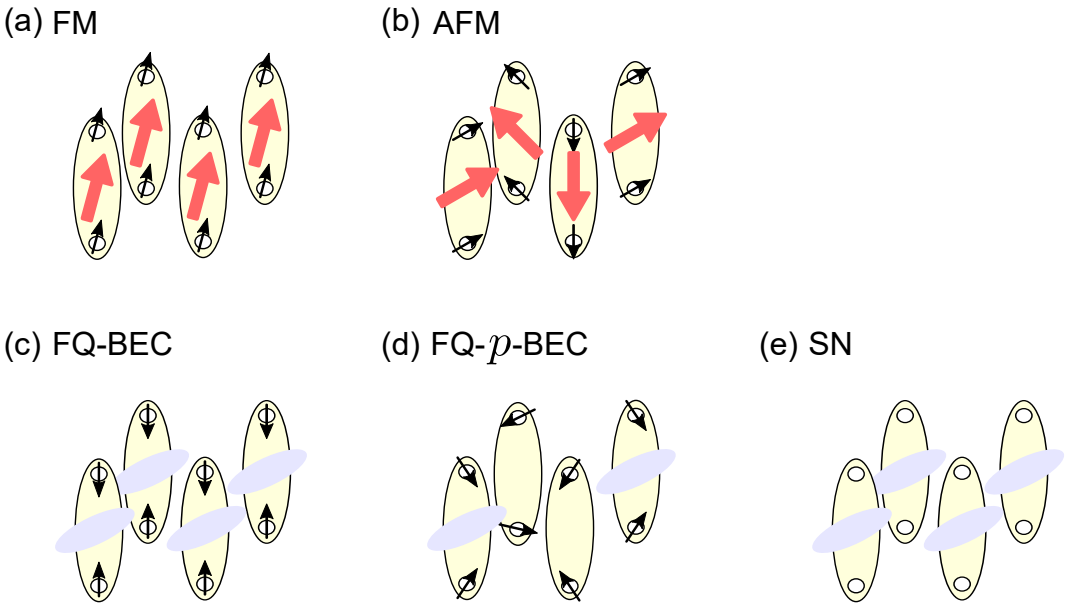

Figure 3.12: Schematic pictures of the (a) FM, (b) AFM, (c) FQ-BEC, (d) FQ-p-BEC, and (e) SN phases. The black arrow on each site denotes the spin moment carried by the site-i_γ, and the red arrow and blue ellipses represent the spin and quadrupolar moments of the i-th dimer, respectively.

order in the spin-1/2 system on the square lattice, where even $S_{\rm tot}$-sector has $\boldsymbol{k} = (0, 0)$ momentum and odd $S_{\rm tot}$-sector has the (π, π)-momentum [81] [16]. As shown in Fig. 3.11, both of $\boldsymbol{q}_i$ and $\boldsymbol{p}_i$ have large correlations, which is consistent with the tower of states structure which contains both of the 120° Néel antiferromagnetic and the vector-chiral properties. One possible scenario is that the 120° Néel ordering is realized in each layer, but the spin moments do not fully align between the layers. However, when we consider the fact that the 120° Néel antiferromagnetic order in the spin-1/2 Heisenberg model on the triangular lattice is somewhat subtle because of the small magnetic moments [176], such type of the ordering might be unstable as a symmetry-breaking long-range order in our system where the active local spin moments are likely to be small. Then, the 120° Néel order of $\boldsymbol{q}$ will be hindered by the intra-dimer quantum fluctuations, where either a pure vector-chiral ordering or a more exotic spin liquid state might be realized.

In Fig. 3.12, we summarize the multiple phases by showing their schematic pictures.

3.3.2.2 Spin nematic phase at the small J'/J and J''/J region

Besides these two FQ phases, FQ-BEC and FQ-p-BEC, we confirm a conventional ferroquadrupolar spin nematic (SN) phase at $1/3 \lesssim B/J$ in a small J'/J and J''/J region, which can only be found by the tower of states analysis. We show in Fig. 3.13(a) the low-lying states consisting of even $S_{\rm tot}$-sector, which suggests the ferroquadrupolar SN phase on the triangular lattice breaking the SU(2) symmetry [17]. The phase boundary between the SN phase and the FQ-BEC phase is determined by the level crossing of the

[16] Here we discuss the low-lying states utilizing the similarity to the ones in Ref. [81]. To more clearly discuss the existence of the p-type property, more detailed symmetry analysis of the low-lying states might be needed.

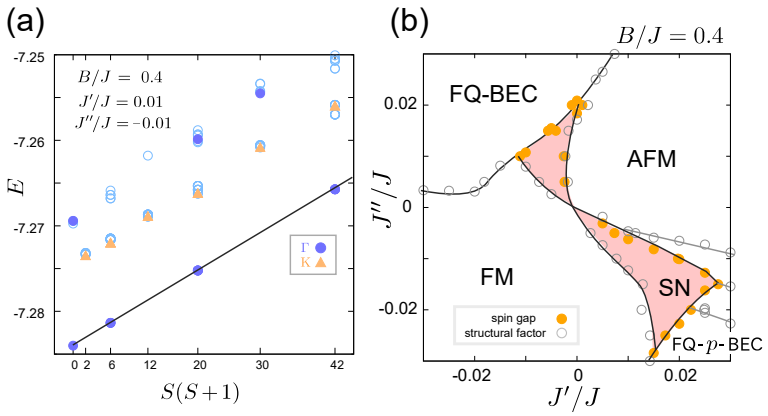

Figure 3.13: (a) Low-energy excitation spectrum plotted against $S(S+1)$ at $J'/J = 0.01$, $J''/J = -0.01$, and $B/J = 0.4$. (b) Phase diagram in the small J'/J and J''/J region at $B/J = 0.4$, which enlarges the region marked with the red square at the center of Fig. 3.5(b). The phase boundaries are determined both by the crossing of $S_{\rm tot} = 1$ and 2 states (filled circle), and by the structure factor (open circle). J'/J dependence of the physical quantities for $J''/J = 0.01$ in this phase diagram is shown in Fig. 3.14. Figures are taken from Ref. [2] (Copyright ©2020, American Physical Society).

$S_{\rm tot} = 1$ and 2 lowest excited states. We show the structure factors in Fig. 3.14(b). The quadrupolar structure factor $\mathcal{Q}(\boldsymbol{k})$ at the Γ-point increases without the increase of $\mathcal{N}(\boldsymbol{k})$ at the Γ-point inside the SN phase, and in the FQ-BEC phase at $J'/J \lesssim -0.015$, $\mathcal{N}(\boldsymbol{k})$ at the Γ-point has a large value and $\mathcal{Q}(\boldsymbol{k})$ at the Γ-point decreases. The triplet density $\langle n_t \rangle$ in the SN phase is $\langle n_t \rangle \sim 1$, which is in agreement with the SN phase in the spin-1 BLBQ model. When B/J takes a large value, the spin-1 dimer state which has the lowest energy is the triplet, replacing the singlet state at small B/J, and as a result, the spin-1 bosons fully occupy the sites and the small inter-dimer interactions J' and J'' play a role of exchanging the spin-1 bosons and realizing the SN phase.

We show the physical quantities when the interdimer interactions J'/J, J''/J are small at $B/J = 0.4$. The J'/J dependence of the low-energy excited states at $J''/J = 0.01$ is shown in Fig. 3.14(a); in its inset, the spin gaps of $\Delta S = 1$ and $\Delta S = 2$ are given. When we change J'/J, the energy levels of the excited states with $S_{\rm tot} = 1$ and $S_{\rm tot} = 2$ cross at $J'/J \sim -0.01$, which implies the quantum phase transition from the FQ-BEC phase to the spin nematic (SN) phase. We can confirm the phase transition also in the variation of the structure factors given in Fig. 3.14(b), where $\mathcal{N}(\boldsymbol{k})$ at the Γ-point decreases and $\mathcal{Q}(\boldsymbol{k})$ at the Γ-point increases at $J'/J \sim -0.01$.

As we increase J'/J, the excited state with $S_{\rm tot} = 1$ again has a lower energy than the excited state with $S_{\rm tot} = 2$. This indicates that the quantum phase transition from the SN phase to the AFN phase occurs, where $\mathcal{Q}(\boldsymbol{k})$ at the Γ-point has a smaller value, and $\mathcal{S}(\boldsymbol{k})$ at the K-point become larger.

In Fig. 3.14(c), we show the partial ground-state energy of several terms in the effective model. When the ground state is the FQ-BEC phase at $J'/J \lesssim -0.01$, the hoppings, e_t, and the pair-creation/annihilation of bosons, e_P, play an important role in realizing the phase. When $-0.01 \lesssim J'/J \lesssim 0$, the ground state turns into the SN phase, where the pair-fluctuation effect of P is still significant. Here, the pair-creation and annihilation term

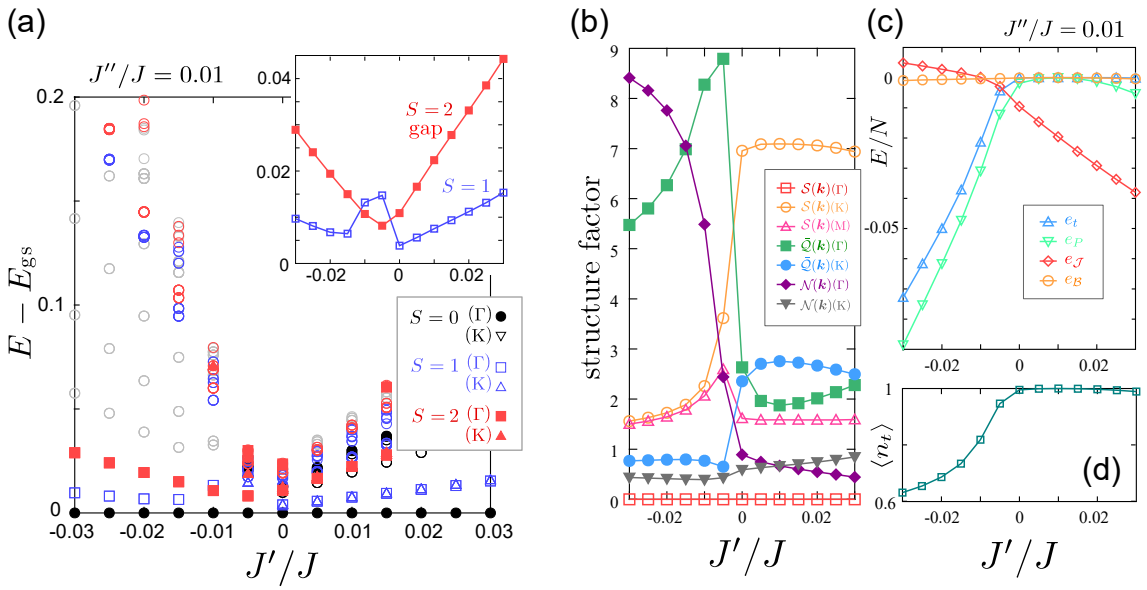

Figure 3.14: Results at $B/J = 0.4$ with fixed $J''/J = 0.01$. (a) Low-energy excited states of $S_{\rm tot} = 0, 1, 2$ sectors with respect to J'/J. The level crossing of the lowest excited states with $S_{\rm tot} = 1$ and 2, which is extracted from the main panel, are seen more clearly in the inset. When $J' \sim -0.01$, the $S_{\rm tot} = 2$ state is the lowest excited state, which signals the spin nematic orderings typically found in the spin-1 BLBQ models. (b) Spin (Eq. (3.28)), quadrupolar (Eq. (3.29)), and staggered spin (Eq. (3.44)) structure factors at the Γ-, K-, and M-points. (c) The partial energy from some terms in the effective Hamiltonian, e_t, e_P, $e_{\mathcal{J}}$, and $e_{\mathcal{B}}$. (d) Boson density $\langle n_t \rangle$. Figures are taken from Ref. [2] with the legend in (c) modified from the capital letters (E_*) to the small letters (e_*) (Copyright ©2020, American Physical Society).

generates the effective biquadratic interactions between the neighboring spin-1 bosons, whereas the explicit biquadratic interaction term $\mathcal{H}_{\mathcal{B}}$ in the effective Hamiltonian does not much contribute to the formation of the SN, which can be confirmed by the fact that $e_{\mathcal{B}}$ is almost zero in the SN phase. In the AFM phase, the Heisenberg interaction term, $\mathcal{H}_J$, largely gains the energy. In Fig. 3.14(d), we show the J'/J dependence of the boson density, $\langle n_t \rangle$, where $\langle n_t \rangle$ increases to $\langle n_t \rangle \sim 1$ around the transition from the FQ-BEC to the SN phases.

3.4 Discussions

3.4.1 Origins of the quadrupolar moments on dimers

As we can see in Figs. 3.6 and 3.8, the pair-creation and annihilation term, $\mathcal{H}_P$, in our effective Hamiltonian of spin-1 bosons, plays a dominant role in the FQ-BEC and FQ-p-BEC phases. In order to elucidate how $\mathcal{H}_P$ works, we set the interaction parameters as $J'' = -J'$ so as to eliminate the Heisenberg term, $\mathcal{H}_{\mathcal{J}}$. Then, the effective Hamiltonian up to the first-order perturbation in J'/J and J''/J is reduced to

$$\begin{aligned}\mathcal{H}_{\rm quad} &= \mathcal{H}_\mu + \mathcal{H}_t + \mathcal{H}_P \\ &= -\mu \sum_{i=1}^{N} n_i + \sum_{\langle i,j \rangle} \sum_{\alpha=x,y,z} \left[\left(t b^\dagger_{i,\alpha} b_{j,\alpha} + P b^\dagger_{i,\alpha} b^\dagger_{j,\alpha} \right) + \text{h.c.} \right]. \end{aligned} \tag{3.47}$$

Performing the Fourier transform as

$$b^\dagger_{i,\alpha} = \frac{1}{\sqrt{N}} \sum_{\boldsymbol{k}} \mathrm{e}^{\mathrm{i}\boldsymbol{k}\cdot\boldsymbol{r}_i} b^\dagger_{\boldsymbol{k},\alpha}, \tag{3.48}$$

the Hamiltonian is rewritten as

$$\begin{aligned}\mathcal{H}_{\rm quad} = \frac{1}{2} \sum_{\boldsymbol{k}} \sum_{\alpha=x,y,z} \Big[&(t\eta_{\boldsymbol{k}} - \mu) \left(b^\dagger_{\boldsymbol{k},\alpha} b_{\boldsymbol{k},\alpha} + b_{\boldsymbol{k},\alpha} b^\dagger_{\boldsymbol{k},\alpha} \right) \\ &+ P\eta_{\boldsymbol{k}} \left(b^\dagger_{\boldsymbol{k},\alpha} b^\dagger_{-\boldsymbol{k},\alpha} + b_{-\boldsymbol{k},\alpha} b_{\boldsymbol{k},\alpha} \right) \Big] + \text{const.}, \end{aligned} \tag{3.49}$$

where $\eta_{\boldsymbol{k}}$ is given as

$$\eta_{\boldsymbol{k}} = 2 \left[\cos k_x + \cos \left(\frac{k_x + \sqrt{3} k_y}{2} \right) + \cos \left(\frac{k_x - \sqrt{3} k_y}{2} \right) \right]. \tag{3.50}$$

Using the Bogoliubov transformation given as

$$\begin{pmatrix} \beta_{\boldsymbol{k},\alpha} \\ \beta^\dagger_{-\boldsymbol{k},\alpha} \end{pmatrix} = \begin{pmatrix} \cosh\theta & \sinh\theta \\ \sinh\theta & \cosh\theta \end{pmatrix} \begin{pmatrix} b_{\boldsymbol{k},\alpha} \\ b^\dagger_{-\boldsymbol{k},\alpha} \end{pmatrix} \tag{3.51}$$

with

$$\tanh 2\theta = \frac{P\eta_{\boldsymbol{k}}}{t\eta_{\boldsymbol{k}} - \mu}, \tag{3.52}$$

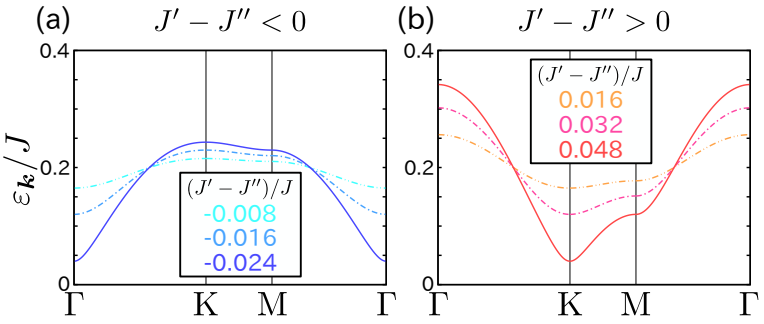

Figure 3.15: Energy bands of the eigenstates of the Hamiltonian (Eq. (3.47)) at $B/J = 0.2$ when (a) $J' - J'' < 0$ and (b) $J' - J'' > 0$. The parameters in the quadratic Hamiltonian, μ, t, and P, whose original forms are given in Eqs. (3.17), (3.18), (3.19), are used at the first-order level. Figures are taken from Ref. [2] (Copyright ©2020, American Physical Society).

the Hamiltonian $\mathcal{H}_{\rm quad}$ is diagonalized as [177]

$$\mathcal{H}_{\rm quad} = \sum_{\boldsymbol{k}} \sum_{\alpha=x,y,z} \varepsilon_{\boldsymbol{k}} \left(\beta^{\dagger}_{\boldsymbol{k},\alpha} \beta_{\boldsymbol{k},\alpha} + \beta_{\boldsymbol{k},\alpha} \beta^{\dagger}_{\boldsymbol{k},\alpha} \right) + \text{const.}, \tag{3.53}$$

where the particle-hole symmetric energy bands, $\varepsilon_{\boldsymbol{k}}$, are given as

$$\varepsilon_{\boldsymbol{k}} = \pm \frac{1}{2} \sqrt{(t\eta_{\boldsymbol{k}} - \mu)^2 - (P\eta_{\boldsymbol{k}})^2}. \tag{3.54}$$

We show in Figs. 3.15(a) and 3.15(b) the energy bands $\varepsilon_{\boldsymbol{k}}/J$ at $B/J = 0.2$ for $J' - J'' < 0$ and $J' - J'' > 0$, respectively. When the bottom of the energy band reaches the zero level, the instability occurs. Then the $\beta_{\boldsymbol{k}}$-bosons of the corresponding wave number condenses and construct a BEC phase. This instability takes place when we increase $J' = -J''$ only up to $|J' - J''|/J \sim 0.05$, which is compatible with the results of the numerical diagonalization that the product state of singlet dimers immediately replaced by the FQ phases along the $J' = -J''$ line. The energy band $\varepsilon_{\boldsymbol{k}}$ takes the minimum values at the Γ-point for $J' - J'' < 0$, while it is minimized at the K-point when $J' - J'' > 0$. The former case corresponds to the uniform FQ ordering of FQ-BEC phase, and the latter well describes the three-sublattice-like configuration of the quadrupolar moments in the FQ-p-BEC phase (see Fig. 3.7(b)).

3.4.2 Classification of "spin-nematic" phases

Conventionally, we identify a standard SN phase in the spin-1 system by the absence of the local sublattice spin ordering and the developments of the quadrupolar ordering. As we mention in Chapter 1, the spin-1 BLBQ model hosts the SN phase when $|\mathcal{J}| \lesssim |\mathcal{B}|$, in which case the magnetic order is suppressed. The tower of states consists of $S_{\rm tot} = 0, 2, 4, \cdots$, suggesting that the bound two-magnon pairs spontaneously break the SU(2) symmetry in the thermodynamic limit.

The condensation of the bound two-magnon in spin-1/2 systems is another series of the spin nematics [51, 68]. The bound two- or multi-magnons can move around, which

is expressed by the quadrupolar order parameter as $\langle b^\dagger_{i,\downarrow} b^\dagger_{j,\downarrow}\rangle = \langle s^-_i s^-_j\rangle = \mathcal{Q}\mathrm{e}^{\mathrm{i}2\theta} \neq 0$ [17]. Near the fully-saturated ferromagnetic phase, the two-magnon pair instability can occur; the adjacent bosons with $\mathcal{S}^z = +1$ and $\mathcal{S}^z = -1$ fluctuate in pair or exchange, and form a quadrupolar moments and consequently the $\mathcal{S}^z = -1$ boson moves in space. This is equivalent to the BEC of spin-2 bosons in cold atoms consisting of $S = 0$ and 2 sectors [178]. For particular models where the $S_{\rm tot} = 1$ sector is excluded from the low-energy manifold, this type of spin nematic phase can be realized without magnetic field, which is identified by the tower of states reflecting the bound multi-bosons like the spin-1 systems [51, 58, 62].

The aforementioned two kinds of n-nematic order is possible only when the spin-1 bosons are bound by the large quantum fluctuations, basically in a strong magnetic field or with the strong ferromagnetic interactions [18].

The other class of the spin nematic phase known so far is the p-type spin nematic phase found in the spin-1/2 systems [16, 66, 67, 81]. The vector-chiral moment $\boldsymbol{p}_i = \boldsymbol{S}_{i_1} \times \boldsymbol{S}_{i_2}$ (Eq. (3.41)), condenses and generates a spin nematic order, with the sublattice magnetic moments suppressed. Then, the vector-chiral order breaks the SU(2) symmetry down to the U(1) symmetry forming a uniaxial rotator, and the tower of states is formed by one state of each $S_{\rm tot}$-sector, which suggests the BEC by a one-magnon instability.

In the one-dimensional and two-dimensional dimer systems, the quadrupolar moment lives on a dimer bond. When we vary the model parameters, we can tune the boson density from zero to one. When the bosons are fully occupied, $\langle n_t\rangle = 1$, the situation is the same as the one of the spin-1 systems, and the SN phase of the spin-1 type appears. When $\langle n_t\rangle < 1$, the quadrupolar ordering of spin-1 bosons, the FQ-BEC phase or F-nematic phase, appears. In the FQ phases, an isolated magnon condenses owing to the hopping and pair-creation/annihilation terms of bosons, and the SU(2) symmetry is broken down to U(1), which is similar to the spinor-BEC in cold atoms [179], and shares the common property with the p-type nematic phase. As the $\mathcal{S} = 1$ dimer always remains nonmagnetic, it could be considered as a sort of "nematic" order in terms of the $\mathcal{S} = 1$ boson. When we separately focus on the upper and lower layers carrying the spin moments in the bilayer lattice, a ferromagnetic sublattice long-range order is realized in each layer, while the overall spin moments in units of a dimer is killed by the quantum flctuations inside the dimers. This kind of ordering is probably a different phase from the interlayer antiferromagnetic and the intralayer ferromagnetic orderings derived by the mean-field analysis, where the large spin moments are present in the spin-1/2 ferromagnetic dimers [87].

We discussed in Sec. 3.3 the FQ-p-BEC phase, where the large vector-chiral correlation and the 120° intralayer magnetic correlation develop, while keeping the dimer unit nonmagnetic. There are two possible scenarios; in a mean-field treatment, these two correlations are incompatible, while our approach fully taking in the quantum many-body effect may provide a new possibility that these two kinds of orders coexist. The other is the absence of the local spin moments, so that the p-type vector-chiral order may be stabilized. Within our present study, the low-energy excited states are not clearly separated

[17] Here, the fully saturated ferromagnetic state is regarded as the vacuum, and the boson operator $b^\dagger_{i,\downarrow}$ creates a magnon with $S^z = -1$. θ is the relative phase between two magnons.

[18] Either the inter-site interactions (mainly in spin-1/2 systems) or the intra-site Hund's couplings (mainly in spin-1 systems) is possible.

into those of the biaxial or uniaxial rotators, namely, whether the SU(2) symmetry is fully broken or broken only down to U(1).

3.4.3 Exchange processes of $\mathcal{S} = 1$ moments

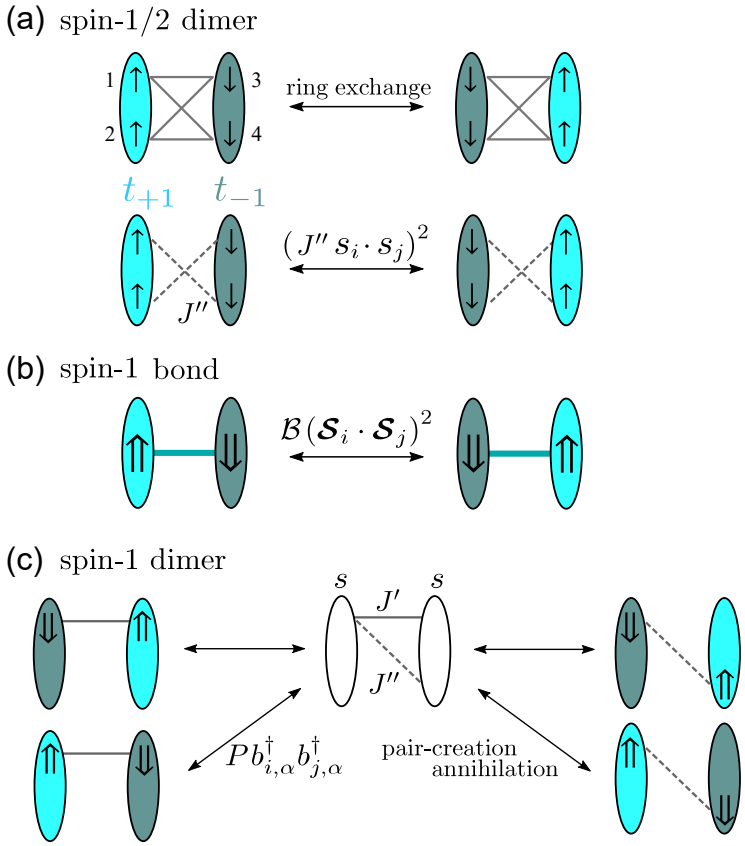

Figure 3.16: Three types of the fluctuations which contribute to the stabilization of the spin nematic phase. The spin-1/2 and spin-1 are denoted by the single and double arrows, respectively. (a) In the spin-1/2 dimer systems, the ring-exchange interactions which changes the spin configurations $(1, 2, 3, 4) \leftrightarrow (2, 3, 4, 1)$ in the upper panel (see Refs. [3, 86]). The interaction $(J'' \boldsymbol{s}_i \cdot \boldsymbol{s}_j)^2$, where $\boldsymbol{s}_i$ is the spin-1/2 operator, appears in the second order perturbation process (see Refs. [87, 180]), and plays a similar role. (b) Fluctuation between two rigid spin-1's, where $\boldsymbol{\mathcal{S}_i}$ is the spin-1 operator, by the biquadratic interaction $(\boldsymbol{\mathcal{S}_i} \cdot \boldsymbol{\mathcal{S}_j})^2$. (c) In the spin-1 dimer system, the pair-creation/annihilation terms (P) (Eq. (3.10)) mainly work, which are generated by the first-order term in J' and J''. Figures are taken from Ref. [2] (Copyright ©2020, American Physical Society).

Previous studies on the spin-1/2 dimer systems showed that the origin of the spin nematic phases in the spin-1/2 dimer systems is the ring-exchange interactions between the neighboring dimers, which permutate the four spin-1/2's along the twisted path, $(1, 2, 3, 4) \to (2, 3, 4, 1)$ [3, 86] (see Fig. 3.16(a)). In the situation, when the two spin-1/2's on a dimer form an $\mathcal{S} = 1$ triplet, the ring-exchange interactions along the twisted path exchanges two spin-1's on the neighboring dimers of $\left(\mathcal{S}_i^z, \mathcal{S}_j^z\right) = (+1, -1)$ with $(-1, +1)$. This exchange process works in the same manner as the biquadratic interactions between

two spin-1's, $\mathcal{B}\left(\boldsymbol{\mathcal{S}}_i \cdot \boldsymbol{\mathcal{S}}_j\right)^2$, and when all of the dimers in the system take the triplet $\mathcal{S} = 1$ states, the system is equivalent to the spin-1 bilinear biquadratic model formed by the triplet.

In the spin-1/2 ferromagnetic dimer model [87], it is demonstrated that the inter-dimer Heisenberg interactions J' and J' ($J_{\parallel}$ and $J_{\times}$ in their notation, respectively) operated twice through the second-order perturbation process play an essential role to generate the spin nematic order. As we show in the schematic picture in Fig. 3.16(a), this second-order process plays a similar role to the ring-exchange interactions, and contributes to the effective biquadratic interactions between triplet dimers [87, 180]. In this case, they need large J' and J'' couplings since the spin nematic order realized there needs to overwhelm the stable ferromagnetic phase.

In our spin-1 dimer system, the pair-creation and annihilation effect (Eq. (3.10)) creates an off-diagonal condensation of two spin-1 pair with $\mathcal{S}^z = +1$ and $\mathcal{S}^z = -1$ through the processes shown in Fig. 3.16(c). When this pair fluctuation is operated twice, the same effect as the biquadratic interaction between spin-1 bosons takes place. The advantageous point of this process is that this effect is a first-order process in the inter-dimer interactions, and will be generated more easily than the biquadratic interaction $\mathcal{B}$ itself or the ring-exchange interactions.

Although in Refs. [87, 180], they did not discuss it in terms of spin-1 bosons, we can also regard the second-order perturbation term in J' and J'' in the spin-1/2 dimer systems that gives the effective biquadratic interactions between triplets as the pair-creation/annihilation process of bosons. Nevertheless, the pair-creation and annihilation effect in our spin-1 dimer system should be stronger than that in the spin-1/2 dimer systems, which is indicated by the construction of triplet state in a spin-1 dimer (Eq. (3.6)), which consists of twice as many terms as the one consisting of two spin-1/2's [19]. This indicates that the entanglement between two $\mathcal{S} = 1$ dimers could be more easily increased. We consider that this should be an origin of various quadrupolar phases in our spin-1 dimer system.

3.5 Possible relevance to Ru-dimer materials

Here, we discuss the possible relevance to the actual dimer compounds $Ba_3MRu_2O_9$ introduced in Sec. 1.6. We expect that the Ru^{5+} ion will carry $S = 1$ for some reasons. The ruthenium ion Ru^{5+} takes $4d^3$ configuration on t_{2g} orbitals with high spin state due to strong Hund's couplings, and in fact the band structure calculation of $M =$ Co indicates that the possibility of the "low-spin" state with $S = 1/2$ proposed in Ref. [181] is excluded [182]. This probably imply that the Ru ion takes $S = 3/2$ moment owing to the $4d^3$ configuration, and indeed there has been an attempt to understand the magnetic susceptibility of $M =$ Ca by $S = 3/2$ model with the biquadratic interaction [183]. Meanwhile, the experimental results suggest that the magnetic moments are suppressed, and take smaller

[19] In a spin-1/2 dimer, the triplet states are given as

$$|t_x\rangle = \frac{\mathrm{i}}{\sqrt{2}}\left(|\uparrow,\uparrow\rangle - |\downarrow,\downarrow\rangle\right),\ |t_y\rangle = \frac{1}{\sqrt{2}}\left(|\uparrow,\uparrow\rangle + |\downarrow,\downarrow\rangle\right),\ |t_z\rangle = -\frac{\mathrm{i}}{\sqrt{2}}\left(|\uparrow,\downarrow\rangle + |\downarrow,\uparrow\rangle\right), \tag{3.55}$$

where $|\uparrow\rangle$ and $|\downarrow\rangle$ are the eigenstates of s^z with $s^z = +1/2$ and $-1/2$, where $\boldsymbol{s}$ is the spin-1/2 operator.

values, for example, 1.0–1.5 $\mu_{\rm B}$ for $M =$ Ni, and 1.16–1.44 $\mu_{\rm B}$ for $M =$ Cu [128, 130]. It is expected that the three-fold degenerate t_{2g} orbitals are split into two-fold degenerate e_g orbitals and an a_{1g} orbital, and the a_{1g} orbitals of Ru^{5+} ions in a dimer strongly hybridize, so that the one singlet is formed in a dimer and reduces the magnetic moment of Ru^{5+} to $S = 1$ effectively. Even if the spin moments of Ru^{5+} are more likely to be $S = 3/2$ than $S = 1$, only the septet states with $S_{\rm tot} = 3$ are added in the highest energy levels, and our treatment in the low-energy manifold holds.

The Heisenberg interactions J, J', and J'' are usually antiferromagnetic, and we can naively consider that the longer inter-dimer distance gives the smaller inter-dimer interactions, J' and J''. In the phase diagram at $B/J = 0.2$, if we make the inter-dimer interactions stronger starting from the center with $J' = J'' = 0$ toward the upper right direction, the ground state of the spin-1 dimer triangular lattice changes from the singlet, the FQ-p-BEC, to the AFM phases. This is consistent with the results in experiments, $(\mathrm{Ca, Sr}) \to (\mathrm{Zn}) \to (\mathrm{Co, Ni, Cu})$. When we assume that the ground state of the $M =$ Zn compound corresponds to the FQ-p-BEC phase, it can be suspected that the absence of the phase transition and the suppression of the magnetic order down to lowest temperature might be compatible with the ambiguous structure of the low-lying states in this phase which cannot be simply ascribed to any type of the symmetry-breaking long-range orderings known so far.

3.6 Summary of this Chapter

In this Chapter, we found a variety of quadrupolar phases formed by triplet dimers in a spin-1 dimer triangular lattice forming a bilayer. When the dimers are decoupled, the dimer takes the singlet state at small B/J and the triplet state at large B/J. We perturbatively took in the inter-dimer Heisenberg exchange interactions, J' and J'' up to the second order, and derived a low-energy effective model described by the hard-core bosons, where the dimer singlet is the vacuum and the dimer triplet is the boson with spin-1. The dominant part of the effective Hamiltonian of bosons is constructed by the hoppings of bosons, t, and the pair-creations and annihilations of bosons, P, in addition to the chemical potential of bosons, μ, and the Heisenberg exchange interactions between spin-1 bosons, $\mathcal{J}$. The dimer bosons are introduced to the system by μ, and the t-term plays a role to form a BEC structure. The ferromagnetic and antiferromagnetic phases are realized owing to the Heisenberg interaction $\mathcal{J}$ with $\mathcal{J} < 0$ and $\mathcal{J} > 0$, respectively. When t and P are large at $J' \sim -J''$, the ferroquadrupolar-BEC (FQ-BEC) and FQ-p-BEC phases appear, where the quadrupolar moments on a dimer condense, which has a similarity to the anisotropic superfluidity in cold atoms [179]. In addition, when $1/3 \lesssim B/J$, we observed the typical spin-1 nematic phase, which is the same as the one found in the spin-1 bilinear-biquadratic models, in a small inter-dimer interaction region, because almost all dimers are occupied by the spin-1 bosons which are exchanged by the pair-fluctuation effect of P. Finally we discussed the possible correspondence to the spin dimer material $Ba_3MRu_2O_9$, where the nontrivial nonmagnetic behavior in $M =$ Zn may correspond to our FQ-p-BEC phase with the 120°-correlation of the spin moments and the p-type vector-chiral correlation.

Chapter 4

Microscopic evaluation of the spin-1 biquadratic interactions by the perturbation calculation

In this Chapter, related to the Chapter 3, we discuss the microscopic origin of the spin-1 biquadratic interaction, which induces the spin nematic orders. By decomposing the two spin-1 into two pairs of electrons with spin-1/2, we perform the perturbation calculation up to the fourth order from the strong coupling limit. We deal with two cases, the four-site–one-orbital system aiming at the spin-1/2 dimer system, and the two-site–two-orbital system which models the degenerate e_g orbital in the transition metal ions. In the former case, we find that only the ring-exchange process at the fourth-order perturbation along the twisted exchange path contributes to the biquadratic interaction, and it can give as large a biquadratic interaction as the Heisenberg interaction. By contrast, in the latter case, we find the biquadratic interaction is small.

4.1 Overview

In the spin-1 systems, a main source of the spin nematic order is the spin-1 biquadratic interaction [19, 33]. When the biquadratic interaction becomes large and breaks the magnetic order, the ferroquadrupolar or antiferroquadrupolar spin nematic order is realized. Here we microscopically evaluate the biquadratic interaction by splitting the spin-1 into two electrons with spin-1/2. The biquadratic interaction is a product of four spin operators, and naively it is derived from the fourth-order perturbation calculation from the strong coupling limit in the electronic system.

We perform the perturbation calculations up to the fourth-order for the two cases shown in Fig. 4.1, the four-site–one-orbital system in Sec. 4.2 and the two-site–two-orbital system in Sec. 4.3 [1]. We discuss the difference between the two cases and other possible schemes to have a larger biquadratic interaction in Sec. 4.4. Sec. 4.5 is the summary of this Chapter.

[1] We note that a part of the contents in Sec. 4.2 is briefly mentioned in Ref. [184].

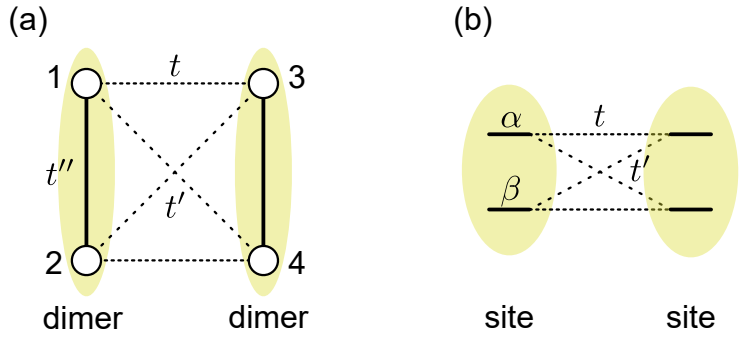

Figure 4.1: Schematic pictures of the lattice geometries that we deal with. (a) Four-site–one-orbital system. The site-1 and 2 on the left and the site-3 and 4 on the right respectively form the dimers. (b) Two-site–two-orbital system. Each site has two degenerate orbitals α and β. Figure is drawn referring to Ref. [3].

4.2 Four-site–one-orbital system

4.2.1 Setup and fourth-order perturbation calculation

In the first case, we consider the single-orbital Hubbard model on the four-site system with half-filling,

$$\mathcal{H} = -\sum_{\langle i,j\rangle,\sigma} t_{ij}\left(c^{\dagger}_{i,\sigma}c_{j,\sigma} + \text{h.c.}\right) + U\sum_{i} n_{i,\uparrow}n_{i,\downarrow}, \tag{4.1}$$

where $c^{\dagger}_{i,\sigma}/c_{i,\sigma}$ represents the creation/annihilation operator of an electron with spin-σ ($\sigma =\uparrow,\downarrow$) on site-$i$, and $n_{i\sigma} = c^{\dagger}_{i,\sigma}c_{i,\sigma}$ denotes the number operator. The transfer integrals t_{ij} in the first term are set as $t_{13} = t_{24} = t$, $t_{14} = t_{23} = t'$, and $t_{12} = t_{34} = t''$ as shown in Fig. 4.1(a). The on-site Coulomb repulsion is denoted as U.

In the strong coupling limit $U \to +\infty$, each site has one electron, and the low-energy manifold of states are described by four localized spin-1/2's. From this limit, we introduce perturbatively the effect of electron hoppings, t_{ij}. Performing the perturbation calculation up to the fourth order in terms of t_{ij}/U by the Schrieffer–Wolff canonical transformation [185, 186], we obtain the effective Hamiltonian of the localized spin-1/2's, $\mathcal{H}_{\text{eff}}$. The effective Hamiltonian is divided into two terms by the order of the perturbation as

$$\mathcal{H}_{\text{eff}} = \mathcal{H}^{(2)}_{\text{eff}} + \mathcal{H}^{(4)}_{\text{eff}}, \tag{4.2}$$

where $\mathcal{H}^{(n)}$ is the term from the n-th order perturbation. We note that the third-order perturbation terms cancel out and do not contribute to the effective Hamiltonian.

As is well known, the second-order perturbation processes give the Heisenberg inter-

[3]When one sees Fig. 2(a) in Ref. [3], one may consider that two of three (2b4s) processes are the 'disconnected' processes, but all three (2b4s) processes should be regarded as the 'disconnected' processes.

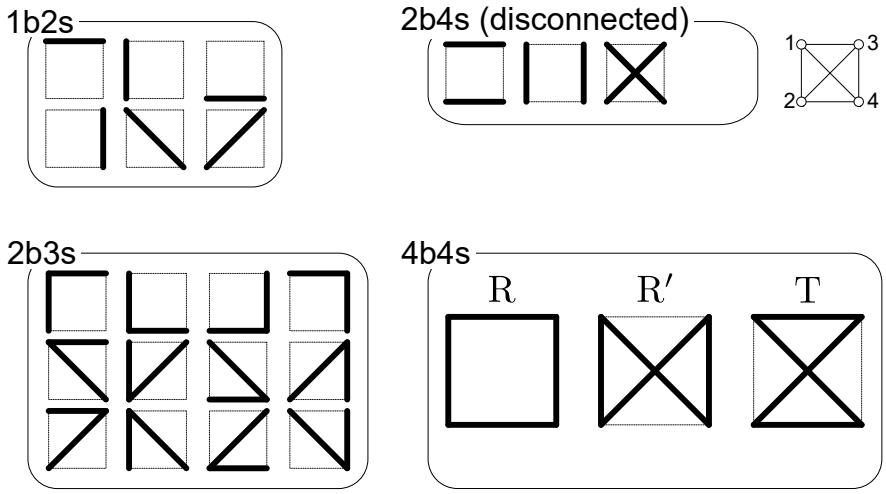

Figure 4.2: Perturbation processes at the fourth order classified by the numbers of bonds and sites involved in the processes. Bold lines denote the bonds where the electrons hop. Figure is drawn referring to Ref. [3] [3].

action,

$$\mathcal{H}_{\text{eff}}^{(2)} = \sum_{\langle i,j \rangle} J_{ij} \boldsymbol{s}_i \cdot \boldsymbol{s}_j, \qquad J_{ij} = \frac{4\left(t_{ij}\right)^2}{U}. \tag{4.3}$$

The effective Hamiltonian derived at the fourth-order, $\mathcal{H}_{\text{eff}}^{(4)}$, can be categorized into four kinds as follows;

$$\mathcal{H}_{\text{eff}}^{(4)} = \mathcal{H}_{\text{eff}}^{(1\text{b}2\text{s})} + \mathcal{H}_{\text{eff}}^{(2\text{b}3\text{s})} + \mathcal{H}_{\text{eff}}^{(2\text{b}4\text{s})} + \mathcal{H}_{\text{eff}}^{(4\text{b}4\text{s})}. \tag{4.4}$$

Here, we classify the perturbation processes at the fourth-order by the numbers of bonds and sites contributing to the processes, namely, $\mathcal{H}_{\text{eff}}^{(m\text{b}n\text{s})}$ consists of the perturbation processes where the m-bonds and n-sites are involved. For example, in the process (1b2s), one bond (1b) and the two sites at the edges of the bond (2s) contribute to the perturbation process. The schematic pictures of these four kinds of the fourth-order perturbation processes are shown in Fig. 4.2. The (4b4s) process, where four bonds and all sites are involved in the fourth-order processes, gives the effective interactions including the four-body interactions called the ring-exchange interactions, which are expressed as

$$\begin{aligned}\mathcal{H}_{\text{eff}}^{(4\text{b}4\text{s})} = &-\frac{1}{5} K_{\mathcal{C}} \sum_{(i<j)\in a,b,c,d} \boldsymbol{s}_i \cdot \boldsymbol{s}_j \\ &+ 4K_{\mathcal{C}} \sum_{[a-b-c-d]} \left[\left(\boldsymbol{s}_a \cdot \boldsymbol{s}_b\right)\left(\boldsymbol{s}_c \cdot \boldsymbol{s}_d\right) + \left(\boldsymbol{s}_a \cdot \boldsymbol{s}_d\right)\left(\boldsymbol{s}_b \cdot \boldsymbol{s}_c\right) - \left(\boldsymbol{s}_a \cdot \boldsymbol{s}_c\right)\left(\boldsymbol{s}_b \cdot \boldsymbol{s}_d\right) \right],\end{aligned} \tag{4.5}$$

$$K_{\mathcal{C}} = \frac{20 t_{ab} t_{bc} t_{cd} t_{da}}{U^3}. \tag{4.6}$$

Here, $\mathcal{C}$ is the closed loop formed by four-sites as a–b–c–d–a. The similar fourth-order per-

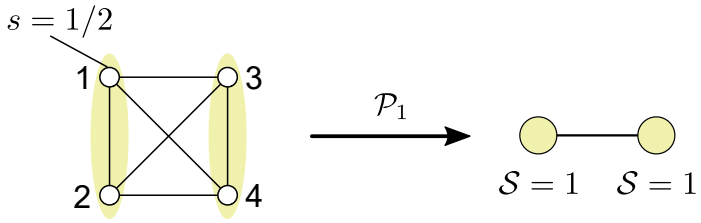

Figure 4.3: Schematic picture of the projection of the spin-1/2 system onto the spin-1 system by pairing two spin-1/2's.

turbation calculations have been performed in several previous studies [187–190], and also in Ref. [191]. The ring-exchange interactions from the (4b4s) processes can be classified into three kinds by the choice of $\mathcal{C}$, which are depicted in Fig. 4.2. When $(a, b, c, d) = (1, 2, 4, 3)$, the standard ring-exchange process appears, which we denote as R here. When we choose $(a, b, c, d) = (1, 2, 3, 4)$, the process denoted as R$'$ is given, and the case of $(a, b, c, d) = (1, 3, 2, 4)$ is denoted as T [4].

4.2.2 Projection onto the triplet subspace

We next transform this effective Hamiltonian $\mathcal{H}_{\rm eff}$ which is described by the spin-1/2 operators into the one expressed in terms of the spin-1 operators. This transformation can be achieved by the projection of the effective Hamiltonian $\mathcal{H}_{\rm eff}$ onto the space spanned by the triplet states consisting of neighboring two spin-1/2's as

$$\tilde{\mathcal{H}}_{\rm eff} = \mathcal{P}_1 \mathcal{H}_{\rm eff} \mathcal{P}_1, \tag{4.7}$$

where $\mathcal{P}_1$ is the projection operator onto the triplet states. Then, there appear two kinds of the interactions between two spin-1's, the Heisenberg (bilinear) interaction, J, and the biquadratic interaction, B. These interactions consist of the contributions from the terms of the effective spin-1/2 Hamiltonian, $\mathcal{H}_{\rm eff}^{(2)}$ and $\mathcal{H}_{\rm eff}^{(nbms)}$ as

$$J = J_2 + \sum_{n,m} J_4^{(nbms)}, \qquad B = \sum_{n,m} B_4^{(nbms)}. \tag{4.8}$$

Here, the contribution from $\mathcal{H}_{\rm eff}^{(2)}$ is denoted as J_2, and that from $\mathcal{H}_{\rm eff}^{(nbms)}$ is expressed as $J_4^{(nbms)}$ or $B_4^{(nbms)}$. For the Heisenberg interaction, J, each contribution is expressed as

$$J_2 = \frac{2\left(t^2 + (t')^2\right)}{U}, \tag{4.9}$$

$$J_4^{(1b2s+2b3s)} = \frac{-8t^4 - 8\,(t')^4 + 4t^2\,(t'')^2 + 4\,(t')^2\,(t'')^2}{U^3}, \tag{4.10}$$

$$J_4^{(\rm R)} = -\frac{K_{\rm R}}{5} = -\frac{4t^2\,(t'')^2}{U^3}, \tag{4.11}$$

[4] The coupling constants described as $K_{\rm R}$, $K_{\rm R'}$, and $K_{\rm T}$ correspond to h_1, h_2, and h_3 in Ref. [190], respectively.

$$J_4^{(\mathrm{R}')} = -\frac{K_{\mathrm{R}'}}{5} = -\frac{4\left(t'\right)^2\left(t''\right)^2}{U^3}, \tag{4.12}$$

$$J_4^{(\mathrm{T})} = \frac{4K_{\mathrm{T}}}{5} = \frac{16t^2\left(t'\right)^2}{U^3}. \tag{4.13}$$

Note that the (4b4s) processes are further divided into R, R′, and T. The biquadratic interaction appears only from the process-T, which is given as

$$B_4^{(\mathrm{T})} = 2K_{\mathrm{T}} = \frac{40t^2\left(t'\right)^2}{U^3}. \tag{4.14}$$

We can see the reason why only the T-process contributes to the biquadratic interaction, and R- and R′-processes do not, in terms of the process of spin flips. The matrix representations of the Heisenberg and the biquadratic interactions in the $S^z_{\mathrm{tot}} = 0$ subspace are given as

$$\boldsymbol{\mathcal{S}}_i \cdot \boldsymbol{\mathcal{S}}_j = \begin{pmatrix} |+1,-1\rangle & |0,0\rangle & |-1,+1\rangle \end{pmatrix} \begin{pmatrix} -1 & 1 & 0 \\ 1 & 0 & 1 \\ 0 & 1 & -1 \end{pmatrix} \begin{pmatrix} \langle +1,-1| \\ \langle 0,0| \\ \langle -1,+1| \end{pmatrix}, \tag{4.15}$$

$$\left(\boldsymbol{\mathcal{S}}_i \cdot \boldsymbol{\mathcal{S}}_j\right)^2 = \begin{pmatrix} |+1,-1\rangle & |0,0\rangle & |-1,+1\rangle \end{pmatrix} \begin{pmatrix} 2 & -1 & 1 \\ -1 & 2 & -1 \\ 1 & -1 & 2 \end{pmatrix} \begin{pmatrix} \langle +1,-1| \\ \langle 0,0| \\ \langle -1,+1| \end{pmatrix}, \tag{4.16}$$

respectively. Here, $|\mathcal{S}_1^z, \mathcal{S}_2^z\rangle = |+1,-1\rangle$, $|0,0\rangle$, and $|-1,+1\rangle$, where $|\mathcal{S}_1^z, \mathcal{S}_2^z\rangle$ is the two spin-1 state with $\mathcal{S}_1^z$ and $\mathcal{S}_2^z$. are chosen as the three basis states. Then, one can see that

$$\langle +1,-1 \,|\, \boldsymbol{\mathcal{S}}_i \cdot \boldsymbol{\mathcal{S}}_j \,|\, -1,+1\rangle = \langle -1,+1 \,|\, \boldsymbol{\mathcal{S}}_i \cdot \boldsymbol{\mathcal{S}}_j \,|\, +1,-1\rangle = 0, \tag{4.17}$$

$$\left\langle +1,-1 \middle|\, \left(\boldsymbol{\mathcal{S}}_i \cdot \boldsymbol{\mathcal{S}}_j\right)^2 \middle|\, -1,+1 \right\rangle = \left\langle -1,+1 \middle|\, \left(\boldsymbol{\mathcal{S}}_i \cdot \boldsymbol{\mathcal{S}}_j\right)^2 \middle|\, +1,-1 \right\rangle = 1 \neq 0, \tag{4.18}$$

hold. This means that the biquadratic interaction exchanges $|+1,-1\rangle$ and $|-1,+1\rangle$, whereas the Heisenberg interaction cannot. Here we go back to the perturbation processes by decomposing two spin-1's with $\mathcal{S}^z = +1$ and $\mathcal{S}^z = -1$ into spin-1/2's as $|+1\rangle = |\uparrow,\uparrow\rangle$ and $|-1\rangle = |\downarrow,\downarrow\rangle$, where $|\uparrow\rangle$ and $|\downarrow\rangle$ are the spin-1/2 state with $s^z = +1/2$ and $-1/2$, respectively. In Fig. 4.4(a), we show an example of the process-T, where two spin-1's with $\mathcal{S}^z = +1$ and $\mathcal{S}^z = -1$ are exchanged through this process, which means that the process-T can contribute to the biquadratic interaction between spin-1's. By contrast, the process-R and R′ only change the $|\mathcal{S}_1^z, \mathcal{S}_2^z\rangle = |+1,-1\rangle$ state into the $|0,0\rangle$ state as shown in Fig. 4.4(b), and cannot generate the spin-1 biquadratic interaction. If one wants to exchange $|+1\rangle$ and $|-1\rangle$ through the perturbation process, one needs to move two electrons with up spin on the site-1 and 2 on the left side to the site-3 and 4 on the right side, and those with down spin on the site-3 and 4 to the site-1 and 2. In process-T, electrons hop only between the left and right sides and do not hop between the two sites on either left or right. In contrast, electrons hop between two-sites on left/right sides in process-R and R′, which disturbs the exchanges of $|+1\rangle$ and $|-1\rangle$. One might consider that the (2b4s) processes shown in Fig. 4.4(c) can also exchange $|+1\rangle$ and $|-1\rangle$ and contribute to the biquadratic interactions. However, the (2b4s) processes consist of two independent pro-

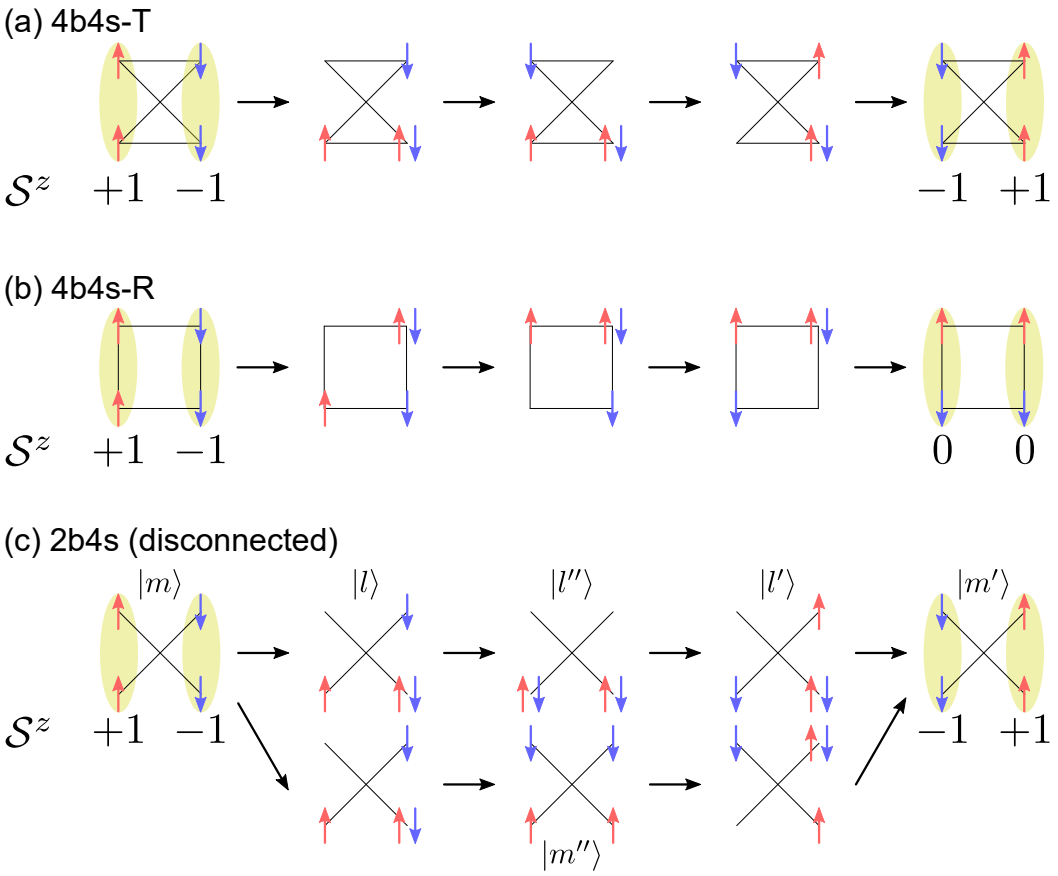

Figure 4.4: (a) An example of the electron hoppings in the (4b4s)-T process that exchanges $\mathcal{S}^z = +1$ and $\mathcal{S}^z = -1$ spin-1's, which contributes to the biquadratic interaction between two spin-1's. (b) An example of the electron hoppings in the (4b4s)-R process which only transforms $(\mathcal{S}_1^z, \mathcal{S}_2^z) = (+1, -1)$ into $(0, 0)$, not reaching $(-1, +1)$. (c) An example of the electron hoppings in the disconnected (2b4s) process which exchanges $\mathcal{S}^z = +1$ and $\mathcal{S}^z = -1$ spins. However, the two kinds of the processes shown above and below cancels out with each other and do not generate the biquadratic interaction when $U' = 0$. Figures (a) and (c) are drawn on the basis of Ref. [3].

cesses at the second order, which we express as "disconnected processes", and they cancel out overall. This cancellation is reasonable, since if it does not occur, one could create numbers of interactions between two pairs of electron spins chosen arbitrarily no matter how far apart they were. We show the t/U dependence of the Heisenberg interaction J and the biquadratic interaction B, and B/J in Fig. 4.5(a), which indicates that the values of B and J become the same order at $U/t \lesssim 5$, which is not too unrealistic.

We note that the projection given in Eq. (4.7) is equivalent to leaving the interactions only between spin-1 bosons in the spin-1 hard-core boson description of the spin-1/2 dimer systems [84–86]. The spin-1 hard-core boson Hamiltonian transformed from the spin-1/2 dimer Hamiltonian is given as

$$\mathcal{H} = -\mu \sum_{i=1}^{N} n_i + t \sum_{\langle i,j \rangle} \sum_{\alpha=x,y,z} \left(b_{i,\alpha}^\dagger b_{j,\alpha} + \text{h.c.} \right) + P \sum_{\langle i,j \rangle} \sum_{\alpha=x,y,z} \left(b_{i,\alpha}^\dagger b_{j,\alpha}^\dagger + \text{h.c.} \right) + V \sum_{\langle i,j \rangle} n_i n_j$$

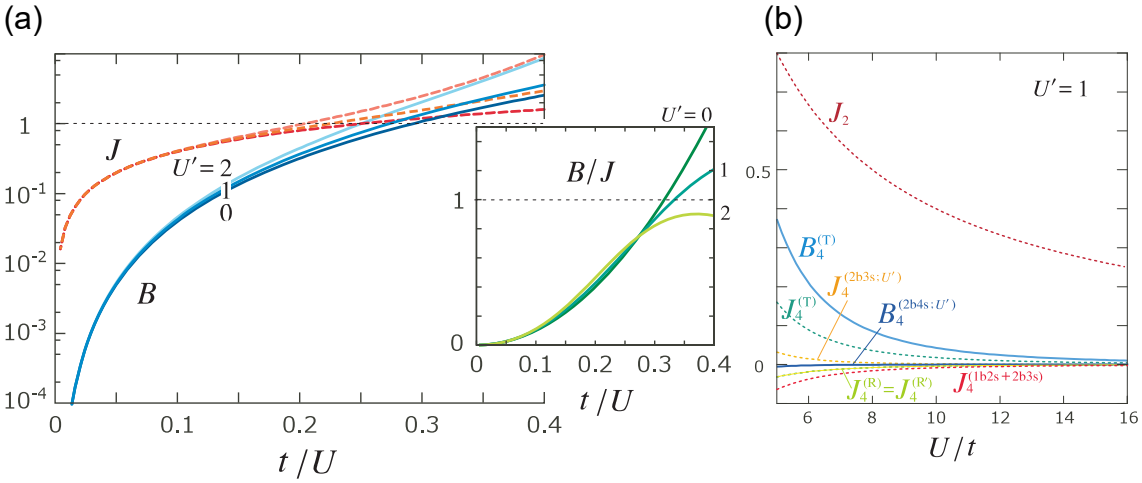

Figure 4.5: (a) The Heisenberg interaction J and the biquadratic interactions B as a function of t/U (Eq. (4.8)) at $U' = 0, 1, 2$. The parameters are set as $t = t' = t'' = 1$. (b) The contribution to J and B from various types of the perturbation processes as a function of U/t. Figures are taken from Ref. [3] (©2018 The Physical Society of Japan (J. Phys. Soc. Jpn. **87**, 023702.)).

$$+\sum_{\langle i,j\rangle}\left[J\boldsymbol{\mathcal{S}}_i\cdot\boldsymbol{\mathcal{S}}_j+B\left(\boldsymbol{\mathcal{S}}_i\cdot\boldsymbol{\mathcal{S}}_j\right)^2\right]n_in_j, \tag{4.19}$$

and we focus only on the last term [5]. The other terms are included in either of $\mathcal{P}_1\mathcal{H}_{\rm eff}\left(1-\mathcal{P}_1\right)$, $\left(1-\mathcal{P}_1\right)\mathcal{H}_{\rm eff}\mathcal{P}_1$, and $\left(1-\mathcal{P}_1\right)\mathcal{H}_{\rm eff}\left(1-\mathcal{P}_1\right)$.

4.2.3 An extension: intradimer Coulomb interaction

We consider a naive extension of this four-site–one-orbital case. We add to the Hubbard Hamiltonian the intra-dimer Coulomb interaction given as

$$\mathcal{H}_{\rm I}=U'\left(n_1n_2+n_3n_4\right). \tag{4.20}$$

Then, two disconnected paths in the (2b4s) process get connected, and the biquadratic interactions from (2b4s) are generated as

$$B_4^{(\mathrm{2b4s};U')}=\frac{4\left(t^4+\left(t'\right)^4\right)}{U^2}\left(\frac{2}{U}-\frac{1}{U-U'}-\frac{1}{U+U'}\right). \tag{4.21}$$

Also, some terms already appearing when $U'=0$ are modified by introducing the finite-U' as

$$J_4^{(\mathrm{T})}=\frac{16t^2\left(t'\right)^2}{U^2\left(U-U'\right)}, \tag{4.22}$$

[5] To be more precise, the V term is also left after the projection, but this term does not contribute to the magnetic interaction. Also, the μ term is generated from the difference of the energy between the singlet and triplet states, which appears using both of $\mathcal{P}_1\mathcal{H}_{\rm eff}\mathcal{P}_1$ and $\left(1-\mathcal{P}_1\right)\mathcal{H}_{\rm eff}\left(1-\mathcal{P}_1\right)$.

$$B_4^{(\mathrm{T})} = t^2 \left(t'\right)^2 \left[\frac{32}{U^2\left(U-U'\right)} + \frac{8}{U^2\left(U+U'\right)}\right], \tag{4.23}$$

$$J_4^{(\mathrm{2b3s};U')} = 16t^2 \left(t'\right)^2 \left[-\frac{1}{U^3} + \frac{1}{U^2\left(U-U'\right)}\right]. \tag{4.24}$$

The evaluation of J and B for the case of $U' \neq 0$ are also shown in Fig. 4.5(a), and the contribution from each perturbation process to J and B at $U' = 1$ is shown in Fig. 4.5(b). When $U' \neq 0$ is introduced, the value of B/J is almost unchanged at large U region, while it is slightly suppressed at smaller U.

4.3 Two-site–two-orbital system

4.3.1 Setup

We consider the two-orbital Hubbard Hamiltonian also known as the Kanamori Hamiltonian [192, 193] with half-filling on two-site system as shown in Fig. 4.1(b),

$$\begin{aligned}\mathcal{H} = &-\sum_{\langle i,j\rangle}\sum_{\mu,\nu=\alpha,\beta} t_{ij}^{\mu\nu}\left(c_{i,\mu,\sigma}^\dagger c_{j,\nu,\sigma} + \mathrm{h.c.}\right) + U\sum_i \sum_{\mu=\alpha,\beta} n_{i,\mu,\uparrow}n_{i,\mu,\downarrow} \\ &+ U'\sum_i \left(n_{i,\alpha,\uparrow}n_{i,\beta,\downarrow} + n_{i,\alpha,\downarrow}n_{i,\beta,\uparrow}\right) + \sum_i\sum_\sigma \left(U' - J_H\right) n_{i,\alpha,\sigma}n_{i,\beta,\sigma} \\ &+ \sum_i J_H\left(c_{i,\alpha,\uparrow}^\dagger c_{i,\beta,\uparrow} c_{i,\beta,\downarrow}^\dagger c_{i,\alpha,\downarrow} + c_{i,\alpha,\downarrow}^\dagger c_{i,\beta,\downarrow} c_{i,\beta,\uparrow}^\dagger c_{i,\alpha,\uparrow}\right) \\ &+ \sum_i J_p\left(c_{i,\alpha,\uparrow}^\dagger c_{i,\beta,\uparrow} c_{i,\alpha,\downarrow}^\dagger c_{i,\beta,\downarrow} + c_{i,\beta,\downarrow}^\dagger c_{i,\alpha,\downarrow} c_{i,\beta,\uparrow}^\dagger c_{i,\alpha,\uparrow}\right).\end{aligned} \tag{4.25}$$

Here, $c_{i,\mu,\sigma}^\dagger$ ($c_{i,\mu,\sigma}$) is the creation (annihilation) operator of an electron with spin-σ on μ-orbital ($\mu = \alpha, \beta$) of site-i, and $n_{i,\mu,\sigma} = c_{i,\mu,\sigma}^\dagger c_{i,\mu,\sigma}$ is the number operator. The transfer integral between the μ-orbital of site-i and the ν-orbital of site-j is described as $t_{ij}^{\mu\nu}$. Here, $t_{12}^{\alpha\alpha} = t_{12}^{\beta\beta} = t$ and $t_{12}^{\alpha\beta} = t_{12}^{\beta\alpha} = t'$. The two degenerate orbitals in each site, α and β, are orthogonal [6], and the t''-path in Sec. 4.2 disappears. When two electrons occupy the same orbital on one site, they feel the intra-orbital Coulomb interaction, U. Two electrons on the different orbitals on the same site gains the energy of the inter-orbital Coulomb interaction U. In each site, there is the Hund's coupling, J_H, which favors the formation of the triplet states by two electron spins on the different orbitals, and the pair-hopping effect, J_p. When the crystal has the rotational symmetry, the relations given as $U = U' + 2J_H$ and $J_H = J_p$ hold [194].

4.3.2 Fourth-order perturbation calculation

Similarly to Sec. 4.2, we perform the fourth-order perturbation calculation from the strong coupling limit of $t_{ij}^{\mu\nu} = 0$. However, the situation becomes more complicated than that in Sec. 4.2. In the case of the spin-1/2 dimer, the low-energy manifold of states only consists of the states where each site (orbital) is occupied by one electron. By contrast,

[6] Even when they are not orthogonal, we can take the linear combinations of the two orbitals such that they become orthogonal.

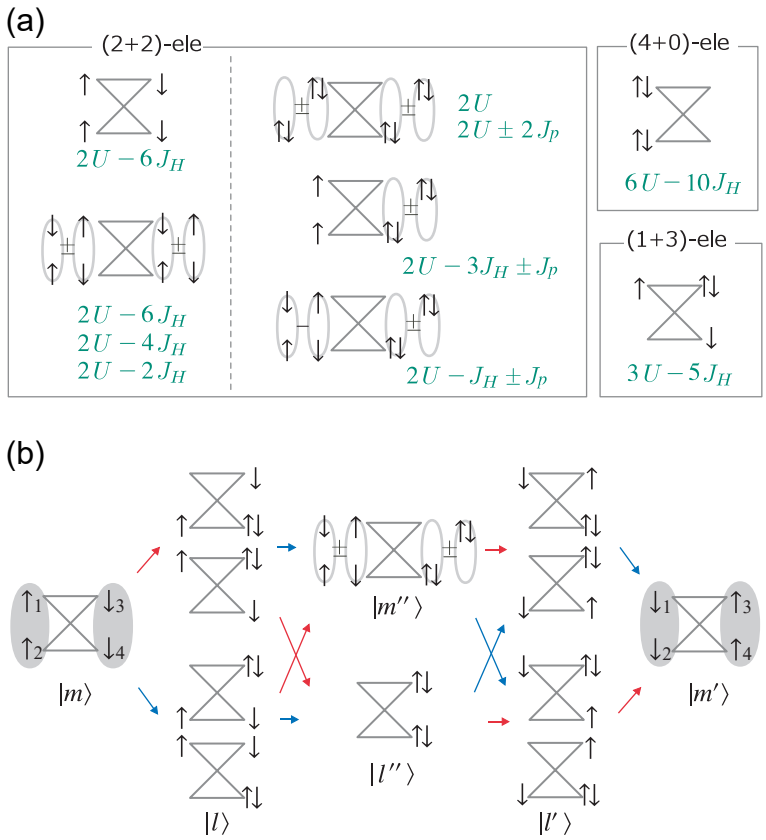

Figure 4.6: (a) Energy eigenvalues and eigenstates categorized by the number of electrons in each site. The low-energy states $\{|m\rangle\}$ consist of the $(2+2)$-electron states, and the $(4+0)$- and $(1+3)$-electron states are the excited states $\{|l\rangle\}$. (b) An example of the perturbation process of (4b4s)-T (see Fig. 4.4(a)). Owing to the Hund's coupling, several states hybridize through the perturbation process. Figures are taken from Ref. [3] (©2018 The Physical Society of Japan (J. Phys. Soc. Jpn. **87**, 023702.)).

in the present case, the states where two electrons occupy the same orbital in both sites such as $|i,j\rangle = |\uparrow_\alpha\downarrow_\alpha,\uparrow_\beta\downarrow_\beta\rangle$ should also be regarded as the low-energy states, because the intra-orbital Coulomb interaction U and the inter-orbital Coulomb interaction U' are different by $2J_H$, which are usually much smaller than U and U' [7]. From this perspective, we denote the states where n_i and n_j electrons occupy the site-i and j respectively as "(n_i+n_j)-electron state". All of the states are categorized into either of the $(2+2)$-, $(3+1)$-, $(1+3)$-, $(4+0)$-, and $(0+4)$-electron states. The $(2+2)$-electron states are the low-energy states, and the other states are the excited states. We show the classification of the (n_i+n_j)-electron states with their energies in Fig. 4.6(a). As the J_H and J_p terms hybridize the s^z-basis states, some of the states are described by the linear combinations of the multiple s^z-basis states. In the hybridization by J_H and J_p, the spins effectively flip and hop inside the sites, which generates the additional paths to the perturbation processes of the electron hoppings between two sites as shown in Fig. 4.6(b).

After performing the perturbation calculation up to the fourth order and obtaining the effective Hamiltonian, $\mathcal{H}_{\text{eff}}$, we project $\mathcal{H}_{\text{eff}}$ onto the subspace spanned by the two-site states where both sites take the triplet states as $\tilde{\mathcal{H}}_{\text{eff}} = \mathcal{P}_1\mathcal{H}_{\text{eff}}\mathcal{P}_1$ in a similar manner to the case of two spin-1/2 dimers. Then, the Heisenberg and biquadratic interactions J and B are obtained. The contribution to the spin-1 Heisenberg interaction appears at the second order, which is given as

$$J_2 = \frac{2\left(t^2+(t')^2\right)}{U+J_H}. \tag{4.26}$$

The fourth-order perturbation terms generate the Heisenberg and biquadratic interactions. The contribution of each path to the Heisenberg interaction is given as

$$J_4^{(\mathrm{T})} = t^2\left(t'\right)^2\left[-\frac{12}{\left(U+J_H\right)^2\left(U-2J_H-J_p\right)} - \frac{4}{\left(U-2J_H-J_p\right)\left(U+J_H\right)}\right], \tag{4.27}$$

$$J_4^{(\mathrm{2b4s})} = \frac{t^4+(t')^4}{2}\left[-\frac{8}{\left(U+J_H\right)^3} + \frac{6}{\left(U+J_H\right)^2\left(U-J_H\right)} + \frac{2}{\left(U+J_H\right)\left(U-J_H\right)^2}\right], \tag{4.28}$$

$$J_4^{(\mathrm{1b2s})} = \frac{t^4+(t')^4}{2}\left[-\frac{8}{\left(U+J_H\right)^3} - \frac{6}{\left(U+J_H\right)^2\left(U-J_H\right)} - \frac{2}{\left(U+J_H\right)\left(U-J_H\right)^2}\right], \tag{4.29}$$

$$J_4^{(\mathrm{2b3s})} = t^2\left(t'\right)^2\left[-\frac{16}{\left(U+J_H\right)^3} - \frac{12}{\left(U+J_H\right)^2\left(U-2J_H-J_p\right)} - \frac{4}{\left(U+J_H\right)\left(U-2J_H-J_p\right)^2}\right], \tag{4.30}$$

In contrast to the spin-1/2 dimer system, the biquadratic interaction is generated from

[7] The perturbation calculation regarding these states where two electrons feel the intra-orbital Coulomb interaction in each site as the excited states was performed in Ref. [195].

the several paths in this case, and the contributions are given as

$$B_4^{(\mathrm{T})} = t^2 \left(t'\right)^2 \left[-\frac{12}{(U+J_H)^2 (U-4J_H-J_p)} - \frac{4}{(U-4J_H-J_p)^2 (U+J_H)} + \frac{4}{(U+J_H)^2 (U-J_H)} - \frac{12}{(U+J_H)^2 (U-2J_H-J_p)} - \frac{4}{(U-2J_H-J_p)^2 (U+J_H)} \right], \tag{4.31}$$

$$B_4^{(\mathrm{2b4s})} = \frac{t^4+(t')^4}{2} \left[\frac{4}{(U+J_H)^3} + \frac{6}{(U+J_H)^2 (U-5J_H+2J_p)} + \frac{6}{(U+J_H)^2 (U-5J_H-2J_p)} + \frac{2}{(U+J_H)(U-5J_H+2J_p)^2} + \frac{2}{(U+J_H)(U-5J_H-2J_p)^2} + \frac{2}{(U+J_H)^2 (U-J_H)} + \frac{2}{(U+J_H)(U-J_H)^2} + \frac{3}{(U+J_H)^2 (U-3J_H)} + \frac{1}{(U+J_H)(U-3J_H)^2} \right], \tag{4.32}$$

$$B_4^{(\mathrm{1b2s})} = \frac{t^4+(t')^4}{2} \left[\frac{4}{(U+J_H)^3} - \frac{6}{(U+J_H)^2 (U-J_H)} - \frac{2}{(U+J_H)(U-J_H)^2} + \frac{3}{(U+J_H)^2 (U-3J_H)} + \frac{1}{(U+J_H)(U-3J_H)^2} \right], \tag{4.33}$$

$$B_4^{(\mathrm{2b3s})} = t^2 \left(t'\right)^2 \left[\frac{8}{(U+J_H)^3} - \frac{6}{(U+J_H)^2 (U-3J_H)} - \frac{2}{(U+J_H)(U-3J_H)^2} - \frac{12}{(U+J_H)^2 (U-2J_H-J_P)} - \frac{4}{(U+J_H)(U-2J_H-J_p)^2} + \frac{12}{(U+J_H)^2 (U-4J_H-J_p)} + \frac{4}{(U+J_H)(U-4J_H-J_p)^2} \right]. \tag{4.34}$$

We show in Fig. 4.7(a) the J_H/t dependence of J and B. We can confirm that the contribution to the Heisenberg interaction from the fourth-order perturbation term, J_4, is ferromagnetic and partially cancels the antiferromagnetic contribution of the second-order term, J_2. The contribution to the Heisenberg interaction from each term is estimated in Fig. 4.7(b). For the biquadratic interaction, the contribution mainly comes from two paths, (2b4s) and (4b4s)-T as shown in Fig. 4.7(b). The former gives the positive biquadratic coupling, and the latter gives the negative one. The coupling constant B is positive on a whole, whose value becomes small because of the cancellation of the contributions from (2b4s) and (4b4s)-T. As a result, the value of B/J becomes smaller in contrast to the case of the spin-1/2 dimers. We note that even when we take the $J_H \to 0$ limit in this case, the result does not match the one in Sec. 4.2 with $U' \to U$. This is because only the present case properly deals with low-energy manifold in the $U' \sim U$ region by constructing the low-energy states by all of the $(2+2)$-electron states.

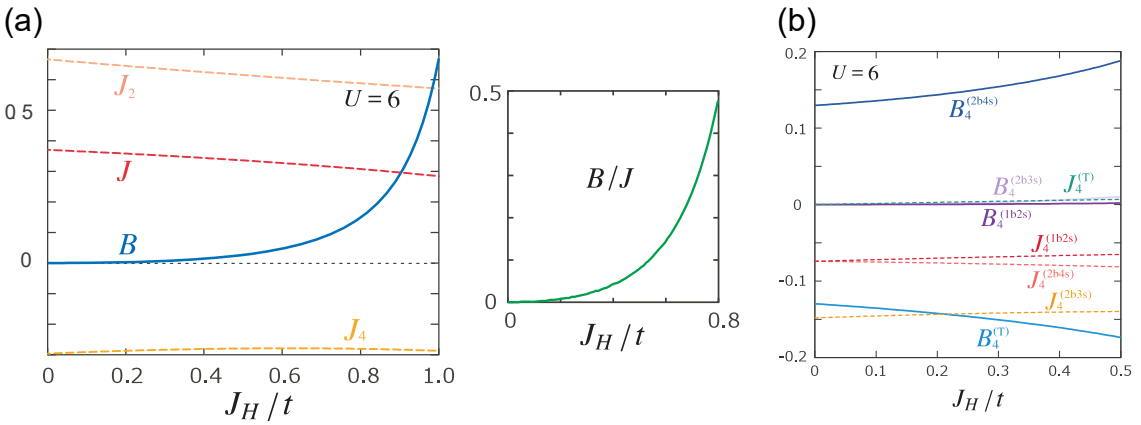

Figure 4.7: (a) The evaluation of the Heisenberg and biquadratic interactions, J and B. The parameters are set as $t = t' = 1$, $J_p = 0$, and $U = 6$. (b) The contribution to the Heisenberg and biquadratic interactions from each process. Figures are taken from Ref. [3] (©2018 The Physical Society of Japan (J. Phys. Soc. Jpn. **87**, 023702.)).

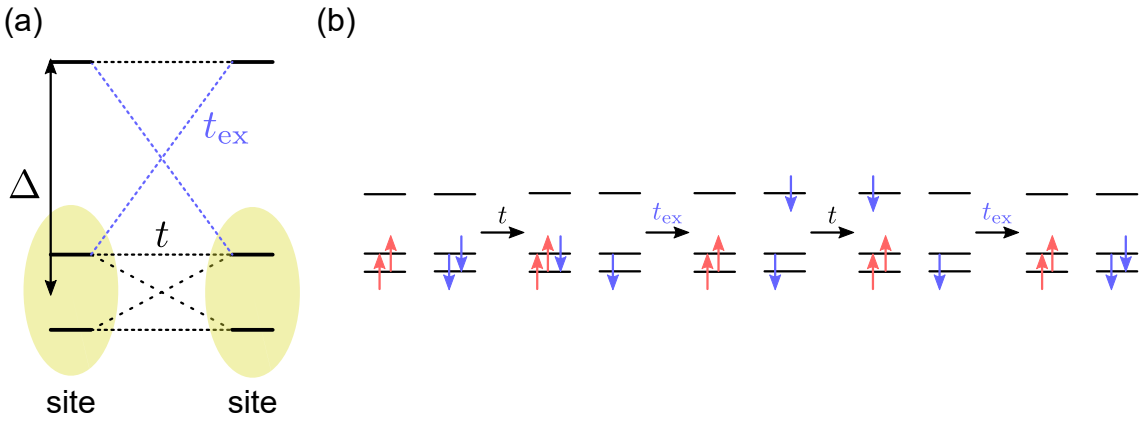

Figure 4.8: (a) Schematic picture of the three-orbital system with two degenerate orbitals and one orbital with a higher energy by Δ (drawn referring to Ref. [3]). (b) Typical fourth-order perturbation process via the excited states drawn referring to Ref. [196].

4.4 Discussion

We have performed the fourth-order perturbation calculations for the two cases so far, the four-site–one-orbital system which aims at the spin-1/2 dimers (Sec. 4.2), and the two-site–two-orbital system mimicking the e_g-orbital in the transition metal ions (Sec. 4.3). As a result, the former case will give the comparable value of B to J, while B is much smaller than J for the latter case. Then, when we just construct the spin-1 systems by the two-orbital Mott insulator and deal with the magnetic interactions with purely electronic origin, the biquadratic interaction does not become large enough to realize the spin nematic phases.

One possible way to overcome this issue in Sec. 4.3 was proposed by Mila and Zhang [196]. They additionally considered one quasi-degenerate orbital in each site which takes a higher energy by the crystal field splitting, Δ, which seems to be realized when the three-fold degenerate t_{2g}-orbitals in the crystal field with octahedral symmetry split

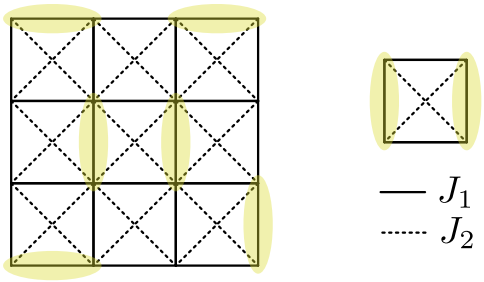

Figure 4.9: The schematic picture of the dimer covering of the ferromagnetic J_1–J_2 square lattice.

into the doubly-degenerate e_g orbitals and the a_{1g} orbital by the trigonal distortion. They showed that the second-order perturbation processes through the orbital with higher energy gives the ferromagnetic Heisenberg interaction, which suppresses the antiferromagnetic one. At the fourth order, the perturbation proceesses similar to (4b4s)-T path, where one of the two degenerate orbital and the orbital with higher energy are involved and the hoppings t and $t_{\rm ex}$ are used as shown in Fig. 4.8(b), appears. Then, they found that the biquadratic interaction generated by the fourth order processes takes a relatively larger value, although they did not take all of the possible perturbation processes into consideration.

Also, we have only treated the Heisenberg and biquadratic interactions of the purely electronic origin, while there are some other sources of the biquadratic interactions. The most representative one might be the electron-phonon interactions, which in fact can generate the large biquadratic interactions in the spinels [40, 41, 45], although the situation will become far complicated.

On the other hand, in the spin-1/2 dimer system, the biquadratic interaction can take a large value, and the spin nematic order will be realized once the dimers take the triplet state. To generate the triplet state, the ferromagnetic interactions inside the dimers are needed. One way to make the system ferromagnetic is applying a strong magnetic field [51, 58, 66, 72]. Another way is utilizing the superexchange processes via the ligand ions. When two transition metal ions and the ligand ion in between are placed forming 90°, the superexchange interaction between two magnetic ions are ferromagnetic according to the Kanamori–Goodenough rule [197, 198]. This situation is similar to the aforementioned scheme given by Mila and Zhang [196].

In the spin-1/2 systems, it has been proposed that the spin nematic order is realized in the ferromagnetic J_1–J_2 models [51, 64, 66, 67]. The origin of the spin nematic order appearing there is ascribed to the frustration effect which suppresses the kinetic motion of the single-magnons. Meanwhile, based on our perturbation calculations, we could understand its microscopic origin as follows; we can break the system into the pieces of dimers similarly to the lattices where the dimers are well-defined [84–87] (see Fig. 4.9), and then the J_1 and J_2 exchange interactions will work as the (4b4s)-T process between two dimer bonds, which generates the effective biquadratic interaction. As each dimer bond favors the triplet dimer state by the ferromagnetic J_1, the effective biquadratic interactions create the spin nematic order.

4.5 Summary of this Chapter

In this Chapter, we microscopically evaluated the spin-1 Heisenberg (bilinear) and biquadratic interactions. We separate the two spin-1's into the two pairs of electrons, each of which carries the spin-1/2, and performed the perturbation calculations in the four electron systems up to the fourth order from the strong coupling limit. We dealt with two cases, the four-site–one-orbital system and the two-site–two-orbital system. For the former case, which aims at the spin-1/2 dimer system, we found that the biquadratic interaction is generated only by the ring-exchange processes at the fourth-order where all four electrons cyclically hop along the twisted paths. The biquadratic interaction in this case can take a large value, which will lead to the possible design of the spin nematic order by making use of the dimer structure. By contrast, for the latter case aiming at the degenerate e_g orbitals in the transition metal ions, the biquadratic exchange is suppressed when we only treat the two-orbital system and the electronic origin.

(The contents in Chapter 5 (p. 101–p. 114) will be published as a journal article, and are undisclosed.)
（Chapter 5 の内容は，雑誌論文として今後刊行する準備中であるため，非公表とする.）

Chapter 6

Summary

In this thesis, we discussed the quadrupolar phases in quantum spin systems from several viewpoints, aiming at finding another clue to probe the spin nematic phase, and offering a platform to realize the quadrupolar phases without difficulties.

First, we investigated the magnetic field effect on the finite-temperature properties of spin-1 nematic phases using the bilinear-biquadratic model, a canonical model of spin nematics. Combining the semiclassical approximation and the classical Monte Carlo simulation, we found that the characteristic field dependence of the specific heat in ferro-quadrupolar phase transition, which will add a thermodynamic hint for detecting spin-1 ferro-nematics in experiments. The peak of the specific heat which implies the phase transition from the paramagnetic phase at high temperature to the ferroquadrupolar phase first goes up in an applied magnetic field, and then decreases in a larger field. The reentrant behavior is ascribed to the entropic effect owing to the quantum fluctuation effect of the quadrupolar moments. Both the paramagnetic and ferroquadrupolar phases respond to the magnetic field paramagnetically, which causes the constant shift of the energy by the Zeeman term in both phases. However, when the system acquires the magnetization, spins align and easily loses its entropy in the paramagnetic phase, whereas the quadrupolar phase keeps its entropy by fluctuating inside the plane perpendicular to the magnetic field, which relatively stabilizes the ferroquadrupolar phase.

Next, we studied the ground-state properties of the bilayer triangular lattice formed that consists of spin-1 dimers. Our direct motivation was understanding the nontrivial nonmagnetic phase in the vicinity of the singlet phase with finite gap in $Ba_3MRu_2O_9$, where M is the divalent cation. We derived the effective Hamiltonian in a spin-1 hard-core boson language which describes the low-energy properties of the original spin-1 dimer system. There, the triplet dimer states are identified as the spin-1 bosons, and the singlet state is the vacuum of the boson. By the numerical diagonalization of the effective model, we found three kinds of the quadrupolar phases formed by the spin-1 bosons. These quadrupolar phases are supported by the pair-creation and annihilation effect of bosons, which generates the effective biquadratic interactions between spin-1 bosons. We further classified these quadrupolar phases by the internal degrees of freedom of dimers, and one of the three phases turned out to be the spin nematic phase which is the same as the one found in the spin-1 bilinear-biquadratic model. Another quadrupolar phase next to the singlet phase may explain $Ba_3MRu_2O_9$.

Additionally, we discussed why the spin dimer system is a suitable platform to realize the spin nematic phases. We took in the effect of electron hopping perturbatively from the Mott insulating limit, and derived the biquadratic interaction between triplet dimers. We found that the large biquadratic interaction between triplets can have a comparable value to the Heisenberg interaction when we adopt the dimer structure, which should be contrasted to the typical spin-1 systems with small biquadratic interactions. So far, it has been considered that realizing the spin nematic phases in usual spin-1 materials is difficult. Therefore, investigating the finite-temperature properties or the observables in the spin-1 nematic phases has not been directly connected to the experimental observation of the spin nematic phases in the spin-1 systems, while the investigation itself is important. Our results suggested that the spin-1 nematic phases can be realized in the spin dimer materials, which will allow us to utilize the finite-temperature properties of the spin-1 nematics. Our results on the magnetic field effect on the spin-1 nematic phases in the bilinear-biquadratic model can also be exploited when we deal with the spin-1 nematics in the dimer systems.

We also gave a hint for discussing the spin nematics in the spin-1 and spin-1/2 systems in a unified description; mapping the spin dimer system to the hard-core boson model allows us to deal with the low-energy properties of the spin-1 dimer and the spin-1/2 dimer systems equivalently. Based on this, we finally described the spin-1/2 system in the terms of the spin dimers, and examined the two-leg ladder system as an example to explain how the two-magnon bound states near the saturation are redescribed using the dimer-basis. As a future prospect, various kinds of spin quadrupolar or nematic phases in different systems will be united in terms of the dimer-basis with internal degrees of freedom.

Acknowledgement

I would like to express my sincere gratitude to Assoc. Prof. Chisa Hotta, my supervisor, for discussing many things and encouraging me throughout my Master and Ph.D. programs for five years, and collaborating on the topics in this thesis. Without her continuous encouragement and support with patience, I could not have accomplished my Ph.D. program.

I am deeply indebted to Yuto Yokoyama for working together on the topics in Chapter 4, and Keisuke Totsuka for collaborating on the contents in Chapter 5. I have learned a lot of things from them through discussion with them.

I am grateful to Hikomitsu Kikuchi, Yutaka Fujii, Karlo Penc, Katsuhiro Morita, Tsutomu Momoi, Daisuke Yamamoto, and Nic Shannon for the valuable discussions and comments on the contents in Chapter 2. I would like to thank Keisuke Totsuka, Tsutomu Momoi, Toshiya Hikihara, Ichiro Terasaki, Masataka Kawano, and Yuto Yokoyama for fruitful discussions and comments on the topics in Chapter 3. I am grateful to Karlo Penc and Frédéric Mila for invaluable comments on the topics in Chapter 4.

I would like to thank the former and current members of Hotta group, Xavier Plat, Takashi Imoto, Takashi Nakamaniwa, Kazumasa Ueda, Yuto Yokoyama, Masataka Kawano, Kenta Watanabe, Atsushi Iwaki, Shunsuke Kimura, Keita Urakami, Manami Sato, Ryo Makuta, Daisuke Taniguchi, Shunsuke Fujisawa, and Hiroki Nakai for daily discussions and communications.

I thank the members of Onose group in UTokyo (now in Tohoku University); Yoshinori Onose, Yoichi Nii, Yusuke Iguchi, Yuji Hirokane, Ryo Sasaki, Yoshiaki Hamahara, Yuta Ishii, Nan Jiang, and Mitsuyoshi Ohtsu for the communications and discussions on many topics, and in particular thank Ryo Sasaki for supporting me a lot.

I would like to thank Yuki Shiomi, Katsuhiro Morita, Kiyu Fukui, and Yu Miyazaki for discussing and communicating, and particularly thank Katsuhiro Morita for the kind support.

Special thanks are due to Yusuke Araki, Hideki Matsuoka, Daisuke Kondo, and Satoshi Watanabe for daily correspondence.

Part of the calculations in Chapter 2 was conducted using the facilities of the Supercomputer Center, Institute of Solid State Physics, University of Tokyo.

Finally, I thank my parents and brother for supporting me a lot.

Appendix A

Details on the Monte Carlo simulation

In this Appendix, we note the details on the numerical methods used in the Monte Carlo simulations.

A.1 Details on the random sampling

Since the $\boldsymbol{d}$-vector has three complex, or six real components, we need to randomly choose one point from the five-dimensional unit hypersphere in updating $\boldsymbol{d}$. For the random sampling from the unit hypersphere, we randomly choose six real numbers r_i (i = 1–6) following the standard distribution [1], and then normalize it [199], namely,

$$r_i' = \frac{r_i}{\sqrt{\sum_{i=1}^{6} r_i^2}}. \tag{A.1}$$

We adopt r_i' as the six real components of the $\boldsymbol{d}$-vector with $|\boldsymbol{d}| = 1$.

To generate random variables following the standard distribution, we utilize the Box–Muller method [200]. Let x and y be the uniform random numbers in an open section $(0, 1)$. Then, z_1 and z_2 defined as

$$z_1 = \sqrt{-2\ln x}\cos(2\pi y),\ z_2 = \sqrt{-2\ln x}\sin(2\pi y), \tag{A.2}$$

are the random numbers independently following the standard distribution.

A.2 Jackknife resampling

To calculate the averages and error bars in the Monte Carlo simulations, we use the jackknife resampling method. Here we write down the process of the jackknife resampling method (see e.g., Ref. [201]).

[1] The standard distribution is the normal distribution whose average is 0 and variance is 1.

Let the number of the samples n and the data set $\{x_i\}_{i=1,\cdots,n}$. We calculate n kinds of averages, where i-th sample x_i is excluded in the i-th average, $\bar{x}(i)$. The explicit form of $\bar{x}(i)$ is given as

$$\bar{x}(i) = \frac{1}{n-1} \sum_{j=1, j\neq i}^{n} x_j. \tag{A.3}$$

Then, the whole average $\bar{x}$ is given by [2]

$$\bar{x} = \frac{1}{n} \sum_{i=1}^{n} \bar{x}(i), \tag{A.4}$$

and the jackknife variance σ^2 is given by

$$\sigma^2 = (n-1)\frac{1}{n} \sum_{i=1}^{n} \left(\bar{x}(i) - \bar{x}\right)^2. \tag{A.5}$$

[2]The average in the jackknife resampling $\bar{x}$ is obviously equal to the simple average $\frac{1}{n}\sum_{i=1}^{n} x_i$.

Appendix B

Appendix on the analysis of spin-1 dimer triangular lattice

In this Appendix, we note the details on Chapter 3.

B.1 Details on the perturbation calculation

Here we denote the quasi-degenerate perturbation theory, which is used for calculating the effective Hamiltonian. This method discussed below is based on the Schrieffer–Wolff transformation [185, 186], the diagonalization of the Hamiltonian matrix by the unitary transformation, but the unitary transformation is cut off by some order in the unitary matrix.

The details of the calculations of the inter-dimer Hamiltonian $\mathcal{H}_{\text{inter}}$ and the matrix elements for the perturbation calculation in the spin-1 dimer system are also given.

B.1.1 Quasi-degenerate perturbation theory

In this section, we explain the quasi-degenerate perturbation theory referring to Ref. [186].

B.1.1.1 Overview

Taking some basis $\{|n\rangle\}$, the Hamiltonian $\mathcal{H}$ can be represented in the matrix form H. The unitary-transformed Hamiltonian of H, $\tilde{H}$, using the anti-Hermitian matrix, S, can be expanded as follows (cf. Baker–Campbell–Hausdorff theorem);

$$\begin{aligned}\tilde{H} &= \mathrm{e}^{-S} H \mathrm{e}^{+S} \\ &= H + [H, S] + \frac{1}{2!}[[H, S], S] + \cdots . \end{aligned} \tag{B.1}$$

When the basis $\{|n\rangle\}$ is separated into two parts, the low-energy part denoted as $\{|m\rangle\}$ and the high-energy part denoted as $\{|l\rangle\}$, the Hamiltonian matrix H can be separated into three parts as

$$H = H_0 + H_1 + H_2. \tag{B.2}$$

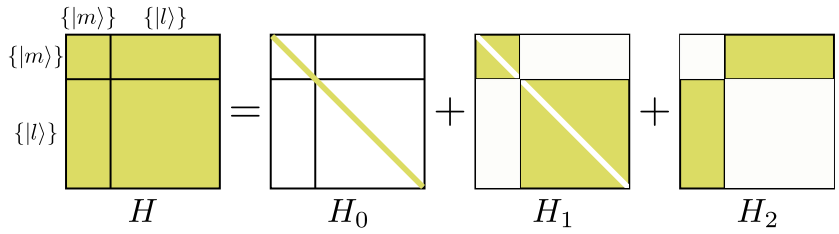

Figure B.1: Schematic view of the Hamiltonian matrices.

Here, H_0 is the diagonal matrix, and H_1 and H_2 is the block-diagonal and block-offdiagonal matrices, respectively. As H_0 is diagonal for $\{|n\rangle\}$, H_0 is regarded as the unperturbed Hamiltonian, and H_1 and H_2, which are offdiagonal matrices for $\{|n\rangle\}$, is the perturbation Hamiltonian. The schematic picture of these Hamiltonian matrices are expressed in Fig. B.1. Then, the unitary-transformed Hamiltonian $\tilde{H}$, can be separated into block-diagonal part, $\tilde{H}_{\text{diag}}$ and the block-offdiagonal part, $\tilde{H}_{\text{offdiag}}$. $\tilde{H}_{\text{diag}}$ and $\tilde{H}_{\text{offdiag}}$ are expressed as

$$\tilde{H}_{\text{diag}} = (H_0 + H_1) + [H_2, S] + \frac{1}{2!}[[H_0 + H_1, S], S] + \frac{1}{3!}[[[H_2, S], S], S] + \cdots, \quad \text{(B.3)}$$

$$\tilde{H}_{\text{offdiag}} = H_2 + [H_0 + H_1, S] + \frac{1}{2!}[[H_2, S], S] + \frac{1}{3!}[[[H_0 + H_1, S], S], S] + \cdots, \quad \text{(B.4)}$$

respectively. Assuming that the anti-Hermitian matrix S is expanded as

$$S = S^{(1)} + S^{(2)} + S^{(3)} + \cdots, \quad \text{(B.5)}$$

where $S^{(n)}$ is the n-th order of the perturbation Hamiltonian, H_1 and/or H_2, $\tilde{H}_{\text{diag}}$ and $\tilde{H}_{\text{offdiag}}$ can be rearranged by the order of perturbation. The expressions up to 2nd order are as follows;

- $\tilde{H}_{\text{diag}}$

  0th: H_0, 1st: H_1, 2nd: $\frac{1}{2}\left[\left[H_0, S^{(1)}\right], S^{(1)}\right]$.

- $\tilde{H}_{\text{offdiag}}$

  1st: $H_2 + \left[H_0, S^{(1)}\right]$, 2nd: $\left[H_0, S^{(2)}\right] + \left[H_1, S^{(1)}\right]$.

The block-diagonalization of the Hamiltonian matrix, namely, setting $\tilde{H}_{\text{offdiag}}$ zero up to a certain order, corresponds to the calculation of the effective Hamiltonian to the order.

B.1.1.2 Effective Hamiltonian up to 2nd order

We write down the matrix elements of the effective Hamiltonian up to the 2nd order. At 1st order, the Hamiltonian H_1 becomes the effective Hamiltonian of the 1st order as it is;

$$\langle m|H^{(1)}|m'\rangle = \langle m|H_1|m'\rangle \quad \text{(B.6)}$$

At the 2nd order, 1st order term of $\tilde{H}_{\text{offdiag}}$ should be zero;

$$H_2 + \left[H_0, S^{(1)}\right] = 0, \tag{B.7}$$

and using this relation, the matrix elements of the effective Hamiltonian are calculated as

$$\langle m|H^{(2)}|m'\rangle = -\frac{1}{2}\sum_l \left(\frac{\langle m|H_2|l\rangle \langle l|H_2|m'\rangle}{\varepsilon_l - \varepsilon_m} + \frac{\langle m|H_2|l\rangle \langle l|H_2|m'\rangle}{\varepsilon_l - \varepsilon_{m'}} \right). \tag{B.8}$$

By setting $\tilde{H}_{\text{offdiag}}$ to be zero at each order, the effective Hamiltonian at the higher-order can be calculated succeedingly.

B.1.2 Details on the derivation of the effective Hamiltonian

Here we write down the matrix elements in the calculation of the effective Hamiltonian.

B.1.2.1 Calculation of the inter-dimer interactions

Combining the above equations, the inter-dimer interactions can be systematically calculated. For example, $\boldsymbol{S}_{i_1} \cdot \boldsymbol{S}_{j_1}$, which is a part of J'-term, for $S^z_{\text{tot}} = 0$ sector is calculated as follows;

$$\begin{aligned}
&\boldsymbol{S}_{i_1} \cdot \boldsymbol{S}_{j_1} |s, s\rangle \\
&= \frac{1}{2}\left(S^+_{i_1}|s\rangle \otimes S^-_{j_1}|s\rangle + S^-_{i_1}|s\rangle \otimes S^+_{j_1}|s\rangle \right) + S^z_{i_1}|s\rangle \otimes S^z_{j_1}|s\rangle \\
&= \frac{1}{2}\left[\left(-\frac{2}{\sqrt{3}}|t_{+1}\rangle\right)\left(\frac{2}{\sqrt{3}}|t_{-1}\rangle\right) + \left(\frac{2}{\sqrt{3}}|t_{-1}\rangle\right)\left(-\frac{2}{\sqrt{3}}|t_{+1}\rangle\right)\right] \\
&\qquad + \left(\frac{\sqrt{2}}{\sqrt{3}}|t_0\rangle\right)\left(\frac{\sqrt{2}}{\sqrt{3}}|t_0\rangle\right) \\
&= -\frac{2}{3}|t_{+1}, t_{-1}\rangle - \frac{2}{3}|t_{-1}, t_{+1}\rangle + \frac{2}{3}|t_0, t_0\rangle,
\end{aligned} \tag{B.9}$$

$$\begin{aligned}
&\boldsymbol{S}_{i_1} \cdot \boldsymbol{S}_{j_1} |s, t_0\rangle \\
&= \frac{1}{2}\left(S^+_{i_1}|s\rangle \otimes S^-_{j_1}|t_0\rangle + S^-_{i_1}|s\rangle \otimes S^+_{j_1}|t_0\rangle \right) + S^z_{i_1}|s\rangle \otimes S^z_{j_1}|t_0\rangle \\
&= \frac{1}{2}\left[\left(-\frac{2}{\sqrt{3}}|t_{+1}\rangle\right)\left(\frac{1}{\sqrt{2}}(|t_{-1}\rangle + |q_{-1}\rangle)\right) + \left(\frac{2}{\sqrt{3}}|t_{-1}\rangle\right)\left(\frac{1}{\sqrt{2}}(|t_{+1}\rangle - |q_{+1}\rangle)\right)\right] \\
&\qquad + \left(\frac{\sqrt{2}}{\sqrt{3}}|t_0\rangle\right)\left(\frac{1}{\sqrt{3}}\left(\sqrt{2}|s\rangle + |q_0\rangle\right)\right) \\
&= -\frac{1}{\sqrt{6}}|t_{+1}, t_{-1}\rangle - \frac{1}{\sqrt{6}}|t_{+1}, q_{-1}\rangle + \frac{1}{\sqrt{6}}|t_{-1}, t_{+1}\rangle - \frac{1}{\sqrt{6}}|t_{-1}, q_{+1}\rangle \\
&\qquad + \frac{2}{3}|t_0, s\rangle + \frac{\sqrt{2}}{3}|t_0, q_0\rangle,
\end{aligned} \tag{B.10}$$

$$\begin{aligned}
&\boldsymbol{S}_{i_1} \cdot \boldsymbol{S}_{j_1} |t_0, s\rangle \\
&= \frac{1}{2}\left(S^+_{i_1}|t_0\rangle \otimes S^-_{j_1}|s\rangle + S^-_{i_1}|t_0\rangle \otimes S^+_{j_1}|s\rangle \right) + S^z_{i_1}|t_0\rangle \otimes S^z_{j_1}|s\rangle \\
&= \frac{1}{2}\left[\left(\frac{1}{\sqrt{2}}(|t_{+1}\rangle - |q_{+1}\rangle)\right)\left(\frac{2}{\sqrt{3}}|t_{-1}\rangle\right) + \left(\frac{1}{\sqrt{2}}(|t_{-1}\rangle + |q_{-1}\rangle)\right)\left(-\frac{2}{\sqrt{3}}|t_{+1}\rangle\right)\right]
\end{aligned}$$

$$
\begin{aligned}
&\quad + \left(\frac{1}{\sqrt{3}}\left(\sqrt{2}\,|s\rangle + |q_0\rangle\right)\right)\left(\frac{\sqrt{2}}{\sqrt{3}}\,|t_0\rangle\right) \\
&= \frac{1}{\sqrt{6}}\,|t_{+1}, t_{-1}\rangle - \frac{1}{\sqrt{6}}\,|q_{+1}, t_{-1}\rangle - \frac{1}{\sqrt{6}}\,|t_{-1}, t_{+1}\rangle - \frac{1}{\sqrt{6}}\,|q_{-1}, t_{+1}\rangle \\
&\qquad + \frac{2}{3}\,|s, t_0\rangle + \frac{\sqrt{2}}{3}\,|q_0, t_0\rangle\,, \qquad \text{(B.11)}
\end{aligned}
$$

$$
\begin{aligned}
&\boldsymbol{S}_{i_1}\cdot\boldsymbol{S}_{j_1}\,|t_0, t_0\rangle \\
&= \frac{1}{2}\left(S^+_{i_1}\,|t_0\rangle \otimes S^-_{j_1}\,|t_0\rangle + S^-_{i_1}\,|t_0\rangle \otimes S^+_{j_1}\,|t_0\rangle\right) + S^z_{i_1}\,|t_0\rangle \otimes S^z_{j_1}\,|t_0\rangle \\
&= \frac{1}{2}\left[\left(\frac{1}{\sqrt{2}}\left(|t_{+1}\rangle - |q_{+1}\rangle\right)\right)\left(\frac{1}{\sqrt{2}}\left(|t_{-1}\rangle + |q_{-1}\rangle\right)\right)\right. \\
&\qquad\qquad \left. + \left(\frac{1}{\sqrt{2}}\left(|t_{-1}\rangle + |q_{-1}\rangle\right)\right)\left(\frac{1}{\sqrt{2}}\left(|t_{+1}\rangle - |q_{+1}\rangle\right)\right)\right] \\
&\qquad\qquad + \left(\frac{1}{\sqrt{3}}\left(\sqrt{2}\,|s\rangle + |q_0\rangle\right)\right)\left(\frac{1}{\sqrt{3}}\left(\sqrt{2}\,|s\rangle + |q_0\rangle\right)\right) \\
&= \frac{1}{4}\,|t_{+1}, t_{-1}\rangle + \frac{1}{4}\,|t_{+1}, q_{-1}\rangle - \frac{1}{4}\,|q_{+1}, t_{-1}\rangle - \frac{1}{4}\,|q_{+1}, q_{-1}\rangle \\
&\qquad + \frac{1}{4}\,|t_{-1}, t_{+1}\rangle - \frac{1}{4}\,|t_{-1}, q_{+1}\rangle + \frac{1}{4}\,|q_{-1}, t_{+1}\rangle - \frac{1}{4}\,|q_{-1}, q_{+1}\rangle \\
&\qquad + \frac{2}{3}\,|s, s\rangle + \frac{\sqrt{2}}{3}\,|s, q_0\rangle + \frac{\sqrt{2}}{3}\,|q_0, s\rangle + \frac{1}{3}\,|q_0, q_0\rangle\,, \qquad \text{(B.12)}
\end{aligned}
$$

$$
\begin{aligned}
&\boldsymbol{S}_{i_1}\cdot\boldsymbol{S}_{j_1}\,|t_{+1}, t_{-1}\rangle \\
&= \frac{1}{2}\left(S^+_{i_1}\,|t_{+1}\rangle \otimes S^-_{j_1}\,|t_{-1}\rangle + S^-_{i_1}\,|t_{+1}\rangle \otimes S^+_{j_1}\,|t_{-1}\rangle\right) + S^z_{i_1}\,|t_{+1}\rangle \otimes S^z_{j_1}\,|t_{-1}\rangle \\
&= \frac{1}{2}\left[\left(-\,|q_{+2}\rangle\right)\left(|q_{-2}\rangle\right) + \left(-\frac{2}{\sqrt{3}}\,|s\rangle + \frac{1}{\sqrt{2}}\,|t_0\rangle + \frac{1}{\sqrt{6}}\,|q_0\rangle\right)\left(\frac{2}{\sqrt{3}}\,|s\rangle + \frac{1}{\sqrt{2}}\,|t_0\rangle - \frac{1}{\sqrt{6}}\,|q_0\rangle\right)\right] \\
&\qquad\qquad + \left(\frac{1}{2}\left(|t_{+1}\rangle + |q_{+1}\rangle\right)\right)\left(\frac{1}{2}\left(-\,|t_{-1}\rangle + |q_{-1}\rangle\right)\right) \\
&= -\frac{1}{2}\,|q_{+2}, q_{-2}\rangle - \frac{2}{3}\,|s, s\rangle - \frac{1}{\sqrt{6}}\,|s, t_0\rangle + \frac{1}{3\sqrt{2}}\,|s, q_0\rangle \\
&\qquad + \frac{1}{\sqrt{6}}\,|t_0, s\rangle + \frac{1}{4}\,|t_0, t_0\rangle - \frac{1}{4\sqrt{3}}\,|t_0, q_0\rangle \\
&\qquad + \frac{1}{3\sqrt{2}}\,|q_0, s\rangle + \frac{1}{4\sqrt{3}}\,|q_0, t_0\rangle - \frac{1}{12}\,|q_0, q_0\rangle \\
&\qquad - \frac{1}{4}\,|t_{+1}, t_{-1}\rangle + \frac{1}{4}\,|t_{+1}, q_{-1}\rangle - \frac{1}{4}\,|q_{+1}, t_{-1}\rangle + \frac{1}{4}\,|q_{+1}, q_{-1}\rangle\,, \qquad \text{(B.13)}
\end{aligned}
$$

$$
\begin{aligned}
&\boldsymbol{S}_{i_1}\cdot\boldsymbol{S}_{j_1}\,|t_{-1}, t_{+1}\rangle \\
&= \frac{1}{2}\left(S^+_{i_1}\,|t_{-1}\rangle \otimes S^-_{j_1}\,|t_{+1}\rangle + S^-_{i_1}\,|t_{-1}\rangle \otimes S^+_{j_1}\,|t_{+1}\rangle\right) + S^z_{i_1}\,|t_{-1}\rangle \otimes S^z_{j_1}\,|t_{+1}\rangle \\
&= \frac{1}{2}\left[\left(\frac{2}{\sqrt{3}}\,|s\rangle + \frac{1}{\sqrt{2}}\,|t_0\rangle - \frac{1}{\sqrt{6}}\,|q_0\rangle\right)\left(-\frac{2}{\sqrt{3}}\,|s\rangle + \frac{1}{\sqrt{2}}\,|t_0\rangle + \frac{1}{\sqrt{6}}\,|q_0\rangle\right) + \left(|q_{-2}\rangle\right)\left(-\,|q_{+2}\rangle\right)\right] \\
&\qquad\qquad + \left(\frac{1}{2}\left(-\,|t_{-1}\rangle + |q_{-1}\rangle\right)\right)\left(\frac{1}{2}\left(|t_{+1}\rangle + |q_{+1}\rangle\right)\right) \\
&= -\frac{2}{3}\,|s, s\rangle + \frac{1}{\sqrt{6}}\,|s, t_0\rangle + \frac{1}{3\sqrt{2}}\,|s, q_0\rangle - \frac{1}{\sqrt{6}}\,|t_0, s\rangle + \frac{1}{4}\,|t_0, t_0\rangle + \frac{1}{4\sqrt{3}}\,|t_0, q_0\rangle
\end{aligned}
$$

$$+\frac{1}{3\sqrt{2}}|q_0,s\rangle-\frac{1}{4\sqrt{3}}|q_0,t_0\rangle-\frac{1}{12}|q_0,q_0\rangle-\frac{1}{2}|q_{-2},q_{+2}\rangle$$
$$-\frac{1}{4}|t_{-1},t_{+1}\rangle-\frac{1}{4}|t_{-1},q_{+1}\rangle+\frac{1}{4}|q_{-1},t_{+1}\rangle+\frac{1}{4}|q_{-1},q_{+1}\rangle\,. \tag{B.14}$$

B.1.2.2 Matrix elements

The matrix elements of the inter-dimer Hamiltonian projected onto the low-energy manifold of states consisting only of singlets and triplets, which correspond to $\langle m|H_1|m'\rangle$ in the above formulation, are given as follows ($S^z_{\rm tot}=0$ sector as an example);

$\|s,s\rangle$	$\|s,t_0\rangle$	$\|t_0,s\rangle$	$\|t_0,t_0\rangle$	$\|t_{+1},t_{-1}\rangle$	$\|t_{-1},t_{+1}\rangle$
0	0	0	$\frac{4}{3}(J'-J'')$	$-\frac{4}{3}(J'-J'')$	$-\frac{4}{3}(J'-J'')$
0	0	$\frac{4}{3}(J'-J'')$	0	0	0
0	$\frac{4}{3}(J'-J'')$	0	0	0	0
$\frac{4}{3}(J'-J'')$	0	0	0	$\frac{1}{2}(J'+J'')$	$\frac{1}{2}(J'+J'')$
$-\frac{4}{3}(J'-J'')$	0	0	$\frac{1}{2}(J'+J'')$	$-\frac{1}{2}(J'+J'')$	0
$-\frac{4}{3}(J'-J'')$	0	0	$\frac{1}{2}(J'+J'')$	0	$-\frac{1}{2}(J'+J'')$

(B.15)

Also the ones which connect the low-energy states and the excited states including the quintet states, which correspond to $\langle m|H_2|l\rangle$ and $\langle l|H_2|m'\rangle$ in the aforementioned formu-

lation, are expressed as follows ($S^z_{\rm tot}=0$ sector as an example);

	$\|s,s\rangle$	$\|s,t_0\rangle$	$\|t_0,s\rangle$	$\|t_0,t_0\rangle$	$\|t_{+1},t_{-1}\rangle$	$\|t_{-1},t_{+1}\rangle$
$\langle s,q_0\|$	0	0	0	$\frac{2\sqrt{2}}{3}$	$\frac{\sqrt{2}}{3}$	$\frac{\sqrt{2}}{3}$
$\langle q_0,s\|$	0	0	0	$\frac{2\sqrt{2}}{3}$	$\frac{\sqrt{2}}{3}$	$\frac{\sqrt{2}}{3}$
$\langle t_0,q_0\|$	0	$\frac{2\sqrt{2}}{3}$	0	0	0	0
$\langle q_0,t_0\|$	0	0	$\frac{2\sqrt{2}}{3}$	0	0	0
$\langle t_{+1},q_{-1}\|$	0	$-\frac{2}{\sqrt{6}}$	0	0	0	0
$\langle q_{-1},t_{+1}\|$	0	0	$-\frac{2}{\sqrt{6}}$	0	0	0
$\langle t_{-1},q_{+1}\|$	0	$-\frac{2}{\sqrt{6}}$	0	0	0	0
$\langle q_{+1},t_{-1}\|$	0	0	$-\frac{2}{\sqrt{6}}$	0	0	0
$\langle q_0,q_0\|$	0	0	0	$\frac{2}{3}$	$-\frac{1}{6}$	$-\frac{1}{6}$
$\langle q_{+1},q_{-1}\|$	0	0	0	$-\frac{1}{2}$	$\frac{1}{2}$	0
$\langle q_{-1},q_{+1}\|$	0	0	0	$-\frac{1}{2}$	0	$\frac{1}{2}$
$\langle q_{+2},q_{-2}\|$	0	0	0	0	-1	0
$\langle q_{-2},q_{+2}\|$	0	0	0	0	0	-1

$$\times\left(J'-J''\right). \tag{B.16}$$

We note that the Hamiltonian conserves total-S^z, and $S^z_{\rm tot}=+3,+4$ states in the two-dimer system do not need to be considered within our calculations.

B.2 Bond-operator approach to spin-1 dimer systems keeping the time-reversal symmetry

Here we show the bond-operator approach of the spin-1 dimer systems. Although the bond-operator approach for a spin-1 dimer was constructed already in Refs. [161–163], the approach there breaks the time-reversal symmetry. We modify those approaches to the time-reversal invariant form. First, we write down the multiplet states of spin-1 dimers keeping the time-reversal symmetry. Using the time-reversal invariant basis states of a spin-1 given in Eq. (1.5), the singlet, triplet and quintet states of a single spin-1 dimer is written as

$$|s\rangle=\frac{1}{\sqrt{3}}\left(|x,x\rangle+|y,y\rangle+|z,z\rangle\right), \tag{B.17}$$

$$|t_\alpha\rangle=-\frac{1}{\sqrt{2}}\sum_{\beta,\gamma}\varepsilon_{\alpha\beta\gamma}\,|\beta,\gamma\rangle\,, \tag{B.18}$$

$$|q_{\alpha\beta}\rangle=-\frac{1}{\sqrt{2}}\left(|\alpha,\beta\rangle+|\beta,\alpha\rangle\right)+\left(\sqrt{2}-1\right)\delta_{\alpha\beta}\,|\alpha,\alpha\rangle\,, \tag{B.19}$$

respectively, where $\alpha, \beta, \gamma = x, y, z$. We can construct 10 states from the above expressions [1]. However, only nine states of those are the linearly independent because there are only nine states in $\{|\alpha, \beta\rangle\}$. Here, $|s\rangle$ and $|q_{\alpha\alpha}\rangle$ are linearly dependent, and we construct two linearly independent quintet states, $|q_{3\alpha^2-r^2}\rangle$ and $|q_{\beta^2-\gamma^2}\rangle$, as the linear combinations of three $|q_{\alpha\alpha}\rangle$ states. The forms of $|q_{3\alpha^2-r^2}\rangle$ and $|q_{\beta^2-\gamma^2}\rangle$ are given as, for instance,

$$|q_{3z^2-r^2}\rangle = \frac{1}{\sqrt{6}}\left(2\,|q_{zz}\rangle - |q_{xx}\rangle - |q_{yy}\rangle\right) = -\frac{1}{\sqrt{6}}\left(2\,|z,z\rangle - |x,x\rangle - |y,y\rangle\right),$$
$$|q_{x^2-y^2}\rangle = \frac{1}{\sqrt{2}}\left(|q_{xx}\rangle - |q_{yy}\rangle\right) = -\frac{1}{\sqrt{2}}\left(|x,x\rangle - |y,y\rangle\right). \tag{B.20}$$

In the above case, we take $(\alpha, \beta, \gamma) = (z, x, y)$. Besides $|t_\alpha\rangle$ and $|q_{\alpha\beta}\rangle$, we use $|s\rangle$, $|q_{3\alpha^2-r^2}\rangle$, and $|q_{\beta^2-\gamma^2}\rangle$, as a basis states for the bond-operator expression of $S^\alpha_{i_\mu}$, namely, we properly choose the basis states $|q_{3\alpha^2-r^2}\rangle$, and $|q_{\beta^2-\gamma^2}\rangle$ depending on the component of the spin operator, α [2].

We regarded the singlet state as a vacuum in the main text, while in the bond-operator approach here, we redefine the vacuum as the state where there are not any multiplets. Then, we do not use $b_{i,\alpha}$ and $b^\dagger_{i,\alpha}$, and instead we use $s_i/s^\dagger_i$ and $t_{i,\alpha}/t^\dagger_{i,\alpha}$ as the annihilation/creation operators of the singlet state and the triplet state with α-component, respectively, and $q_{i,\alpha}/q^\dagger_{i,\alpha}$ as the ones of the quintet state with α-component [3]. The bond-operator form of the spin-1 operators $S^\alpha_{i_\mu}$ $(\mu = 1, 2)$ of the i-th dimer is written in the following form;

$$\begin{aligned} S^\alpha_{i_1} = {} & \mathrm{i}\frac{\sqrt{2}}{\sqrt{3}}\left(t^\dagger_{i,\alpha}s_i - s^\dagger_i t_{i,\alpha}\right) - \frac{\mathrm{i}}{2}\sum_{\beta,\gamma}\varepsilon_{\alpha\beta\gamma}t^\dagger_{i,\beta}t_{i,\gamma} - \frac{\mathrm{i}}{\sqrt{3}}\left(q^\dagger_{i,3\alpha^2-r^2}t_{i,\alpha} - t^\dagger_{i,\alpha}q_{i,3\alpha^2-r^2}\right) \\ & - \frac{\mathrm{i}}{2}\sum_{\beta\neq\alpha}\left(q^\dagger_{i,\alpha\beta}t_{i,\beta} - t^\dagger_{i,\beta}q_{i,\alpha\beta}\right) - \frac{\mathrm{i}}{2}\sum_{\beta,\gamma}\varepsilon_{\alpha\beta\gamma}q^\dagger_{i,\alpha\beta}q_{i,\gamma\alpha} \\ & - \frac{\mathrm{i}}{2}\sum_{\beta,\gamma}\varepsilon_{\alpha\beta\gamma}\left(q^\dagger_{i,\beta^2-\gamma^2}q_{i,\beta\gamma} - q^\dagger_{i,\beta\gamma}q_{i,\beta^2-\gamma^2}\right), \end{aligned} \tag{B.24}$$

$$\begin{aligned} S^\alpha_{i_2} = {} & -\mathrm{i}\frac{\sqrt{2}}{\sqrt{3}}\left(t^\dagger_{i,\alpha}s_i - s^\dagger_i t_{i,\alpha}\right) - \frac{\mathrm{i}}{2}\sum_{\beta,\gamma}\varepsilon_{\alpha\beta\gamma}t^\dagger_{i,\beta}t_{i,\gamma} + \frac{\mathrm{i}}{\sqrt{3}}\left(q^\dagger_{i,3\alpha^2-r^2}t_{i,\alpha} - t^\dagger_{i,\alpha}q_{i,3\alpha^2-r^2}\right) \\ & + \frac{\mathrm{i}}{2}\sum_{\beta\neq\alpha}\left(q^\dagger_{i,\alpha\beta}t_{i,\beta} - t^\dagger_{i,\beta}q_{i,\alpha\beta}\right) - \frac{\mathrm{i}}{2}\sum_{\beta,\gamma}\varepsilon_{\alpha\beta\gamma}q^\dagger_{i,\alpha\beta}q_{i,\gamma\alpha} \\ & - \frac{\mathrm{i}}{2}\sum_{\beta,\gamma}\varepsilon_{\alpha\beta\gamma}\left(q^\dagger_{i,\beta^2-\gamma^2}q_{i,\beta\gamma} - q^\dagger_{i,\beta\gamma}q_{i,\beta^2-\gamma^2}\right). \end{aligned} \tag{B.25}$$

[1] 10 states: $|s\rangle$, $|t_x\rangle$, $|t_y\rangle$, $|t_z\rangle$, $|q_{xx}\rangle$, $|q_{yy}\rangle$, $|q_{zz}\rangle$, $|q_{xy}\rangle$, $|q_{yz}\rangle$, $|q_{zx}\rangle$. By construction, $|q_{\alpha\beta}\rangle = |q_{\beta\alpha}\rangle$ holds.

[2] In an explicit form, we use $|q_{3x^2-r^2}\rangle$ and $|q_{y^2-z^2}\rangle$ for $S^x_{i_\mu}$, $|q_{3y^2-r^2}\rangle$ and $|q_{z^2-x^2}\rangle$ for $S^y_{i_\mu}$, and $|q_{3z^2-r^2}\rangle$ and $|q_{x^2-y^2}\rangle$ for $S^z_{i_\mu}$, respectively.

[3] For example, when we set the vacuum as $|0\rangle$,

$$s^\dagger_i\,|0\rangle = |s\rangle\,,\ s_i\,|s\rangle = |0\rangle\,, \tag{B.21}$$
$$t^\dagger_{i,x}\,|0\rangle = |t_{i,x}\rangle\,,\ t_{i,x}\,|t_{i,x}\rangle = |0\rangle\,, \tag{B.22}$$
$$q^\dagger_{i,xy}\,|0\rangle = |q_{i,xy}\rangle\,,\ q_{i,xy}\,|q_{i,xy}\rangle = |0\rangle\,, \tag{B.23}$$

hold.

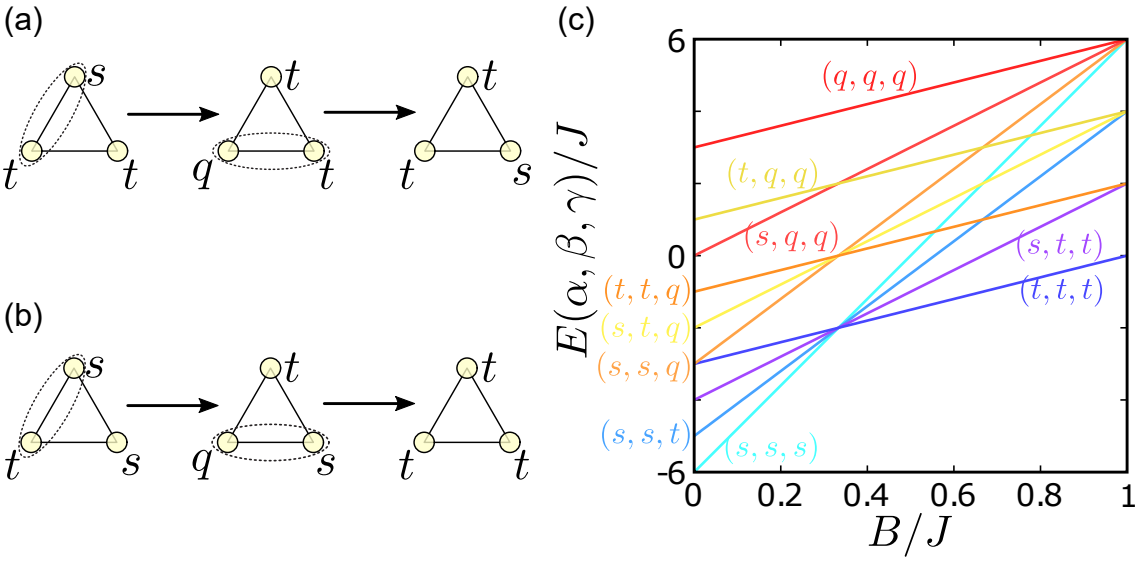

Figure B.2: (a), (b) Examples of the second-order perturbation processes among three dimers. (a) Process of the 'correlated hopping', and (b) pair-creation of spin-1 bosons. Dotted ellipses represent the pair of dimers where the perturbation term $\mathcal{H}_{\rm inter}$ operates. s, t, and q denote the singlet, triplet, and quintet states of the spin-1 dimer, respectively. (c) B/J dependence of the $\mathcal{H}_{\rm intra}$ of the three isolated spin-1 dimers. (α,β,γ) $(\alpha,\beta,\gamma = s,t,q)$ expresses the state where α, β-, and γ-multiplets exist. Figures are taken from Ref. [2] (Copyright ©2020, American Physical Society).

B.3 Effect of the three-dimer interactions

In the main text, we discarded the three-dimer interactions $\mathcal{H}_{\rm 3body}$. Here we evaluate the effects of these three-dimer interactions.

First, we mention some details on the $\mathcal{H}_{\rm 3body}$, whose origin is the second-order perturbation processes involving the three dimers. In Figs. B.2(a) and (b), we give two instances of these second-order processes, where s, t, and q represent the singlet, triplet, and quintet states, respectively. The Process in Fig. B.2(a) is similar to the correlated hoppings appearing in the Heisenberg model on the Shastry–Sutherland lattice [75, 76]. The one in Fig. B.2(b) shows the pair-creation of spin-1 bosons (triplets).

When we deal with these perturbation processes over three dimers, we see the validity of expressing the low-energy states only by the singlet and triplet states. We show the energy diagram of the three isolated spin-1 dimers ($J' = J'' = 0$), $E(\alpha,\beta,\gamma)$ with $\alpha,\beta,\gamma = s,t,q$, in Fig. B.2(c). We find that at $B/J = 0$ the (s,s,q) and (t,t,t) states are degenerate, while these two states are well separated in introducing a small $B/J > 0$.

Then, we compare the energies of the ground states of the effective Hamiltonian $\mathcal{H}_{\rm eff}$ (Eq. (3.7)) with and without the three-dimer term $\mathcal{H}_{\rm 3body}$, and those of the original spin-1 dimer Hamiltonian $\mathcal{H}$ (Eq. (3.1)). We performed the numerical diagonalization on the nine-dimer triangular lattice under the periodic boundary condition. The results at $B/J = 0.2$ are shown in Fig. B.3(a) and (b), and those at $B/J = 0.4$ are shown in Fig. B.3(c) and

(d). The inter-dimer interaction parameters are fixed as $(J' + J'')/J = +0.2$ and -0.2. We see that the energies of $\mathcal{H}_{\rm eff}$ with $\mathcal{H}_{\rm 3body}$ do not always take closer values to those of $\mathcal{H}$ than those of $\mathcal{H}_{\rm eff}$ without $\mathcal{H}_{\rm 3body}$ though $\mathcal{H}_{\rm eff}$ with $\mathcal{H}_{\rm 3body}$ fully incorporate the effect of the second-order perturbation terms. We found that the energies are in good agreement with each other when $|J'/J|, |J''/J| \lesssim 0.2$. When either J'/J or J''/J takes a large value, the effective model might not qualitatively reproduce the original model. This would be because the three-dimer interactions which appear at the higher order perturbation terms in J'/J and J''/J may cancel out the ones appearing at the second order.

As we mentioned in the main text, the overall structure of the phase diagram is determined by the terms up to the first order, and the second-order perturbation terms do not qualitatively affect on the ground state properties. Therefore, even when $\mathcal{H}_{\rm 3body} = 0$, the results are not largely changed. The benefit of dealing with the Hamiltonian $\mathcal{H}_{\rm eff}$ in a simpler form is that it exactly corresponds to the spin-1 boson model derived from the spin-1/2 dimer models [84, 86], and thus the two kinds of the models with different spin quantum numbers can be treated on an equal footing.

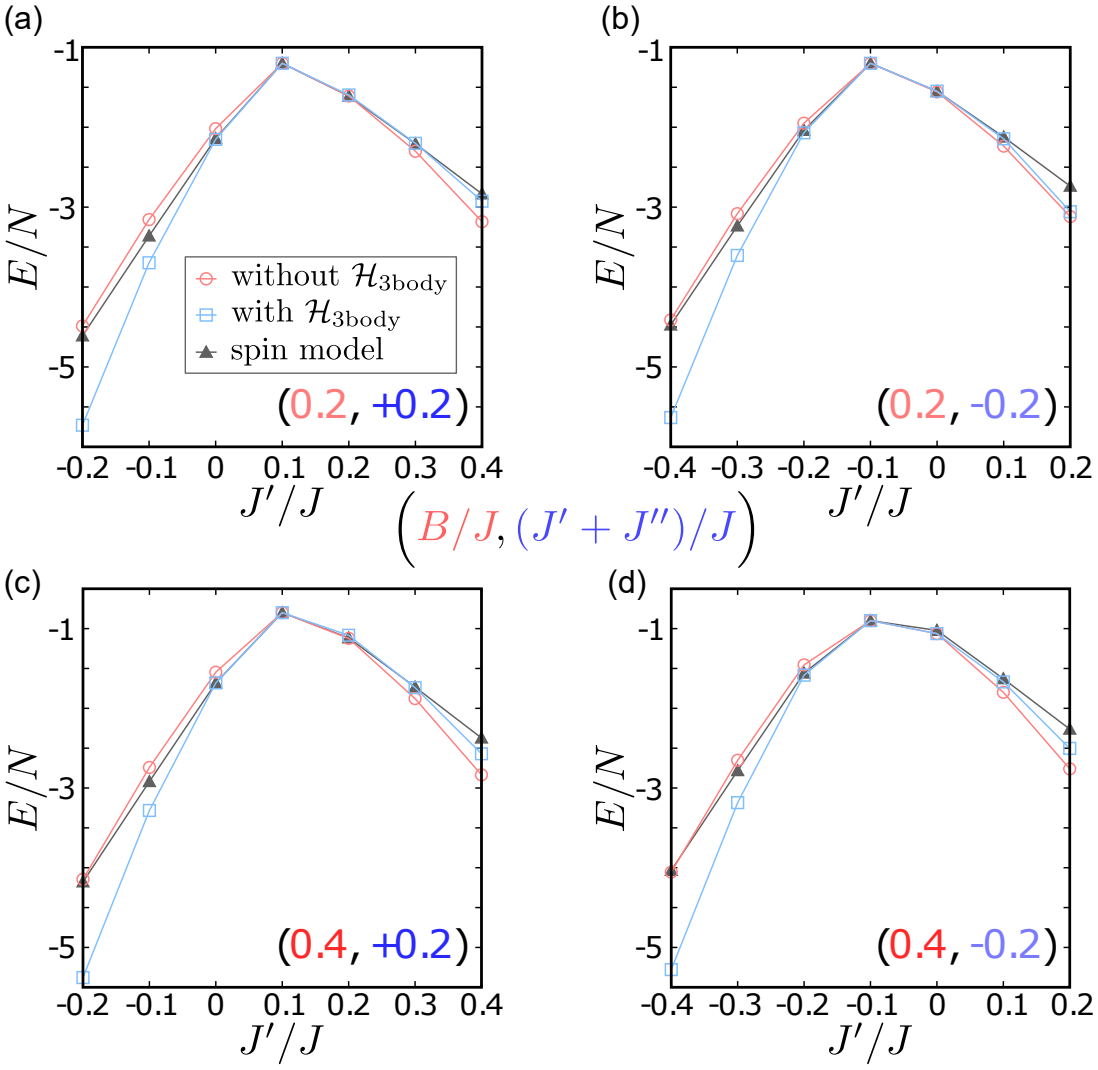

Figure B.3: J'/J dependence of the energies of the ground states of the effective boson model $\mathcal{H}_{\mathrm{eff}}$ with (open square) and without (open circle) the three-dimer interactions $\mathcal{H}_{3\mathrm{body}}$, and of the original spin model $\mathcal{H}$ (filled triangle) on the nine-dimer triangular lattice under the periodic boundary condition at $(B/J, (J'+J'')/J) =$ (a) (0.2, +0.2), (b) (0.2, -0.2), (c) (0.4, +0.2), and (d) (0.4, -0.2). Figures are taken from Ref. [2] (Copyright ©2020, American Physical Society).

Appendix C

Details on the numerical diagonalizations

In this Appendix, we note the details on the numerical diagonalization methods used in this thesis, the Lanczos method and the thick-restart Lanczos method.

C.1 Lanczos method

To write this section, we partly referred to Refs. [135, 202].

C.1.1 Overview

Lanczos method [165] is the Arnordi method for the Hermite matrices [202]. The Arnordi method is the application to the Krylov subspace of the Rayleigh–Ritz method, a method calculating the approximated eigenvalues and eigenvectors of a matrix, A. The Krylov subspace is spanned by the vectors calculated by multiplying A to some initial vector, $\boldsymbol{v}$, namely, $\left\{\boldsymbol{v}, A\boldsymbol{v}, A^2\boldsymbol{v}, \cdots\right\}$.

C.1.2 Algorithm

Let the initial vector $\boldsymbol{u}_0$, and we calculate $\{\alpha_i\}_{i=1,\cdots,m}$ and $\{\beta_i\}_{j=1,\cdots,m-1}$ as follows;

$$\boldsymbol{v} = A\boldsymbol{u}_0, \tag{C.1}$$

$$\alpha_i = {}^t\boldsymbol{u}_{i-1}\boldsymbol{v}, \tag{C.2}$$

$$\beta_i = \left\|\boldsymbol{v} - \alpha_i\boldsymbol{u}_{i-1} - \beta_{i-1}\boldsymbol{u}_{i-2}\right\|, \tag{C.3}$$

$$\boldsymbol{u}_i = \frac{1}{\beta_i}\left(\boldsymbol{v} - \alpha_i\boldsymbol{u}_{i-1} - \beta_{i-1}\boldsymbol{u}_{i-2}\right). \tag{C.4}$$

Then, the tridiagonal matrix consisting of $\{\alpha_i\}_{i=1,\cdots,m}$ and $\{\beta_i\}_{j=1,\cdots,m-1}$,

$$T_m = \begin{pmatrix} \alpha_1 & \beta_1 & 0 & \cdots & 0 \\ \beta_1 & \alpha_1 & \beta_2 & \ddots & \vdots \\ 0 & \beta_2 & \ddots & \ddots & 0 \\ \vdots & \ddots & \ddots & \ddots & \beta_{m-1} \\ 0 & \cdots & 0 & \beta_{m-1} & \alpha_m \end{pmatrix}, \tag{C.5}$$

is diagonalized. This iteration process is repeated until the eigenvalues of T_m converge. Then, the eigenvalues of $\{e_i\}_{i=1,\cdots,m}$, gives the eigenvalues of the original matrix. Using the eigenvector of T_m corresponding to e_i, $\boldsymbol{y}_i$, the eigenvectors of the original matrix, $\boldsymbol{w}_i$, is given by calculating the Ritz vector,

$$\boldsymbol{w}_i = \begin{pmatrix} \boldsymbol{u}_0 & \boldsymbol{u}_1 & \cdots & \boldsymbol{u}_{m-1} \end{pmatrix} \boldsymbol{y}_i. \tag{C.6}$$

It should be noted that the eigenvalues and eigenvectors found in this standard Lanczos method are usually correct only for a few smallest (or largest) eigenvalues.

C.1.3 Remarks

In the iteration process of the Lanczos method, theoretically, the Lanczos vectors $\{\boldsymbol{u}_i\}_{i=0,\cdots}$ are orthonormalized. Practically, however, the orthogonality of the Lanczos vectors sometimes breaks down, and we need to reorthonormalize the Lanczos vectors using some methods such as the Gram–Schmidt reorthonormalization.

The standard Gram–Schmidt reorthonormalization correctly gives a set of the orthonormalized vectors in theory (Algorithm 1). However, numerically, the conventional Gram–Schmidt reorthonormalization sometimes does not work well due to the round-off errors. Thus, in practice, the modified Gram–Schmidt orthonormalization method (Algorithm 2) is applied to reorthonormalize the vectors [202]. Algorithms 1 and 2 are cited from Ref. [202].

Algorithm 1 Algorithm of the standard Gram–Schmidt reorthonormalization.

for $i = 1, n$ **do**
  $\boldsymbol{v}_i = \boldsymbol{a}_i$
  for $j = 1, i-1$ **do**
    $\boldsymbol{v}_i = \boldsymbol{v}_i - \left({}^t\boldsymbol{a}_i\ \boldsymbol{e}_j\right) \boldsymbol{e}_j$
  end for
  $\boldsymbol{e}_i = \dfrac{\boldsymbol{v}_i}{\|\boldsymbol{v}_i\|}$
end for

C.2 Thick-restart Lanczos method

C.2.1 Overview

The thick-restart Lanczos method is an algorithm to calculate the multiple eigenvalues and eigenvectors of the real symmetric matrices proposed by Wu and Simon [166, 167].

Algorithm 2 Algorithm of the modified Gram–Schmidt reorthonormalization.

for $i = 1, n$ **do**
  $\boldsymbol{e}_i = \dfrac{\boldsymbol{v}_i}{\|\boldsymbol{v}_i\|}$
  for $j = i+1, n$ **do**
    $\boldsymbol{v}_j = \boldsymbol{v}_j - \left({}^t\boldsymbol{v}_j\ \boldsymbol{e}_i\right)\boldsymbol{e}_i$
  end for
end for

Instead of using one vector in the usual Lanczos method (Sec. C.1), this method uses a set of multiple vectors, which ensures the accuracy of the multiple eigenvalues and the eigenstates. Also, the iteration process is cut off at some numbers, and the generated vectors are reused as the set of the initial vectors in the next iteration process.

The thick-restart Lanczos method is mathematically equivalent to the implicitly restart Lanczos method [167].

C.2.2 Algorithm

We write the algorithm of the thick-restart Lanczos method following Ref. [167]. Let the number of vectors in the restart, or the numbers of eigenvalues and eigenvectors we want, k, and the largest number of iterations, or the number of the linearly independent vectors in the Krylov subspace, m.

C.2.2.1 First step

First we perform the standard Lanczos method. Let the initial vector $\boldsymbol{u}_0$, and we calculate $\{\alpha_i\}_{i=1,\cdots,m}$ and $\{\beta_j\}_{j=1,\cdots,m-1}$. Here we keep all of the Lanczos vectors $\{\boldsymbol{u}_k\}_{k=0,\cdots,m}$ and perform the modified Gram–Schmidt reorthonormalization. Then, we construct the tridiagonal matrix T_m using the sets of $\{\alpha_i\}_{i=1,\cdots,m}$ and $\{\beta_j\}_{j=1,\cdots,m-1}$ as

$$T_m = \begin{pmatrix} \alpha_1 & \beta_1 & 0 & \cdots & 0 \\ \beta_1 & \alpha_1 & \beta_2 & \ddots & \vdots \\ 0 & \beta_2 & \ddots & \ddots & 0 \\ \vdots & \ddots & \ddots & \ddots & \beta_{m-1} \\ 0 & \cdots & 0 & \beta_{m-1} & \alpha_m \end{pmatrix}, \tag{C.7}$$

and diagonalize T_m. The eigenvalues of T_m is written as e_i, and the eigenvector corresponding to e_i is written as $\boldsymbol{y}_i$. $m \times k$ matrix using $\boldsymbol{y}_i$ is defined as $Y = \begin{pmatrix} \boldsymbol{y}_1 & \cdots & \boldsymbol{y}_k \end{pmatrix}$.

C.2.2.2 Restart

Next we restart the Lanczos calculations. The quantities in the restart process is distinguished from those in the first step by using $\hat{\bullet}$. We keep k-pairs of eigenvalues and eigenvectors $\{(e_i, \boldsymbol{y}_i)\}_{i=1,\cdots,k}$, and calculate the set of the approximated eigenvectors of A,

$\{\hat{\boldsymbol{u}}_i\}_{i=0,\cdots,k-1}$ as

$$\hat{\boldsymbol{u}}_i = \begin{pmatrix} \boldsymbol{u}_0 & \cdots & \boldsymbol{u}_{m-1} \end{pmatrix} \boldsymbol{y}_{i+1}. \tag{C.8}$$

Then, k-th vector, $\hat{\boldsymbol{u}}_k$, is set as

$$\hat{\boldsymbol{u}}_k = \boldsymbol{u}_m, \tag{C.9}$$

and $k+2$-th vector, $\hat{\boldsymbol{u}}_{k+1}$, is calculated as

$$\boldsymbol{v} = A\hat{\boldsymbol{u}}_k \,(= A\boldsymbol{u}_k)\,, \tag{C.10}$$

$$\hat{\alpha}_{k+1} = {}^t\hat{\boldsymbol{u}}_k \boldsymbol{v} \left(= {}^t\boldsymbol{u}_k A \boldsymbol{u}_k\right), \tag{C.11}$$

$$\hat{\beta}_{k+1} = \left\| \boldsymbol{v} - \hat{\alpha}_{k+1}\hat{\boldsymbol{u}}_k - \sum_{i=0}^{k-1} \beta_{i+1}\hat{\boldsymbol{u}}_i \right\|, \tag{C.12}$$

$$\hat{\boldsymbol{u}}_{k+1} = \frac{1}{\hat{\beta}_{k+1}} \left(\boldsymbol{v} - \hat{\alpha}_{k+1}\hat{\boldsymbol{u}}_k - \sum_{i=0}^{k-1} \beta_{i+1}\hat{\boldsymbol{u}}_i \right). \tag{C.13}$$

Notice that there is a difference from the standard Lanczos method in the calculation of $\hat{\boldsymbol{u}}_{k+1}$. Then we perform the same iteration as the standard Lanczos method, namely, we calculate

$$\boldsymbol{v} = A\hat{\boldsymbol{u}}_{i-1}, \tag{C.14}$$

$$\hat{\alpha}_i = {}^t\hat{\boldsymbol{u}}_{i-1} \boldsymbol{v} \left(= {}^t\hat{\boldsymbol{u}}_{i-1} A \hat{\boldsymbol{u}}_{i-1}\right), \tag{C.15}$$

$$\hat{\beta}_i = \left\| \boldsymbol{v} - \hat{\alpha}_i\hat{\boldsymbol{u}}_{i-1} - \hat{\beta}_{i-1}\hat{\boldsymbol{u}}_{i-2} \right\|, \tag{C.16}$$

$$\hat{\boldsymbol{u}}_i = \frac{1}{\hat{\beta}_i} \left(\boldsymbol{v} - \hat{\alpha}_i\hat{\boldsymbol{u}}_{i-1} - \hat{\beta}_{i-1}\hat{\boldsymbol{u}}_{i-2} \right), \tag{C.17}$$

for $i = k+2, k+3, \cdots$. However, we diagonalize not the tridiagonalized matrix but $\hat{T}_{k+i}$ given by

$$\hat{T}_{k+i} = \begin{pmatrix} \hat{T}_k & \beta_m \boldsymbol{s} & \boldsymbol{0}_m & \cdots & \cdots & \cdots & \boldsymbol{0}_m \\ \beta_m {}^t\boldsymbol{s} & \hat{\alpha}_{k+1} & \hat{\beta}_{k+1} & 0 & \cdots & \cdots & 0 \\ {}^t\boldsymbol{0}_m & \hat{\beta}_{k+1} & \hat{\alpha}_{k+2} & \hat{\beta}_{k+2} & 0 & \cdots & 0 \\ \vdots & 0 & \hat{\beta}_{k+2} & \ddots & \ddots & \ddots & \vdots \\ \vdots & \vdots & \ddots & \ddots & \ddots & \ddots & 0 \\ \vdots & \vdots & \ddots & \ddots & \ddots & \ddots & \hat{\beta}_{k+i-1} \\ {}^t\boldsymbol{0}_m & 0 & \cdots & \cdots & 0 & \hat{\beta}_{k+i-1} & \hat{\alpha}_{k+i} \end{pmatrix}. \tag{C.18}$$

Here, $\hat{T}_k$, $\mathbf{0}_m$, and $\boldsymbol{s}$ are given as

$$\hat{T}_k := {}^tY T_m Y = \begin{pmatrix} e_1 & 0 & \cdots & 0 \\ 0 & e_2 & \ddots & \vdots \\ \vdots & \ddots & \ddots & 0 \\ 0 & \cdots & 0 & e_k \end{pmatrix},$$

$$\mathbf{0}_m := \left.\begin{pmatrix} 0 \\ \vdots \\ 0 \end{pmatrix}\right\} m,$$

$$\boldsymbol{s} := {}^tY \left.\begin{pmatrix} 0 \\ \vdots \\ 0 \\ 1 \end{pmatrix}\right\} m = \begin{pmatrix} {}^t\boldsymbol{y}_1 \\ \vdots \\ {}^t\boldsymbol{y}_k \end{pmatrix} \begin{pmatrix} 0 \\ \vdots \\ 0 \\ 1 \end{pmatrix} = \begin{pmatrix} y_{1m} \\ \vdots \\ y_{km} \end{pmatrix}, \tag{C.19}$$

respectively. To unify the notations, we introduce $\hat{\alpha}_i$ and $\hat{\beta}_i$ $(i = 1, \cdots, k)$ as

$$\hat{\alpha}_i = e_i, \qquad \hat{\beta}_i = \beta_m y_{im}, \tag{C.20}$$

and then $\hat{T}_{k+i}$ is rewritten as

$$\hat{T}_{k+i} = \begin{pmatrix} \hat{\alpha}_1 & 0 & \cdots & 0 & \hat{\beta}_1 & 0 & \cdots & 0 \\ 0 & \hat{\alpha}_2 & \ddots & \vdots & \hat{\beta}_2 & 0 & \cdots & 0 \\ \vdots & \ddots & \ddots & 0 & \vdots & \vdots & \ddots & \vdots \\ 0 & \cdots & 0 & \hat{\alpha}_k & \hat{\beta}_k & 0 & \ddots & 0 \\ \hat{\beta}_1 & \hat{\beta}_2 & \cdots & \hat{\beta}_k & \hat{\alpha}_{k+1} & \hat{\beta}_{k+1} & \ddots & \vdots \\ 0 & \cdots & \cdots & 0 & \hat{\beta}_{k+1} & \ddots & \ddots & 0 \\ \vdots & \ddots & \ddots & \vdots & \ddots & \ddots & \ddots & \hat{\beta}_{k+i-1} \\ 0 & \cdots & \cdots & 0 & \cdots & 0 & \hat{\beta}_{k+i-1} & \hat{\alpha}_{k+i} \end{pmatrix}. \tag{C.21}$$

We diagonalize $\hat{T}_{k+i}$, and obtain the eigenvalues and eigenvectors.

When we perform the restart again, T_m is replaced by $\hat{T}_m$, and perform the same calculation written above. When the eigenvalues are converged for T_l, the set of eigenvectors of the original matrix, $\{\boldsymbol{w}_i\}_{i=1,\cdots,k}$, is calculated using the Lanczos vectors $\{\hat{\boldsymbol{u}}_i\}_{i=0,\cdots,l-1}$ and the eigenvectors of $\hat{T}_l$, $\{\boldsymbol{y}_i\}_{i=1,\cdots,k}$,

$$\begin{pmatrix} \boldsymbol{w}_1 & \cdots & \boldsymbol{w}_k \end{pmatrix} = \begin{pmatrix} \hat{\boldsymbol{u}}_0 & \hat{\boldsymbol{u}}_1 & \cdots & \hat{\boldsymbol{u}}_{l-1} \end{pmatrix} \begin{pmatrix} \boldsymbol{y}_1 & \cdots & \boldsymbol{y}_k \end{pmatrix}. \tag{C.22}$$

C.2.3 Remarks

Similarly to the standard Lanczos method, the reorthonormalization of the Lanczos vectors are sometimes needed because of the round-off errors, and the way of the reorthonormalization affects the calculation results in the thick-restart Lanczos method. According to Ref. [167], "full reorthonormalization", in which all of the Lanczos vectors are re-

orthonormalized, correctly gives all the eigenvalues and the eigenvectors. Also, in "partial reorthonormalization", where a part of the Lanczos vectors are reorthonormalized, only the eigenvalues are correctly calculated. In our calculation, "full reorthonormalization" is performed.

Bibliography

[1] K. Tanaka and C. Hotta, "Finite-temperature thermodynamic properties of spin-1 nematics in an applied magnetic field," Phys. Rev. B **102**, 140401 (2020).

[2] K. Tanaka and C. Hotta, "Multiple quadrupolar or nematic phases driven by the Heisenberg interactions in a spin-1 dimer system forming a bilayer," Phys. Rev. B **101**, 094422 (2020).

[3] K. Tanaka, Y. Yokoyama, and C. Hotta, "Origin of Biquadratic Exchange Interactions in a Mott Insulator as a Driving Force of Spin Nematic Order," J. Phys. Soc. Jpn. **87**, 023702 (2018).

[4] J. Valasek, "Piezo-Electric and Allied Phenomena in Rochelle Salt," Phys. Rev. **17**, 475–481 (1921).

[5] K. I. Kugel and D. I. Khomskii, "Crystal structure and magnetic properties of substances with orbital degeneracy," Sov. Phys. JETP **37**, 725 (1973), [Zh. Eksp. Teor. Fiz. **64**, 1429 (1973)].

[6] K. I. Kugel and D. I. Khomskii, "The Jahn-Teller effect and magnetism: transition metal compounds," Sov. Phys. Usp. **25**, 231 (1982), [Usp. Fiz. Nauk **136**, 621 (1982)].

[7] Y. Kuramoto, H. Kusunose, and A. Kiss, "Multipole Orders and Fluctuations in Strongly Correlated Electron Systems," J. Phys. Soc. Jpn. **78**, 072001 (2009), https://doi.org/10.1143/JPSJ.78.072001 .

[8] N. A. Spaldin, M. Fiebig, and M. Mostovoy, "The toroidal moment in condensed-matter physics and its relation to the magnetoelectric effect," J. Phys.: Condens. Matter **20**, 434203 (2008).

[9] S. Hayami, H. Kusunose, and Y. Motome, "Toroidal order in metals without local inversion symmetry," Phys. Rev. B **90**, 024432 (2014).

[10] S. Hayami and H. Kusunose, "Microscopic Description of Electric and Magnetic Toroidal Multipoles in Hybrid Orbitals," J. Phys. Soc. Jpn. **87**, 033709 (2018), https://doi.org/10.7566/JPSJ.87.033709 .

[11] S. Hayami, M. Yatsushiro, Y. Yanagi, and H. Kusunose, "Classification of atomic-scale multipoles under crystallographic point groups and application to linear response tensors," Phys. Rev. B **98**, 165110 (2018).

[12] H. Watanabe and Y. Yanase, "Group-theoretical classification of multipole order: Emergent responses and candidate materials," Phys. Rev. B **98**, 245129 (2018).

[13] H. Saito, K. Uenishi, N. Miura, C. Tabata, H. Hidaka, T. Yanagisawa, and H. Amitsuka, "Evidence of a New Current-Induced Magnetoelectric Effect in a Toroidal Magnetic Ordered State of UNi_4B," J. Phys. Soc. Jpn. **87**, 033702 (2018), https://doi.org/10.7566/JPSJ.87.033702 .

[14] M. Blume and Y. Y. Hsieh, "Biquadratic Exchange and Quadrupolar Ordering," J. Appl. Phys. **40**, 1249–1249 (1969).

[15] H. H. Chen and P. M. Levy, "Quadrupole Phase Transitions in Magnetic Solids," Phys. Rev. Lett. **27**, 1383–1385 (1971).

[16] A. F. Andreev and I. A. Grishchuk, "Spin nematics," Sov. Phys. JETP **60**, 267 (1984), [Zh. Eksp. Teor. Fiz. **87**, 467 (1984)].

[17] K. Penc and A. M. Läuchli, "Spin Nematic Phases in Quantum Spin Systems," in Introduction to Frustrated Magnetism, edited by C. Lacroix, P. Mendels, and F. Mila (Springer-Verlag Berlin Heidelberg, 2011) Chap. 13, p. 331.

[18] B. A. Ivanov and A. K. Kolezhuk, "Effective field theory for the $S = 1$ quantum nematic," Phys. Rev. B **68**, 052401 (2003).

[19] A. Läuchli, F. Mila, and K. Penc, "Quadrupolar Phases of the $S = 1$ Bilinear-Biquadratic Heisenberg Model on the Triangular Lattice," Phys. Rev. Lett. **97**, 087205 (2006), Erratum: Phys. Rev. Lett. 97, 229901 (2006).

[20] S. Hu, A. M. Turner, K. Penc, and F. Pollmann, "Berry-Phase-Induced Dimerization in One-Dimensional Quadrupolar Systems," Phys. Rev. Lett. **113**, 027202 (2014).

[21] A. V. Chubukov, "Spontaneous dimerization in quantum-spin chains," Phys. Rev. B **43**, 3337–3344 (1991).

[22] R. Moessner, S. L. Sondhi, and E. Fradkin, "Short-ranged resonating valence bond physics, quantum dimer models, and Ising gauge theories," Phys. Rev. B **65**, 024504 (2001).

[23] T. Grover and T. Senthil, "Quantum Spin Nematics, Dimerization, and Deconfined Criticality in Quasi-1D Spin-One Magnets," Phys. Rev. Lett. **98**, 247202 (2007).

[24] F. D. M. Haldane, Private communication.

[25] A. Läuchli, G. Schmid, and S. Trebst, "Spin nematics correlations in bilinear-biquadratic $S = 1$ spin chains," Phys. Rev. B **74**, 144426 (2006).

[26] K. Harada and N. Kawashima, "Quadrupolar order in isotropic Heisenberg models with biquadratic interaction," Phys. Rev. B **65**, 052403 (2002).

[27] N. Papanicolaou, "Unusual phases in quantum spin-1 systems," Nucl. Phys. B **305**, 367–395 (1988).

[28] K. Tanaka, A. Tanaka, and T. Idogaki, "Long-range order in the ground state of the $S = 1$ isotropic bilinear-biquadratic exchange Hamiltonian," J. Phys. A: Math. Gen. **34**, 8767 (2001).

[29] I. Niesen and P. Corboz, "A tensor network study of the complete ground state phase diagram of the spin-1 bilinear-biquadratic Heisenberg model on the square lattice," SciPost Phys. **3**, 030 (2017).

[30] T. A. Tóth, A. M. Läuchli, F. Mila, and K. Penc, "Competition between two- and three-sublattice ordering for $S = 1$ spins on the square lattice," Phys. Rev. B **85**, 140403 (2012).

[31] J. Oitmaa and C. J. Hamer, "$S = 1$ bilinear biquadratic spin model on the square lattice: A series expansion study," Phys. Rev. B **87**, 224431 (2013).

[32] S. Nakatsuji, Y. Nambu, H. Tonomura, O. Sakai, S. Jonas, C. Broholm, H. Tsunetsugu, Y. Qiu, and Y. Maeno, "Spin Disorder on a Triangular Lattice," Science **309**, 1697–1700 (2005), http://science.sciencemag.org/content/309/5741/1697.full.pdf .

[33] H. Tsunetsugu and M. Arikawa, "Spin Nematic Phase in S=1 Triangular Antiferromagnets," J. Phys. Soc. Jpn. **75**, 083701 (2006).

[34] H. Tsunetsugu and M. Arikawa, "The spin nematic state in triangular antiferromagnets," J. Phys.: Condens. Matter **19**, 145248 (2007).

[35] S. Bhattacharjee, V. B. Shenoy, and T. Senthil, "Possible ferro-spin nematic order in $NiGa_2S_4$," Phys. Rev. B **74**, 092406 (2006).

[36] M. Moreno-Cardoner, H. Perrin, S. Paganelli, G. De Chiara, and A. Sanpera, "Case study of the uniaxial anisotropic spin-1 bilinear-biquadratic Heisenberg model on a triangular lattice," Phys. Rev. B **90**, 144409 (2014).

[37] T. Liu, W. Li, A. Weichselbaum, J. von Delft, and G. Su, "Simplex valence-bond crystal in the spin-1 kagome Heisenberg antiferromagnet," Phys. Rev. B **91**, 060403 (2015).

[38] H. J. Changlani and A. M. Läuchli, "Trimerized ground state of the spin-1 heisenberg antiferromagnet on the kagome lattice," Phys. Rev. B **91**, 100407 (2015).

[39] H. H. Zhao, C. Xu, Q. N. Chen, Z. C. Wei, M. P. Qin, G. M. Zhang, and T. Xiang, "Plaquette order and deconfined quantum critical point in the spin-1 bilinear-biquadratic Heisenberg model on the honeycomb lattice," Phys. Rev. B **85**, 134416 (2012).

[40] O. Tchernyshyov, R. Moessner, and S. L. Sondhi, "Order by Distortion and String Modes in Pyrochlore Antiferromagnets," Phys. Rev. Lett. **88**, 067203 (2002).

[41] O. Tchernyshyov, R. Moessner, and S. L. Sondhi, "Spin-Peierls phases in pyrochlore antiferromagnets," Phys. Rev. B **66**, 064403 (2002).

[42] H. Ueda, H. A. Katori, H. Mitamura, T. Goto, and H. Takagi, "Magnetic-Field Induced Transition to the 1/2 Magnetization Plateau State in the Geometrically Frustrated Magnet $CdCr_2O_4$," Phys. Rev. Lett. **94**, 047202 (2005).

[43] H. Ueda, H. Mitamura, T. Goto, and Y. Ueda, "Successive field-induced transitions in a frustrated antiferromagnet $HgCr_2O_4$," Phys. Rev. B **73**, 094415 (2006).

[44] A. Miyata, H. Ueda, Y. Ueda, H. Sawabe, and S. Takeyama, "Magnetic Phases of a Highly Frustrated Magnet, $ZnCr_2O_4$, up to an Ultrahigh Magnetic Field of 600 T," Phys. Rev. Lett. **107**, 207203 (2011).

[45] K. Penc, N. Shannon, and H. Shiba, "Half-Magnetization Plateau Stabilized by Structural Distortion in the Antiferromagnetic Heisenberg Model on a Pyrochlore Lattice," Phys. Rev. Lett. **93**, 197203 (2004).

[46] N. Shannon, K. Penc, and Y. Motome, "Nematic, vector-multipole, and plateau-liquid states in the classical $O(3)$ pyrochlore antiferromagnet with biquadratic interactions in applied magnetic field," Phys. Rev. B **81**, 184409 (2010).

[47] E. Takata, T. Momoi, and M. Oshikawa, "Nematic ordering in pyrochlore antiferromagnets: high-field phase of chromium spinel oxides," (2015), arXiv:1510.02373 .

[48] A. Völl and S. Wessel, "Spin dynamics of the bilinear-biquadratic $S = 1$ Heisenberg model on the triangular lattice: A quantum Monte Carlo study," Phys. Rev. B **91**, 165128 (2015).

[49] E. M. Stoudenmire, S. Trebst, and L. Balents, "Quadrupolar correlations and spin freezing in $S = 1$ triangular lattice antiferromagnets," Phys. Rev. B **79**, 214436 (2009).

[50] R. K. Kaul, "Spin nematic ground state of the triangular lattice $S = 1$ biquadratic model," Phys. Rev. B **86**, 104411 (2012).

[51] N. Shannon, T. Momoi, and P. Sindzingre, "Nematic Order in Square Lattice Frustrated Ferromagnets," Phys. Rev. Lett. **96**, 027213 (2006).

[52] H. T. Ueda and K. Totsuka, "Ground-state phase diagram and magnetic properties of a tetramerized spin-1/2 J_1–J_2 model: BEC of bound magnons and absence of the transverse magnetization," Phys. Rev. B **76**, 214428 (2007).

[53] R. Shindou and T. Momoi, "$SU(2)$ slave-boson formulation of spin nematic states in $S = \frac{1}{2}$ frustrated ferromagnets," Phys. Rev. B **80**, 064410 (2009).

[54] R. Shindou, S. Yunoki, and T. Momoi, "Projective studies of spin nematics in a quantum frustrated ferromagnet," Phys. Rev. B **84**, 134414 (2011).

[55] R. Shindou, S. Yunoki, and T. Momoi, "Dynamical spin structure factors of quantum spin nematic states," Phys. Rev. B **87**, 054429 (2013).

[56] E. E. Kaul, H. Rosner, N. Shannon, R. V. Shpanchenko, and C. Geibel, "Evidence for a frustrated square lattice with ferromagnetic nearest-neighbor interaction in the new compound $Pb_2VO(PO_4)_2$," J. Mag. Mag. Mater. **272-276**, 922 – 923 (2004), Proceedings of the International Conference on Magnetism (ICM 2003).

[57] H. Kageyama, T. Kitano, N. Oba, M. Nishi, S. Nagai, K. Hirota, L. Viciu, J. B. Wiley, J. Yasuda, Y. Baba, Y. Ajiro, and K. Yoshimura, "Spin-Singlet Ground State in Two-Dimensional $S = 1/2$ Frustrated Square Lattice: $(CuCl)LaNb_2O_7$," J. Phys. Soc. Jpn. **74**, 1702–1705 (2005), https://doi.org/10.1143/JPSJ.74.1702 .

[58] T. Momoi, P. Sindzingre, and K. Kubo, "Spin Nematic Order in Multiple-Spin Exchange Models on the Triangular Lattice," Phys. Rev. Lett. **108**, 057206 (2012).

[59] K. Ishida, M. Morishita, K. Yawata, and H. Fukuyama, "Low Temperature Heat-Capacity Anomalies in Two-Dimensional Solid ^3He," Phys. Rev. Lett. **79**, 3451–3454 (1997).

[60] R. Masutomi, Y. Karaki, and H. Ishimoto, "Gapless Spin Liquid Behavior in Two-Dimensional Solid ^{3}He," Phys. Rev. Lett. **92**, 025301 (2004).

[61] T. Momoi and N. Shannon, "Nematic Order in the Multiple-Spin Exchange Model on the Triangular Lattice," Prog. Theor. Phys. Suppl. **159**, 72–76 (2005).

[62] T. Momoi, P. Sindzingre, and N. Shannon, "Octupolar Order in the Multiple Spin Exchange Model on a Triangular Lattice," Phys. Rev. Lett. **97**, 257204 (2006).

[63] F. Heidrich-Meisner, A. Honecker, and T. Vekua, "Frustrated ferromagnetic spin-$\frac{1}{2}$ chain in a magnetic field: The phase diagram and thermodynamic properties," Phys. Rev. B **74**, 020403 (2006).

[64] L. Kecke, T. Momoi, and A. Furusaki, "Multimagnon bound states in the frustrated ferromagnetic one-dimensional chain," Phys. Rev. B **76**, 060407 (2007).

[65] T. Vekua, A. Honecker, H.-J. Mikeska, and F. Heidrich-Meisner, "Correlation functions and excitation spectrum of the frustrated ferromagnetic spin-$\frac{1}{2}$ chain in an external magnetic field," Phys. Rev. B **76**, 174420 (2007).

[66] T. Hikihara, L. Kecke, T. Momoi, and A. Furusaki, "Vector chiral and multipolar orders in the spin-$\frac{1}{2}$ frustrated ferromagnetic chain in magnetic field," Phys. Rev. B **78**, 144404 (2008).

[67] J. Sudan, A. Lüscher, and A. M. Läuchli, "Emergent multipolar spin correlations in a fluctuating spiral: The frustrated ferromagnetic spin-$\frac{1}{2}$ Heisenberg chain in a magnetic field," Phys. Rev. B **80**, 140402 (2009).

[68] M. E. Zhitomirsky and H. Tsunetsugu, "Magnon pairing in quantum spin nematic," Europhys. Lett. **92**, 37001 (2010).

[69] H. Onishi, "Magnetic Excitations of Spin Nematic State in Frustrated Ferromagnetic Chain," J. Phys. Soc. Jpn. **84**, 083702 (2015), https://doi.org/10.7566/JPSJ.84.083702 .

[70] H. T. Ueda and K. Totsuka, "Magnon Bose-Einstein condensation and various phases of three-dimensonal quantum helimagnets under high magnetic field," Phys. Rev. B **80**, 014417 (2009).

[71] M. Sato, T. Hikihara, and T. Momoi, "Spin-Nematic and Spin-Density-Wave Orders in Spatially Anisotropic Frustrated Magnets in a Magnetic Field," Phys. Rev. Lett. **110**, 077206 (2013).

[72] T. Hikihara and S. Yamamoto, "Magnetic Phase Diagram of Spin-1/2 Two-Leg Ladder with Four-Spin Ring Exchanges," J. Phys. Soc. Jpn. **77**, 014709 (2008).

[73] B. S. Shastry and B. Sutherland, "Exact ground state of a quantum mechanical antiferromagnet," Physica B+C **108**, 1069 – 1070 (1981).

[74] S. Miyahara and K. Ueda, "Exact Dimer Ground State of the Two Dimensional Heisenberg Spin System $SrCu_2(BO_3)_2$," Phys. Rev. Lett. **82**, 3701–3704 (1999).

[75] T. Momoi and K. Totsuka, "Magnetization plateaus of the Shastry-Sutherland model for $SrCu_2(BO_3)_2$: Spin-density wave, supersolid, and bound states," Phys. Rev. B **62**, 15067–15078 (2000).

[76] T. Momoi and K. Totsuka, "Magnetization plateaus as insulator-superfluid transitions in quantum spin systems," Phys. Rev. B **61**, 3231–3234 (2000).

[77] Y. Fukumoto, "Two-Triplet-Dimer Excitation Spectra in the Shastry-Sutherland Model for $SrCu_2(BO_3)_2$," J. Phys. Soc. Jpn. **69**, 2755–2758 (2000), https://doi.org/10.1143/JPSJ.69.2755 .

[78] C. Knetter, A. Bühler, E. Müller-Hartmann, and G. S. Uhrig, "Dispersion and Symmetry of Bound States in the Shastry-Sutherland Model," Phys. Rev. Lett. **85**, 3958–3961 (2000).

[79] K. Totsuka, S. Miyahara, and K. Ueda, "Low-Lying Magnetic Excitation of the Shastry-Sutherland Model," Phys. Rev. Lett. **86**, 520–523 (2001).

[80] Z. Wang and C. D. Batista, "Dynamics and Instabilities of the Shastry-Sutherland Model," Phys. Rev. Lett. **120**, 247201 (2018).

[81] A. Läuchli, J. C. Domenge, C. Lhuillier, P. Sindzingre, and M. Troyer, "Two-Step Restoration of SU(2) Symmetry in a Frustrated Ring-Exchange Magnet," Phys. Rev. Lett. **95**, 137206 (2005).

[82] P. Chandra and P. Coleman, "Quantum spin nematics: Moment-free magnetism," Phys. Rev. Lett. **66**, 100–103 (1991).

[83] L. Gor'kov and A. Sokol, "Nematic state in an exchange Heisenberg Hamiltonian," Pis'ma Zh. Eksp. Teor. Fiz. **52**, 1103 (1990), [JETP Lett. **52**, 504 (1990)].

[84] K. Totsuka, P. Lecheminant, and S. Capponi, "Semiclassical approach to competing orders in a two-leg spin ladder with ring exchange," Phys. Rev. B **86**, 014435 (2012).

[85] P. Lecheminant and K. Totsuka, "Competing orders and hidden duality symmetries in two-leg spin ladder systems," Phys. Rev. B **74**, 224426 (2006).

[86] Y. Yokoyama and C. Hotta, "Spin nematics next to spin singlets," Phys. Rev. B **97**, 180404 (2018).

[87] T. Hikihara, T. Misawa, and T. Momoi, "Spin nematics in frustrated spin-dimer systems with bilayer structure," Phys. Rev. B **100**, 214414 (2019).

[88] M. Sato, T. Momoi, and A. Furusaki, "NMR relaxation rate and dynamical structure factors in nematic and multipolar liquids of frustrated spin chains under magnetic fields," Phys. Rev. B **79**, 060406 (2009).

[89] M. Sato, T. Hikihara, and T. Momoi, "Field and temperature dependence of NMR relaxation rate in the magnetic quadrupolar liquid phase of spin-$\frac{1}{2}$ frustrated ferromagnetic chains," Phys. Rev. B **83**, 064405 (2011).

[90] M. Sato, T. Hikihara, and T. Momoi, "NMR relaxation rate in the field-induced octupolar liquid phase of spin-$\frac{1}{2}$ J_1-J_2 frustrated chains," J. Phys.: Conf. Ser. **320**, 012014 (2011).

[91] A. Smerald and N. Shannon, "Theory of NMR $1/T_1$ relaxation in a quantum spin nematic in an applied magnetic field," Phys. Rev. B **93**, 184419 (2016).

[92] A. Smerald and N. Shannon, "Theory of spin excitations in a quantum spin-nematic state," Phys. Rev. B **88**, 184430 (2013).

[93] A. Smerald, H. T. Ueda, and N. Shannon, "Theory of inelastic neutron scattering in a field-induced spin-nematic state," Phys. Rev. B **91**, 174402 (2015).

[94] S. C. Furuya, "Angular dependence of electron spin resonance for detecting the quadrupolar liquid state of frustrated spin chains," Phys. Rev. B **95**, 014416 (2017).

[95] S. C. Furuya and T. Momoi, "Electron spin resonance for the detection of long-range spin nematic order," Phys. Rev. B **97**, 104411 (2018).

[96] B. Schmidt, P. Thalmeier, and N. Shannon, "Magnetocaloric effect in the frustrated square lattice J_1-J_2 model," Phys. Rev. B **76**, 125113 (2007).

[97] F. Michaud, F. Vernay, and F. Mila, "Theory of inelastic light scattering in spin-1 systems: Resonant regimes and detection of quadrupolar order," Phys. Rev. B **84**, 184424 (2011).

[98] M. Sato and Y. Morisaku, "Two-photon driven magnon-pair resonance as a signature of spin-nematic order," Phys. Rev. B **102**, 060401 (2020).

[99] M. Enderle, C. Mukherjee, B. Fåk, R. K. Kremer, J.-M. Broto, H. Rosner, S.-L. Drechsler, J. Richter, J. Malek, A. Prokofiev, W. Assmus, S. Pujol, J.-L. Raggazzoni, H. Rakoto, M. Rheinstädter, and H. M. Rønnow, "Quantum helimagnetism of the frustrated spin-$\frac{1}{2}$ chain $LiCuVO_4$," Europhys. Lett. **70**, 237–243 (2005).

[100] L. E. Svistov, T. Fujita, H. Yamaguchi, S. Kimura, K. Omura, A. Prokofiev, A. I. Smirnov, Z. Honda, and M. Hagiwara, "New high magnetic field phase of the frustrated S = 1/2 chain compound $LiCuVO_4$," JETP Lett. **93**, 21–25 (2011).

[101] A. Orlova, E. L. Green, J. M. Law, D. I. Gorbunov, G. Chanda, S. Krämer, M. Horvatić, R. K. Kremer, J. Wosnitza, and G. L. J. A. Rikken, "Nuclear Magnetic Resonance Signature of the Spin-Nematic Phase in $LiCuVO_4$ at High Magnetic Fields," Phys. Rev. Lett. **118**, 247201 (2017).

[102] K. Nawa, Y. Okamoto, A. Matsuo, K. Kindo, Y. Kitahara, S. Yoshida, S. Ikeda, S. Hara, T. Sakurai, S. Okubo, H. Ohta, and Z. Hiroi, "$NaCuMoO_4(OH)$ as a Candidate Frustrated J_1–J_2 Chain Quantum Magnet," J. Phys. Soc. Jpn. **83**, 103702 (2014), https://doi.org/10.7566/JPSJ.83.103702 .

[103] M. Hase, H. Kuroe, K. Ozawa, O. Suzuki, H. Kitazawa, G. Kido, and T. Sekine, "Magnetic properties of $Rb_2Cu_2Mo_3O_{12}$ including a one-dimensional spin-1/2 Heisenberg system with ferromagnetic first-nearest-neighbor and antiferromagnetic second-nearest-neighbor exchange interactions," Phys. Rev. B **70**, 104426 (2004).

[104] M. Hase, K. Ozawa, O. Suzuki, H. Kitazawa, G. Kido, H. Kuroe, and T. Sekine, "Magnetism of $A_2Cu_2Mo_3O_{12}$ (A = Rb or Cs): Model compounds of a one-dimensional spin-1/2 Heisenberg system with ferromagnetic first-nearest-neighbor and antiferromagnetic second-nearest-neighbor interactions," J. Appl. Phys. **97**, 10B303 (2005), https://doi.org/10.1063/1.1851675 .

[105] A. U. B. Wolter, F. Lipps, M. Schäpers, S.-L. Drechsler, S. Nishimoto, R. Vogel, V. Kataev, B. Büchner, H. Rosner, M. Schmitt, M. Uhlarz, Y. Skourski, J. Wosnitza, S. Süllow, and K. C. Rule, "Magnetic properties and exchange integrals of the frustrated chain cuprate linarite $PbCuSO_4(OH)_2$," Phys. Rev. B **85**, 014407 (2012).

[106] B. Willenberg, M. Schäpers, K. C. Rule, S. Süllow, M. Reehuis, H. Ryll, B. Klemke, K. Kiefer, W. Schottenhamel, B. Büchner, B. Ouladdiaf, M. Uhlarz, R. Beyer, J. Wosnitza, and A. U. B. Wolter, "Magnetic Frustration in a Quantum Spin Chain: The Case of Linarite $PbCuSO_4(OH)_2$," Phys. Rev. Lett. **108**, 117202 (2012).

[107] Z. Hiroi, M. Hanawa, N. Kobayashi, M. Nohara, H. Takagi, Y. Kato, and M. Takigawa, "Spin-1/2 Kagomé-Like Lattice in Volborthite $Cu_3V_2O_7(OH)_2 \cdot 2H_2O$," J. Phys. Soc. Jpn. **70**, 3377–3384 (2001), https://doi.org/10.1143/JPSJ.70.3377 .

[108] F. Bert, D. Bono, P. Mendels, F. Ladieu, F. Duc, J.-C. Trombe, and P. Millet, "Ground State of the Kagomé-Like $S = 1/2$ Antiferromagnet Volborthite $Cu_3V_2O_7(OH)_2 \cdot 2H_2O$," Phys. Rev. Lett. **95**, 087203 (2005).

[109] R. Nath, A. A. Tsirlin, H. Rosner, and C. Geibel, "Magnetic properties of $BaCdVO(PO_4)_2$: A strongly frustrated spin-$\frac{1}{2}$ square lattice close to the quantum critical regime," Phys. Rev. B **78**, 064422 (2008).

[110] R. Nath, Y. Furukawa, F. Borsa, E. E. Kaul, M. Baenitz, C. Geibel, and D. C. Johnston, "Single-crystal ^{31}P NMR studies of the frustrated square-lattice compound $Pb_2(VO)(PO_4)_2$," Phys. Rev. B **80**, 214430 (2009).

[111] M. Gen, T. Nomura, D. I. Gorbunov, S. Yasin, P. T. Cong, C. Dong, Y. Kohama, E. L. Green, J. M. Law, M. S. Henriques, J. Wosnitza, A. A. Zvyagin, V. O. Cheranovskii, R. K. Kremer, and S. Zherlitsyn, "Magnetocaloric effect and spin-strain coupling in the spin-nematic state of $LiCuVO_4$," Phys. Rev. Research **1**, 033065 (2019).

[112] D. Hirobe, M. Sato, M. Hagihala, Y. Shiomi, T. Masuda, and E. Saitoh, "Magnon Pairs and Spin-Nematic Correlation in the Spin Seebeck Effect," Phys. Rev. Lett. **123**, 117202 (2019).

[113] M. Yoshida, K. Nawa, H. Ishikawa, M. Takigawa, M. Jeong, S. Krämer, M. Horvatić, C. Berthier, K. Matsui, T. Goto, S. Kimura, T. Sasaki, J. Yamaura, H. Yoshida, Y. Okamoto, and Z. Hiroi, "Spin dynamics in the high-field phases of volborthite," Phys. Rev. B **96**, 180413 (2017).

[114] Y. Kohama, H. Ishikawa, A. Matsuo, K. Kindo, N. Shannon, and Z. Hiroi, "Possible observation of quantum spin-nematic phase in a frustrated magnet," Proc. Natl. Acad. Sci. USA (2019), 10.1073/pnas.1821969116, https://www.pnas.org/content/early/2019/05/08/1821969116.full.pdf .

[115] O. Janson, J. Richter, P. Sindzingre, and H. Rosner, "Coupled frustrated quantum spin-$\frac{1}{2}$ chains with orbital order in volborthite $Cu_3V_2O_7(OH)_2 \cdot 2H_2O$," Phys. Rev. B **82**, 104434 (2010).

[116] H. Yoshida, J.-i. Yamaura, M. Isobe, Y. Okamoto, G. J. Nilsen, and Z. Hiroi, "Orbital switching in a frustrated magnet," Nat. Commun. **3**, 1–5 (2012).

[117] H. Ishikawa, M. Yoshida, K. Nawa, M. Jeong, S. Krämer, M. Horvatić, C. Berthier, M. Takigawa, M. Akaki, A. Miyake, M. Tokunaga, K. Kindo, J. Yamaura, Y. Okamoto, and Z. Hiroi, "One-Third Magnetization Plateau with a Preceding Novel Phase in Volborthite," Phys. Rev. Lett. **114**, 227202 (2015).

[118] H. Yoshida, Y. Okamoto, T. Tayama, T. Sakakibara, M. Tokunaga, A. Matsuo, Y. Narumi, K. Kindo, M. Yoshida, M. Takigawa, and Z. Hiroi, "Magnetization "Steps" on a Kagome Lattice in Volborthite," J. Phys. Soc. Jpn. **78**, 043704 (2009), https://doi.org/10.1143/JPSJ.78.043704 .

[119] Y. Okamoto, M. Tokunaga, H. Yoshida, A. Matsuo, K. Kindo, and Z. Hiroi, "Magnetization plateaus of the spin-$\frac{1}{2}$ kagome antiferromagnets volborthite and vesignieite," Phys. Rev. B **83**, 180407 (2011).

[120] O. Janson, S. Furukawa, T. Momoi, P. Sindzingre, J. Richter, and K. Held, "Magnetic Behavior of Volborthite $Cu_3V_2O_7(OH)_2 \cdot 2H_2O$ Determined by Coupled Trimers Rather than Frustrated Chains," Phys. Rev. Lett. **117**, 037206 (2016).

[121] H. Ohta, W. Zhang, S. Okubo, M. Tomoo, M. Fujisawa, H. Yoshida, Y. Okamoto, and Z. Hiroi, "S = 1/2 kagome lattice antiferromagnet $Cu_3V_2O_7(OH)_2 \cdot 2H_2O$ studied by high field ESR," J. Phys.: Conf. Ser. **145**, 012010 (2009).

[122] K. Y. Povarov, V. K. Bhartiya, Z. Yan, and A. Zheludev, "Thermodynamics of a frustrated quantum magnet on a square lattice," Phys. Rev. B **99**, 024413 (2019).

[123] M. Skoulatos, F. Rucker, G. J. Nilsen, A. Bertin, E. Pomjakushina, J. Ollivier, A. Schneidewind, R. Georgii, O. Zaharko, L. Keller, C. Rüegg, C. Pfleiderer, B. Schmidt, N. Shannon, A. Kriele, A. Senyshyn, and A. Smerald, "Putative spin-nematic phase in $BaCdVO(PO_4)_2$," Phys. Rev. B **100**, 014405 (2019).

[124] S. Meyer, B. Mertens, and H. Müller-Buschbaum, "$SrZn(VO)(PO_4)_2$ und $BaCd(VO)(PO_4)_2$: Zum $BaZn(VO)(PO_4)_2$-Typ verwandte, jedoch nicht isotype Vanadylphosphate / $SrZn(VO)(PO_4)_2$ and $BaCd(VO)(PO_4)_2$: Vanadylphosphates Related but not Isotypic to the $BaZn(VO)(PO_4)_2$ Type," Z. Naturforsch. B: Chem. Sci. **52**, 985–988 (1997).

[125] I. Terasaki, T. Igarashi, T. Nagai, K. Tanabe, H. Taniguchi, T. Matsushita, N. Wada, A. Takata, T. Kida, M. Hagiwara, K. Kobayashi, H. Sagayama, R. Kumai, H. Nakao, and Y. Murakami, "Absence of Magnetic Long Range Order in $Ba_3ZnRu_2O_9$: A Spin-Liquid Candidate in the $S = 3/2$ Dimer Lattice," J. Phys. Soc. Jpn. **86**, 033702 (2017).

[126] T. D. Yamamoto, H. Taniguchi, and I. Terasaki, "Dynamical coupling of dilute magnetic impurities with quantum spin liquid state in the S = 3/2 dimer compound $Ba_3ZnRu_2O_9$," J. Phys.: Condens. Matter **30**, 355801 (2018).

[127] J. Darriet, M. Drillon, G. Villeneuve, and P. Hagenmuller, "Interactions magnétiques dans des groupements binucléaires du Ruthénium +V," J. Solid State Chem. **19**, 213 – 220 (1976).

[128] P. Lightfoot and P. D. Battle, "The crystal and magnetic structures of $Ba_3NiRu_2O_9$, $Ba_3CoRu_2O_9$, and $Ba_3ZnRu_2O_9$," J. Solid State Chem. **89**, 174 – 183 (1990).

[129] J. T. Rijssenbeek, P. Matl, B. Batlogg, N. P. Ong, and R. J. Cava, "Electrical and magnetic properties of a series of ternary barium metal ruthenates: $Ba_3MRu_2O_9$ (M = Fe, Co, Ni, Cu, and In)," Phys. Rev. B **58**, 10315–10318 (1998).

[130] J. T. Rijssenbeek, Q. Huang, R. W. Erwin, H. W. Zandbergen, and R. J. Cava, "The Crystal Structure of $Ba_3CuRu_2O_9$ and Comparison to $Ba_3MRu_2O_9$ (M=In, Co, Ni, and Fe)," J. Solid State Chem. **146**, 65 – 72 (1999).

[131] M. S. Senn, A. M. Arevalo-Lopez, T. Saito, Y. Shimakawa, and J. P. Attfield, "Nonmagnetic spin-singlet dimer formation and coupling to the lattice in the 6H perovskite $Ba_3CaRu_2O_9$," J. Phys.: Condens. Matter **25**, 496008 (2013).

[132] P. Beran, S. A. Ivanov, P. Nordblad, S. Middey, A. Nag, D. D. Sarma, S. Ray, and R. Mathieu, "Neutron powder diffraction study of $Ba_3ZnRu_{2-x}Ir_xO_9$ (x = 0, 1, 2) with 6H-type perovskite structure," Solid State Sci. **50**, 58 – 64 (2015).

[133] H. Kawamura and A. Yamamoto, "Vortex-Induced Topological Transition of the Bilinear–Biquadratic Heisenberg Antiferromagnet on the Triangular Lattice," J. Phys. Soc. Jpn. **76**, 073704 (2007), https://doi.org/10.1143/JPSJ.76.073704 .

[134] 夏目雄平・小川建吾, 『計算物理 I（基礎物理学シリーズ 13)』(朝倉書店, 2002).

[135] 夏目雄平・小川建吾・鈴木敏彦, 『計算物理 III（基礎物理学シリーズ 15)』(朝倉書店, 2002).

[136] 伊庭幸人・種村正美・大森裕浩・和合肇・佐藤整尚・高橋明彦, 『統計科学のフロンティア 12　計算統計 II マルコフ連鎖モンテカルロ法とその周辺』(岩波書店（岩波オンデマンドブックス）, 2018) オンデマンド版.

[137] N. Metropolis, A. W. Rosenbluth, M. N. Rosenbluth, A. H. Teller, and E. Teller, "Equation of State Calculations by Fast Computing Machines," J. Chem. Phys. **21**, 1087–1092 (1953), https://doi.org/10.1063/1.1699114 .

[138] H. Suwa and S. Todo, "Markov Chain Monte Carlo Method without Detailed Balance," Phys. Rev. Lett. **105**, 120603 (2010).

[139] K. Hukushima and K. Nemoto, "Exchange Monte Carlo Method and Application to Spin Glass Simulations," J. Phys. Soc. Jpn. **65**, 1604–1608 (1996), https://doi.org/10.1143/JPSJ.65.1604 .

[140] H. Kawamura, "Spin-Wave Analysis of the Antiferromagnetic Plane Rotator Model on the Triangular Lattice—Symmetry Breaking in a Magnetic Field," J. Phys. Soc. Jpn. **53**, 2452–2455 (1984), https://doi.org/10.1143/JPSJ.53.2452 .

[141] C. L. Henley, "Ordering due to disorder in a frustrated vector antiferromagnet," Phys. Rev. Lett. **62**, 2056–2059 (1989).

[142] N. D. Mermin and H. Wagner, "Absence of Ferromagnetism or Antiferromagnetism in One- or Two-Dimensional Isotropic Heisenberg Models," Phys. Rev. Lett. **17**, 1133–1136 (1966).

[143] V. L. Berezinskii, "Destruction of long-range order in one-dimensional and two-dimensional systems having a continuous symmetry group I. Classical systems," Sov. Phys. JETP **32**, 493–500 (1971), [Zh. Eksp. Teor. Fiz. **59**, 907 (1970)].

[144] V. L. Berezinskii, "Destruction of long-range order in one-dimensional and two-dimensional systems possessing a continuous symmetry group. II. quantum systems," Sov. Phys. JETP **34**, 610–616 (1972), [Zh. Eksp. Teor. Fiz. **61**, 1144 (1971)].

[145] J. M. Kosterlitz and D. J. Thouless, "Ordering, metastability and phase transitions in two-dimensional systems," J. Phys. C: Solid State Phys. **6**, 1181–1203 (1973).

[146] R. Pohle, Y. Akagi, K. Remund, and N. Shannon, "Numerical Integration of Equations of Motion for Spin-1 Magnets," (2020), JPS 2020 Autumn Meeting, 10aC1-3.

[147] D. Yamamoto, C. Suzuki, G. Marmorini, S. Okazaki, and N. Furukawa, "Quantum and Thermal Phase Transitions of the Triangular SU(3) Heisenberg Model under Magnetic Fields," Phys. Rev. Lett. **125**, 057204 (2020).

[148] N. D. Mermin, "The topological theory of defects in ordered media," Rev. Mod. Phys. **51**, 591–648 (1979).

[149] H. Kawamura and S. Miyashita, "Phase Transition of the Two-Dimensional Heisenberg Antiferromagnet on the Triangular Lattice," J. Phys. Soc. Jpn. **53**, 4138–4154 (1984), https://doi.org/10.1143/JPSJ.53.4138 .

[150] H. Kawamura, A. Yamamoto, and T. Okubo, "Z_2-Vortex Ordering of the Triangular-Lattice Heisenberg Antiferromagnet," J. Phys. Soc. Jpn. **79**, 023701 (2010), https://doi.org/10.1143/JPSJ.79.023701 .

[151] R. C. Richardson, "The Pomeranchuk effect," Rev. Mod. Phys. **69**, 683–690 (1997).

[152] I. Pomeranchuk, "On the theory of liquid ^{3}He," Zh. Eksp. Teor. Fiz. **20**, 919 (1950).

[153] H. Kawamura and S. Miyashita, "Phase Transition of the Heisenberg Antiferromagnet on the Triangular Lattice in a Magnetic Field," J. Phys. Soc. Jpn. **54**, 4530–4538 (1985), https://doi.org/10.1143/JPSJ.54.4530 .

[154] L. Seabra, T. Momoi, P. Sindzingre, and N. Shannon, "Phase diagram of the classical Heisenberg antiferromagnet on a triangular lattice in an applied magnetic field," Phys. Rev. B **84**, 214418 (2011).

[155] H. Tsujii, C. R. Rotundu, T. Ono, H. Tanaka, B. Andraka, K. Ingersent, and Y. Takano, "Thermodynamics of the up-up-down phase of the $S = \frac{1}{2}$ triangular-lattice antiferromagnet Cs_2CuBr_4," Phys. Rev. B **76**, 060406 (2007).

[156] M. A. Continentino and A. S. Ferreira, "Solid state Pomeranchuk effect in unstable Kondo lattice systems," Solid State Commun. **131**, 195 – 199 (2004).

[157] M. A. Continentino and A. S. Ferreira, "Pomeranchuk effect in unstable materials based on $YbInCu_4$," Phys. Rev. B **69**, 233104 (2004).

[158] M. A. Continentino, A. S. Ferreira, P. G. Pagliuso, C. Rettori, and J. L. Sarrao, "Solid state pomeranchuk effect," Physica B: Condensed Matter **359-361**, 744 – 746 (2005), Proceedings of the International Conference on Strongly Correlated Electron Systems.

[159] A. V. Chubukov, "A difference in the properties of one-dimensional antiferromagnets with integer and half-integer spins," JETP Lett. **49**, 129 (1989), [Pis'ma Zh. Eksp. Teor. Fiz. **49**, 108 (1989)].

[160] S. Sachdev and R. N. Bhatt, "Bond-operator representation of quantum spins: Mean-field theory of frustrated quantum Heisenberg antiferromagnets," Phys. Rev. B **41**, 9323–9329 (1990).

[161] W. Brenig and K. W. Becker, "Magnetism of a tetrahedral cluster spin chain," Phys. Rev. B **64**, 214413 (2001).

[162] H.-T. Wang, H. Q. Lin, and J.-L. Shen, "Bond-operator analysis of the magnetization of spin chains," Phys. Rev. B **61**, 4019–4025 (2000).

[163] B. Kumar, "Bond operators and triplon analysis for spin-S dimer antiferromagnets," Phys. Rev. B **82**, 054404 (2010).

[164] T. Nikuni, M. Oshikawa, A. Oosawa, and H. Tanaka, "Bose-Einstein Condensation of Dilute Magnons in $TlCuCl_3$," Phys. Rev. Lett. **84**, 5868–5871 (2000).

[165] C. Lanczos, "An Iteration Method for the Solution of the Eigenvalue Problem of Linear Differential and Integral Operators," J. Res. Natl. Bur. Stand. **45**, 255 (1950).

[166] K. Wu, A. Canning, H. Simon, and L.-W. Wang, "Thick-Restart Lanczos Method for Electronic Structure Calculations," J. Comput. Phys. **154**, 156 – 173 (1999).

[167] K. Wu and H. Simon, "Thick-Restart Lanczos Method for Large Symmetric Eigenvalue Problems," SIAM J. Matrix Anal. Appl. **22**, 602–616 (2000), https://doi.org/10.1137/S0895479898334605 .

[168] P. W. Anderson, "An Approximate Quantum Theory of the Antiferromagnetic Ground State," Phys. Rev. **86**, 694–701 (1952).

[169] K. Penc, M. Mambrini, P. Fazekas, and F. Mila, "Quantum phase transition in the SU(4) spin-orbital model on the triangular lattice," Phys. Rev. B **68**, 012408 (2003).

[170] B. Bernu, C. Lhuillier, and L. Pierre, "Signature of Néel order in exact spectra of quantum antiferromagnets on finite lattices," Phys. Rev. Lett. **69**, 2590–2593 (1992).

[171] B. Bernu, P. Lecheminant, C. Lhuillier, and L. Pierre, "Exact spectra, spin susceptibilities, and order parameter of the quantum Heisenberg antiferromagnet on the triangular lattice," Phys. Rev. B **50**, 10048–10062 (1994).

[172] C. Lhuillier, "Frustrated Quantum Magnets," (2005), arXiv:cond-mat/0502464 [cond-mat.str-el] (Lecture notes (fall 2002) " Ecole de troisieme cycle de Suisse Romande").

[173] G. Misguich and P. Sindzingre, "Detecting spontaneous symmetry breaking in finite-size spectra of frustrated quantum antiferromagnets," J. Phys.: Condens. Matter **19**, 145202 (2007).

[174] A. W. Sandvik, "Computational Studies of Quantum Spin Systems," AIP Conf. Proc. **1297**, 135–338 (2010), https://aip.scitation.org/doi/pdf/10.1063/1.3518900 .

[175] P. Lecheminant, B. Bernu, C. Lhuillier, L. Pierre, and P. Sindzingre, "Order versus disorder in the quantum Heisenberg antiferromagnet on the kagomé lattice using exact spectra analysis," Phys. Rev. B **56**, 2521–2529 (1997).

[176] F. Mezzacapo and J. I. Cirac, "Ground-state properties of the spin-1/2 antiferromagnetic Heisenberg model on the triangular lattice: a variational study based on entangled-plaquette states," New J. Phys. **12**, 103039 (2010).

[177] J. H. P. Colpa, "Diagonalization of the quadratic boson hamiltonian," Physica A **93**, 327–353 (1978).

[178] M. Ueda and M. Koashi, "Theory of spin-2 Bose-Einstein condensates: Spin correlations, magnetic response, and excitation spectra," Phys. Rev. A **65**, 063602 (2002).

[179] T.-L. Ho, "Spinor Bose Condensates in Optical Traps," Phys. Rev. Lett. **81**, 742–745 (1998).

[180] T. Hikihara and O. A. Starykh, "Phase diagram of the frustrated spin ladder," Phys. Rev. B **81**, 064432 (2010).

[181] H. D. Zhou, A. Kiswandhi, Y. Barlas, J. S. Brooks, T. Siegrist, G. Li, L. Balicas, J. G. Cheng, and F. Rivadulla, "Orbital, charge, and spin couplings in $Ru_2{}^{5+}O_9$ dimers of $Ba_3CoRu_2O_9$," Phys. Rev. B **85**, 041201 (2012).

[182] S. V. Streltsov, "Magnetic moment suppression in $Ba_3CoRu_2O_9$: Hybridization effect," Phys. Rev. B **88**, 024429 (2013).

[183] M. Drillon, "Biquadratic exchange interaction between Ru^{5+} ions in (Ru_2O_9) clusters," Solid State Commun. **21**, 425 – 427 (1977).

[184] 横山祐人, "リング交換相互作用が誘起するネマティック固体・液体相," (2018), 修士論文（東京大学大学院総合文化研究科広域科学専攻）.

[185] J. R. Schrieffer and P. A. Wolff, "Relation between the Anderson and Kondo Hamiltonians," Phys. Rev. **149**, 491–492 (1966).

[186] R. Winkler, "Quasi-Degenerate Perturbation Theory," in Spin–Orbit Coupling Effects in Two-Dimensional Electron and Hole Systems (Springer Berlin Heidelberg, Berlin, Heidelberg, 2003) pp. 201–206.

[187] M. Takahashi, "Half-filled Hubbard model at low temperature," J. Phys. C: Solid State Phys. **10**, 1289–7301 (1977).

[188] A. Yoshimori and S. Inagaki, "Fourth Order Interaction Effects on the Antiferromagnetic Structures. I. fcc Hubbard Model," J. Phys. Soc. Jpn. **44**, 101–107 (1978), https://doi.org/10.1143/JPSJ.44.101 .

[189] A. H. MacDonald, S. M. Girvin, and D. Yoshioka, "$\frac{t}{U}$ expansion for the Hubbard model," Phys. Rev. B **37**, 9753–9756 (1988).

[190] C. J. Calzado and J.-P. Malrieu, "Origin and evaluation of the four-spin operators in magnetic lattices," Phys. Rev. B **69**, 094435 (2004).

[191] M. Hoffmann and S. Blügel, "Systematic derivation of realistic spin models for beyond-Heisenberg solids," Phys. Rev. B **101**, 024418 (2020).

[192] J. Kanamori, "Electron Correlation and Ferromagnetism of Transition Metals," Prog. Theor. Phys. **30**, 275–289 (1963).

[193] A. Georges, L. d. Medici, and J. Mravlje, "Strong Correlations from Hund's Coupling," Ann. Rev. Condens. Matter Phys. **4**, 137–178 (2013), https://doi.org/10.1146/annurev-conmatphys-020911-125045 .

[194] 上村洸・菅野暁・田辺行人, 『配位子場理論とその応用』 (裳華房, 1969) [第 16 版 7 刷 (2014)].

[195] F. Michaud, F. Vernay, S. R. Manmana, and F. Mila, "Antiferromagnetic Spin-S Chains with Exactly Dimerized Ground States," Phys. Rev. Lett. **108**, 127202 (2012).

[196] F. Mila and F.-C. Zhang, "On the origin of biquadratic exchange in spin 1 chains," Euro. Phys. J. B **16**, 7–10 (2000).

[197] J. B. Goodenough, "An interpretation of the magnetic properties of the perovskite-type mixed crystals $La_{1-x}Sr_xCoO_{3-\lambda}$," J. Phys. Chem. Solids **6**, 287 – 297 (1958).

[198] J. Kanamori, "Superexchange interaction and symmetry properties of electron orbitals," J. Phys. Chem. Solids **10**, 87 – 98 (1959).

[199] G. Marsaglia, "Choosing a Point from the Surface of a Sphere," Ann. Math. Statist. **43**, 645–646 (1972).

[200] G. E. P. Box and M. E. Muller, "A Note on the Generation of Random Normal Deviates," Ann. Math. Statist. **29**, 610–611 (1958).

[201] R. G. Miller, "The Jackknife–A Review," Biometrika **61**, 1–15 (1974).

[202] 杉原正顯，室田一雄, 『線形計算の数理』(岩波書店（岩波オンデマンドブックス），2016) オンデマンド版.